2009

The Behaviour of Micropiles and Tiebacks in Cohesionless Soils

Cosmin Dan Urian
Western University

The Behaviour of Micropiles and Tiebacks in Cohesionless Soils

(Thesis Format: Monograph)

by

Cosmin Dan Urian

Graduate program in Engineering Science
Department of Civil and Environmental Engineering

A thesis submitted in partial fulfillment of
the requirements for
the degree of Master of Engineering Science

School of Graduate and Postdoctoral Studies
The University of Western Ontario
London, Ontario, Canada

Abstract

This thesis examines: (i) the response of reduced-scale micropiles and (ii) the pullout capacity of grouted tieback anchors in cohesionless soil. The primary objectives are to investigate how micropiles and grouted tiebacks obtain their compressive and pull-out capacity, respectively, to assess current design practices for micropiles and to correlate the pull-out capacity of grouted tieback anchors to standard penetration test (SPT) N-values, referring to American Society for Testing and Materials (ASTM D1586) and construction method. To achieve these objectives, the following tests were conducted and/or evaluated: (i) compression load tests on reduced-scale micropiles constructed in sand, and (ii) pull-out tests on full-scale grouted anchors constructed in sand and silt.

Thirty-two reduced-scale micropiles were constructed in cohesionless soil and load tested to failure to assess the adequacy of current Federal Highway Administration (FHWA) design methods for micropiles. Six of these reduced-scale micropiles were constructed in cohesionless soil with earth pressure cells in the sand to assess the stress regime around the micropiles during loading. Finally, the pullout capacity of 78 grouted anchors installed in cohesionless soil was assessed from full-scale tieback anchor tests and the capacity is correlated to basic soil parameters. The results reported in this thesis highlight the importance of interface friction and dilatancy as well as the stiffness of the soil surrounding micropiles and anchors.

Keywords: Micropile, Tieback, Friction Factors, Pile-Soil Interaction, Dilation Angle, Cavity Expansion, Grout Pressure, Finite Element, Experimental Investigation

For from Him and through Him and to Him are all things.
To Him be the glory forever.

Romans 11:36

Acknowledgements

The preparation of this thesis has been funded through the National Science and Engineering Research Council of Canada, to whom I am really grateful for the opportunity to spend 5 months within a geostructural engineering company where I obtained very useful hands-on experience.

I would like to express my appreciation to my advisor Dr. Sean Hinchberger for his support, guidance and assistance throughout the entire period of my Masters program. I would like to thank him for the patience he has shown to me and the mentoring he provided, which helped me to complete this thesis.

Special thanks to my sponsoring company Isherwood Associates especially to Daniela Ramirez for her involvement and dedication in showing and explaining me how micropiles and tiebacks are designed and constructed.

The experimental work would not have been possible without the help and guidance of my advisor, Dr. Sean Hinchberger and also Mr. Wilbert Logan and Ms. Melodie Richards as UWO technical support staff, Clayton of UWO Machine Services and some of the UWO graduate students. Thank you all!

Table of Contents

Chapter 3: Geotechnical Characterization of Clarke Side Road Sand

List of Tables

Page

Chapter 2: Literature Review - Micropiles and Tieback Anchors

Chapter 3: Geotechnical Characterization of Clarke Side Road Sand

Chapter 4: Reduced-scale Load Tests on Micropiles in Cohesionless Soil

Chapter 5: Investigation of the Radial Stress Field around Micropiles

Chapter 6: Case Study - Tieback Anchors in Sandy Soils

List of Figures

Page

Chapter 2: Literature Review - Micropiles and Tieback Anchors

Chapter 3: Geotechnical Characterization of Clarke Side Road Sand

Chapter 4: Reduced-scale Load Tests on Micropiles in Cohesionless Soil

Chapter 5: Investigation of The Radial Stress Field around Micropiles

Chapter 6: Case Study - Tieback Anchors in Sandy Soils

Appendix B: Earth Pressure Cells

Appendix C: Load-displacement Curves for Tieback Anchors in Sandy Soils in the GTA

Nomenclature

α_g	*anchorage coefficient that depends on the soil type and density conditions*
α_r	*roughness angle (°)*
a	*radius of the cylindrical cavity (m)*
a_0	*initial radius of the cylindrical cavity (m)*
$\frac{a}{a_0}$	*radial strain in cavity expansion*
a_d	*dimensionless empirical coefficient*
A	*cross-sectional area of the specimen for permeability test (m^2)*
A_b	*end area of micropile (m^2)*
A_s	*area of the shaft in contact with the soil (m^2)*
θ	*tieback inclination angle (°)*
β	*empirical correlations depending on the soil type and drilling method*
c	*temperature correction for hydraulic conductivity*
c'	*effective cohesion intercept*
c_c	*coefficient of curvature*
c_u	*coefficient of uniformity*
δ	*effective friction angle of the pile-to-soil interface (°)*
δ_v	*vertical displacement of micropiles (mm)*
$\boldsymbol{\delta_{cr}}$	*creep movement at 10min or 60min at the performance test load (mm)*
δ_e	*elastic movement at maximum load (mm)*
δ_p	*inelastic movement at maximum load (mm)*
δ_v	*vertical displacement of micropile (mm)*

d_{10}	*diameter of soil particles corresponding to percent finer than 10% (mm)*
d_{30}	*diameter of soil particles corresponding to percent finer than 30% (mm)*
d_{60}	*diameter of soil particles corresponding to percent finer than 60% (mm)*
d_{85}	*diameter of soil particles corresponding to percent finer than 85% (mm)*
$\Delta_{1\ to\ 4}$	*15-cm segments along micropile shaft for roughness measurements*
ΔP	*pressure increment (kPa)*
ΔS	*settlement induced by ΔP (mm)*
$\Delta\sigma_v$	*stress changes in vertical direction (kPa)*
Δt	*time interval for water in casing to drop from h_1 to h_2 (s)*
D_1	*distance from ground surface to position of tieback (m)*
D_b	*diameter at micropile tip (cm)*
D_c	*outer diameter of micropile casing(cm)*
D_g	*diameter of grouted section of micropile or tieback (cm)*
D_r	*relative density of sand (%)*
E	*elastic modulus (Young's modulus)(MPa)*
E_s	*secant elastic modulus (MPa)*
$\emptyset'$	*effective friction angle (°)*
$\emptyset_i$	*internal friction angle at the inteface (°)*
$\emptyset'_{cv}$	*constant volume effective internal friction angle (°)*
$\emptyset'_p$	*peak effective internal friction angle (°)*
$\emptyset_s$	*soil angle used in finite element analysis (°)*
f_s	*skin resistance (kPa)*
γ	*bulk unit weight of soil (kN/m^3)*

G	*shear modulus (MPa)*
h	*difference in total head applied between the manometers during test (m)*
h_1	*head of water at the start of the test (m)*
h_2	*head of water at the end of the elapsed time (m)*
$\boldsymbol{h_r}$	*roughness height (mm)*
$\boldsymbol{H_r}$	*mean roughness height (mm)*
i	*mean roughness angle (°)*
k	*hydraulic conductivity (m/s) or (cm/s)*
k_H	*horizontal hydraulic conductivity (cm/s)*
k_V	*vertical hydraulic conductivity (cm/s)*
K'	*combined factor depending on grout pressure*
K_0	*coefficient of lateral earth pressure at rest*
K_s	*lateral earth pressure coefficient*
L	*length between manometer outlets (m)*
L_c	*length of cased section of a micropile or tieback (m)*
L_f	*unbonded of free length of tieback anchor (m)*
L_g	*length of grouted section of a micropile or tieback (m)*
ν	*Poisson's ratio*
n	*empirical factor that depends on the permeability of the soil, the grout pressure and the depth of overburden*
N	*shear force (N)*
N_{60}	*SPT value without correction for overburden pressure*
N_q	*bearing capacity factor*
p_0	*initial internal cavity pressure (kPa)*

p	*final internal cavity pressure (kPa)*
P	*vertical load (kN)*
$\boldsymbol{P_D}$	*design load (kN)*
p_g	*grout pressure (kPa)*
$\boldsymbol{P_{max}}$	*maximum load applied during performance tests (kN)*
$\boldsymbol{p_0}$	*micropile initial radial stresses in cavity expansion theory (kPa)*
P_{ULT}	*ultimate load capacity (kN)*
P_{ult}^{test}	*ultimate capacity from the test (kN)*
P_{ult}^{FHWA}	*ultimate load capacity of micropiles using FHWA expressions (kN)*
P^Y	*ultimate load at yielding (kN)*
Q	*quantity of water discharged during test (volume of flow) (m^3)*
Q_b	*tip bearing resistance of a micropile (kN)*
Q_b^Y	*tip bearing resistance of a micropile at yielding (kN)*
Q_s^Y	*shaft resistance of micropiles at yielding (kN)*
Q_s^{FHWA}	*shaft resistance of micropiles calculated using FHWA expressions (kN)*
Q_s	*shaft resistance of micropiles (kN)*
ρ_d	*dry density (kN/m^3)*
$\rho_{d\,max}$	*maximum dry density (kN/m^3)*
r	*micropile radius (m)*
r_p	*radius of plastic zone around micropile (m)*
R	*internal radius of casing (m)*
r_0	*distance from center of micropile to considered point (m)*
σ_1,σ_2	*distribution of pressure around tieback (kPa)*

σ_H	*stress in horizontal direction (radial stress) (kPa)*
σ'_N	*normal stress in shear test (kPa)*
σ_r, σ_θ	*stress field around the cylindrical cavity (kPa)*
σ'_R	*radial effective stress (kPa)*
σ'_V	*vertical effective stress (kPa)*
σ'_{V0}	*vertical effective stress in soil before loading (kPa)*
τ_{mob}	*mobilized shear strength of the anchor in bonded zone (kPa)*
θ	*roughness angle (°)*
t	*time for quantity Q to be discharged during test (s)*
u	*pore water pressure at z_m (kPa)*
V_g	*volume of injected grout (cm^3)*
w/c	*water to cement ratio*
w_{opt}	*optimum moisture content (%)*
W_p	*weight of micropile (kN)*
ψ_0	*initial dilatation angle (°)*
ψ_i	*interface dilation angle (°)*
ψ_p	*peak dilation angle (°)*
ψ_s	*soil dilation angle (°)*
z	*distance from ground surface to a certain point in ground (ft)*
z_m	*distance from tieback midpoint to ground surface (m)*

Chapter 1

Introduction

1.1 General

This thesis examines the behaviour of micropiles and grouted tieback anchors in cohesionless soils during loading to failure. Tieback anchors (tiebacks) are often used for earth retention systems, which are required during the construction of buried structures in congested urban centers. Micropiles are typically used to upgrade the capacity of existing foundations that have degraded or have been damaged since construction or that require upgrading to meet new codes or to support new loads. Construction methods for tiebacks and micropiles are very similar. Typically, for both, a borehole is drilled through soil, a structural element such as a post-tensioning tendon (tiebacks) or a casing and rebar (micropiles) are centered in the borehole, and the borehole is subsequently grouted under pressure. In spite of numerous studies involving tiebacks and micropiles, there is still much to be learned about how these geostructural elements perform.

In order to study micropiles in cohesionless soils, thirty-two reduced scale micropiles were constructed in a 1.35m diameter by 1.55m deep cylindrical steel calibration chamber filled with uniform sand and loaded to failure. The micropile diameter and grout pressure were varied to study the influence of these factors on micropile capacity. Six of the micropiles had earth pressure cells embedded in the soil around the micropiles to measure the radial and vertical stress regime during construction and loading. These load tests help to obtain a better understanding of the mechanism by which micropiles resist

axial loads. For the tieback study, seventy-eight anchor pull-out tests were evaluated. The tieback pullout tests were performed by Isherwood Associates and the data was analyzed by the author to assess factors such as construction method and soil density on anchor capacity.

The following sections described the main objective of this thesis and describe the thesis outline and content of the chapters. In general, the research presented in this thesis should be of interest to construction engineers in the micropile and tieback industry.

1.2 Thesis Objective

This thesis had the following objectives organized according to micropiles and tieback anchors, respectively.

Micropiles ***(Chapter 4** and **Chapter5)***

(i) To assess the accuracy of current methods used to estimate the geotechnical capacity of micropiles constructed in cohesionless soils and subject to axial compression.

(ii) To evaluate the influence of grout pressure on the ultimate geotechnical resistance of micropiles in cohesionless soils and subject to axial compression.

(iii) To assess the influence of grout pressure on the roughness of micropiles constructed in cohesionless soils.

(iv) To measure the stress regime in the soil around micropiles during construction and loading in axial compression.

*Tieback Anchors (**Chapter 6**)*

(i) To compile case records for seventy-eight tieback pullout tests performed on tieback anchors in cohesionless soils in the Greater Toronto Area (*GTA*).

(ii) To evaluate if the pullout capacity of tieback anchors in cohesionless soils is affected by the standard penetration test (SPT) N-values of the soil surrounding the anchor, where SPT tests are performed according to American Society for Testing and Materials (ASTM), standard D1586.

(iii) To assess the influence of construction method on the pullout capacity of tieback anchors in cohesionless soils.

(iv) To assess whether there is evidence that the mechanisms governing the pullout capacity of tieback anchors in cohesionless soils are similar to those governing micropiles.

1.3 Outline of Thesis

This thesis contains seven chapters and three appendixes as described below.

Chapter 2 contains a brief literature review. It describes the classification of micropiles and tiebacks, and methods for calculating their geotechnical resistance. The current state-of-the-art for assessing the performance of micropiles during load testing is discussed and existing studies involving micropile and anchor capacities are summarized.

Chapter 3 describes a laboratory study that was performed to characterize the engineering properties of the sand used during the micropile load tests described in ***Chapter 4*** and ***Chapter 5***. Parameters such as internal friction angle, dialation angle and relative density were measured and are reported in this chapter.

Chapter 4 describes a series of reduced-scale micropile load tests performed to assess the accuracy of current methods for estimating the geotechnical capacity of micropiles subject to axial compression. This chapter also summarizes design equations used to calculate the axial capacity of micropiles, and the results of thirty-two load tests on micropiles constructed in uniform sand in a 1.35m by 1.55m cylindrical steel calibration chamber. To conclude, the measured micropile loads at failure are compared with the capacity estimated using design equations, and the influence of factors such as micropile roughness and grout pressure during construction are assessed.

Chapter 5 describes the methodology and results of six micropile tests that were performed with earth pressure cells embedded in the soil surrounding the piles. The results of these tests show the detailed radial and vertical stress regime around micropiles during loading. In addition, the micropile load tests are interpreted using a non-linear finite element program to show that dilation on the pile-to-soil interface has a major impact on the ultimate geotechnical capacity of micropiles in axial compression.

Chapter 6 investigates the influence of the *SPT N-values* and construction methods on the mobilized shear strength of tiebacks in the Greater Toronto Area during pullout tests in sandy soils.

A summary of the findings of this study and their significance with respect to the design and construction of micropiles and tieback anchors is presented in ***Chapter 7***. In addition some recommendations for future research are provided.

Chapter 2
Literature Review - Micropiles and Tieback Anchors

2.1 Introduction

The objectives of this chapter are to define the specific micropile and tieback anchor geometry considered in this thesis, and to give a brief overview of typical design equations used to calculate the capacity of micropiles, and tiebacks. Micropiles are used mainly as foundation elements to resist static and seismic loads from structures. In contrast, tieback anchors are used to stabilize the sides of excavations.

2.2 Micropiles

2.2.1 General

Micropiles are small diameter (less than 300 mm), drilled and grouted piles that can be installed to provide foundation support for structures or general earth reinforcement. ***Figure 2.1*** shows the typical geometry of a micropile. The length of the micropile, L, can vary from a few meters to more than 30m. Typically the upper part of the micropile is equipped with a steel casing to provide flexural capacity to resist lateral loads. The casing length is denoted by L_c as in ***Figure 2.1***. The diameter of the casing, D_c, is approximately equal to the diameter of the borehole. Below the casing there is typically an uncased section represented by L_g in ***Figure 2.1***. The grout in this section, L_g, is typically injected under pressure and consequently the interface between the grout and soil is rough. In addition, the diameter of the micropile, D_g, varies along the micropile shaft. The degree of variation depends on the heterogeneity of the surrounding soil and its permeability to grout.

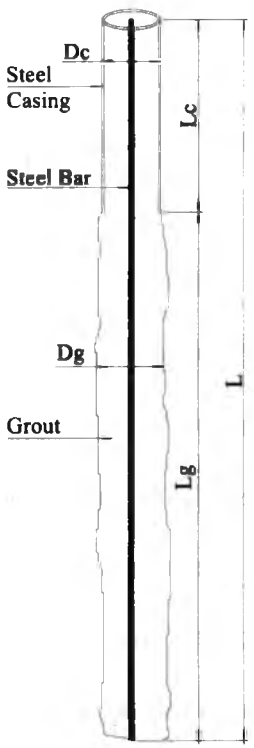

Figure 2.1 *Micropile Geometry*

Micropiles can be categorized into two groups depending on their load transfer mechanism: friction and end-bearing micropiles. Friction micropiles develop their resistance through the friction between its shaft and the adjacent soil. End-bearing micropiles provide resistance from the micropile tip that rests on or is socketed into firm soil or rock. Most micropiles operate as a combination of the two. However, the side resistance of micropiles is usually fully mobilized well before the maximum base resistance is reached (Franke 1993).

2.2.2 Micropile Construction Method

Micropiles can be constructed in a variety of geological environments using several different construction methods. However, this study considers the performance of micropiles constructed in cohesionless soils and built using the construction sequence illustrated in ***Figure 2.2***. The construction sequence is referred to below as the rotary duplex drilling (*RDD*) method.

Referring to ***Figure 2.2a***, rotary duplex drilling involves advancing a cased borehole through cohesionless soils using a rotary drill rig. In this construction method, an expandable drill bit is used to create a borehole that is slightly larger that the casing. The casing is advanced by applying pressure to the drill string, which expands the drill bit and also advances the casing. Water is typically used as the drilling fluid. After reaching the required depth (see ***Figure 2.2b***), the drill string is removed from the cased borehole and the casing is filled with tremied grout. Then, the casing is retracted incrementally (***Figure 2.2c***) and grout is injected into the surrounding soil under pressure during each increment. After several grout increments, the casing is cut-off slightly above the ground surface, and a steel bar is inserted into and centered in the micropile. On completion, the micropile comprises a cased section of length, L_c, and an uncased section, L_g, with a steel bar centered in the micropile as depicted in ***Figure 2.1***. Further details of the rotary duplex drill method can be found in Federal Highway Administration (*FHWA)* Drilled and Grouted Micropile Design Manual (*FHWA*, 1997).

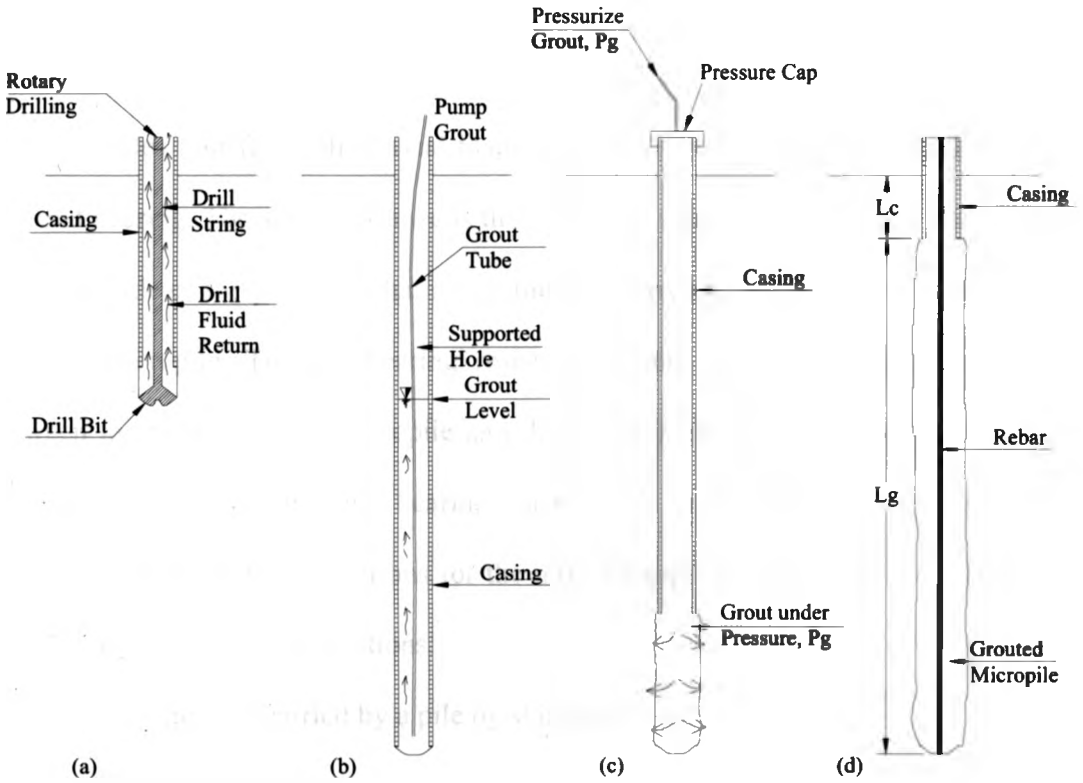

***Figure 2.2** Drilling Method*

It is generally agreed that the soil type and grouting method used (i.e., gravity or pressure grouting) influence the micropile-soil interface strength. The role of the drilling method is also influential, although is not well quantified. The special drilling and grouting methods used in micropile installation also influence the micropile-soil interface resistance along the interface, L_g. International practice, both in micropiles and ground anchors confirms that the method of grouting is generally the most significant construction control over the grout-to-soil interface strength. This thesis examines the influence of grout pressure on micropile capacity but ignores the influence of drilling method.

2.2.3 Design Philosophy

Micropiles transfer applied axial loads to the soil by two mechanisms: skin friction and end bearing. The skin resistance is the result of relative movement and displacement along the side of the pile and what is commonly referred to as adhesion between the soil and the micropile. The end-bearing resistance is the result of compressive loading between the bottom of the micropile and the soil. Design equations commonly used to estimate skin friction and end bearing capacity are used extensively throughout this thesis. The problem with equations for the ultimate capacity P_{ult} is that the relations are largely based on empirical relations.

For example, the load carried by a pile by skin friction is

$$P_{ult} = \int_0^{L_g} \sigma_v^{'} \cdot K_s \tan(\delta) \cdot \pi \cdot D_g \cdot dl \qquad [2.1]$$

where σ_v' is the vertical effective stress, K_s is the lateral earth pressure coefficient, δ is the friction angle between the pile and soil and D_g is the pile diameter. Normally, K_s and $tan\,\delta$ are lumped into a simple parameter called β and the pile capacity is given by (see Reese and O'Neil 1988 and Bowles 1982):

$$P_{ult} = \int_0^{L_g} \beta \cdot \sigma_v^{'} \cdot \pi \cdot D_g \cdot dl \qquad [2.2]$$

Table 2.1 shows ranges of β depending on the soil type and drilling method. From ***Table 2.1*** it can be seen that there is considerable variation of β.

According to the *FHWA* Drilled and Grouted Micropiles Design Manual (*FHWA,* 1997), the axial capacity of a micropile in compression is equal to the end-bearing resistance, Q_b, plus the shaft resistance, Q_s, as follows:

$$P_{ult} = Q_b + Q_s - W_p \qquad [2.3]$$

where W_p is the weight of the pile and can be neglected in calculations

Although the end-bearing resistance is often ignored for very slender micropiles, this study considers both end-bearing and shaft resistance due to the slenderness ratio of the reduced-scale micropiles studied in subsequent chapters (e.g. $13.3 < L_g/D_g < 20$).

From bearing capacity theory, the end-bearing resistance of a micropile is

$$Q_b = N_q \cdot \sigma_{v0}^{'} \cdot A_b \qquad [2.4]$$

where N_q is a bearing capacity factor σ'_{v0} is the vertical effective stress at the tip of the micropile before loading, and A_b is the end area. N_q varies from 5 to 250 depending on L_g/D_g and $\emptyset'$.

In accordance with *FHWA* (1997), the shaft resistance of the micropiles is

$$Q_s = \int_0^{L_g} \sigma_v^{'} \cdot K^{'} \cdot \tan(\delta) \cdot \pi \cdot D_g \cdot dl \qquad [2.5]$$

where K' is an empirical factor that varies between 4 and 7 (see *FHWA* 1997) depending on the grout pressure (e.g. from 0.2 to 0.35MPa), δ is the effective friction angle of the pile-to-soil interface, and πD_g is the shaft circumference in contact with the soil.

For large displacement of micropiles in sand, Bhushan (1982) recommends using the β-method for computing skin-friction.

$$f_s = \int_0^{L_g} \beta \cdot \sigma_z' \cdot \pi \cdot D_g \cdot dl \qquad [2.6]$$

where $\beta = 0.18 + 0.65\ D_r$ and D_r is the relative density of the sand. Alternatively, O'Neil and Reese (1999) recommend assessing β using

$$\beta = \frac{N_{60} \cdot \left(1.5 - 0.135 \cdot \sqrt{z}\right)}{1.5} \qquad \text{for } 1.2 \geq \beta \geq 0.25 \text{ and } N_{60} < 15 \qquad [2.7]$$

and

$$\beta = 15 - 1.35 \cdot \sqrt{z} \qquad \text{for } 1.2 \geq \beta \geq 0.25 \text{ and } N_{60} \geq 15 \qquad [2.8]$$

where N_{60} is the *SPT* value uncorrected for overburden pressure and z is the depth in feet. In summary, there is considerable empiricism in the design of micropiles, with considerable variation in design parameters leading to high uncertainty.

Table 2.1 *Range of β Coefficients*

Soil Type	Cast-in–place Piles	Driven Piles
Silt	0.2-0.3	0.3-0.5
Loose sand	0.2-0.4	0.3-0.8
Medium sand	0.3-0.5	0.6-1.0
Dense sand	0.4-0.6	0.8-1.2
Gravel	0.4-0.7	0.8-1.5

2.3 Tiebacks

2.3.1 General

Permanent ground anchors are widely used for stabilization of natural slopes, cuts, cliffs, excavations, dam abutments, reinforced concrete retaining walls, cast-in-place and pre-cast panel slurry walls, soldier pile and lagging walls, and sheet pile walls. The use of soil and rock anchors to support the sidewalls of excavations has increased significantly during the last 20 years. Tiebacks (or anchors) have been used to support the sides of both temporary and permanent excavations. The following section describes the geometry and construction of tieback anchors.

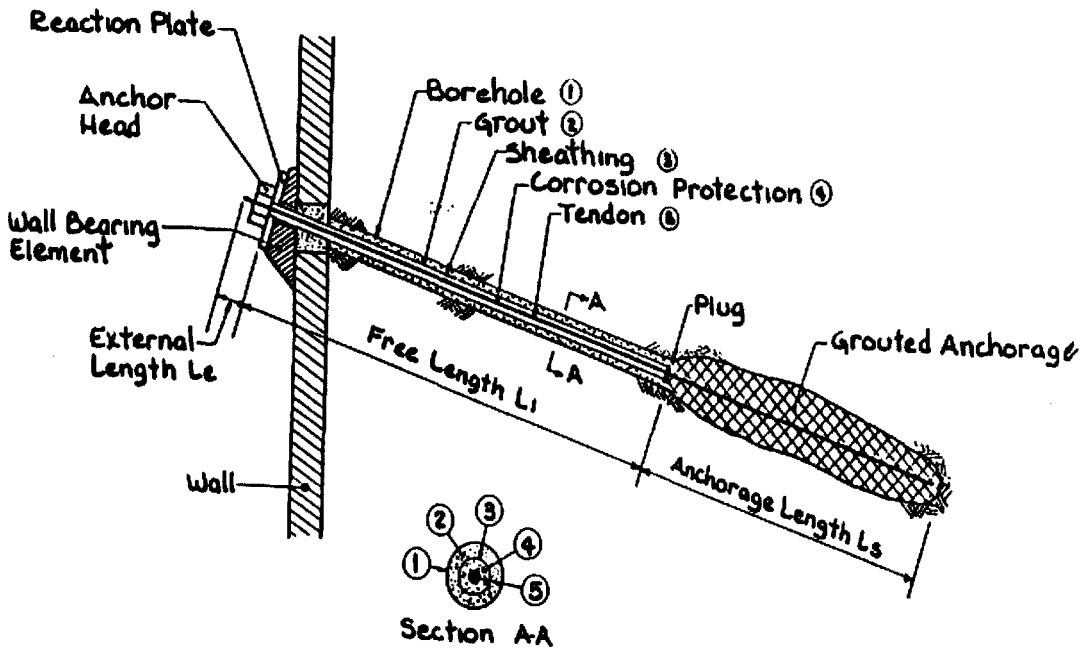

Figure 2.3 *Anchor Details (Schnabel, 1982)*

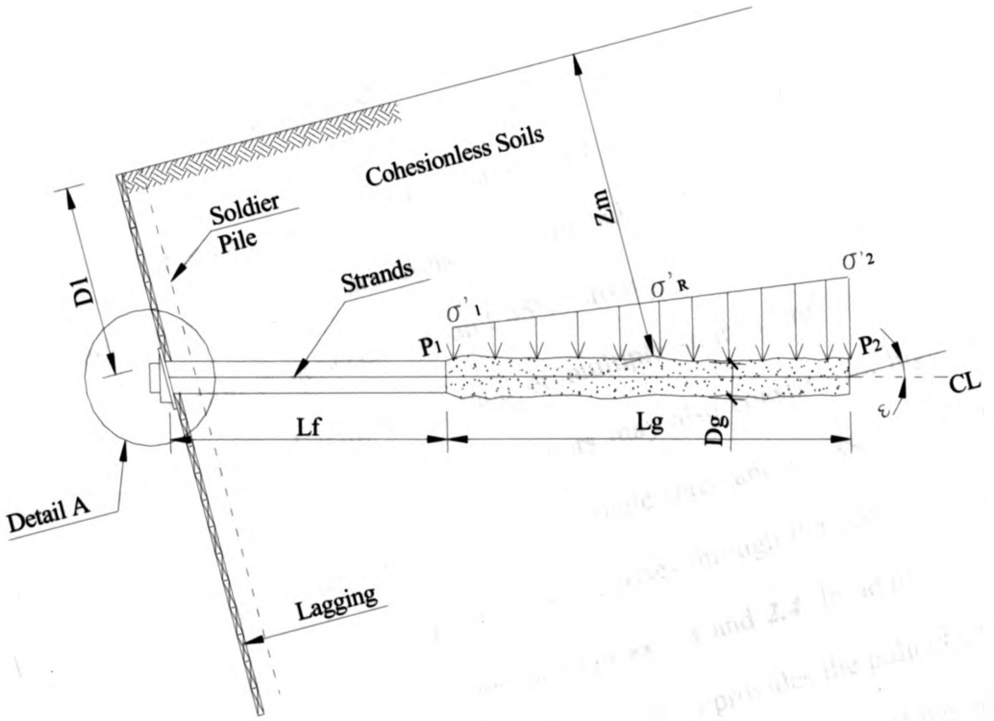

***Figure 2.4** Tieback Geometry and Stresses*

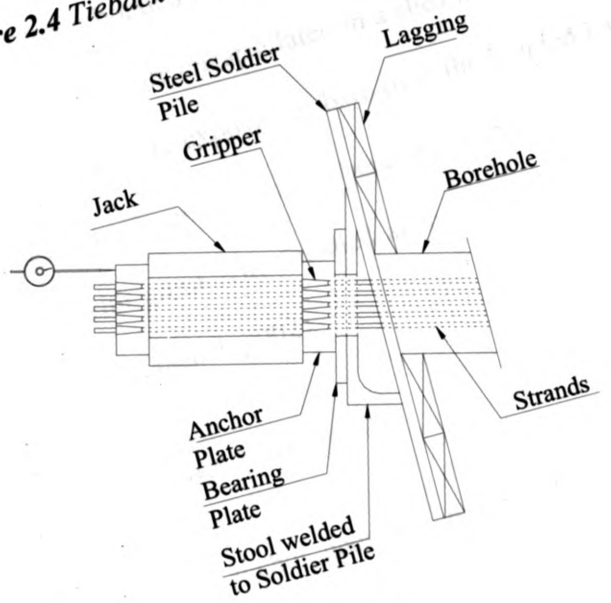

***Figure 2.5** Tieback Testing Setup*

2.3.2 Tieback Construction Method

Figure 2.3 and ***Figure 2.4*** show the geometry of a typical single stage tieback anchor. Tieback anchors in soil are constructed by advancing an inclined borehole (typically the inclination is between 10° and 45°) through soil using a rotary drill rig. After reaching the required length, a strand or multiple strands are inserted into the borehole and centered using centralizers. Anchors may also consist of a high strength steel bar instead of post-tensioning strands. For single stage anchor systems, the tieback anchor has an unbonded or free length, L_f, as it passes through the active earth pressure zone behind a shoring wall as depicted in ***Figures 2.3*** and ***2.4***. In addition, the tieback anchor has a bonded length, L_g, of diameter D_g, which provides the pullout capacity. The anchor strands are encapsulated in a sheath in the unbonded portion of the tieback anchor whereas they are exposed or bare over the bonded length. In most cases, centralizers and spacers are inserted into the borehole to position the strands, and the borehole is tremie filled with grout. The finished anchor has an anchor head which attaches to the shoring wall (see Macnab 2002).

2.3.3 Design Philosophy

For the anchor geometry presented in ***Figure 2.3 and 2.4***, the pullout capacity in cohesionless soils is:

$$P_{ult} = \int_0^{L_g} \sigma_R' \cdot \tan(\delta) \cdot \pi \cdot D_g \cdot dl \qquad [2.9]$$

where σ'_R is the effective radial stress on the bonded section of the tieback anchor, δ is the effective friction angle between grout and soil, and πD_g is the circumference of the bonded length that is in contact with the soil. If the tieback anchor is gravity grouted, then

$$P_{ult} = \left(\frac{(1+K_0)}{2} - \frac{(1-K_0)}{2} \cos(2 \cdot \varepsilon) \right) (\gamma \cdot z_m - u) \cdot \pi \cdot D_g \cdot L_g \qquad [2.10]$$

where K_0 is the coefficient of lateral earth pressure at rest, ε is the tieback inclination, γ is the bulk unit weight of the soil, z_m is the depth to the center of the bonded length and u is the pore water pressure at z_m. If the tieback is post-grouted, then the ultimate pullout capacity is

$$P_{ult} = (p_g - u) \cdot \tan(\delta) \cdot \pi \cdot D_g \cdot L_g \qquad [2.11]$$

where p_g is the post-grouted pressure.

Most modern tiebacks use grout injected under pressure to improve the soil surrounding the anchor and increase the anchor capacity. As the grout is injected, it exerts a radial pressure on the soil and it may also permeate into coarse-grained soils. The pressure of the grout on the soil and grout permeating the voids can dramatically improve the capacity of this type of anchor.

In many instances, anchors in cohesionless soil can sustain loads in excess of 1300kN over a fixed length of 4-8 m and with a shaft diameter 10-15 cm. The classical laws and theories of soil mechanics cannot explain these reported loads. Thus, the load capacity has been typically back-calculated using empirical correlations developed from field test

data. Similar to micropiles, this has lead to significant empiricism in design approaches as illustrated below.

Computation of the pullout resistance, P_{ult}, for tremie-grouted anchors in cohesionless soils can be estimated from the following equations:

$$P_{ult} = \alpha_g \cdot \sigma_z' \cdot A_s \cdot L_g \qquad [2.12]$$

where σ_z' is the effective vertical stress at the midpoint of the load carrying length, A_s is the effective unit surface area of the anchor bond zone, L_g is the effective length of the anchor bond zone (limited to 8 m) and α_g is an anchorage coefficient that depends on the soil type and its density. ***Table 2.2*** summarizes typical values for α_g.

Table 2.2 *Anchorage Coefficient* α_g

Soil Type	**Relative Density**		
	Loose	**Compact**	**Dense**
Silt	0.1	0.4	1.0
Fine Sand	0.2	0.6	1.5
Medium Sand	0.5	1.2	2.0
Coarse Sand, Gravel	1.0	2.0	3.0

For low-pressure grouted anchors, Littlejohn (1997) suggested the following empirical expression:

$$P_{ult} = n \cdot L_g \cdot \tan(\phi) \qquad [2.13]$$

where L_g is the bonded anchor length (m), $\emptyset$ is the angle of internal friction, and n is an empirical factor that depends on the permeability of the soil, the grout pressure and the depth of overburden. Littlejohn suggests n values of 400-600 kN/m for $k > 10^{-4}$ m/s and 130-165 kN/m for $k = 10^{-4}$ to 10^{-6} m/s.

For anchors grouted using high injection pressure, equation *[2.13]* has been modified by Littlejohn (1977) as follows:

$$P_{ult} = a_d \cdot p_g \cdot \tan(\delta) \cdot \pi \cdot D_g \cdot L_g \qquad [2.14]$$

where p_g is the grout injection pressure and a_d is a dimensionless empirical coefficient (<1).

Finally, Wernick (1977) has shown large increases in the radial or normal stress on high pressure injection grouting. In addition, Lee (2000) showed that the high pullout capacity was due dilation. The role of this phenomenon in the functioning of anchors in granular soils is significant but when such anchors are to be loaded in a repetitive manner, caution is warranted until the effects of repeated loading on this dilatancy component of strength are understood.

2.3.4 Micropile and Tieback Testing

Micropile testing is typically undertaken by performing static load tests. A hydraulic jack and reaction frame are used to apply the load to the top of a micropile. Vertical displacement of the micropile is measured using dial gauges that rest on steel plate placed on top of the micropile head. The dial gauges are mounted to independent frames. During the tests, an incremental axial load is applied until the micropile fails by reaching a predetermined movement or creep rate.

Figure 2.5 shows a typical setup for tieback pullout tests. A stool or reaction frame is commonly welded to the soldier pile after the anchor grout has cured. Then a bearing

plate and hydraulic jack are set on the stool. The strands pass through the stool, bearing plate and the jack. In conjunction with this setup, two sets of mechanical grippers are placed over the post-tensioning strands. One set is situated at the top of the jack to transfer the jack forces to the strands. A second set of grippers is placed over the strands between the jack and the bearing plate to lock in the final anchor loads. Typically, the load applied to the tieback anchor is measured using a pressure gauge attached to the hydraulic jack. Before conducting pullout tests, it is common practice to calibrate the jack and pressure gauge. Displacement or elongation of the strands is measured using a dial gauge supported by a frame that is anchored outside the zone of influence of the test.

Normally, there are two types of load tests performed on tieback anchors: first, all tieback anchors are proof tested to about 1.3 times the design anchor load, P_D. In addition, performance tests are done on select anchors by applying up to 2 times the design load, P_D. This study examines the response of performance tests only.

Performance tests are performed by first applying a seating load of about 0.1 P_D to the anchor and then zeroing the dial gauges. Then, the tieback anchor is loaded sequentially to loads of 0.25 P_D, 0.5 P_D, 0.75 P_D, 1.0 P_D, 1.25 P_D, 1.5 P_D, 1.75 P_D and finally to 2.0 P_D. At loads of 0.5 P_D, 1.0 P_D, 1.5 P_D and 2.0 P_D, the load is cycled to the seating load and then back to the applied load to measure the inelastic elongation, δ_p, and elastic elongation, δ_e, of the tieback anchor. In addition to cycling the load in the tieback, each load is held for at least 10 minutes during which time the creep deformations are recorded, if any occur. If the creep exceeds 1mm in 10 minutes then the load is maintained an additional 50 minutes to measure the creep over the time interval 6-60 minutes. Further details are presented in ***Chapter 6***.

2.4 Summary and Conclusions

This chapter has provided a brief overview of the design and construction of micropiles and tieback anchors. Additional details are provided in ***Chapter 3-6***. From this literature review, it can be seen that design equations for micropiles and tiebacks are based on empirical relationships for parameters that have a high degree of variation and uncertainty. Accordingly, new research and better knowledge of the behaviour of these geostructural elements would be beneficial.

Chapter 3

Geotechnical Characterization of Clarke Side Road Sand

3.1. Introduction

This chapter describes a laboratory investigation performed to characterize the geotechnical properties of concrete sand from the Lafarge quarry in London, Ontario, near Clarke Side Road. The sand was placed and compacted into a 1.35m diameter by 1.55m deep calibration chamber to perform the micropile load tests described in ***Chapter 4*** and ***Chapter 5***. ***Figure 3.1*** shows the micropile load-test setup. Two grain size analyses, eleven permeability tests (constant-head and falling-head tests), three Standard Proctor tests, twenty-three plate load tests and eight direct shear tests were performed and the methodology and results are described below.

3.2. Methodology

3.2.1 Grain-size Analysis

The sand used in the experimental work described in ***Chapters 4*** and ***Chapter 5*** was from the Lafarge quarry near Clark Side Road in London, Ontario; hereafter referred to as Clark Side Road (C.S.) sand. C.S. sand is a concrete sand according to American Society for Testing and Materials (ASTM), ASTM D 2487-00. First, two grain size analyses were performed according to ASTM D422 to classify the soil using the Unified Soil Classification System (ASTM D 2487). No. 4, 10, 20, 40, 60, 140 and 200 sieves sizes were used. One grain size analysis test was done at the beginning of the micropile

tests and another at the end of the tests. The purpose of the two tests was to check if the grain size distribution changed due to mechanical compaction of the sand.

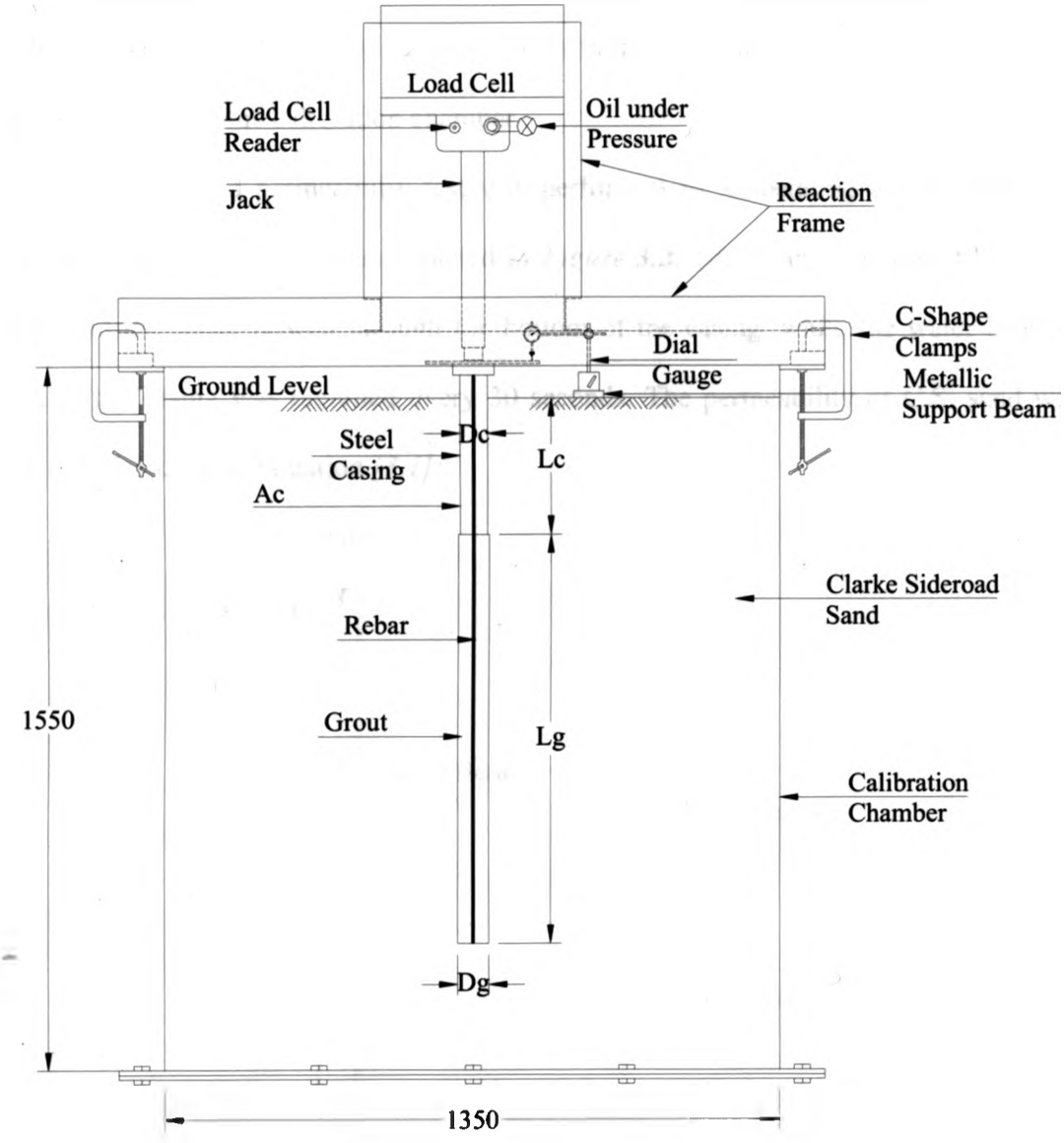

Figure 3. 1** Micropile Test Setup used in **Chapter 4

3.2.2 Hydraulic Conductivity

The permeability of C.S. sand was measured using a constant head permeability test performed according to ASTM D 2434 and a falling-head test performed according to ASTM D698-70 in the calibration chamber.

The falling-head permeability test was performed by embedding a 1.5-meter long AW-size casing in C.S. sand as depicted in ***Figure 3.2.*** The casing was then filled with water and the water flowed through the bottom of the casing, while the water level or head in the casing was recorded every 30 seconds. The permeability of C.S. sand was then calculated using Equation *[3.1]:*

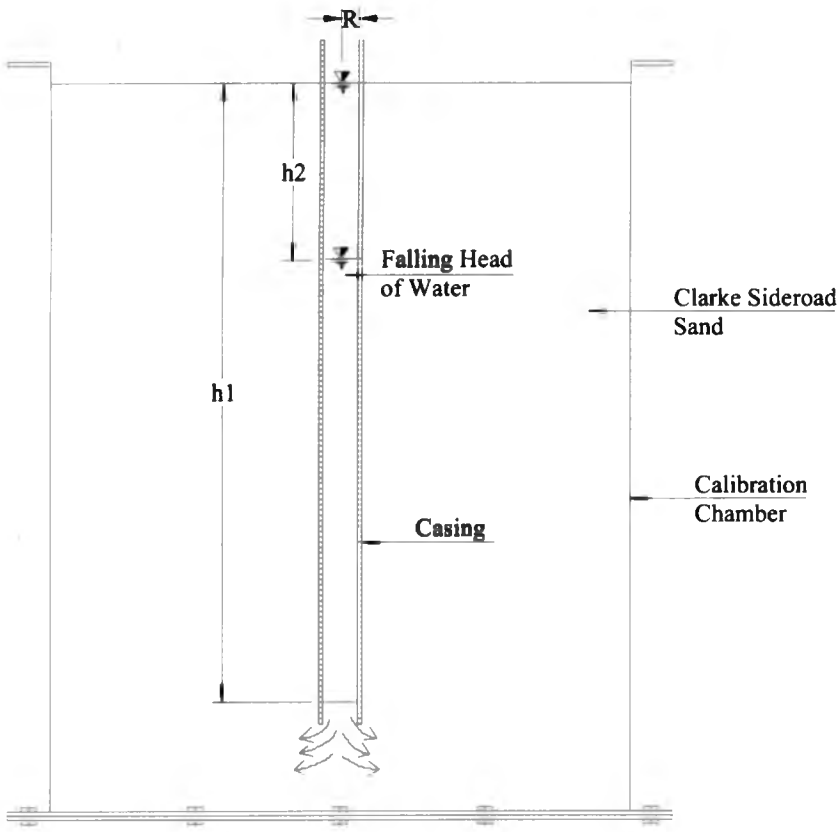

Figure 3.2 *Falling Head Setup*

$$k = \frac{(\pi \cdot R + 5.5 \cdot 0.1)}{(11 \cdot (t_1 - t_2))} \cdot \ln\left(\frac{h_1}{h_2}\right) \qquad (cm/sec) \qquad [3.1]$$

where R is the internal radius of the casing, h_1 is the head of water at the start of the test, h_2 is the head of water at the end of the elapsed time Δt, and (t_1-t_2) is the time interval for water in the casing to drop from h_1 to h_2.

In addition to falling head permeability tests, constant head permeability tests were also performed using the permeameter shown in ***Figure 3.3.***

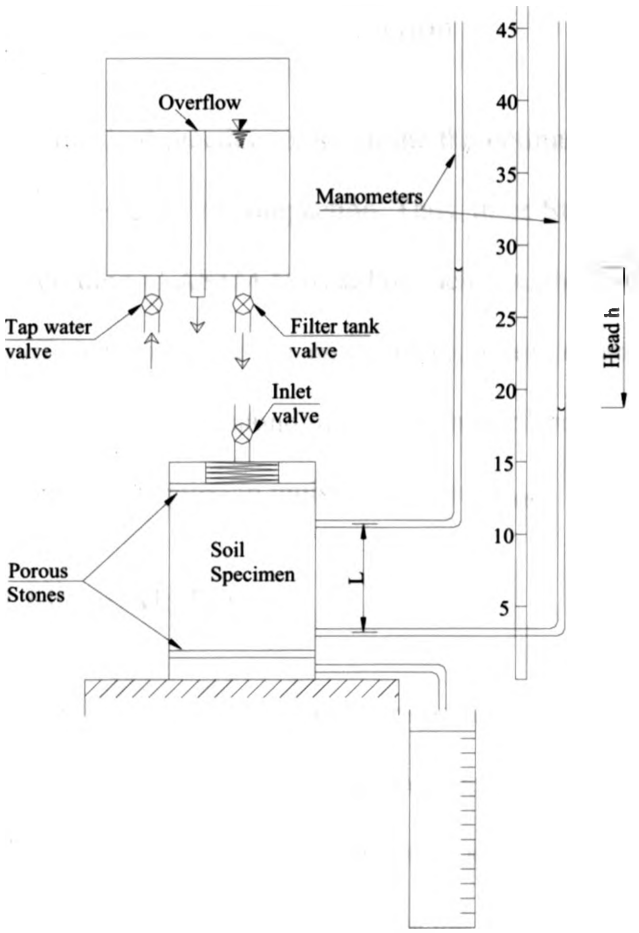

Figure 3.3 *Constant-Head Permeameter*

For constant-head tests, the hydraulic conductivity is:

$$k = \frac{Q \cdot L}{A \cdot t \cdot h} \qquad [3.2]$$

where Q is the quantity of water discharged during the test, L is the length between manometer outlets, A is the cross-sectional area of the specimen, t is the time for a quantity Q to be discharged during the test and h is the difference in total head between the manometers during the test.

3.2.3 Standard Proctor Compaction

It is standard practice to determine the optimum moisture content and maximum dry density of soil prior to compaction. Thus, three Standard Proctor tests were done on C.S. sand according to ASTM D 698. For each test, the range in moisture content considered was sufficient to define the optimum moisture content and maximum dry density. The moisture content corresponding to the standard proctor maximum dry density (*SPMDD*) is defined as the optimum moisture content, w_{opt}.

3.2.4 Elastic Modulus

Twenty-three plate load tests were performed to determine the elastic modulus of C.S. sand. These tests were done in accordance with ASTM D1194-94 and conducted in the calibration chamber using the test set up shown in ***Figure 3.4***. Referring to ***Figure 3.4***, plate load tests were performed by placing a 28.3-cm diameter steel plate on leveled C.S. sand. The plate was loaded by means of a hydraulic jack attached to a reaction frame that was connected to the calibration chamber using C-shape clamps. The load was applied

incrementally at a rate of 1kN/min and the settlement readings were recorded using a dial gauge for each load increment.

The elastic modulus was then estimated using the following equation:

$$E = \left(1 - \nu^2\right) \cdot 1.0 \cdot 0.79 \cdot \frac{\Delta P}{\Delta S} \qquad (MPa) \qquad [3.3]$$

where ΔP is the pressure increment, ΔS is the settlement induced by ΔP and ν is Poisson's ratio with an assumed value of 0.3.

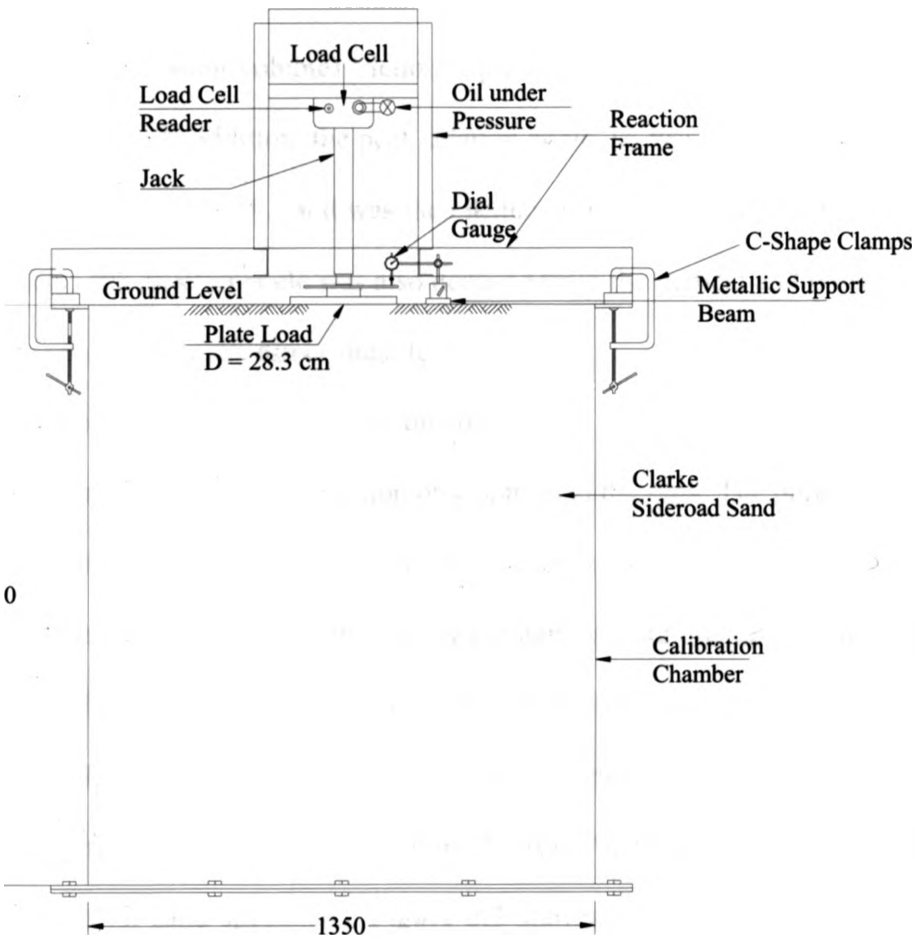

Figure 3.4 *Plate Load Test Setup*

3.2.5 Direct Shear Tests

Finally, the shear strength of C.S. sand was measured using direct shear tests following ASTM D3080. The capacities of the micropiles described in ***Chapter 4*** and ***Chapter 5*** were studied using C.S. sand placed into the calibration chamber (see ***Figure 3.1***) at two different densities. The first series of micropiles load tests were performed using C.S. sand placed at a moisture content, w, of about 10% (±1.0%) with dry density, ρ_d, of 1.84g/cm^3 (± 0.02g/cm^3). The second series was undertaken at a moisture content, w, of about 3% (±2.0%) and ρ_d of 1.80g/cm^3 (± 0.02g/cm^3). Consequently, the peak and residual (constant volume) friction angle of C.S. sand was measured for loose and dense sand states. In addition, the peak dilation angle, ψ_p was measured. The peak and residual friction angle of C.S. sand was then deduced from shear stress τ versus normal stress σ'_N plots. The dilation angle was also deduced from the vertical and horizontal displacements recorded during the direct shear tests.

For the direct shear tests on loose sand, C.S. sand was placed in the shear box without causing any compaction or vibration to the sand. The purpose was to get the sand state as loose as possible. For direct shear tests on dense sand, C.S. sand was compacted in the shear box and then sheared. A constant loading rate of 0.4mm/min was used for all tests. The normal loads were applied using weights and a hanger system that rested on a load plate placed on top of 6cm by 6cm specimens. Samples were tested in direct shear using effective normal stresses of 50kPa, 100kPa, 150kPa, and 200kPa for both loose and dense C.S. sand specimens. ***Figure 3.5*** shows a drawing of the direct shear apparatus. Vertical displacement of the sand during shear was measured using a dial gauge resting on the top load plate.

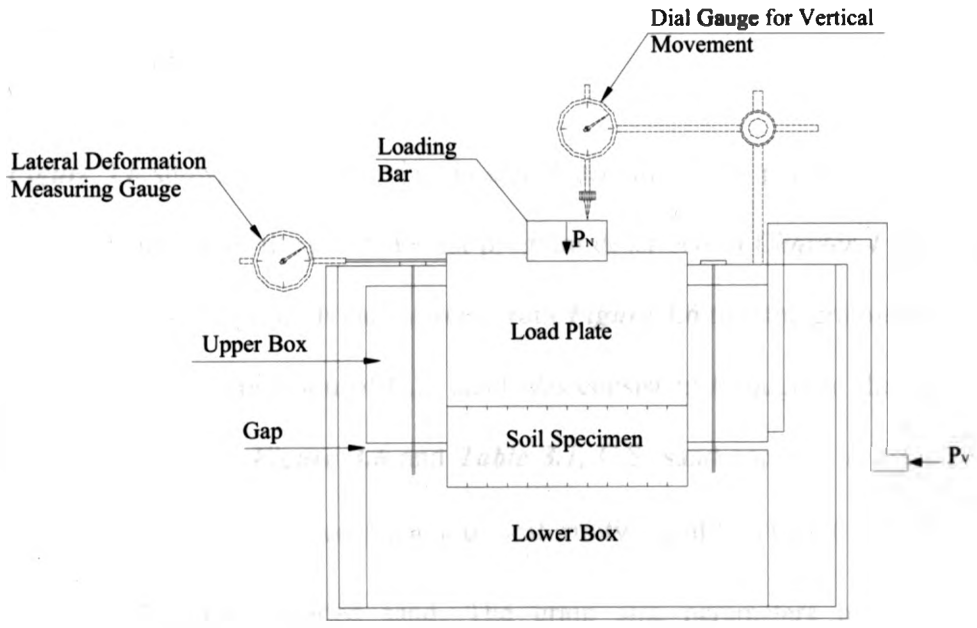

***Figure 3.5** Direct Shear Test Setup (Wykeham Farrance Type)*

3.3. Results

3.3.1 Grain-size Analysis

Figure 3.6 shows the results of grain-size distribution tests performed on C.S. sand: one at the beginning of the pile load test program described in ***Chapter 4*** and another at the end of the test program. It can be seen from ***Figure 3.6*** that the grain-size curves are similar and thus the gradation of C.S. sand was consistent throughout the pile-load test program. Referring to ***Figure 3.6*** and ***Table 3.1,*** C.S. sand contains less then 5% fine particles (<75μm) and has a coefficient of uniformity, C_u of less than 6. These values are consistent with poorly graded sand. The grain size parameters of C.S. sand are summarized in ***Table 3.1***.

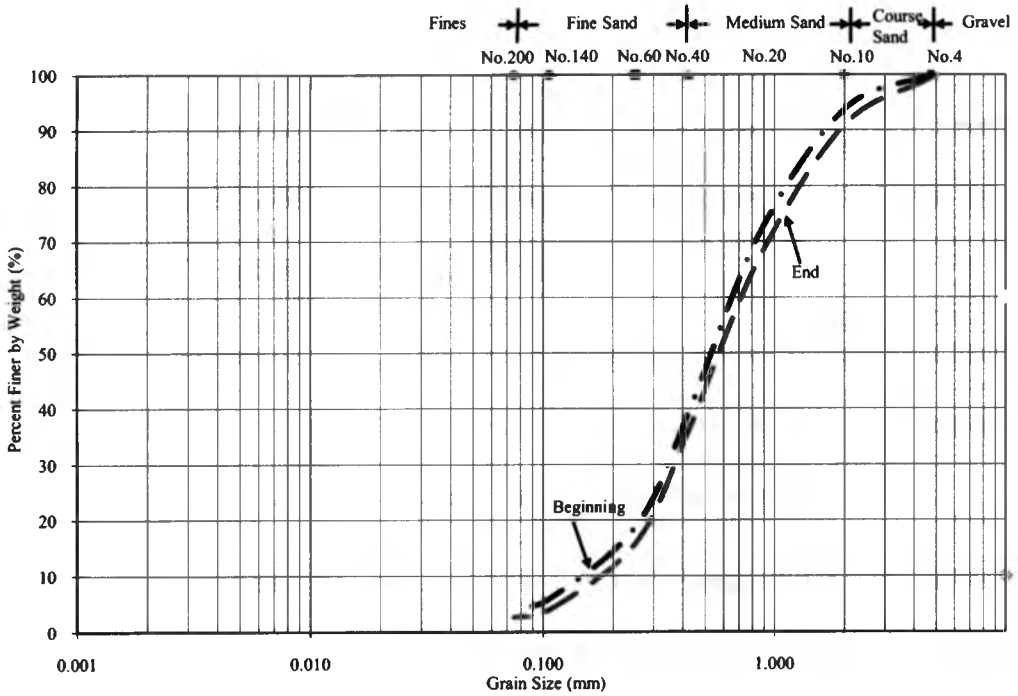

Figure 3.6 *Grain Size Distribution Curve at the Beginning and the End of Lab Experiments*

Table 3.1 *Soil Classification*

Parameter	Soil	
	Beginning	End
d_{10}	0.15	0.18
d_{30}	0.34	0.37
d_{60}	0.65	0.72
d_{85}	1.30	1.50
C_u	4.33	4.00
C_c	1.19	1.06
w_{opt} (%)	13.00	12.00
ρ_{dmax} (g/cm^3)	1.86	1.86
<75μm (%)	1.29	2.63
Soil Type	Sand	Sand
USC Classification	SP	SP

3.3.2 Hydraulic Conductivity

Figure 3.7 shows the results of a falling-head hydraulic conductivity test performed according to *ASTM D698-70.* From ***Figure 3.7*** and equation *[3.1],* the hydraulic conductivity of C.S. sand is $k = 1.24 \times 10^{-2}$ cm/sec.

Table 3.2 summarizes the constant-head test results. From the constant-head tests, (ASTM D2434), the hydraulic conductivity of C.S. sand is $k = 6.8 \times 10^{-3}$cm/sec. The results from both tests are consistent and within the normal range for sands.

The hydraulic conductivity of C.S. sand is thus in the range of 6.8×10^{-3}cm/sec - 1.24×10^{-2} cm/sec. Since k from the constant head test is slightly lower than for the falling head tests, it is concluded that $k_H > k_V$, since there is a component of radial flow in the falling head tests.

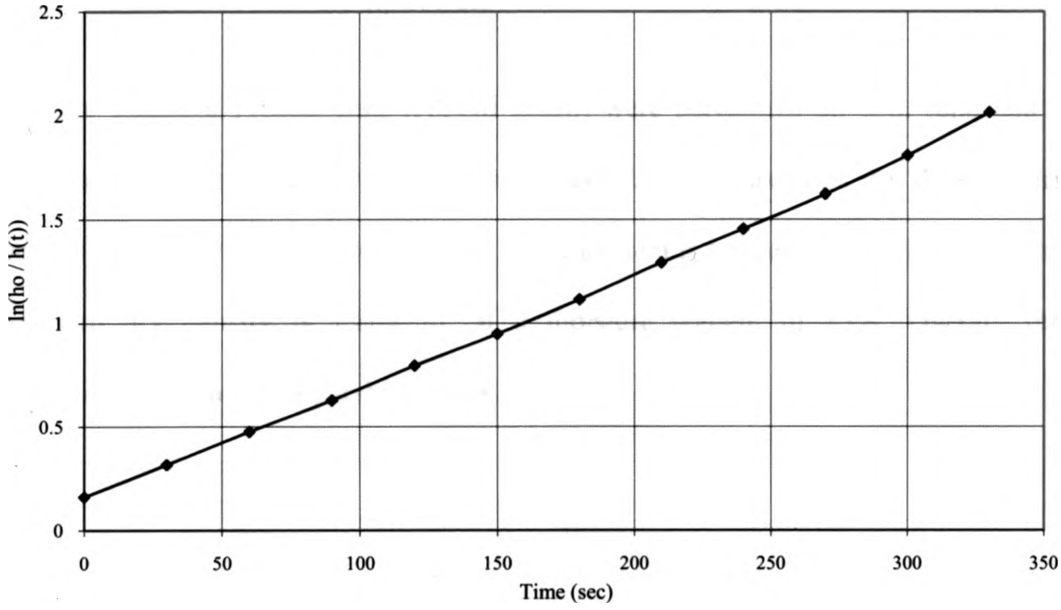

Figure 3.7 *Head Variation versus Time in Falling Head Permeability Test for Water*

Table 3.2 *Constant Head Test Results*

Test No.	**1**			**2**			**3**		
Volume of Flow, Q(cm^3)	100	98	98	77	77	76	58	57	57.5
Average Flow, Q(cm^3)		98.67			76.67			57.5	
Temperature of Water, T(°C)		10			10			10	
Total Head Difference, h(cm)		148			124			99.5	
Diameter Specimen, D(cm)		7.4			6.35			6.35	
Length of Specimen, L(cm)		17.5			17.5			17.5	
Area of Specimen, A(cm^2)		43.008			31.669			31.669	
k=(Q*L) / (A*h*t), (cm/s)		0.00452			0.00569			0.00532	
Average Permeability, k					0.00518				
Temperature Correction, c		1.31			1.31			1.31	
$k_{20}oc$ = k*c, (cm/s), k(corrected)					**0.00678**				

3.3.3 Standard Proctor Compaction

Three Standard Proctor tests (ASTM D698) were performed on C.S. sand and the results are presented in ***Figure 3.8***. From ***Figure 3.8***, the maximum dry density varies from 1.84 to 1.87g/cm^3 and the optimum water content is between 12-14%. The average maximum dry density is 1.86g/cm^3 at a moisture content of 13%. Overall, three compaction tests gave comparable results.

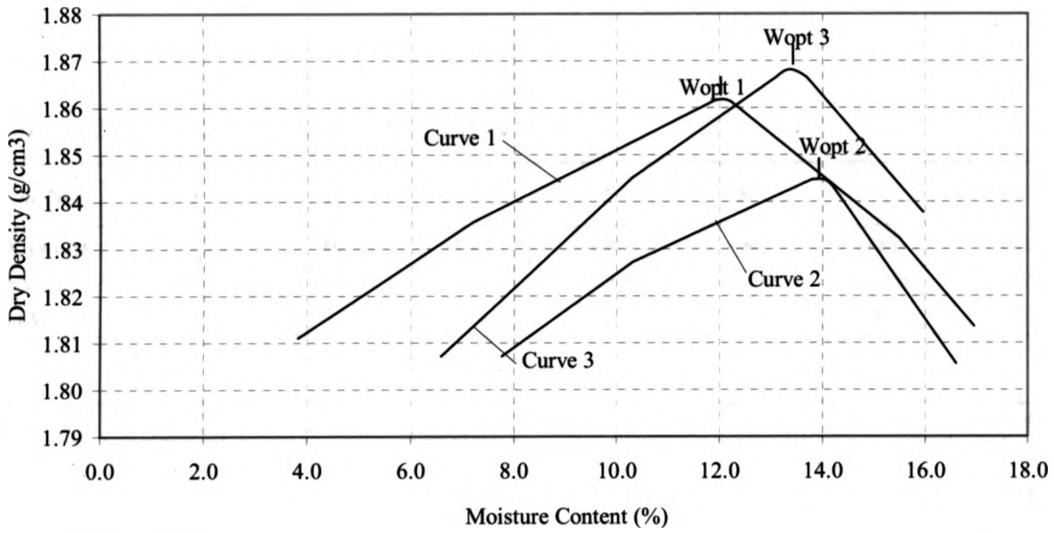

Figure 3.8 *Standard Proctor Test for C.S. Sand Used in Laboratory Tests*

3.3.4 Elastic Modulus

Table 3.3 summarizes the secant elastic modulus from plate load tests performed on C.S. sand.

Referring to ***Table 3.3***, it can be seen that the secant elastic modulus of C.S. sand typically varies between 15.6 MPa and 40.7MPa for deformations ranging from 2.09mm to 0.8mm. The corresponding mean value and standard deviation are 24.3MPa and 6.4MPa, respectively. As noted above, ***Figure 3.4*** shows the plate load test setup.

Table 3.3 *Elastic Modulus from Plate Load Tests*

Test No.	**1**	**2**	**3**	**4**	**5**	**6**	**7**
ΔP (kPa)	160	160	160	160	160	160	160
ΔS (m)	0.0017	0.00132	0.00182	0.00105	0.00147	0.00134	0.00165
E_s (MPa)	19.1	24.7	17.9	31.0	22.1	24.3	19.7

Test No.	**8**	**9**	**10**	**11**	**12**	**13**	**14**	**15**
ΔP (kPa)	160	160	160	160	160	160	160	160
ΔS (m)	0.00129	0.00144	0.00174	0.00107	0.00147	0.00083	0.00209	0.00114
E_s (MPa)	25.2	22.6	18.7	30.4	22.1	39.2	15.6	28.6

Test No.	**16**	**17**	**18**	**19**	**20**	**21**	**22**	**23**
ΔP (kPa)	160	160	160	160	160	160	160	160
ΔS (m)	0.00125	0.00167	0.002	0.0008	0.0014	0.00125	0.00117	0.00123
E_s (MPa)	26.0	19.5	16.3	40.7	23.3	26.0	27.8	26.5

3.3.5 Direct Shear

Table 3.4 summarizes the peak and constant volume effective friction angles, $\emptyset'$, for both dense and loose C.S. sand. The peak friction angle, $\emptyset'_p$is 51° for dense C.S. sand and 37° for loose C.S. sand, respectively. The constant volume friction angle $\emptyset'_{cv}$ is 36° for both dense and loose sand, as shown in ***Figure 3.9*** and ***Figure 3.10.***

Table 3.4 *Peak & Residual Internal Friction Angle & Dilatancy for Dense and Loose C.S. Sand*

Sand State	(*Dense*)	(*Loose*)
$\emptyset'_p$ (°)	51	37
$\emptyset'_{cv}$ (°)	36	36
ψ_p(°)	21	2.5

Figure 3.11 and ***Figure 3.12*** present the shear stress versus horizontal displacement response of C.S. sand.

The peak strength envelopes were plotted from the peak stresses reached during each test. The constant volume strength envelopes were plotted from the large displacement post peak stresses.

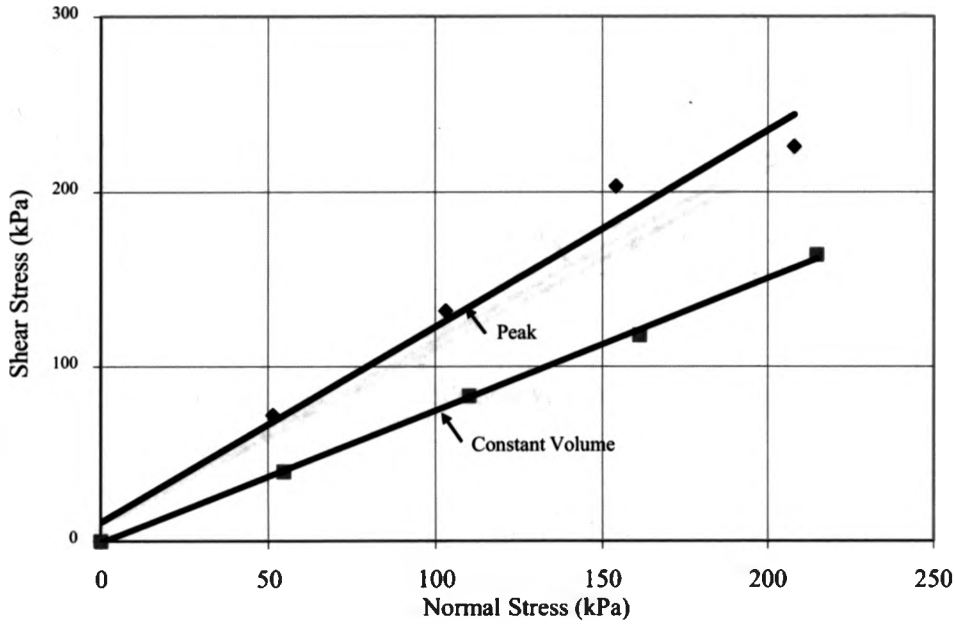

Figure 3.9 *Peak and Constant Volume Strength Envelopes of Dense C.S. Sand*

Sand samples tend to dilate or expand when they are sheared. ***Figure 3.13*** and ***Figure 3.14*** show the response of C.S. sand during direct shear. Initially, all samples contracted during shearing. At a horizontal displacement of 1-2mm, however, the specimens began to expand or dilate due to shearing. Referring to ***Figure 3.13*** and ***Figure 3.14***, the dilation was initiated between 70-90% of the peak shear stress and the results suggest a dilation angle $\psi_p = 21°$ for dense samples and $\psi_p = 2.5°$ for loose samples. In theory, the peak dilation angle for loose sand should be zero, and peak and constant volume friction angles equal. From the direct shear tests, ψ_p is very small but not zero due to high normal stresses applied and difficulty obtaining ideal loose sand. From the results in ***Table 3.4*** it can be seen that the peak and constant volume friction angles are very close for loose sand and almost identical to the constant volume friction angle of dense sand.

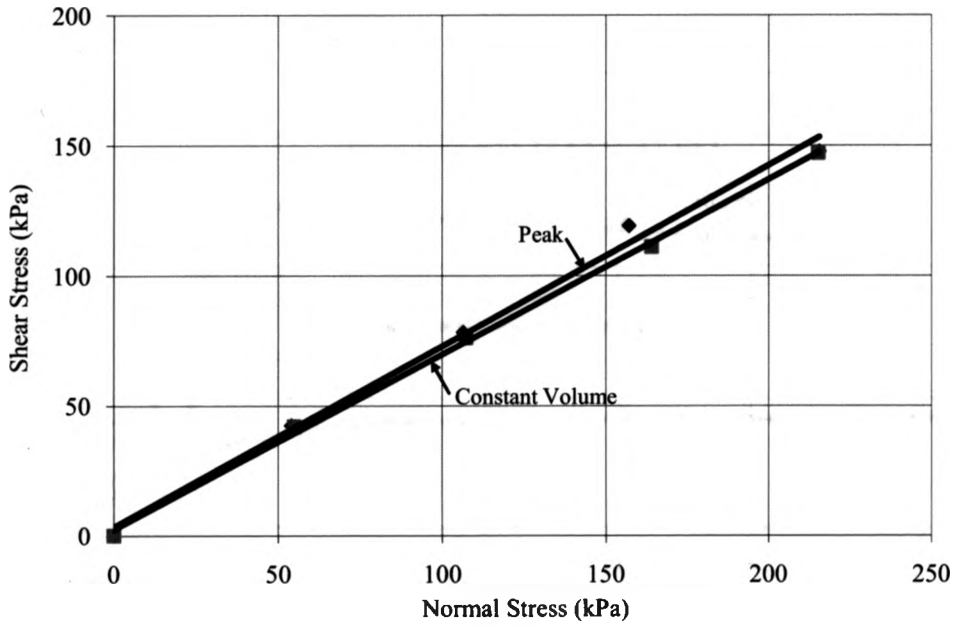

Figure 3.10 *Peak and Constant Volume Strength Envelopes of Loose C.S. Sand*

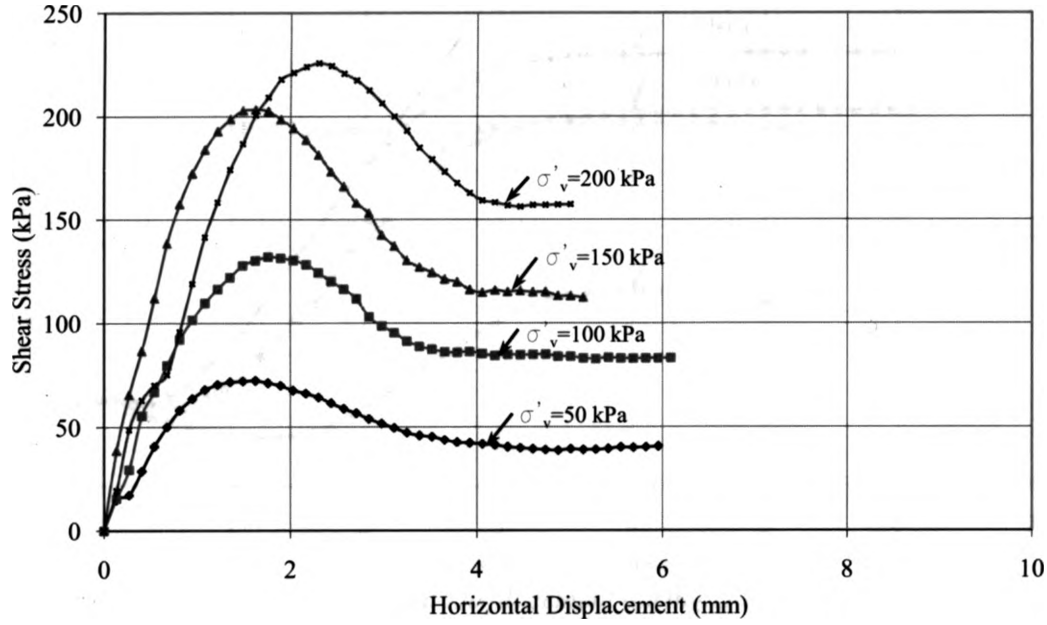

Figure 3.11 *Shear Stress vs. Horizontal Displacement from Direct Shear Test under Normal Stresses for Dense C.S. Sand Samples*

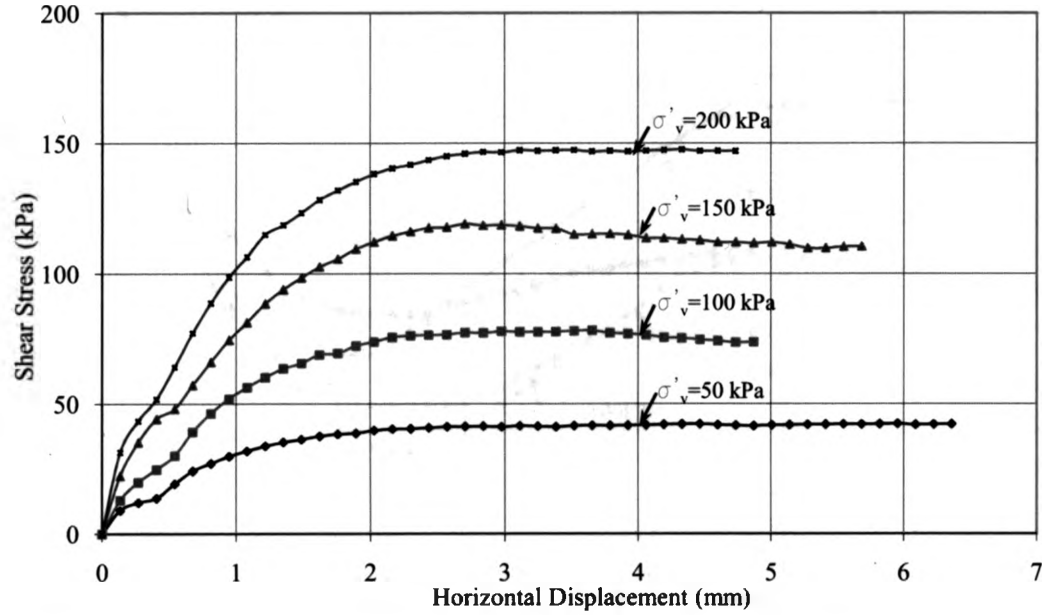

Figure 3.12 *Shear Stress vs. Horizontal Displacement from Direct Shear Test under Normal Stresses for Loose C.S. Sand Samples*

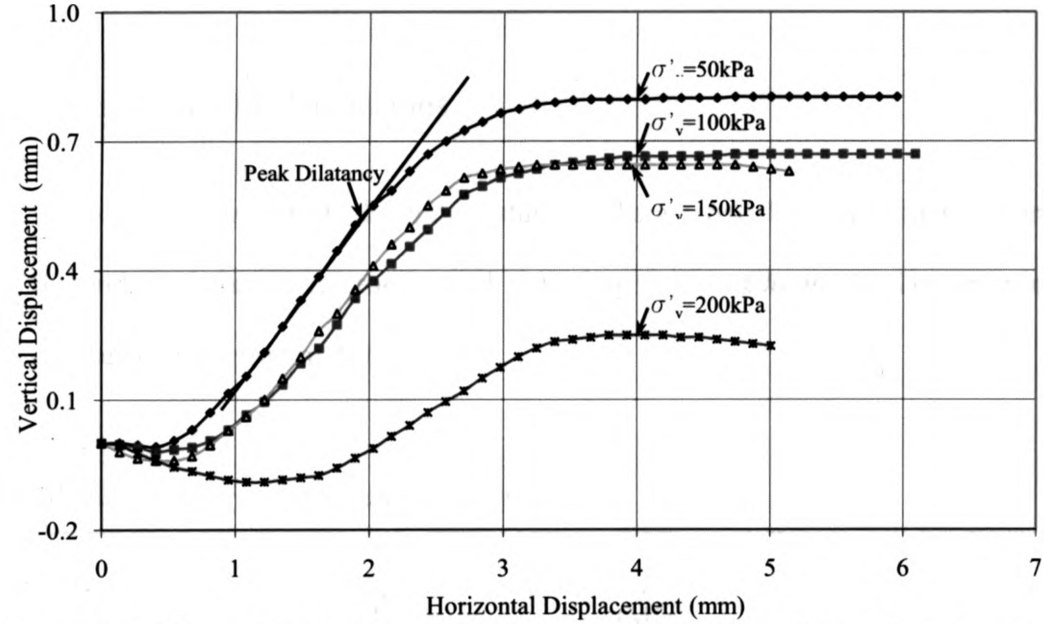

Figure 3.13 *Vertical vs. Horizontal Displacement during Direct Shear Tests for Dense C.S. Sand*

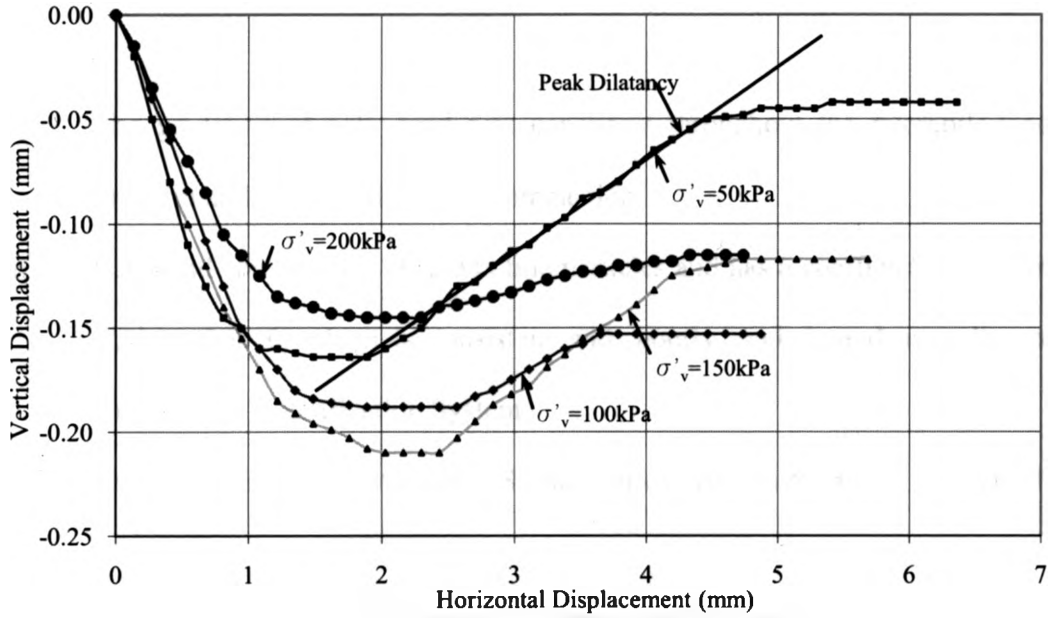

Figure 3.14 *Vertical vs. Horizontal Displacement during Direct Shear Tests for Loose C.S. Sand*

3.4 Summary and Conclusions

This chapter described a laboratory study to characterize the engineering properties of C.S. sand used for the micropile load tests described in ***Chapter 4***. The experimental results are summarized in ***Table 3.5.***

Table 3.5 *Summary of C.S. Sand Properties*

Poorly-graded Sand	$\emptyset'_p$	$\emptyset'_{cv}$	ψ_p	E_s (MPa)	k (cm/s)	ρ_{dmax} (g/cm^3)	w_{opt} (%)
Dense	51	36	21	26-40	6.8×10^{-3}-1.24×10^{-2}	1.86	13
Loose	37	36	2.5	16-26	6.8×10^{-3}-1.24×10^{-2}	1.86	13

The following is a summary of the findings from this study:

(i) The gradation of C.S. sand was consistent throughout the micropile-load test program and was not altered by compaction.

(ii) C.S. sand contains less then 5% fine particles and has a coefficient of uniformity C_u less than 6, which is consistent with poorly graded sand according to the Unified Soil Classification System.

(iii) The hydraulic conductivity of C.S. sand varies between 6.8 x 10^{-3} cm/s and 1.24 x 10^{-2} cm/s.

(iv) The standard proctor maximum dry density of C.S. sand is about 1.86g/cm^3 at a moisture content of 13%.

(v) From plate load tests, the mean secant elastic modulus was 24.3MPa and the corresponding standard deviation was 6.4MPa.

(vi) The constant volume friction angle of dense C.S. sand is $\emptyset'_{cv}$= 36°

(vii) The peak and constant volume friction angles of loose C.S. sand, $\emptyset'_p$, are essentially equal (37° versus 36°) and the peak friction angle of loose sand is equal to the constant volume friction angle of dense sand.

Chapter 4

Reduced-scale Load Tests on Micropiles in Cohesionless Sand

4.1. Introduction

The main objective of this chapter is to experimentally evaluate current methods for estimating the axial compressive capacity of micropiles in cohesionless soils. To achieve this objective, thirty-two reduced-scale micropiles were built in a 1.35-meter diameter by 1.55-meter deep calibration chamber and load tested to failure. This chapter provides details of the micropiles, their geometry and construction sequence, the load test methodology and the measured axial response during loading in compression. In addition, the measured load capacity is compared with the capacity calculated using the *FHWA* (Federal Highway Administration) Micropile Design Manual (*FWHA* 1997). The grout pressure was varied and pile roughness was measured to assess if the pile capacity was influenced by these parameters. Finally, the results and conclusions arising from this study are presented.

4.2 Background

4.2.1 Micropile Construction Method

Typically, micropiles can be constructed in a variety of geological environments using several different construction methods. However, this study considers the performance of micropiles constructed in cohesionless soils and built using the construction sequence illustrated in ***Figure 4.1***. The construction sequence is referred to below as the rotary duplex drilling method (*RDD*).

Referring to ***Figure 4.1a***, rotary duplex drilling involves advancing a cased borehole through cohesionless soils using a rotary drill rig. In this construction method, an expandable drill bit is used to create a borehole that is slightly larger than the casing. The casing is advanced by applying pressure to the drill string, which expands the drill bit and also advances the casing. Water is typically used as the drilling fluid. After drilling to the required depth (see ***Figure 4.1b***), the drill string is removed from the cased borehole and the casing is filled with tremied grout. Then, the casing is retracted incrementally (see ***Figure 4.1c***) and grout is injected into the surrounding soil under pressure during each increment. After several grout increments, the casing is cut-off slightly above the ground surface, and a steel bar is inserted into and centered in the pile. On completion, the pile comprises a cased section of length, L_c, and an uncased section of length, L_g, with a steel bar centered in the pile as depicted in ***Figure 4.2***. The casing provides lateral resistance for horizontal loads. Further details of the rotary duplex drill method can be found in the *FHWA* Manual (1997).

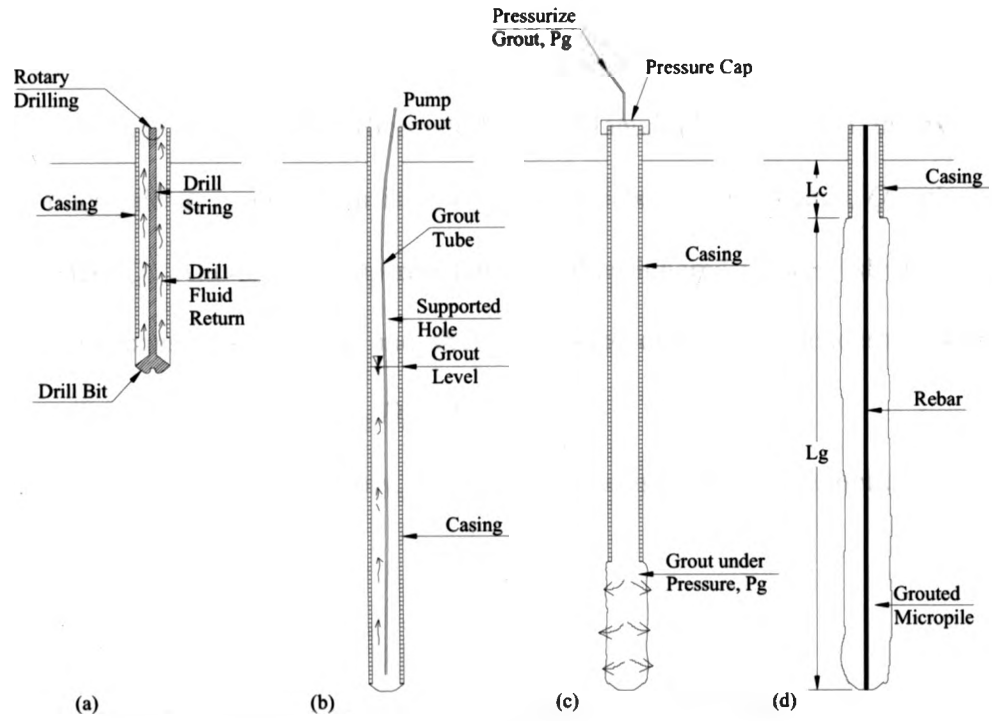

***Figure 4.1** Drilling Method*

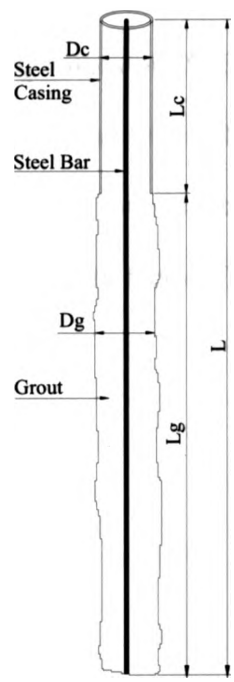

***Figure 4.2** Micropile Geometry*

4.2.2 Compressive Capacity of Micropiles

According to the *FHWA* Micropile Design Manual (*FHWA* 1997), the axial capacity of a micropile in compression is equal to the tip bearing resistance, Q_b, plus the shaft resistance, Q_s. Although the tip resistance is often ignored for very slender micropiles, this study considers both tip and shaft resistance due to the slenderness ratio of the micropiles tested (e.g. $13.3 < L_g/D_g < 20$).

From bearing capacity theory, the tip bearing resistance of a micropile is:

$$Q_b = N_q \cdot \sigma'_{v0} \cdot A_b \qquad [4.1]$$

where N_q is a bearing capacity factor (see ***Figure 4.3***), σ'_{v0} is the vertical effective stress in the soil at the tip of the micropile before loading, and A_b is the end area. From ***Figure 4.3***, N_q varies from 5 for friction angle of 25° to 250 for friction angle of 42° corresponding to L_g/D_g values of 20. Since N_q is very sensitive to the effective friction angle of the soil, a series of micropile load tests were undertaken as described in ***Section 4.3.4*** using piles that were constructed to have negligible skin friction and only end bearing. The bearing capacity factor N_q deduced from these tests was compared with N_q shown in ***Figure 4.3***.

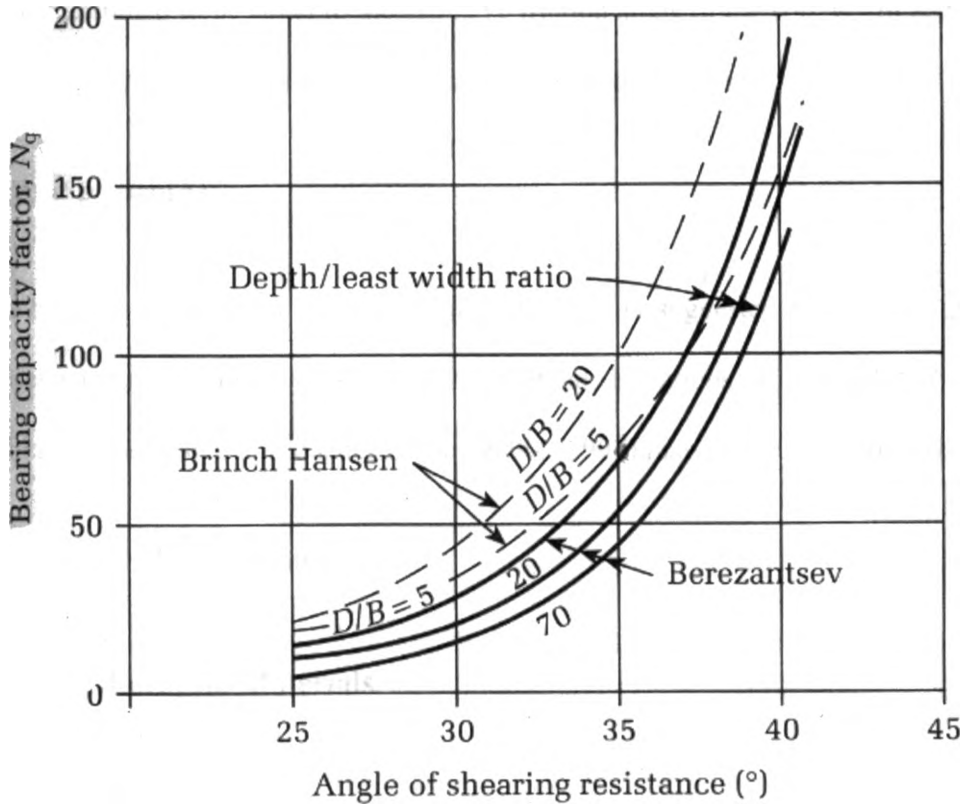

***Figure 4.3** Berezantsev and Brinch Hansen End-Bearing Capacity Factors*

For micropiles, it is generally recognized that skin friction along the micropile shaft is influenced by the grout pressure during construction. In accordance with *FHWA* (1997), the theoretical shaft resistance of the micropiles studied in this chapter is

$$Q_s = K' \cdot \sigma_v \cdot \tan(\delta) \cdot A_s \qquad [4.2]$$

where K' is an empirical factor that varies between 4 and 7 (see *FHWA* 1997) depending on the grout pressure (e.g. from 0.2 to 0.35MPa), δ is the effective friction angle of the pile-to-soil interface, and A_s is the area of the shaft in contact with the soil. For the present study, the theoretical capacity of micropiles was estimated assuming $K' = 4$ and δ

was assumed to be equal to the effective friction angle of the soil, $\emptyset'$. In addition to using equation *[4.2]*, shaft resistance was also estimated using the equation

$$f_s = p_g \cdot \tan(\delta) \qquad [4.3]$$

where p_g is the grout pressure. Equation *[4.3]* is suggested for the design of grouted tieback anchors in the *FHWA* (1997) Manual. Equations *[4.2]* and *[4.3]* were used to bracket the design approaches in the *FHWA* (1997) manual for estimating skin friction.

4. 3 Lab Methodology

4.3.1 Micropile Materials

4.3.1.1 Casing

In this study, both 2-inch (6-cm OD) and 3-inch (9-cm OD) steel (*ASTM* A53) casings were used in the experiments. The casing comprised Schedule 40 pipe, with a minimum tensile yield strength of 205 MPa, and minimum ultimate tensile strength of 330MPa. The steel has a modulus of elasticity of 2.0×10^5 MPa and the pipes have a wall thickness of 3.8mm for 6-cm diameter pipe and 5.6mm for 9-cm diameter.

4.3.1.2 Reinforcing Steel Bar

Both 6-cm and 9-cm OD micropiles were constructed with a 10M Grade 400 steel reinforcement bar, which extended from the pile head to the pile tip and was centered in the pile using wire centralizers. The minimum yield stress of the steel is 400MPa

according to *CSA* Standard G3018 and the bar had a coarse pitch, continuous ribbed thread to ensure a good grout-to-steel bond.

4.3.1.3 Grout

The grout comprised standard Type 10 Portland cement mixed with water. The reduced-scale micropiles were constructed using grout that had a water to cement ratio *w/c* of 0.55.

The grout was prepared by adding water and cement in a plastic bucket and then mixed for at least five minutes with a 40cm long by 10cm diameter mixing vane rotated at 1500 rpm. The grout was then tremie placed into the micropile using the positive displacement pump described below and each micropile was constructed within 30 minutes from the time the grout was mixed. ***Section 4.3.2*** contains additional details of the pile construction.

Before constructing micropiles, the unconfined compressive strength of the grout was measured by casting cylinders that were subsequently tested to failure in compression. Three-inch diameter by six-inches in height cylinders were prepared according to *ASTM* C192 using grout that had a water to cement ratio *w/c* of 0.45 and 0.55. The cylinders were filled with grout and subsequently stored in a steam room until the compression tests were performed. Prior to conducting compression tests, the cylinders were removed from the steam room and sulphur capped as described in *ASTM* C617. Compression tests were performed according to *ASTM* C39 at 1, 3, 7, 14 and 28 days after mixing to evaluate the grout strength versus curing time. As noted above, the piles were constructed with $w/c = 0.55$ grout even though compression tests were performed on both $w/c = 0.45$ and 0.55 grouts.

4.3.2 Micropile Construction

The micropile load tests performed in this study were undertaken in the steel calibration chamber shown in ***Figure 4.4***. The dimensions of the calibration chamber are 1.35-meter in diameter by 1.55-meter in height.

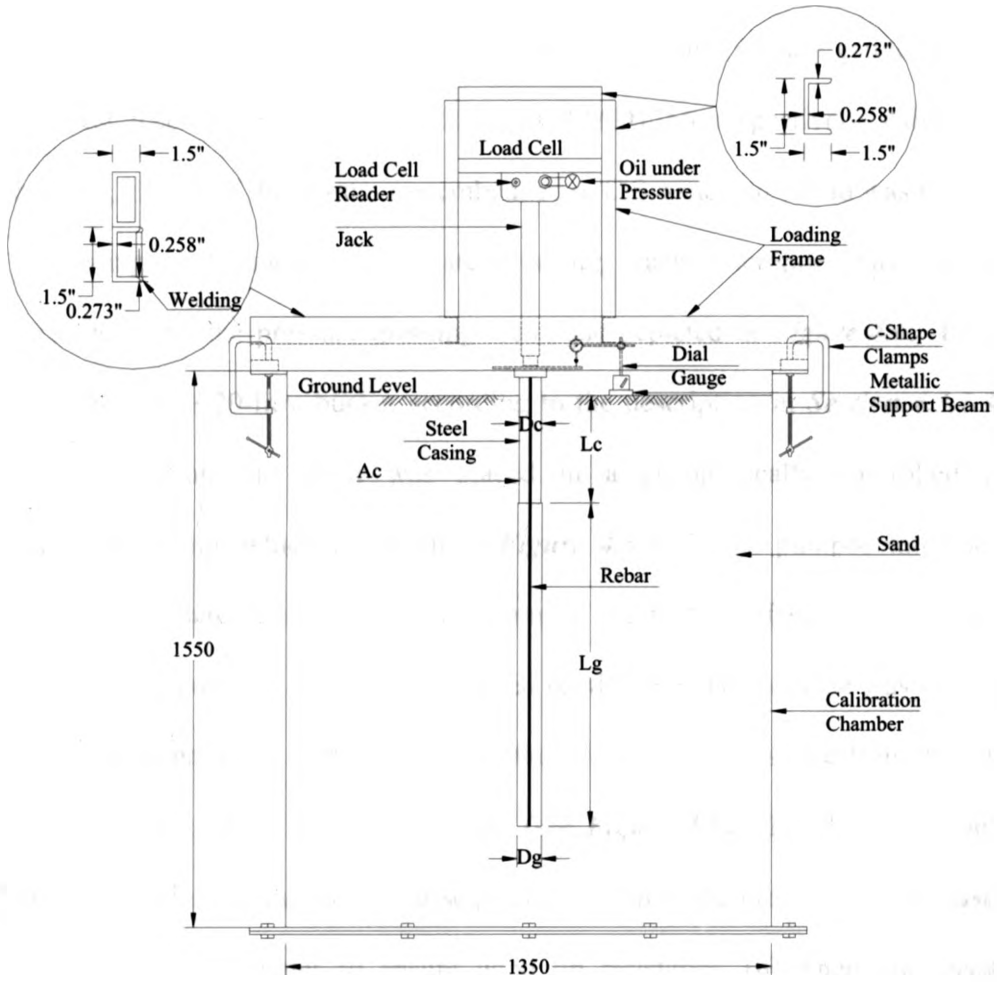

Figure 4.4 *Compression Test Setup*

The calibration chamber was filled by placing and compacting sand from the Lafarge Clarke Side Road pit in London Ontario (C.S. sand) in equal 25cm thick lifts. Each lift was manually compacted using a 10kg tamping rod equipped with a 20cm by 20 cm

bearing plate at the end and using the same numbers of blows per lift (500). After the first lift was compacted, a steel casing (either 6-cm or 9-cm OD) was centered inside the calibration chamber and laterally braced using timbers. Then, C.S. sand was compacted around the casing in 25cm thick lifts until the calibration chamber was filled to the finished level (see ***Figure 4.4***). For each micropile, the density and moisture content of C.S sand was measured occasionally using either a nuclear density gauge or sand-cone density test according to *ASTM* D2922 and *ASTM* D1556, respectively. After placement of the sand, 120cm of the casing was embedded in C.S. sand and 30 cm was sticking out.

Following embedment of the steel casing, each micropile was subsequently constructed using the pressure grouting technique depicted in ***Figure 4.6***. First, grout was prepared in a 20-litre bucket according to the description in ***Section 4.3.1.3***. After mixing the grout, the grout was placed in a pneumatically controlled positive displacement pump, which is shown in ***Figure 4.5*** and then pumped into the casing through a hose that extended from the pump to the bottom of the pile. The hose was subsequently removed, a top cap was placed on the pile and the hose was connected to the cap. Additional grout was pumped into the pile while air was bled from the micropile using the air bleeder valve on the top cap (see ***Figure 4.5***). Then, each micropile was pressure grouted using the following sequence: (i) First, the grout inside the casing was pressurized for 10 minutes to ensure good tip resistance, (ii) Then, the casing was retracted 30cm while maintaining constant grout pressure and the grout pressure was subsequently maintained for 10 minutes to permit a very small quantity of grout to penetrate into the soil (see ***Figure 4.6 b***). (iii) Following this, the casing was retracted an additional 30cm, while holding the grout pressure constant for 10 minutes (see ***Figure***

4.6 c). (iv) Finally, the casing was retracted a final 30cm and pressure grouted for 10 min (***Figure 4.6 d***). Upon completion of the grouting, the grout was given at least 24h to cure and then the casing was cut-off 5cm above the top of the sand. As noted above, the grout pump and pressure system is shown in ***Figure 4.5***. In this study, micropiles were constructed using grout pressures of either 100kPa or 175kPa, which was low enough to avoid hydro-fracturing of the C.S. sand. As indicated in the following sections, some micropiles were also constructed by gravity grouting only.

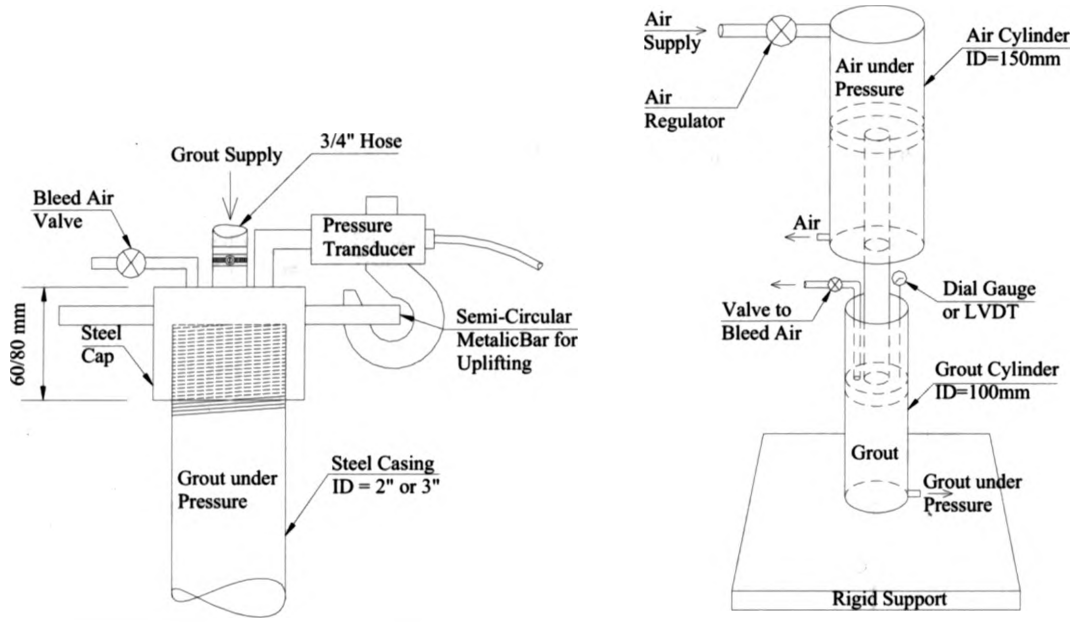

Figure 4.5 *Grouting Pressure System*

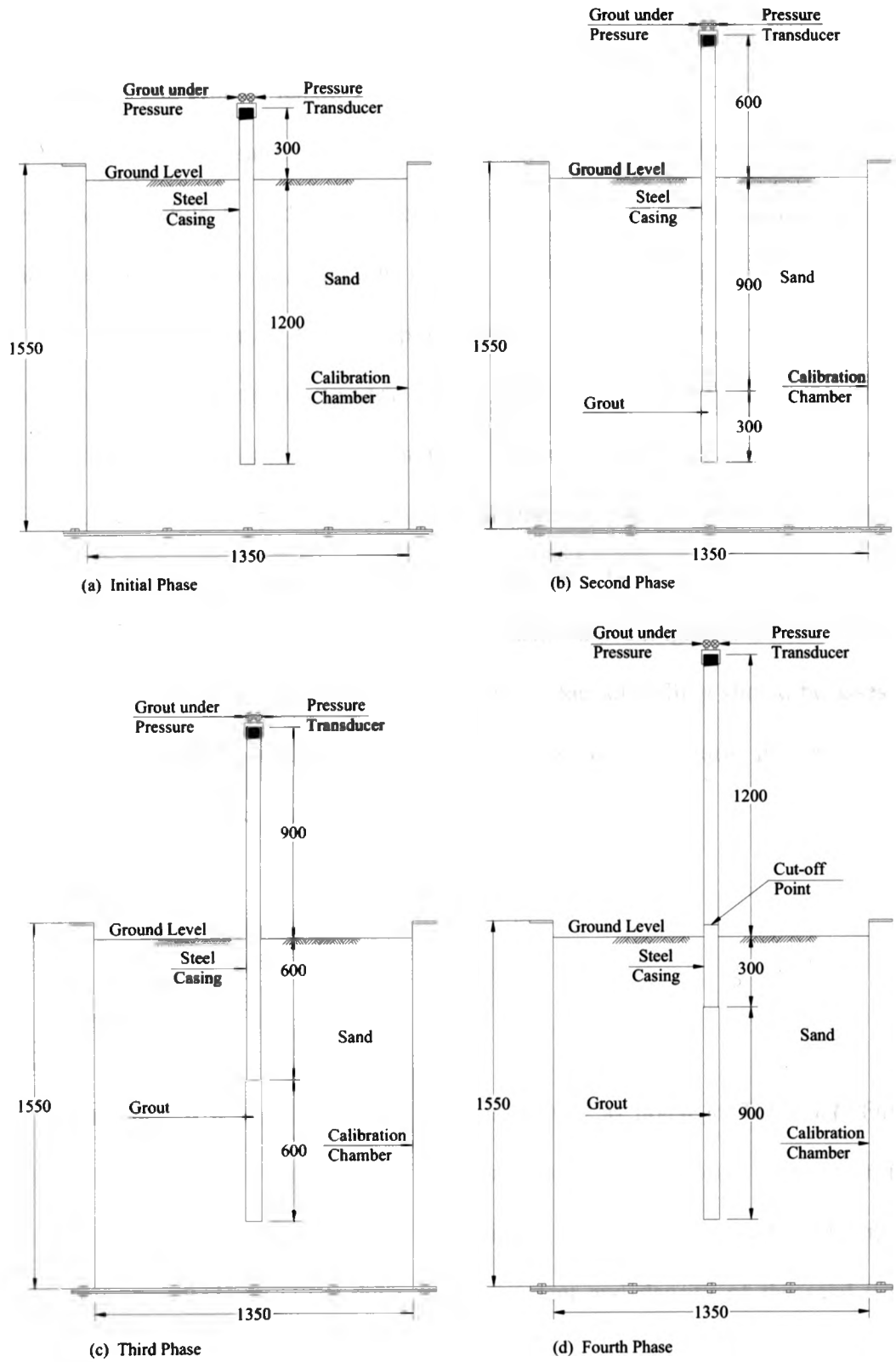

***Figure 4.6** Grouting Sequences*

On completion of construction, the typical micropile looked like that presented in ***Figure 4.2***. The grouted length was irregular in shape. In the following sections, L_c and L_g are used to represent the length of the casing and length of the grouted-soil contact, respectively, while D_c and D_g denote the outer diameter of the casing and the average diameter of the grouted section of the micropile.

Table 4.1 summarizes the micropile geometry and grout pressures used for each of the reduced-scale micropiles constructed and tested in this study. For each micropile, the pile geometry was determined by exhuming the micropile after testing and measuring the diameter at the micropile base, D_b, and taking several measurements of the shaft diameter, D_g and the length of the grouted section, L_g. It should be noted that the construction method followed in this study is idealized and it ignores the influence of the drilling process on the micropile behavior. The impact of drilling should be assessed in future studies; whereas, this study attempts to focus on the ideal pile behaviour by removing uncertainty created by drilling.

4.3.3 Tests Performed

Preliminary Tests

Two types of tests were performed in this study as noted in ***Table 4.1***. First, 12 preliminary tests were performed to gain experience with the load test system and to determine an adequate method for determining failure of the micropiles. During these tests (micropiles [1] to [12]), the moisture content and density of the sand was not measured or controlled.

Research Tests

The second types of tests (micropiles [13] to [32]) are labeled "Research tests". During these tests, the moisture content and compaction effort was controlled sufficiently to obtain repeatable results. These later tests form the basis for evaluating the capacity of micropiles in C.S. sand.

Table 4. 1 *Geometric Characteristics of Micropiles*

Test Type	Micropile No	*w/c*	D_c(cm)	p_g (kPa)	L_g (cm)	D_b (mm)	D_g (mm)
Preliminary Tests	1	0.45	6	100	-	-	-
	2	0.75	6	415	-	-	-
	3	0.55	6	Gravity	88	63	65
	4	0.55	6	100	89.5	61	67
	5	0.55	6	100	93	62.5	65.5
	6	0.55	6	175	90	62.5	67
	7	0.55	6	Tip	120	60.8	60.8
	8	0.55	9	100	90.5	89.5	94
	9	0.55	9	Gravity	96	91	93.5
	10	0.55	9	100	98	90	95
	11	0.55	9	100	89	90.5	94
	12	0.55	9	175	90	94	96
Research Tests	13	0.55	6	Tip	120	60.8	60.8
	14	0.55	6	Tip	120	60.8	60.8
	15	0.55	6	Tip	122	60.8	60.8
	16	0.55	9	Tip	110	89.3	89.3
	17	0.55	9	Tip	110	89.3	89.3
	18	0.55	9	Tip	110	89.3	89.3
	19	0.55	6	100	91	60.8	68.4
	20	0.55	6	100	86	57	66.3
	21	0.55	6	100	91	60	66.8
	22	0.55	6	100	92	62.5	66.7
	23	0.55	6	100	89	56.5	68.2
	24	0.55	6	175	93	62.5	65
	25	0.55	6	175	94	62	68.3
	26	0.55	6	175	94	62.5	66.3
	27	0.55	6	100	96	61	66
	28	0.55	6	100	92	68	69
	29	0.55	6	175	92	70	68
	30	0.55	6	175	90	70	69
	31	0.55	9	100	89	90.5	95
	32	0.55	9	Gravity	50	93	93

Note: *w/c* water to cement ratio
L_g length of the grouted section
D_g mean diameter of the grouted section
D_b diameter at the micropile tip

4.3.4 Micropile Loading

Each micropile was loaded in axial compression using the apparatus shown in ***Figure 4.4***. A hydraulic jack and reaction frame were used to apply the load to the top of a micropile. The reaction frame was fixed to the calibration chamber using C-shape clamps. A 45kN INTERFACE load cell (S.N. 76691) was attached to the reaction frame and in series with the jack to measure the applied load.

The load cell was connected to a digital readout unit and the loads were recorded manually during the tests. Vertical displacement of the micropile was measured using a 0.001mm precision dial gauge that rested on steel bearing plates placed on top of the micropile head. The dial gauge was mounted to an independent frame that was supported on the edges of the calibration chamber.

Each load test was performed by manually increasing the axial load using the hydraulic jack by increments of either 1kN or 2kN for 6-cm OD and 9-cm OD micropiles, respectively. For each increment, the load was maintained constant for 1 to 2 minutes until the displacement stabilized and the micropile-head deflection was recorded at the end of each load increment.

4.3.4 Special Tests

A series of tip-resistance tests (3 for 6-cm OD micropiles and 3 for 9-cm OD micropiles) was performed to determine the bearing capacity factor, N_q, at the tip of the micropile. To obtain almost zero or negligible skin friction, 120 cm long 6-cm OD and 9-cm OD steel casings were embedded in C.S. sand and filled with grout. Grease was applied to the outer surface of the casing prior to embedment to reduce the skin friction.

For one of the end-bearing tests, the pile was constructed inside a PVC sleeve with sufficient clearance to ensure zero skin friction between the micropile and casing. This test was done to confirm the results from the "greased" tests. Details regarding the tip-resistance tests are presented in ***Figure 4.7.*** Each of the tip resistance micropiles was load tested to failure and the end-bearing capacity factor N_q was deduced from the failure load.

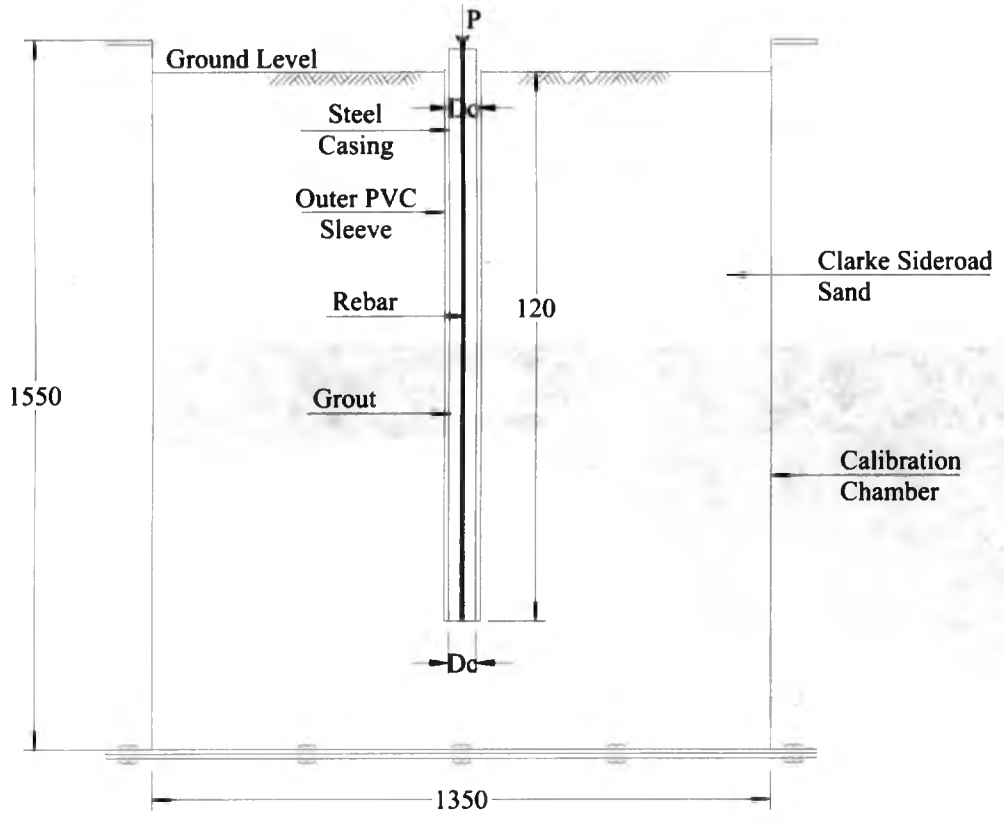

Figure 4.7 *Tip-resistance Setup using an Outer PVC Sleeve*

4.3.6 Pile Roughness

Prior to undertaking this study, it was hypothesized that increasing the pressure during grouting may increase the roughness of the micropile and potentially increase its axial capacity in compression. As a result, the roughness of each micropile was measured using the methodology summarized in ***Figure 4.8***. Each micropile was exhumed from the calibration chamber after completion of the compression test and cleaned using compressed air. Then the micropile profile was traced using a profiling tool that is shown in ***Figure 4.8a-c***. Longitudinal profiles were obtained on four longitudinal orthogonal axes over a distance of 60 cm as shown in ***Figure 4.8a***.

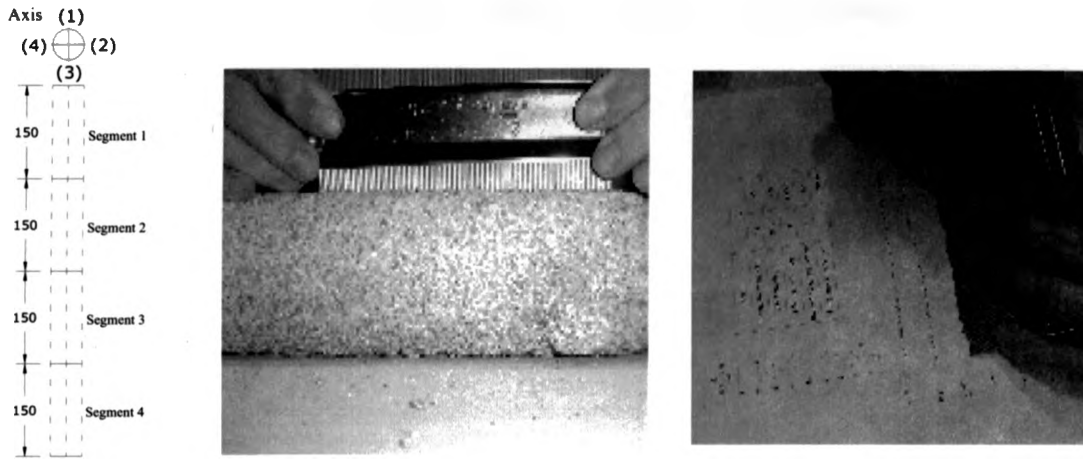

Figure 4.8 *Micropile Profile, Profiling Tool and Roughness Measurement*

A comb-like profiling tool was used to measure the roughness of each micropile. The tool consisted of linear-arranged wires that took the shape of the micropile when pressed against its surface. The shape of the profiling tool was then transferred to paper by tracing

with a sharp pen. After tracing the micropile profile, the pile roughness was measured using two methods:

(i) First, the roughness angle,α_r, was measured over a length of 12 mm as shown in ***Figure 4.8d***. A length of 12mm was chosen because it is comparable to the micropile displacement at failure for 6-cm OD micropiles. The mean roughness angle, *i*, was computed from 70-85 measurements for micropile along the four axes shown in ***Figure 4.8a***.

(ii) The mean roughness height, H_r, was deduced as shown in ***Figure 4.8d***, for each segment, on each of the four axes shown in ***Figure 4.8a***, the mean roughness height is reported for each micropile in ***Table 4.8***.

Appendix A provides additional details of the roughness measurements.

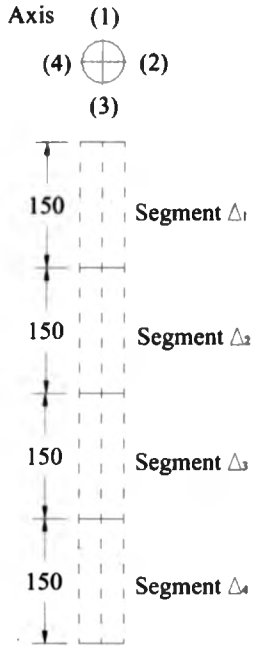

Pile No.	25	
Grout Pressure (P_g)	175	kPa
Pile Length (L_g)	94	cm
Pile Diameter (D_c)	6	cm
Ultimate Capacity (P_{ult})	28	kN

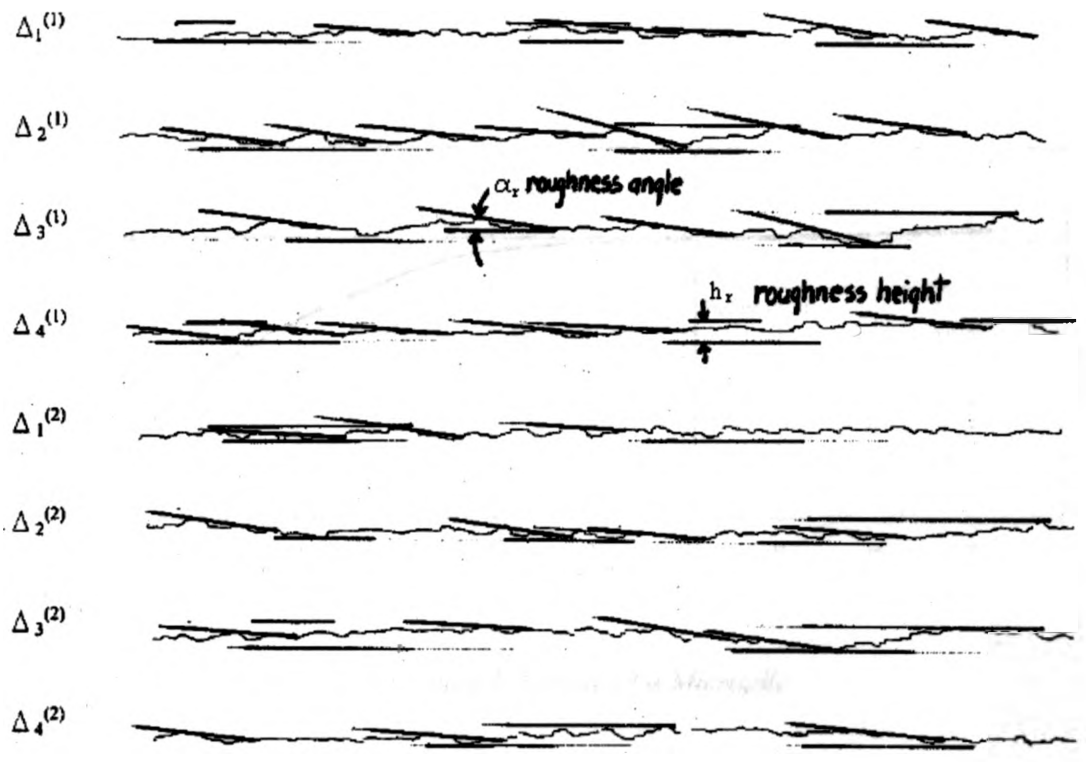

Figure 4.8d *Typical Profile for Measuring the Roughness of a Micropile*

4.4 Load Test Interpretation

Lastly, the ultimate load of a full-scale micropile is typically evaluated using criteria such as Davisson's or Terzaghi's criteria, which are based on deflection considerations (see Poulos 1980). However, the application of these criteria to the reduced-scale micropiles in this study was found to give misleading results as shown below in ***Section 4.5.2***. Thus, the failure load for the test micropiles was evaluated using a deflection criterion that was compatible with the micropile load-displacement response obtained in this study. The ultimate load was taken as the load carried by 6-cm and 9-cm micropiles at a vertical deflection of 12mm. ***Figure 4.9*** shows a typical load-displacement response and the interpreted failure load, which will be hereafter referred to as the large displacement ultimate capacity or P_{ult}.

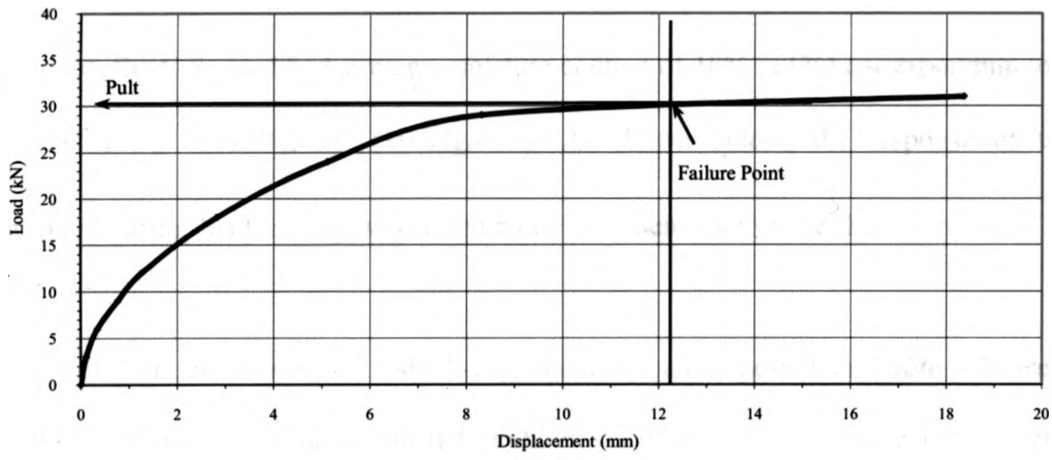

Figure 4. 9 *Typical Load-Displacement Response of a Micropile*

4.5 Results

The moisture content and the percent standard Proctor maximum dry density (*SPMDD*) of the C.S. sand for each micropile test are presented in ***Table 4.2***. The relative density of the sand in each test was not less than 94%. For micropile tests 13-32, the moisture content varied in the range of 0.7% to 10.37%. As indicated in ***Table 4.2***, the micropiles are grouped according to the moisture content of the C.S. sand during the test and based on the stiffness and ultimate capacity of the micropiles during load testing. The grouping is intended to differentiate sand conditions during the tests based on density. The density of the sand was deduced from its moisture content and *Curve 1* in ***Figure 3.8*** and confirmed by occasional density tests performed during placement of the sand (see ***Table 4.2***).

For the *Group 1* micropiles, C.S. sand had an average moisture content of 3% (±2%) corresponding to a dry density, ρ_d, of 1.80g/cm^3 (±0.02g/cm^3). For the *Group 2* micropiles, the C.S. sand had average moisture content of 10% (±1%) corresponding to a dry density ρ_d of 1.84g/cm^3 (±0.02g/cm^3). As shown below, the response of the micropiles during load testing was found to be very sensitive to the density of the C.S. sand.

As noted in ***Section 4.3.3***, tests 1-12, which are not reported in ***Table 4.2***, were preliminary tests that were conducted without controlling the moisture content and density of C.S. sand.

***Table 4. 2** Densities and Moisture Contents for Group 1 and Group 2 Micropiles*

	Pile No[1]	ρ_d (g/cm^3)		w (%)	SPMDD (%)
		Measured	Deduced[2]		From deduced density
Group 1	**13**	1.75	1.81	4.35	97.3
	14	1.82	1.80	3.91	96.8
	16	1.76	1.80	3.56	96.8
	17	1.80	1.80	3.20	96.8
	19	1.76	1.80	2.6	96.8
	20	1.81	1.79	0.7	96.2
	21	1.77	1.79	1.14	96.2
	22	1.79	1.79	1.01	96.2
	23	1.85	1.79	1.02	96.2
	24	1.83	1.79	1.65	96.2
	25	1.85	1.79	1.86	96.2
	26	1.80	1.79	2.14	96.2
	27	1.82	1.79	2.05	96.2
	31	1.76	1.81	4.39	97.3
	32	1.76	1.81	5.3	97.3
Group 2	**15**	1.83	1.85	10.27	99.5
	18	1.87	1.84	9.67	98.9
	28	1.87	1.84	9.28	98.9
	29	1.77	1.84	9.86	98.9
	30	1.84	1.85	10.37	99.5

[1] Note the density and moisture content was not recorded during tests 1-12

[2] Estimated from *Curve 1* in ***Figure 3.8*** and moisture content, *w*

4.5.1 Compressive Strength of Grout

The results of compression tests on grout cylinders with *w/c* ratio of 0.45 and 0.55 are summarized in ***Table 4.3*** and plotted in ***Figure 4.10,*** which shows the variation of grout strength with curing time. During the tests, the type of failure was predominantly cone and in a few cases columnar. From ***Figure 4.10***, it can be seen that the average 28day compressive strength of the grout is 28.7MPa for *w/c* = 0.55 and 48.8MPa for *w/c* = 0.45.

Table 4. 3 *Ultimate Compressive Load on Grout Samples for w/c ratio of 0.55 and 0.45*

Time (days)	Compressive Strength (*w/c* = 0.55)				Compressive Strength (*w/c* = 0.45)			
	Test 1	Test 2	Test 3	Average	Test 1	Test 2	Test 3	Average
1	9.8	10.7	10.5	*10.3*	21.2	17.6	19.1	*19.3*
3	18.3	20.5	19.4	*19.4*	26.4	24.7	21.8	*24.3*
7	27.6	23.8	28.1	*26.5*	38.0	38.5	41.9	*39.5*
28	27.0	31.8	27.3	*28.7*	50.7	51.7	43.9	*48.8*

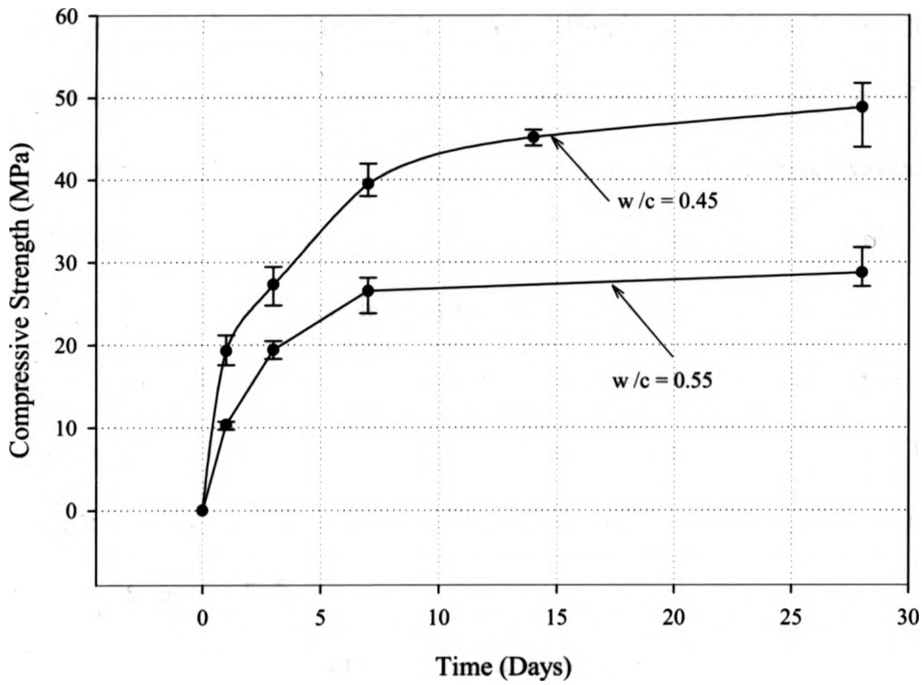

Figure 4.10 *Grout Strength for Samples with w/c of 0.45 and 0.55*

4.5.2 Preliminary Micropile Tests

The first twelve tests summarized in ***Table 4.1*** were preliminary tests and they demonstrate that it was difficult to obtain repeatable results from load test to load test without careful control of the moisture content and compaction of the C.S. sand. It will be shown later that this was due to variations in the moisture content of the C.S. sand and consequent sand density. ***Figures 4.11*** and ***Figure 4.12*** show the measured load versus micropile head displacement for 6-cm and 9-cm diameter micropiles, respectively.

The load-displacement results for 5 load tests performed on 6-cm OD micropiles are summarized in ***Figure 4.11***. At the time of these tests, failure was determined using Davison's criterion. From ***Figure 4.11***, it can be seen that the micropile capacity varied from 8kN for micropile [1] to 56kN for micropile [2]. The average load capacity using Davison's criterion was about 30kN. The stiffness and ultimate loads of micropiles [1]-[5] were extremely variable, which made it difficult to reach conclusions from the tests.

Figure 4.12 shows similar results for the 9-cm OD micropiles (tests [8]-[12]). Using Davison's criterion, the ultimate load for the 9-cm OD micropiles varied from 40kN to 52kN, with a mean of about 48kN. Again, the results were not repeatable.

Two conclusions can be drawn from these results:

(i) The use of Davison's method is not suitable for evaluating micropile failure, since all micropiles were able to support significantly higher loads than the Davison load. In fact, Davison's criterion is actually a serviceability criterion, and as such it is not well suited to assess failure.

(ii) It is important to control the moisture content, compaction effort and consequent soil density of the C.S. sand to achieve repeatable load-displacement behaviour.

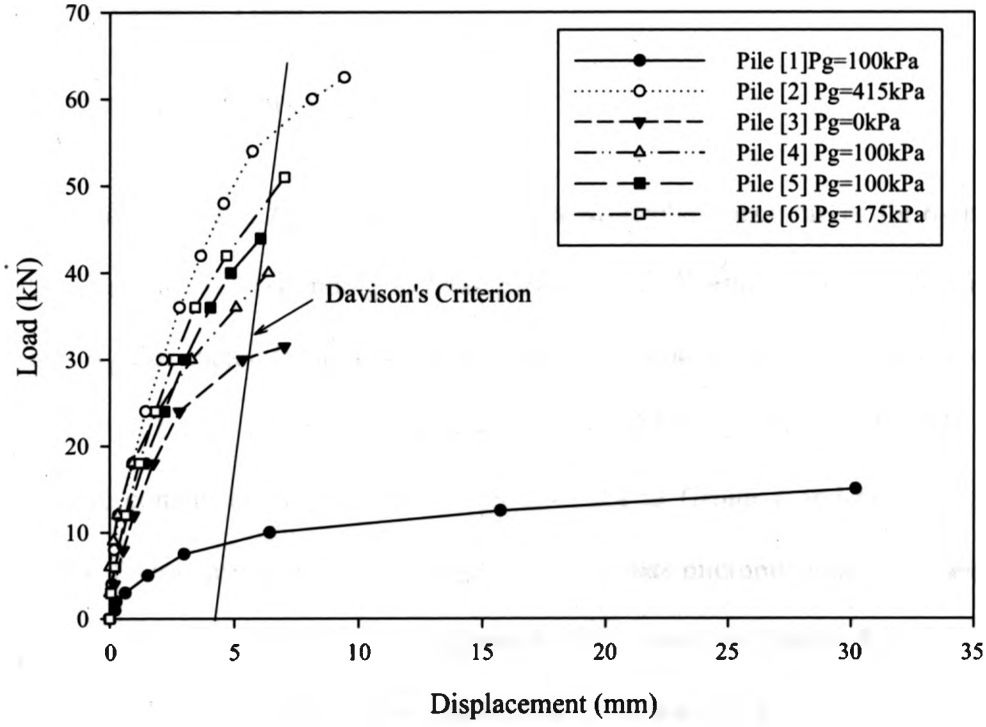

Figure 4.11 *Preliminary Compression Tests for 6-cm OD Micropiles*

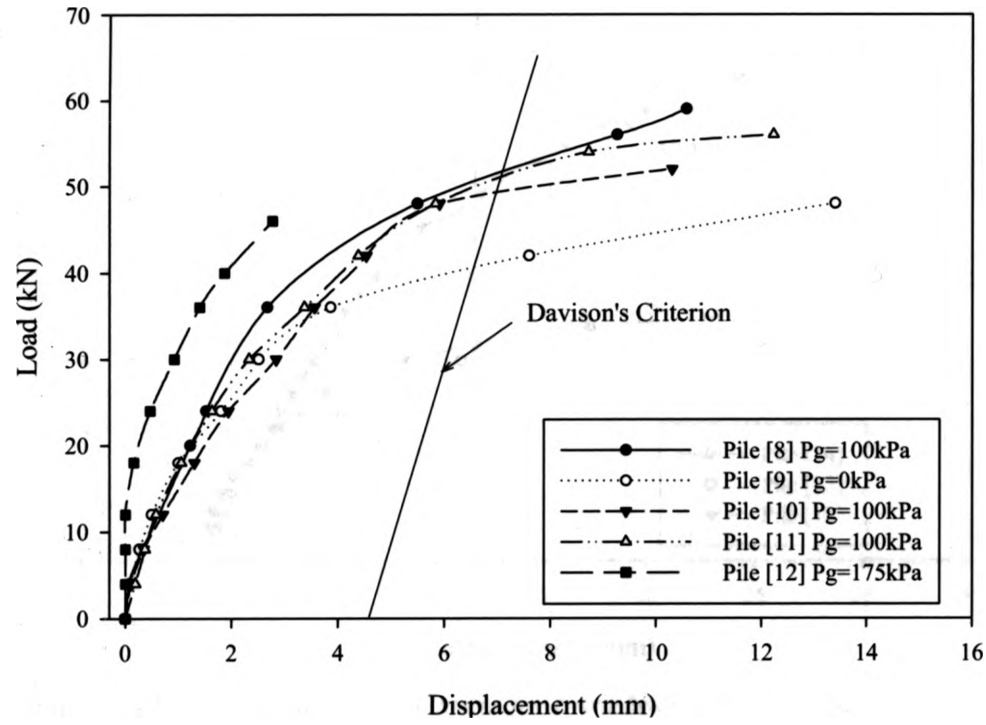

Figure 4.12 *Preliminary Compression Tests for 9-cm OD Micropiles*

4.5.3 Research Tests

End-bearing Factors (N_q)

Figure 4.13 and ***Figure 4.14*** show the load-displacement curves for 6-cm and 9-cm OD micropiles corresponding to tests performed to determine the end-bearing capacity factor N_q. For each micropile diameter, tests were done in sand compacted to either 96 % *SPMDD* (±2.0%) at moisture content of 3% (±2.0%) or 99.5% *SPMDD* (±1.0%) at moisture content of 10% (±1.0%) corresponding to *Group 1* and *Group 2* micropiles. ***Table 4.4*** summarizes the large displacement ultimate micropile loads, P_{ult}, and N_q and $\emptyset'$ deduced from the test result using ***Figure 4.3***. The curves in ***Figure 4.13*** and ***Figure 4.14*** are labeled by their group and test number (see also ***Table 4.4***).

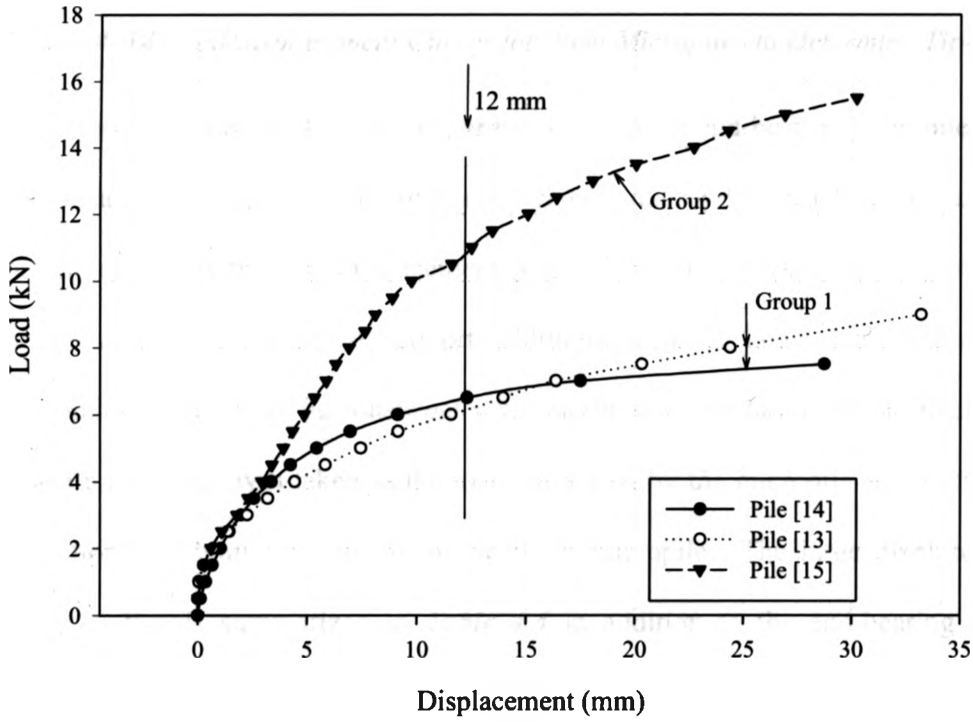

Figure 4. 13 *Load-displacement Curves for 6-cm Micropiles to Determine Tip-resistance*

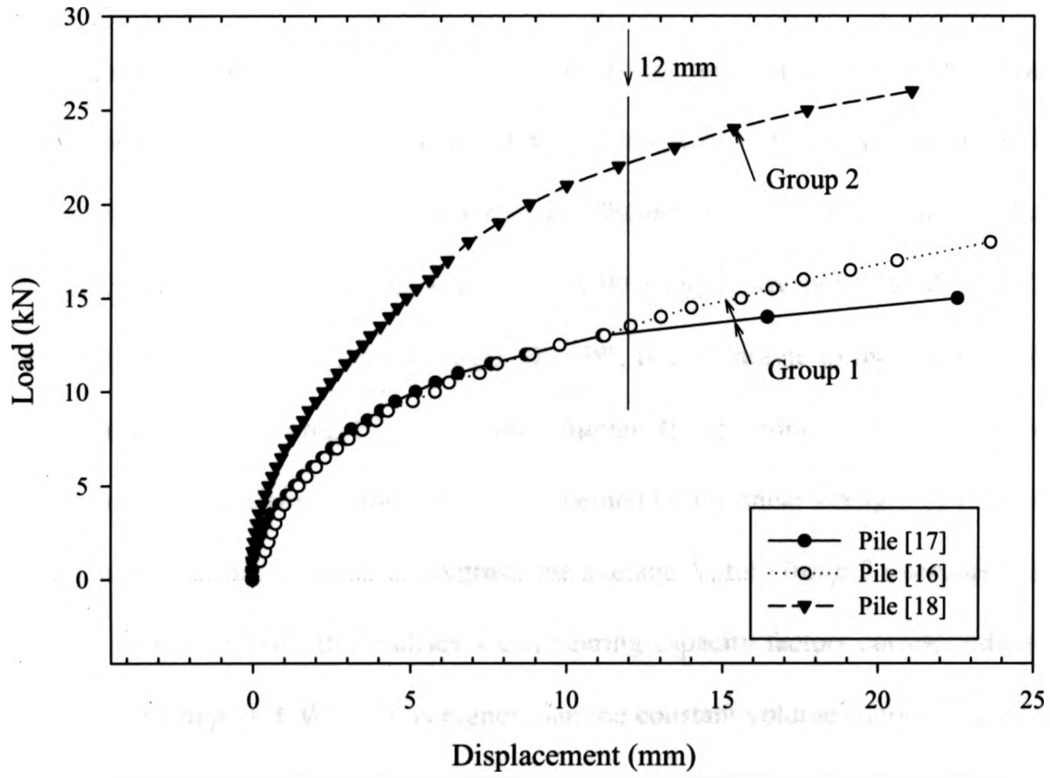

Figure 4. 14 *Load-displacement Curves for 9-cm Micropiles to Determine Tip-resistance*

Referring to ***Figure 4.13*** and ***Figure 4.14***, all of the end-bearing micropiles exhibited non-linear load-displacement response. Some micropiles reached an ultimate or maximum load with large displacement (e.g. see Micropile test [14]); whereas most of the micropiles continued to support additional load at large deformation (e.g. see Micropile test [13]). To be consistent with interpretation of failure for all micropiles, the ultimate load, P_{ult}, was taken as the load supported by the micropile at a micropile head deflection of 12mm for both 6-cm and 9-cm micropiles. The large displacement load capacity, P_{ult}, is summarized in ***Table 4.4*** in addition to the end-bearing factor, N_q, corresponding to P_{ult}.

In ***Table 4.4***, there are distinct end-bearing factors for the *Group 1* and *Group 2* micropiles. Furthermore, given the geometry of the micropiles ($L_g/D_g \approx 20$) the measured end-bearing factors reported in ***Table 4.4*** are consistent with ***Figure 4.3*** (Tomlinson 2001) and the direct shear tests reported in ***Chapter 3***. For *Group 1* micropiles, the average N_q deduced from the measured P_{ult} is 99 which corresponds to $\emptyset' = 38°$ from ***Figure 4.3***. This effective friction angle, $\emptyset'= 38°$, is comparable to the constant volume friction angle of C.S. sand, $\emptyset'_{cv}= 36°$ (See ***Chapter 3***). Accordingly, it is concluded that the response of the *Group 1* micropiles is governed by the shear strength of C.S. sand at or very near constant volume. In contrast, the average N_q for *Group 2* micropiles is 165, which is consistent with Berezantsev's end-bearing capacity factors corresponding to $\emptyset' = 40°$. From ***Chapter 3***, $\emptyset' = 40°$ is higher than the constant volume friction angle of C.S. sand, which suggests that *Group 2* micropiles is governed by the shear strength of C.S. sand in a state that is slightly more dense than at constant volume.

Table 4. 4 *Results of Tip Resistance Tests*

D_c (cm)	Group	Pile No.	P_{ult}† (kN)	N_q	Avg. N_q	$\emptyset'$†† (deg)
6	1	13	6	95	99	38
		14	6.5	103		
	2	15	10.5	165	165	40
9	1	17	14	96	99	38
		16	15	103		
	2	18	24	164	164	40

† Large displacement load capacity (δ_v = 12mm for 6-cm and 9-cm OD micropiles)

†† Deduced from average N_q using ***Figure 4.3*** and Berezantsev's Curve

Ultimate Pile Loads

This section compares the measured P_{ult} of *Group 1* and *Group 2* micropiles in compression with the P_{ult} calculated according to equations from the *FHWA* Design Manual (*FHWA* 1997).

The load-displacement response of *Group 1* and *Group 2* 6-cm OD micropiles is summarized in ***Figure 4.15*** and ***Figure 4.16***. ***Table 4.5*** lists the measured P_{ult} at δ_v = 12mm. From ***Figure 4.15*** and ***Figure 4.16***, it can be seen that all *Group 1* and *Group 2* 6-cm OD micropiles exhibited a non-linear load-displacement response and have a reasonably well-defined ultimate load at large displacement. For the *Group 1* micropiles, P_{ult} varied from 27kN to 33kN. As expected, P_{ult} for the *Group 2* micropiles was higher varying from 50kN to 57kN due to the higher sand density. From ***Figure 4.15*** and ***Figure 4.16,*** it can be seen that the density of C.S. sand strongly influences the micropile capacity. Based on the load tests on 6-cm OD micropiles, P_{ult} is 54kN (± 3kN) for micropiles in C.S. sand with ρ_d = 1.84g/cm^3 versus P_{ult} = 30kN (± 3kN) for micropiles with ρ_d = 1.80g/cm^3. It is noted that micropile test [22] deviated from the average values of the ultimate capacity of *Group 1* micropiles due to unknown reasons even though the soil parameters and construction procedures were the same as for the other micropiles tested.

The load-displacement response of *Group 1* 9-cm OD micropiles is summarized in ***Figure 4.17***. Similar trends can also be observed for these micropiles. For *Group 1* 9-cm OD micropiles, P_{ult} varies between 39kN and 40kN.

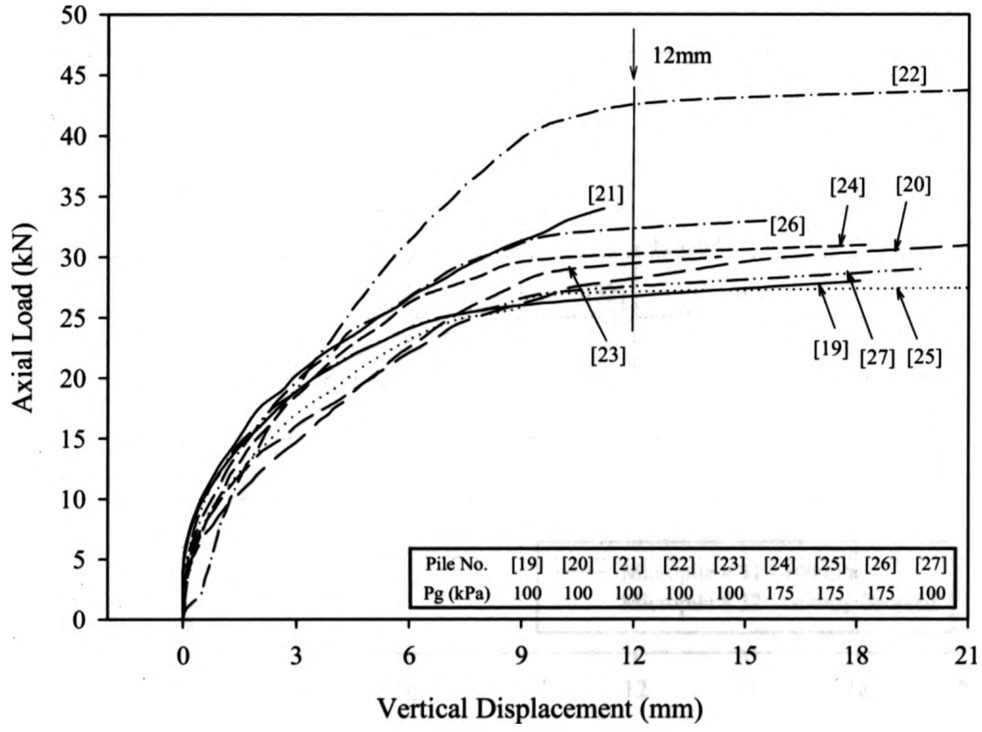

Figure 4.15 *Load-Displacement Curves for 6-cm Micropiles of Group 1 Micropiles*

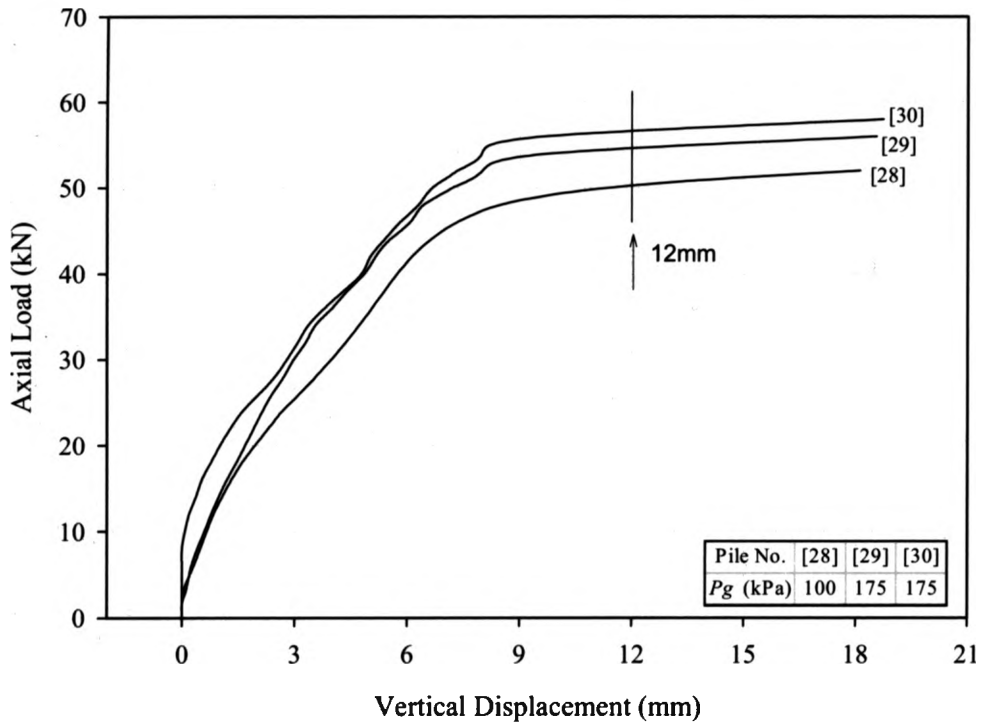

Figure 4.16 *Load-Displacement Curves for 6-cm Micropiles of Group 2 Micropiles*

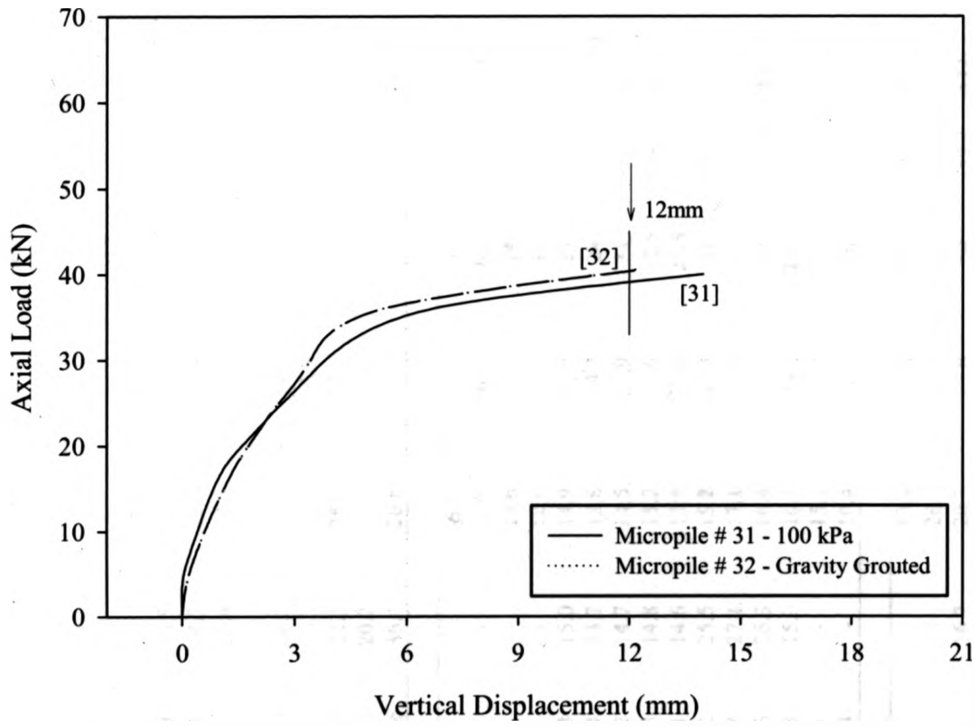

Figure 4.17 *Compression Tests for 9-cm OD Group 1 Micropiles*

Table 4. 5 Ultimate Load Calculation using FHWA Expression for Type B Micropiles in Cohesionless Soils Compared with Test Results

Test	OD (cm)	Pile No	Group	p_g (kPa)	D_g (mm)	D_b (mm)	L_g (cm)	Q_b (kN)	Q^1s_{FHWA} (kN) Eq.[4.2]	Q^2s_{FHWA} (kN) Eq.[4.3]	Calculated $P^1_{ULT}{}^{FHWA}$ (kN)	Calculated $P^2_{ULT}{}^{FHWA}$ (kN)	Measured P_{ULT} (kN)	Error[1] (%)	Error[2] (%)
Preliminary Tests	6	**1**	-	100	-	-	-	-	-	-	-	-	**12**	-	-
	6	**2**	-	415	-	-	-	-	-	-	-	-	**>62**	-	-
	6	**3**	-	0	65.00	63.00	88.0	6.74	0.7	-	7.5	6.7	**32**	-76.6	-78.9
	6	**4**	-	100	67.00	61.00	89.5	6.40	8.0	14.5	14.4	20.9	**40**	-64.0	-47.9
	6	**5**	-	100	65.50	62.50	93.0	6.91	8.3	14.7	15.2	21.6	**44**	-65.4	-50.9
	6	**6**	-	175	67.00	62.50	90.0	6.74	8.1	25.4	14.8	32.2	**51**	-71.0	-36.9
	6	**7**	-	*Toe*	60.75	60.75	120.0	6.37	-	-	6.4	6.4	**11.5**	-44.6	-44.6
	9	**8**	-	100	94.00	89.50	90.5	13.88	11.4	20.5	25.3	34.4	**60**	-57.8	-42.7
	9	**9**	-	0	93.50	91.00	96.0	15.01	1.2	-	16.2	15.0	**47**	-65.5	-68.1
	9	**10**	-	100	94.50	90.00	98.0	14.91	13.1	22.3	28.0	37.2	**52**	-46.2	-28.4
	9	**11**	-	100	94.00	90.50	89.0	14.02	11.1	20.2	25.1	34.2	**56**	-55.1	-39.0
	9	**12**	-	175	96.00	94.00	90.0	15.25	11.6	36.4	26.8	51.7	**47**	-43.0	10.0
Group 1	6	**13**	1	*Toe*	60.75	60.75	120.0	6.37	-	-	6.4	6.4	**6**	6.2	6.2
	6	**14**	1	*Toe*	60.75	60.75	120.0	6.37	-	-	6.4	6.4	**6.5**	-2.0	-2.0
	9	**16**	1	*Toe*	89.25	89.25	110.0	12.60	-	-	12.6	12.6	**14**	-10.0	-10.0
	9	**17**	1	*Toe*	89.25	89.25	110.0	12.60	-	-	12.6	12.6	**14**	-10.0	-10.0
	6	**19**	1	100	68.40	61.00	91.0	6.5	8.4	15.0	14.9	21.5	**27**	-45.0	-20.4
	6	**20**	1	100	66.30	57.00	86.0	5.4	7.4	13.7	12.8	19.2	**28**	-54.1	-31.5
	6	**21**	1	100	66.80	60.00	91.0	6.3	8.2	14.7	14.5	20.9	**34**	-57.5	-38.5
	6	**22**	1	100	66.70	62.50	92.0	6.9	8.3	14.8	15.2	21.6	**42.5**	-64.3	-49.1
	6	**23**	1	100	68.20	56.50	89.0	5.5	8.1	14.6	13.5	20.1	**29.5**	-54.1	-31.9
	6	**24**	1	175	65.00	62.50	93.0	6.9	8.2	25.5	15.2	32.4	**31**	-51.1	4.6
	6	**25**	1	175	68.30	68.30	94.0	8.3	8.8	27.1	17.1	35.4	**27**	-36.5	31.1
	6	**26**	1	175	66.30	66.30	94.0	7.8	8.6	26.3	16.4	34.1	**33**	-50.3	3.4
	6	**27**	1	100	66.00	66.00	96.0	7.9	8.8	15.3	16.7	23.2	**27.5**	-39.2	-15.7
	9	**31**	1	0	95.00	90.50	89.0	14.02	1.1	-	15.1	14.0	**39**	-61.2	-64.1
	9	**32**	1	0	93.00	93.00	50.0	9.95	0.4	-	10.4	10.0	**40**	-74.0	-75.1
Group 2	6	**15**	2	***Toe***	60.75	60.75	122.0	13.45	-	-	13.4	13.4	**10.5**	28.1	28.1
	9	**18**	2	*Toe*	89.25	89.25	110.0	26.74	-	-	26.7	26.7	**22**	21.5	21.5
	6	**28**	2	***100***	69	61	92.0	10.9	9.4	16.7	20.3	27.6	**50**	-59.4	-44.8
	6	**29**	2	***175***	68	70	92.0	14.3	9.3	28.9	23.6	43.2	**54.5**	-56.7	-20.7
	6	**30**	2	***175***	69	70	90.0	14.1	9.1	28.6	23.2	42.7	**57**	-59.3	-25.0

[1]Skin friction was estimated using equation [4.2] assuming K'=4 and $\emptyset' = 38°$ for Group 1 and $\emptyset' = 40°$ for Group 2 micropiles

[2]Skin friction was estimated using equation [4.3]

Table 4.5 summarizes the measured and calculated P_{ult} for the micropile load tests performed. As noted above in the methodology section, the ultimate capacity was calculated using two approaches. The first approach used equation *[4.1]* and *[4.2]* to deduce the theoretical ultimate micropile capacity and the results are listed in the 12th column. The second approach used equation *[4.1]* and *[4.3]*. The corresponding results are in the 13th column.

On inspection of ***Table 4.5*** it can be seen that there is considerable difference between the calculated and measured micropile capacities. To illustrate the differences, ***Figure 4.18*** shows a plot of calculated versus measured P_{ult} and ***Figure 4.19*** shows the ratio of calculated versus measured P_{ult} with 95% confidence intervals for micropiles [19] to [32]. Overall, the difference between calculated and measured P_{ult} is substantial for the relatively controlled conditions of the micropile load tests. From ***Figure 4.19***, the measured P_{ult} was double that calculated using equations *[4.1]* and *[4.2]*. In addition, the variation was in the order of 35%, which introduces considerable uncertainty.

To conclude, ***Figure 4.20*** compares P_{ult} calculated using equations *[4.1]* and *[4.3]* with the measured P_{ult} and ***Figure 4.21*** shows the corresponding ratio of calculated and measured P_{ult}. The micropiles considered in these figures are only the ones built using grout under pressure such as [19] to [30]. Recalling that equation *[4.3]* relates the skin friction, Q_s to the grout pressure, p_g. From ***Figure 4.20*** and ***Figure 4.21***, it can be seen that, the calculated micropile capacities also deviate significantly from the measured capacity. Based on these figures, there is up to 50% variation between calculated and measured ultimate loads. However, for the case of P_{ult} calculated using equations *[4.1]* and *[4.3]*, the calculated capacity is on average 75% of the measured capacity. In some

instances, the calculated capacity is 35% higher than measured, which is not desirable. From ***Figure 4.20*** it can be seen that the calculated results exceeded the measured ones and were not conservative only for the micropiles with a grouting pressure of 175kPa,.

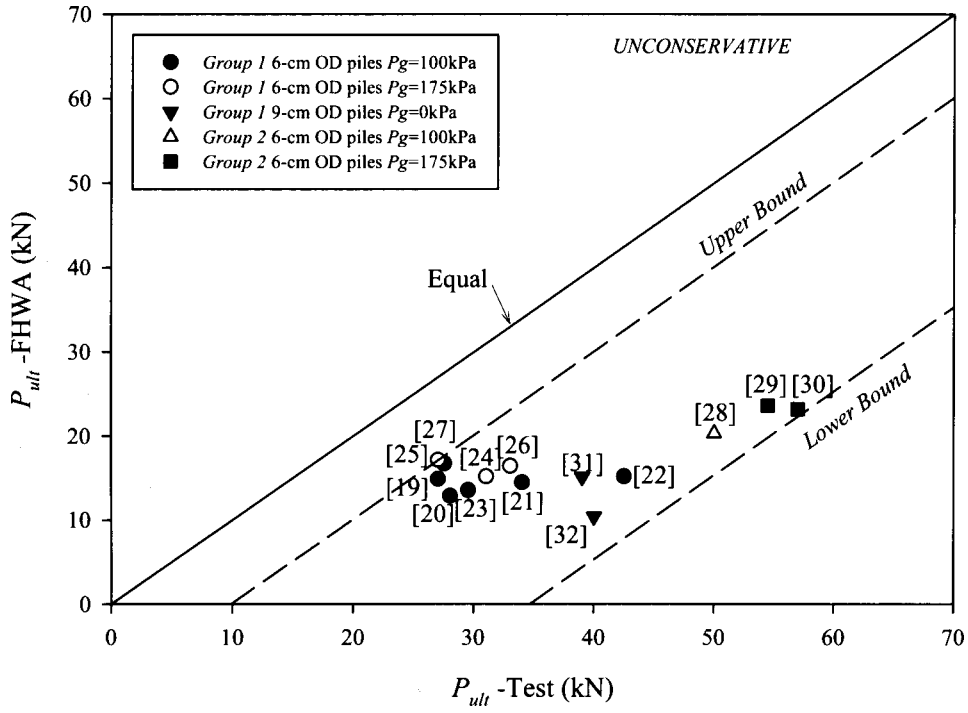

Figure 4.18 *Measured P_{ult} versus Calculated P_{ult} using Equations [4.1] and [4.2]*

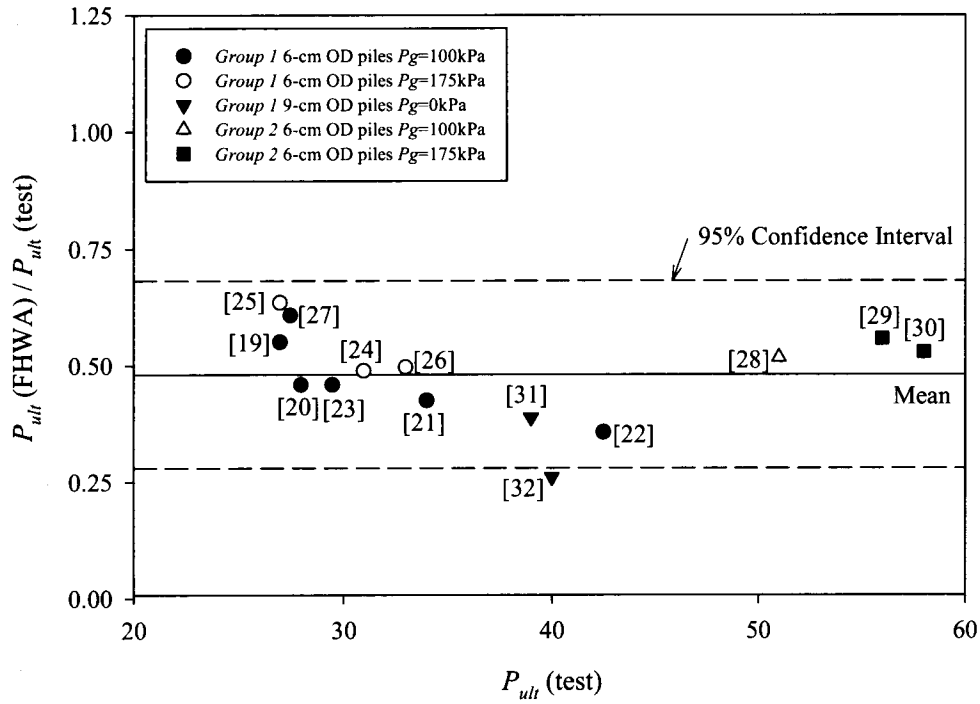

Figure 4.19 *95% Confidence Intervals of Measured P_{ult} versus Calculated P_{ult} using Equations [4.1] and [4.2]*

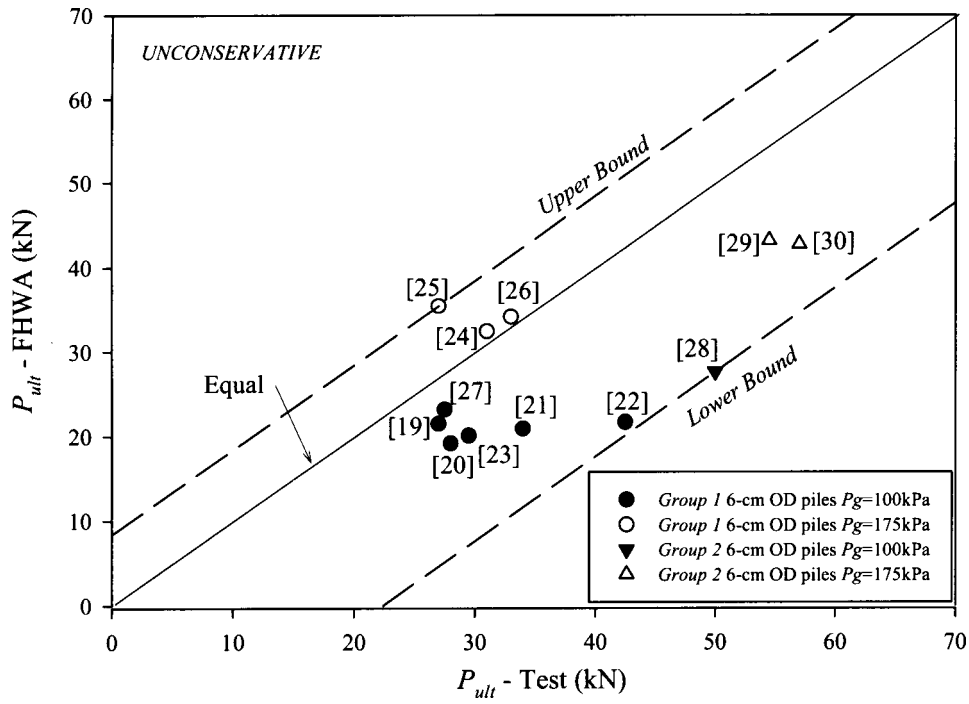

Figure 4.20 *Measured P_{ult} versus Calculated P_{ult} using Equations [4.1] and [4.3]*

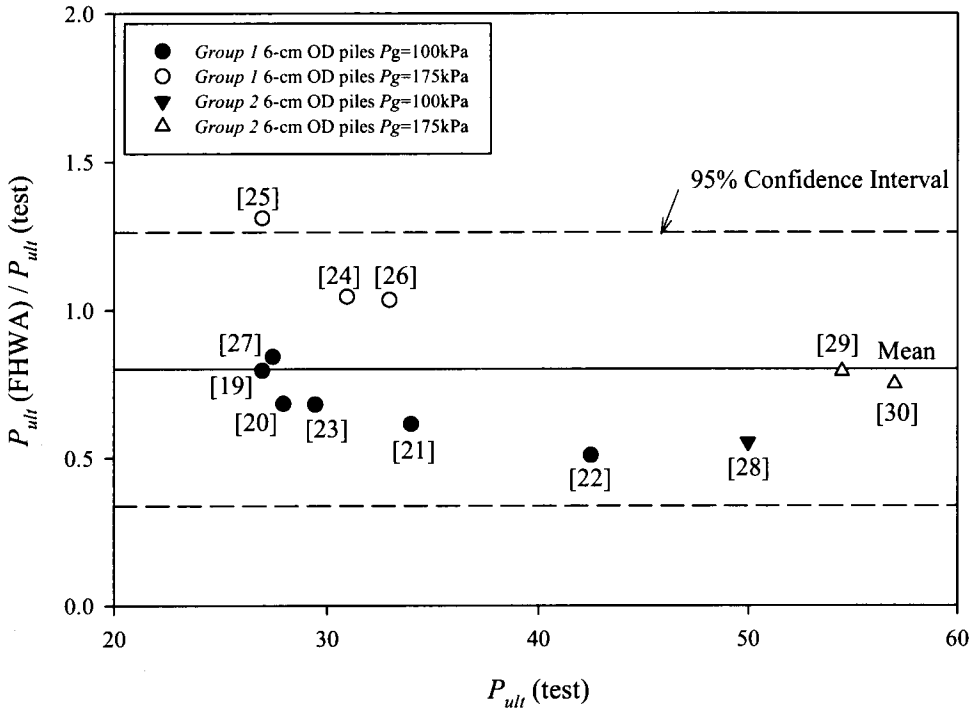

Figure 4.21 *95% Confidence Intervals of Measured P_{ult} versus Calculated P_{ult} using Equations [4.1] and [4.3]*

4.5.4 Micropile Capacity versus Grout Pressure

The results from *Group 1* and *Group 2* micropile tests were also used to investigate the influence of grout pressure on the axial capacity of micropiles.

Group 1 and *Group 2* micropiles were constructed using gravity grouting or pressure grouting at pressures of 100kPa or 175kPa. ***Figure 4.22*** shows that P_{ult} for the 6-cm OD *Group 1* micropiles varies from 27 to 33kN for 175-kPa grout pressure and from 27.5 to 34kN for 100kPa grout pressure. Only test [3] was gravity grouted. The ultimate capacity for this test was 32kN, which is in the same range as the other tests. Similar trends can be observed for 6-cm *Group 2* micropiles as shown in ***Figure 4.23.*** On the basis of ***Figure***

4.22 and ***Figure 4.23***, the grout pressure does not appear to have a major impact on the P_{ult} reached in this study. The influence of grout pressure appears to be minor for *Group 1* and *Group 2* 6-cm OD micropiles in C.S. sand.

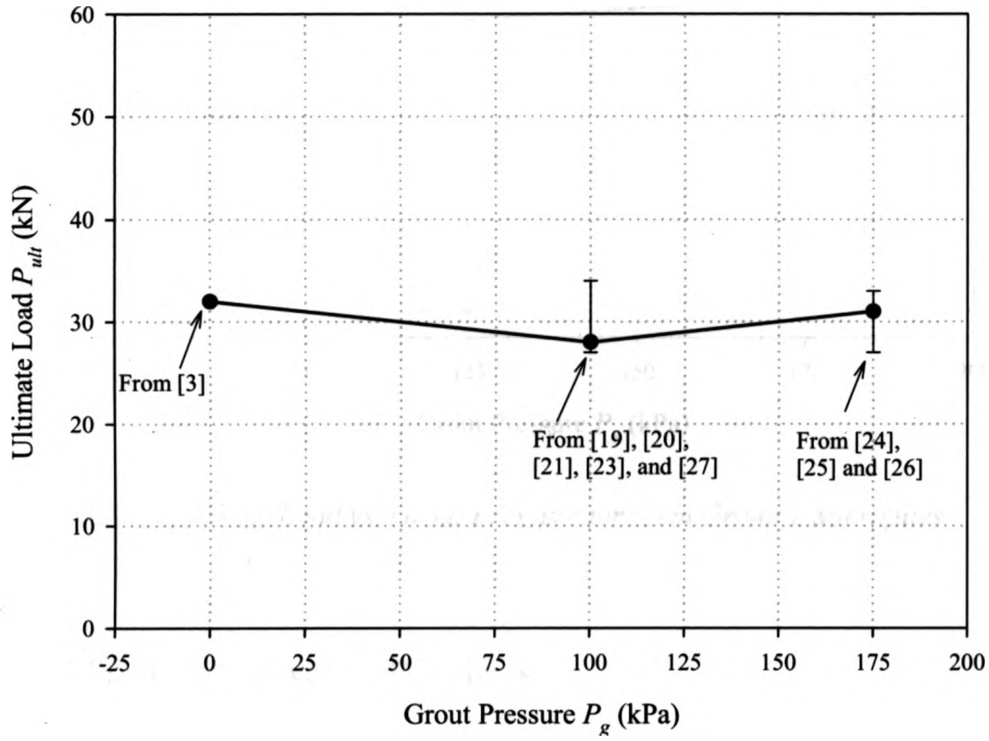

Figure 4.22 *Ultimate Load vs. Grout Pressure for 6-cm Group 1 Micropiles*

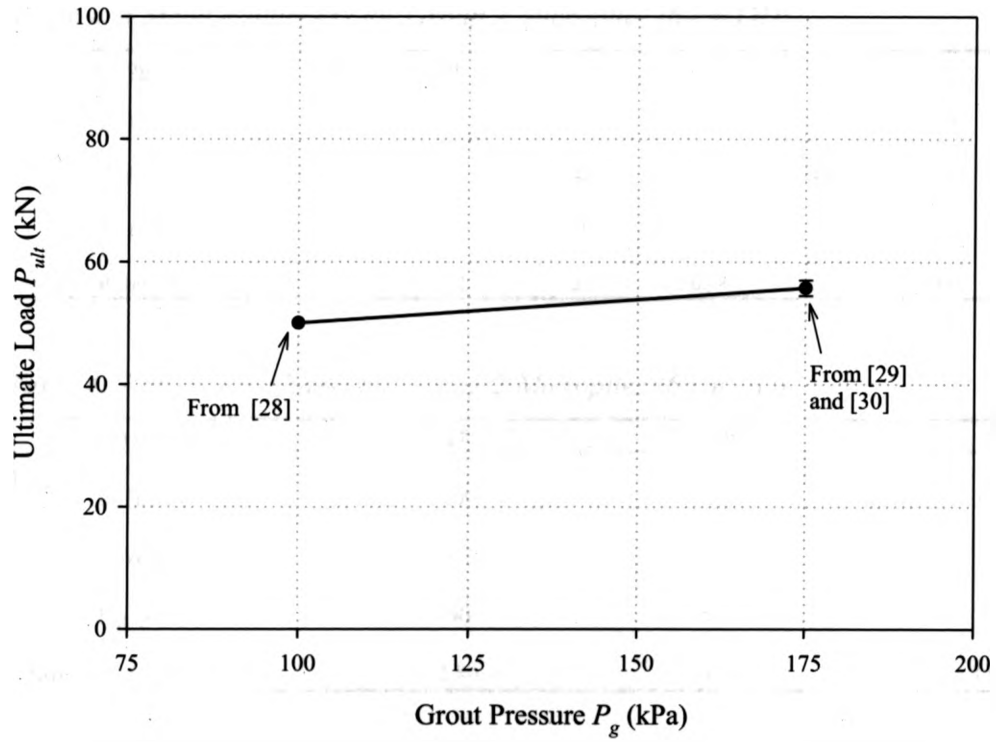

Figure 4.23 *Ultimate Load vs. Grout Pressure for 6-cm Group 2 Micropiles*

4.5.5 Pile Capacity versus Roughness

To conclude, the influence of micropile roughness on P_{ult} was studied. The measured roughness of *Group 1* and *Group 2* micropiles is presented in ***Table 4.6*** and ***Table 4.7,*** respectively. ***Figure 4.24*** and ***Figure 4.25*** show the mean roughness angles, *i*, versus grout pressure for micropiles [19]-[20], [23]-[30]. The grout pressure was varied for these *Group 1* 6-cm OD micropiles.

***Table 4. 6** Mean Roughness for Group 1 Micropiles (6-cm OD)*

Micropile #	19	20	23	27	24	25	26
p_g (kPa)	100	100	100	100	175	175	175
i (deg)	6.9	7.5	7.4	7.9	6.5	6.8	6.8
P_{ult} (kN)	27	28	29.5	27.5	31	28	33
Standard deviation of i	2.43	3.52	3.2	2.08	2.78	3.09	2.86

***Table 4. 7** Mean Roughness for Group 2 Micropiles (6-cm OD)*

Micropile #	28	29	30
p_g (kPa)	100	175	175
i (deg)	6.2	6.7	5.7
P_{ult} (kN)	50	54.5	57
Standard deviation of i	2.86	3.16	3.03

On review of ***Figure 4.24, Table 4.6*** and ***Table 4.7,*** it can be seen that the roughness of *Group 1* micropiles is comparable irrespective of the grout pressure used. Thus, it can be concluded that increasing the grout pressure does not significantly affect the pile roughness.

Figure 4.25 shows a plot of the measured P_{ult} versus mean roughness, i, where it can be seen that the mean roughness angle does not significantly influence the ultimate capacity of either *Group 1* or *Group 2* micropiles. In addition, ***Table 4.8*** shows the measured mean roughness height, H_r, for *Group 1* and *Group 2* 6-cm OD micropiles. As expected, the grout pressure does not influence the roughness height, h_r, of the pile.

Overall, it is concluded that the pile roughness is not an important parameter.

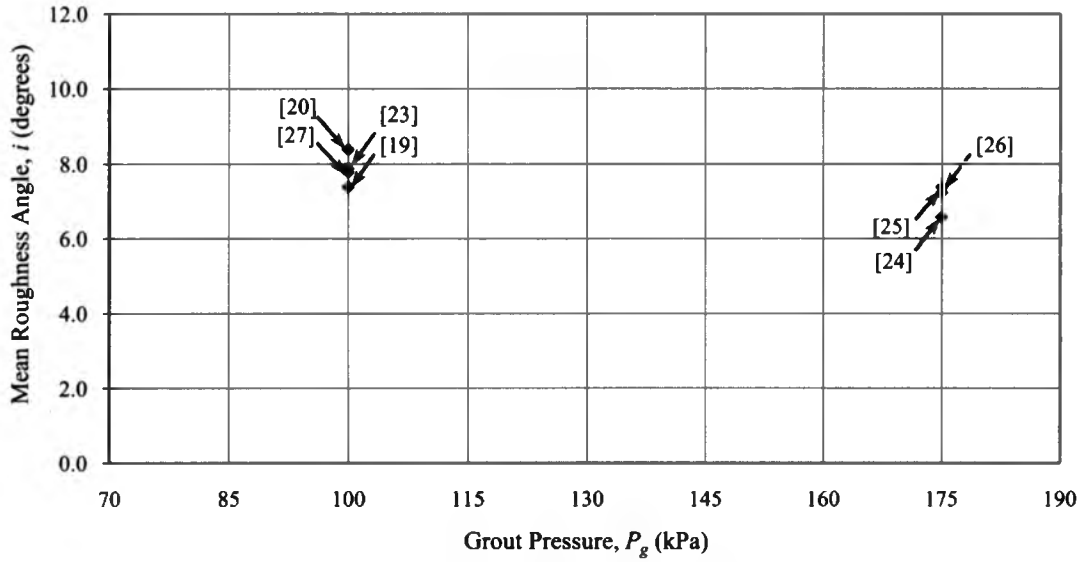

Figure 4.24 *Grout Pressure vs. Mean Roughness Angle for Group 1 Micropiles*

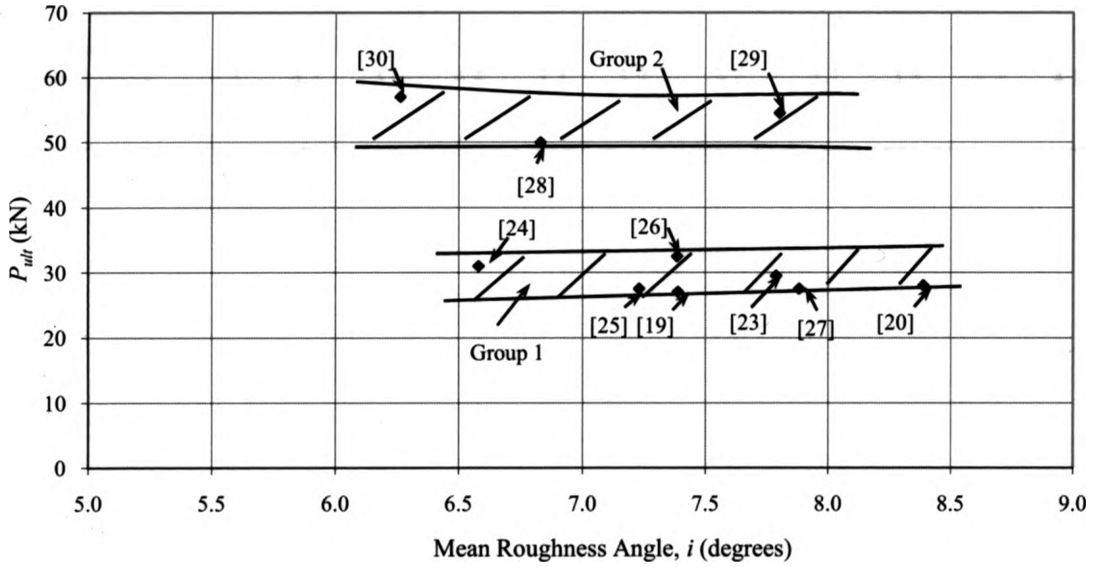

Figure 4.25 *Ultimate Capacity vs. Mean Roughness Angle for Group 1 and Group2 Micropiles*

Table 4.8 *Micropile Mean Roughness Height*

	Roughness Height, h_r(mm)										
Micropile #	**19**	**20**	**21**	**23**	**24**	**25**	**26**	**27**	**28**	**29**	**30**
Segment Δ_1	5.3	3.8	3.4	3.9	2.4	2.8	4.0	2.7	3.0	3.2	3.8
	4.3	3.2	4.0	3.8	3.2	5.1	4.3	3.5	5.0	4.7	3.8
	4.2	3.0	4.6	5.3	4.5	5.2	3.0	3.4	3.8	5.3	5.8
	4.5	4.8	3.0	4.3	3.2	2.9	3.9	3.5	3.8	6.0	3.3
Segment Δ_2	4.9	5.2	3.2	4.0	3.0	2.5	2.8	3.7	3.1	2.7	3.9
	6.1	4.5	2.5	4.0	3.5	3.7	3.0	3.2	3.8	-	6.0
	4.0	4.3	4.2	4.6	3.4	3.7	5.4	3.2	3.2	4.9	6.3
	5.7	6.0	5.8	4.5	3.5	3.4	3.0	3.0	3.5	6.4	6.7
Segment Δ_3	4.3	6.2	3.5	5.5	3.0	3.1	4.1	3.1	2.9	3.5	4.8
	4.6	2.8	3.8	4.2	3.7	3.6	3.9	3.8	4.0	6.6	4.4
	2.7	4.0	3.5	3.5	4.0	5.0	5.5	2.8	3.7	4.8	3.0
	5.7	3.9	3.6	5.0	4.0	2.8	3.2	2.7	3.8	5.2	3.5
Segment Δ_4	3.7	4.7	2.5	5.5	2.8	4.2	3.8	2.5	4.6	4.2	-
	5.3	3.0	3.6	4.8	2.8	4.3	3.5	2.5	4.3	4.3	-
	3.2	3.2	4.5	3.9	2.7	5.2	2.7	3.0	4.8	6.0	4.8
	4.0	5.2	4.8	3.5	3.5	4.2	3.2	2.8	2.7	-	5.6
Mean Roughness Height, H_r *(mm)*	**4.5**	**4.2**	**3.8**	**4.4**	**3.3**	**3.9**	**3.7**	**3.1**	**3.8**	**4.2**	**4.1**

4.6 Summary and Conclusions

This chapter described the results of thirty-two load tests on reduced-scale micropiles in a calibration chamber. The tip resistance, ultimate load in compression, P_{ult} and end-bearing factors, N_q were measured from load tests on micropiles constructed in C.S. sand with a density of ρ_d = 1.80g/cm^3 ±0.02g/cm^3 and ρ_d = 1.84g/cm^3 ±0.02g/cm^3, respectively. P_{ult} calculated using the *FHWA* Design Manual was compared with the measured P_{ult} for gravity grouted micropiles and micropiles constructed using grout pressure of 100kPa and 175kPa. The effect of grout pressure, roughness angle and roughness height on the ultimate capacity of micropiles was also evaluated.

Based on the results and analyses presented above, the following conclusions may be drawn:

(i) Based on the tip resistance tests, it can be concluded that the bearing capacity factors suggested by Berezantsev and reproduced in ***Figure 4.3*** (Tomlinson 2001) are reasonable.

(ii) The density of C.S. sand plays an important role in the load-displacement response and P_{ult} of micropiles. For example, there is a 50% increase in average tip resistance from *Group 1* micropiles compared to *Group 2* micropiles for sand densities of 1.80g/cm^3 (±0.02g/cm^3) and 1.84g/cm^3 (±0.02g/cm^3), respectively. Based on the ultimate loads reached by the micropiles in this study, the P_{ult} of *Group 2* micropiles is about double the P_{ult} of *Group 1* micropiles; due primarily to variations in the density of the C.S. sand.

(iii)The design equations presented in the *FHWA* Manual (*FHWA* 1997) do not agree well with the measured capacity of the micropiles constructed in this study. There is up to 75% variation between calculated and measured ultimate loads for P_{ult} calculated using equations *[4.1]* and *[4.2]*. For P_{ult} calculated using equations *[4.1]* and *[4.3]*, the calculated P_{ult} occasionally exceeded the measured P_{ult} by almost 35%, which is not desirable. Occasionally, the calculated P_{ult} was 50% lower than the measured $P_{ult,}$ which is also undesirable. The error is significant for the controlled conditions of the research micropiles reported in this study, suggesting that the *FHWA* design equations do not account for all aspects of the mechanical response of micropiles.

(iv)For the range of P_g examined in this thesis, the grout pressure does not have a major influence on the ultimate capacity of the test micropiles. It is noted, however, that P_g would likely have had a bigger impact on P_{ult} if (a) the permeability, k of the soil was higher and significant volumes of grout could penetrate into the soil during grouting or (b) if $p_g$was large enough to hydrofracture the sand.

(v) In addition, the micropile roughness has a negligible influence on the ultimate capacity of the micropiles, and it does not appear to be affected by the grout pressure, noting the comments above about the limited range ofP_g.

Chapter 5

Investigation of the Radial Stress Field around Micropiles in Sand

5.1 Introduction

In ***Chapter 4***, it was shown that the measured ultimate compressive loads for 6-cm and 9-cm OD (outer diameter) micropiles were 1.4 to 2 times higher than predicted using design equations in the Drilled and Grouted Micropile Design Manual (*FHWA* 1997). In addition, it was concluded that the grout pressure did not have a significant impact on micropile capacity for pressures in the range of 0-175kPa, which contradicts current design philosophy for micropiles.

This chapter describes the results of six instrumented micropile load tests on 6-cm OD micropiles constructed in sand with earth pressure cells embedded in the sand around each micropile. The primary objective of the instrumented tests was to explain the discrepancy between calculated and measured axial capacity observed in ***Chapter 4***. The micropiles were also modeled using the finite element (*FE*) program *PLAXIS* to interpret the load-displacement results.

The following sections of this chapter describe: (i) the test methodology, (ii) instrumentation layout, (iii) load test results, (iv) and evaluation of the results. The radial stress field around the micropiles during construction and subsequent loading is examined in detail using earth pressure cells and finite element analysis to interpret the measured response. In this study, it is shown that the ultimate axial capacity of micropiles constructed in cohesionless sand is strongly influenced by dilation on the pile-

soil interface and in the soil immediately surrounding the pile. Dilation and its effects are ignored in current design methods.

5.2 Methodology

5.2.1 Micropile Construction

Figures 5.1 and ***Figure 5.2*** show (i) the experimental setup used in this study and (ii) the location of earth pressure measurements around each pile. Referring to ***Figure 5.1,*** load tests were performed by filling a 1.35m diameter by 1.55m deep calibration chamber with C.S. sand. The sand was placed in equal 25cm thick lifts that were compacted by hand using a 10kg-tamping rod with a 10cm×10cm end plate. Each lift was tamped 500 times. After placing the bottom 25cm thick lift of sand, a 6-cm outer diameter (OD) steel casing was placed on the sand, centered in the chamber and braced using timbers. Then, C.S. sand was compacted around the casing. During placement of the C.S. sand, occasional moisture content and density tests were performed according to ASTM D4643 and D1556/D2922 and earth pressure cells were installed at various locations around each pile. When finished, the final geometry comprised a steel casing embedded in C.S. sand with earth pressure cells situated at monitoring points P1-P5 in the sand as illustrated in ***Figure 5.2a-b***.

After placing the C.S. sand, the micropile was grouted using the following sequence:

(i) The steel casing was tremie filled with grout using a pneumatic pump (see ***Chapter 4***). Air was bleed from the grout lines and casing through a pressure cap connected to the top of the casing (see ***Figure 5.2a-b***). The pressure cap was equipped with a de-airing valve and pressure transducer.

(ii) Then, the grout in the casing was pressurized for 10 minutes permitting a small amount of grout to penetrate the soil at the micropile toe.

(iii) Next, the casing was retracted 30 cm while maintaining constant grout pressure and the grout pressure was held for 10 minutes. Again, a small amount of grout penetrated into the soil formation.

(iv) The casing was then retracted by 30 cm two more times while maintaining constant the grout pressure for 10 minutes each time.

(v) During each grout interval, the quantity of grout that penetrated the soil was less than 10 cm^3.

(vi) After three grouting intervals, the pressure was removed and the grout was allowed to cure for 24 hours.

(vii) Finally, after the grout hardened, the casing was cut off 5 cm above the top of the sand giving the geometry depicted in ***Figure 5.1***. The finished micropiles consisted of a 90-cm long grouted section, L_g, and a 30cm long cased section, L_c.

5.2.2 Load Tests

Each micropile was loaded to failure using the experimental set up shown in ***Figure 5.1***. Two bearing plates were placed on the micropile head and leveled with steel shims to transfer load from the jack to the micropile. A reaction frame was clamped to the calibration chamber using heavy duty C-clamps and a hydraulic jack was attached to the reaction frame in series with a 45kN INTERFACE load cell (S.N. 76691). The jack and load cell were positioned so that the jacking head was aligned with the micropile head and rested on the bearing plates. The pile head displacement was measured using a dial

gauge that rested on the bearing plates and was supported by a beam connected to the calibration chamber.

During loading, axial compressive loads were applied manually using the hydraulic jack and held constant for 1-2 minutes. During each load increment, the earth pressures were measured and the pile-head displacement and axial load were recorded.

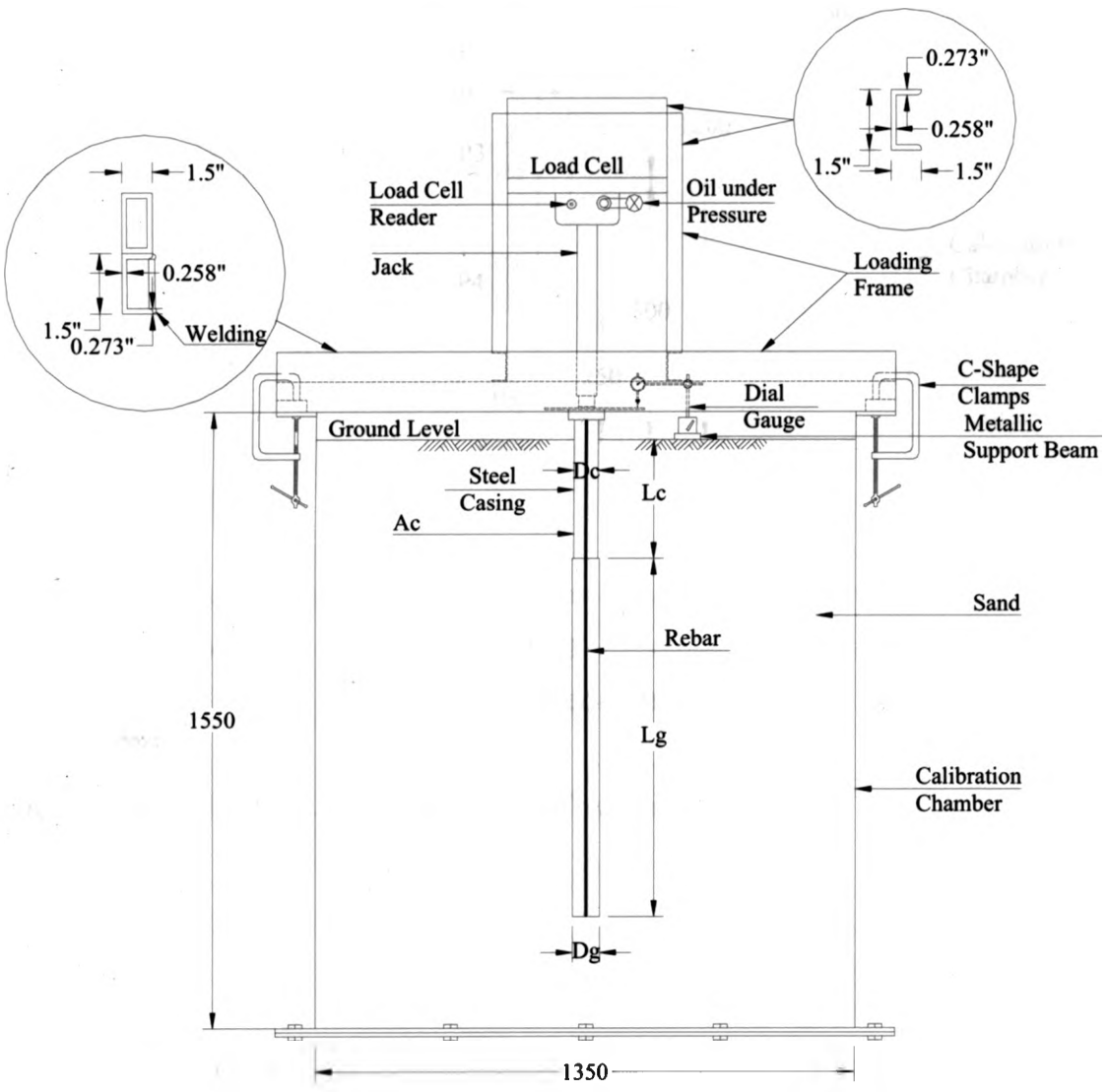

Figure 5.1*Micropile Geometry and Test Setup*

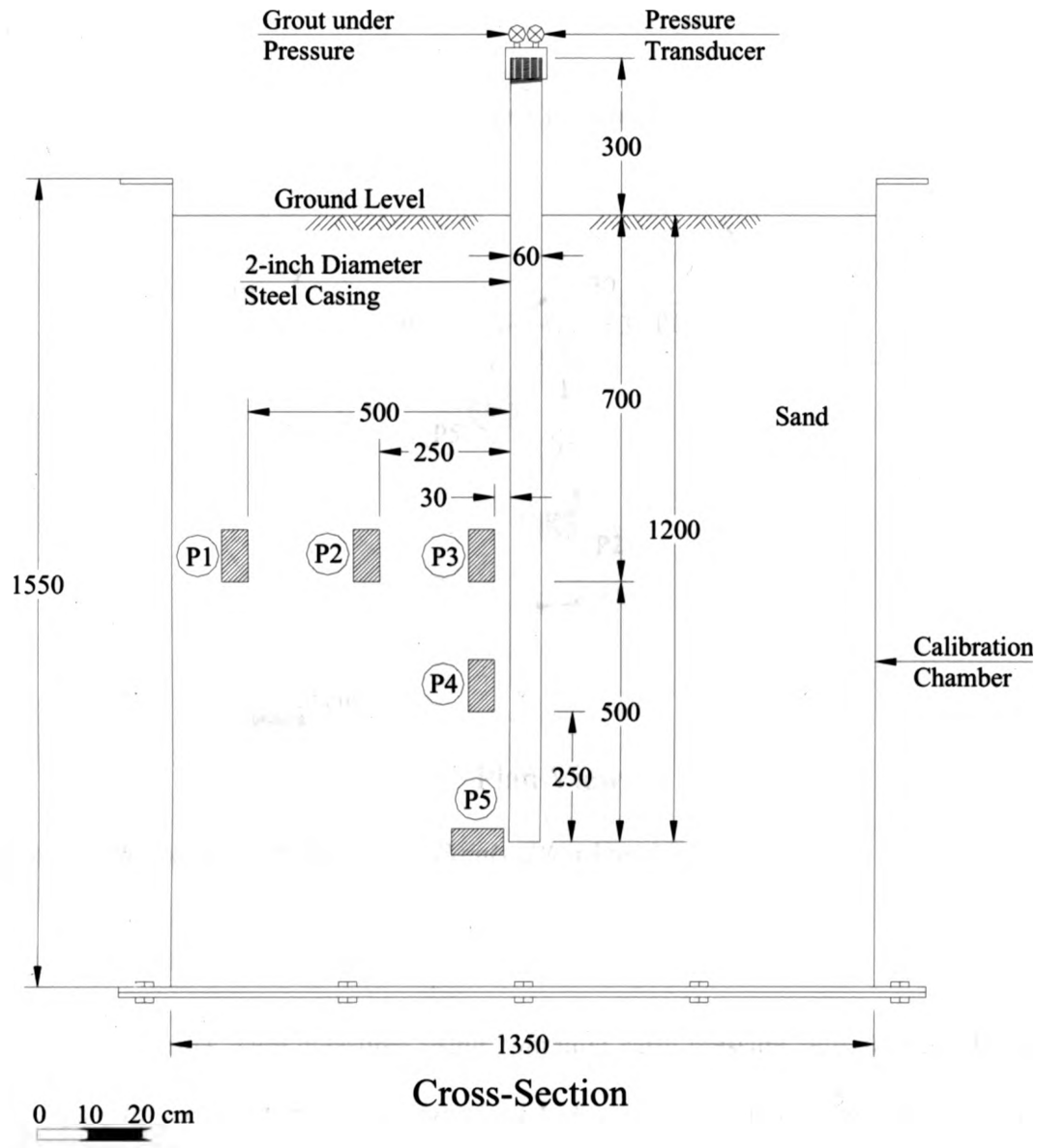

Figure 5.2a *Positions of Monitoring Points (Cross-section)*

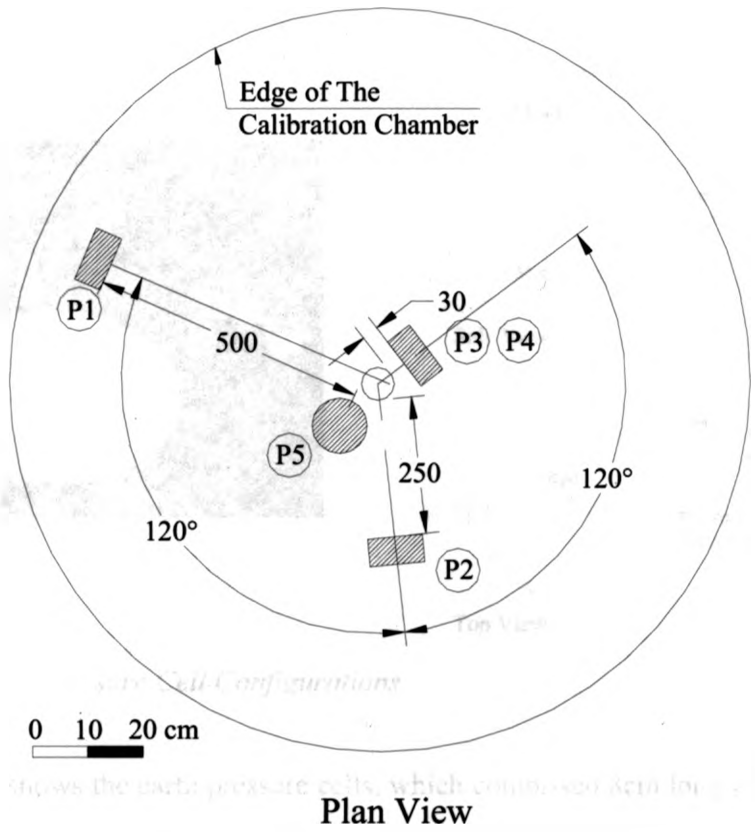

***Figure 5.2b** Positions of Monitoring Points (Plan View)*

5.2.3 Earth Pressure Measurements

Earth pressures were measured using hydraulic earth pressure cells fabricated at the University of Western Ontario. ***Figure 5.2a-b*** shows the location of earth pressure cells during the micropile load tests. Radial stresses were measured at monitoring points P1 – P4 and vertical stress was measured at P5. The following is a brief description of the earth pressure cells and their accuracy.

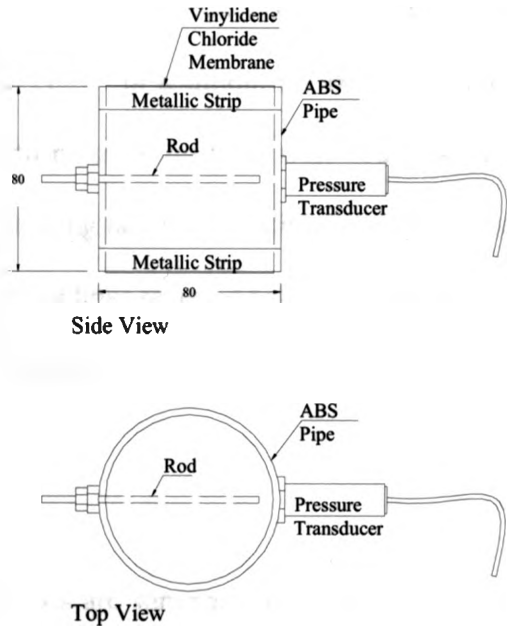

***Figure 5.3** Earth Pressure Cell Configurations*

Figure 5.3 shows the earth pressure cells, which comprised 8cm long × 8cm diameter Schedule 80 ABS pipe covered at both ends with a vinylidene chloride membrane. The membrane was attached to each end of the ABS pipe using metallic compression fittings that were pressed over the pipe ends to clamp the membrane to the ABS pipe. In addition, waterproof epoxy was applied between the membrane, pipe and compression fittings to seal the cells.

Two holes were drilled through the ABS pipe on opposite sides as shown in ***Figure 5.3***. A 200kPa (full-scale) Lucas pressure transducer was connected to one side of the cell and a hydraulic compression fitting equipped with a 12-cm long 8mm diameter stainless steel rod was attached to the other side. The cells were assembled submerged under de-aired water to eliminate air. The stainless steel rod served two functions: (i) it was used as a plunger to facilitate de-airing the cells, and (ii) it was used to pre-stress the cells after filling them creating an outward camber in the membranes. Three earth pressure cells

were fabricated for the testing. ***Appendix B*** describes tests that were performed to characterize the accuracy and precision of the cells. In addition, the cells were buried under 1.5m of C.S. sand and the resultant earth pressure readings were found to be the same as corresponding measurements obtained using larger 30cm diameter Geokon cells (Model 4800). In summary, the earth pressure readings reported below are considered to be 15%±, which is normal for earth pressure readings.

5.2.4 Tests Performed

Details of the six instrumented micropile tests are summarized in ***Table 5.1***, which lists the soil dry density (ρ_d) and moisture content (w), the location of earth pressure cells (P1-P5), pile geometry (D_g, L_g, D_c and L_c) and the grout pressure (P_g) used during construction. As discussed above in ***Section 5.2.3***, only three earth pressure cells were fabricated for use in the micropile tests; however, ***Figure 5.2*** indicates that earth pressure was measured at five monitoring points labeled P1-P5. Accordingly, during any given test, earth pressure cells were placed at only three of the five monitoring points labeled P1 through P5 in ***Figure 5.2***. ***Table 1*** lists the locations that were monitored (e.g. P1, P2 and P3 for Test 1). Detailed drawings of the instrumentation layout for specific tests are provided in ***Appendix B***.

Table 5.1 *Earth Pressure Cell Placements*

Micropile Test	Soil State		Stress Monitoring			Geometry				
	ρ_d(g/cm^3)	w (%)	*Cell 1*	*Cell 2*	*Cell 3*	L_g (cm)	D_g (cm)	L_c (cm)	D_c (cm)	P_g (kPa)
1	1.77	1.14	P2	P1	P3	91	66.8	29	6	100
2	1.85	1.02	P3	P5	P5	89	68.2	32	6	100
3	1.83	1.65	P2	P5	P3	93	65	29	6	175
4	1.85	1.86	P2	P3	P5	94	68.3	28	6	175
5	1.80	2.14	P3	P4	P5	94	66.3	28	6	175
6	1.82	2.05	P4	P3	P5	96	66	26	6	100

Referring to ***Table 5.1***, six tests were performed on 6-cm OD micropiles constructed in C.S. sand. The C.S. sand was placed and compacted at essentially the same moisture content (1.02-2.14%) and density (1.77-1.85g/cm^3) in an attempt to achieve repeatable load versus displacement results. The results of Tests 1-6 were then compiled to obtain the average response of a 6-cm OD micropile for assessment and evaluation by finite element analysis.

5.2.5 Cavity Expansion Theory

As shown below, there were significant increases in the radial stresses in the soil surrounding each micropile during loading. Later in this chapter, it will be shown that the increase is due to dilation on the micropile-soil interface, which can be interpreted using cavity expansion theory. Accordingly, the radial stresses, σ_r, measured adjacent to the micropiles during loading is often compared with the Yu and Houlsby (1991) solution for elasto-plastic expansion of a cylindrical cavity. In the elastic region, the equations governing cavity expansion are (Yu and Houlsby 1991),

$$\dot{\varepsilon}_r = \frac{\partial \dot{u}}{\partial r} = \frac{E}{1-\nu^2}\left\{\dot{\sigma}_r - \frac{\nu}{1-\nu}\dot{\sigma}_\theta\right\} \quad [5.1]$$

$$\dot{\varepsilon}_\theta = \frac{\dot{u}}{r} = \frac{E}{1-\nu^2}\left\{-\frac{\nu}{1-2\nu}\dot{\sigma}_r + \dot{\sigma}_\theta\right\} \quad [5.2]$$

$$\dot{\varepsilon}_z = 0 \quad [5.3]$$

and

$$\sigma_r = -p_o - (p - p_o)\left(\frac{a}{r}\right)^2 \quad [5.4]$$

$$\sigma_\theta = -p_o + (p - p_o)\left(\frac{a}{r}\right)^2 \quad [5.5]$$

$$u = \frac{p-p_o}{2G}\left(\frac{a}{r}\right)^2 r \quad [5.6]$$

where G is the shear modulus, E is Young's modulus, ν is Poisson's ratio, a is the radius of the cylindrical cavity, r is the radial distance from the cavity axis, and p_o *and* p are the initial and final internal cavity pressure, respectively.

After yielding occurs, a plastic zone forms in the region $a \leq r \leq b$ around the cavity with increasing p and the stress field around the cylindrical cavity can be divided into elastic and plastic regions. In the plastic region, the stress field is

$$\sigma_r = \frac{Y}{\alpha-1} + Ar^{[-(\alpha-1)]/\alpha} \quad [5.7]$$

$$\sigma_\theta = \frac{Y}{\alpha-1} + \frac{A}{\alpha} r^{[-(\alpha-1)]/\alpha} \quad [5.8]$$

where

$$A = -\frac{\alpha}{\alpha-1} 2\delta G b^{(\alpha-1)/\alpha} \quad [5.9]$$

In the elastic region, $r \geq b$, the stresses are

$$\sigma_r = -p_o - B/r^2 \quad [5.10]$$

$$\sigma_\theta = -p_o + B/r^2 \quad [5.11]$$

where

$$B = 2\delta G b^2 \quad [5.12]$$

$$\alpha = \frac{1+sin\phi}{1-sin\phi} \quad [5.13]$$

$$\delta = \frac{Y+(\alpha-1)p_o}{2(1+\alpha)G} \quad [5.14]$$

$$(b/a) = R^{\alpha/(\alpha-1)} \quad [5.15]$$

$$Y = \frac{2c\,cos\phi}{1-sin\phi} \quad [5.16]$$

and

$$R = \frac{(1+\alpha)[Y+(\alpha-1)p]}{2\alpha[Y+(\alpha-1)p_o]} \quad [5.17]$$

The elasto-plastic displacement is expressed in terms of the radial strain, a/a_o, where a_o is the initial radius of the cylindrical cavity. From Yu and Houlsby (1990), the pressure-expansion relationship is

$$\frac{a}{a_o} = \left\{\frac{R^{-\gamma}}{(1-\delta)^{(\beta+1)/\beta} - (\gamma/\eta)\Lambda_1(R,\xi)}\right\}^{\beta/(\beta+1)} \quad [5.18]$$

where

$$\Lambda_1(x,y) = \sum_{n=0}^{\infty} A_n^1 \quad [5.19]$$

$$A_n^1 = \begin{cases} \frac{y^n}{n!}\ln x, & if\ n = \gamma \\ \frac{y^n}{n!(n-\gamma)}[x^{n-\gamma} - 1], & n \neq \gamma \end{cases} \quad [5.20]$$

$$\beta = \frac{1+sin\psi}{1-sin\psi} \quad [5.21]$$

$$\gamma = \frac{\alpha(\beta+1)}{(\alpha-1)\beta} \quad [5.22]$$

$$\eta = exp\left\{\frac{(\beta+1)(1-2\nu)[\gamma+(\alpha-1)p_o][1+\nu]}{E(\alpha-1)\beta}\right\} \quad [5.23]$$

and

$$\xi = \frac{[1-\nu^2]2\delta}{(1+\nu)(\alpha-1)\beta}\left[\alpha\beta + (1-2\nu) + 2\nu - \frac{m\nu(\alpha+\beta)}{1-\nu}\right] \quad [5.24]$$

5.2.6 Numerical Analysis

Finally, the finite element program *PLAXIS* was used to interpret the micropile load test results and to ensure that boundary effects were negligible in the calibration chamber tests. ***Figure 5.4*** shows the finite element mesh and geometry, which corresponds to the geometry of the calibration chamber. The following is a discussion of the numerical methodology.

The *FE* analysis was performed using 1339 15-noded cubic strain triangle elements, 48 interface elements and assuming axi-symmetric conditions. A rough rigid boundary was assumed at the base of the calibration chamber and a smooth rigid boundary along the sidewalls. The 6-cm OD micropile was modeled as a linear elastic material with Young's Modulus, E, and Poisson's ratio, v. The axial stiffness, EA, used in the analysis corresponded to the EA derived from the cross-section of the upper cased and lower uncased segments, respectively. ***Table 5.2*** summarizes the material parameters adopted for the micropile.

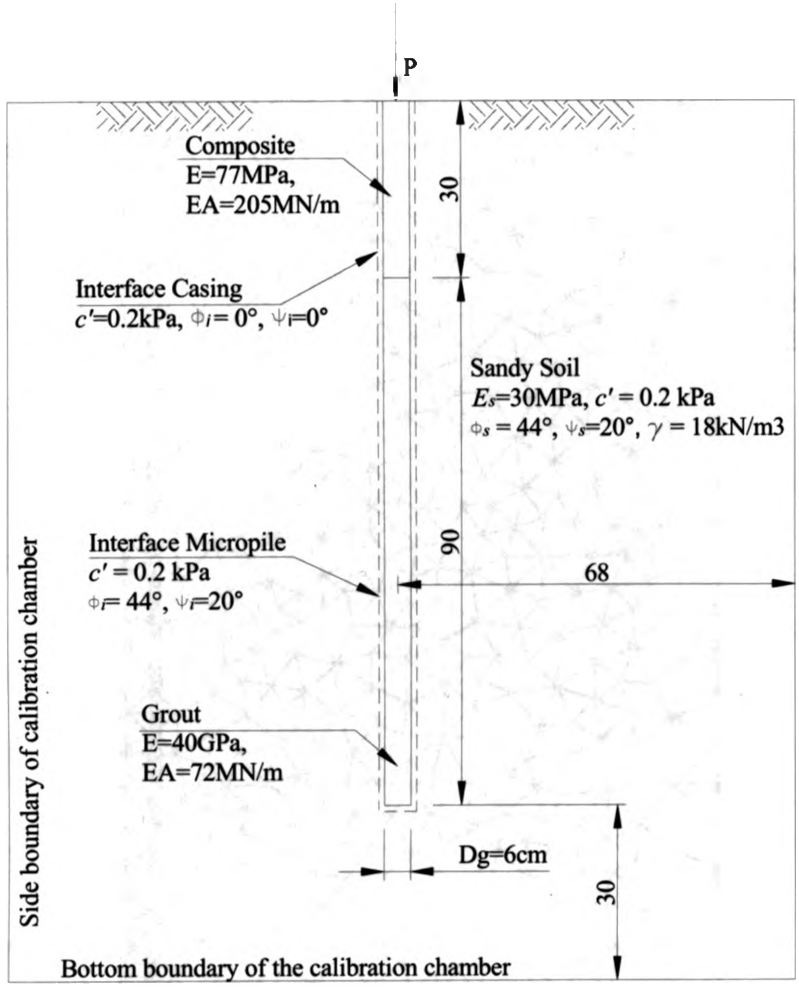
P
Composite
E=77MPa,
EA=205MN/m
30
Interface Casing
c'=0.2kPa, ϕI= 0°, ψI=0°
Sandy Soil
Es=30MPa, c' = 0.2 kPa
ϕs = 44°, ψs=20°, γ = 18kN/m3
Interface Micropile
c' = 0.2 kPa
ϕI= 44°, ψI=20°
90
68
Grout
E=40GPa,
EA=72MN/m
Dg=6cm
30
Side boundary of calibration chamber
Bottom boundary of the calibration chamber

(a) Geometry

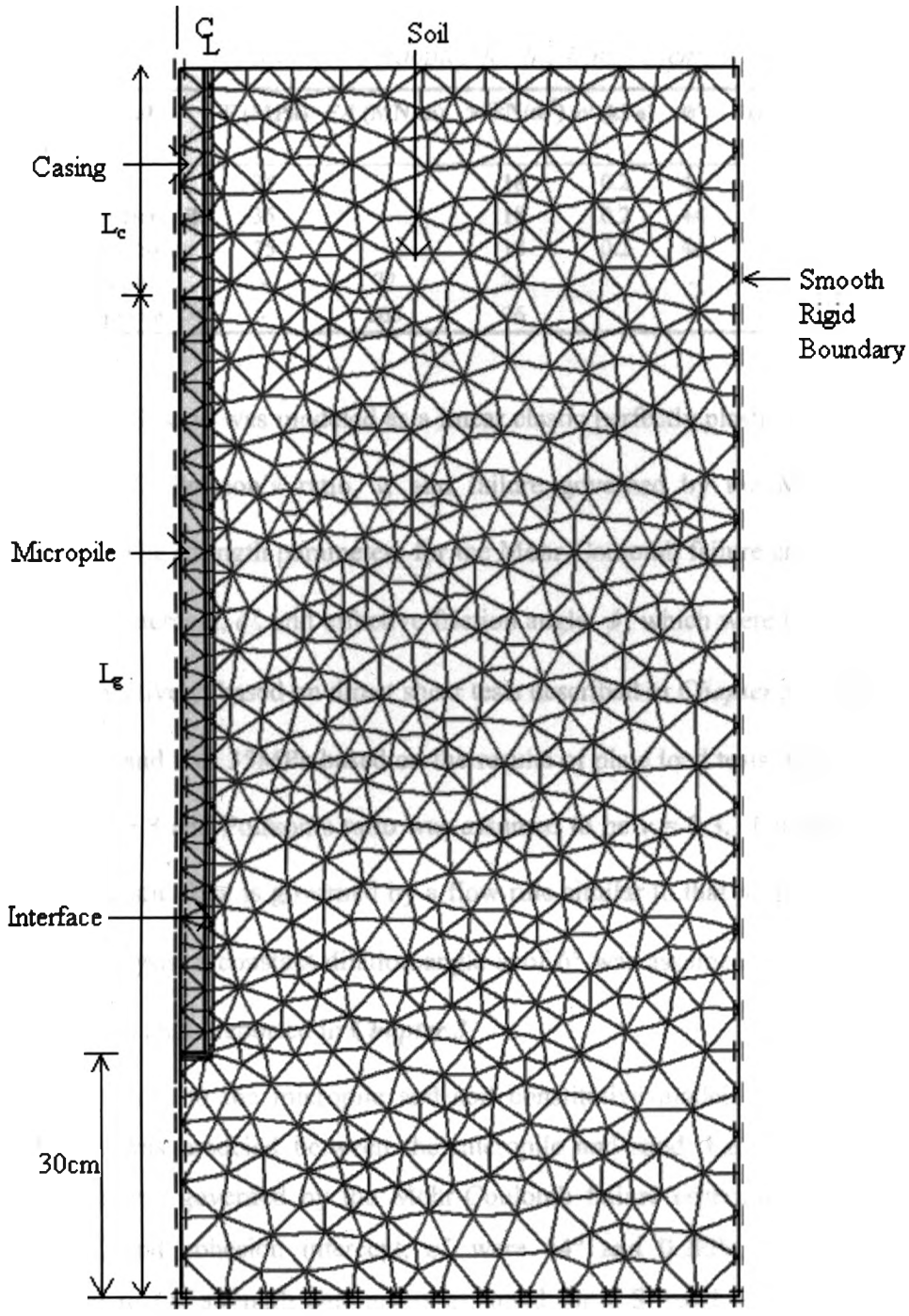

(b) *FE* Mesh

Figure 5.4 *Finite Element Mesh and Geometry*

Table 5.2 *Material Parameters Adopted for the Finite Element Analysis*

Material	E (MPa)	EA (MN/m)	γ (kN/m^3)	c' (kPa)	$\emptyset'$	ψ'	ν	R_θ
Sand	35	-	18	0.2	44	6	0.3	1
Interface Micropile	35	-	18	0.2	44	20	0.3	1
Interface Casing	35	-	18	0.2	44	20	0.3	0.01
Micropile	-	72	25	-	-	-	-	-
Composite	-	205	26	-	-	-	-	-

The C.S. sand was modeled as a linear elastic perfectly plastic material with Young's modulus, E, Poisson's ratio, ν, and failure governed by the Mohr-Coulomb failure criterion. The strength parameters for the Mohr-Coulomb failure criteria are the effective cohesion intercept, c', and effective friction angle, ϕ', which were taken to be 0.2kPa and 44°, respectively, based on direct shear tests described in ***Chapter 3***. The elastic modulus E of the sand was 35MPa based on the results of plate load tests, which are summarized in ***Chapter 3*** and Poisson's ratio was assumed to be $\nu = 0.3$. For the elasto-plastic soil model, plastic flow is governed by a flow rule similar to that proposed by Davis (1982). In the analysis, a constant dilation angle ψ of 6° was assumed, which is consistent with the dilation angle reported in ***Chapter 3***.

In addition to the micropile and soil constitutive models, a rigid perfectly plastic interface was modeled between the micropile and sand. Failure of the micropile-soil interface was governed by the Mohr-Coulomb failure criterion. The effective friction angle, ϕ', and cohesion intercept, c', were 44° and 0.2kPa, respectively, which are identical to the strength parameters assumed for C.S. sand surrounding the micropile. The interface dilation angle, ψ_i, was taken to be 20°, which is consistent with the peak dilation angle measured during direct shear tests. ***Table 5.2*** also summarizes the soil material parameters.

5.3 Results

5.3.1 The Influence of Pile-soil Interface Displacement

Figure 5.5 shows the calculated horizontal displacement (relative to the rigid pile) versus vertical pile head displacement at three points on the micropile-soil interface. As it can be seen, the choice of constant dilation angle on the pile-soil interface results in essentially linear variation of horizontal displacement versus vertical pile head displacement. The maximum horizontal displacement (due to dilation) on the pile-soil interface is between 0.7 to 0.8 mm corresponding to 12 mm of vertical displacement, which is similar to the pile roughness height reported in ***Chapter 3***.

The effect of the soil dilation angle is summarized in ***Figure 5.6***. This figure shows the calculated load versus displacement of a 6-cm OD micropile corresponding to soil dilation angles, ψ_s, of 0°, 3° and 6°. It is noted that for these analyses, the soil and interface dilation angle were assumed to be equal. The corresponding horizontal displacement (dilation) on the interface was 0.8mm, 0.3mm and 0mm. From ***Figure 5.6***, it can be seen that the load-displacement response of the micropile is strongly influenced by the dilation angle of the soil. For ψ_s=0°, the load-displacement response is similar to that obtained in ***Chapter 3*** for piles that were encased in a PVC sleeve to minimize the skin friction. The analyses presented in ***Figures 5.5*** and ***Figure 5.6*** confirm the choice of dilation angle used in the FE analyses. A value of ψ_s=6° gives pile-soil interface dilation (0.8mm) that is in the same order of magnitude as the pile roughness.

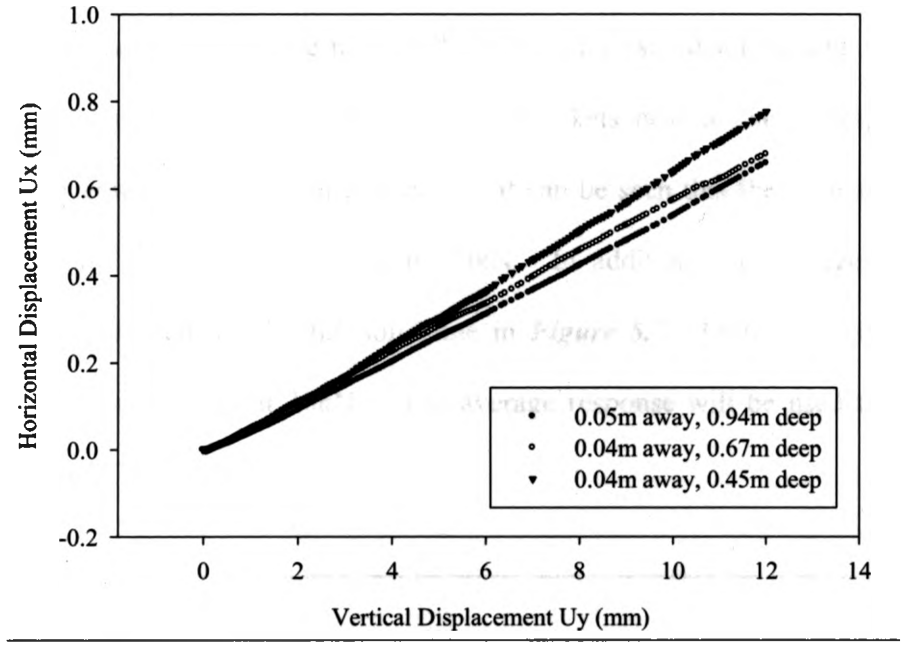

Figure 5.5 *Horizontal Displacements of Soil Particles along the Axial Loaded Pile*

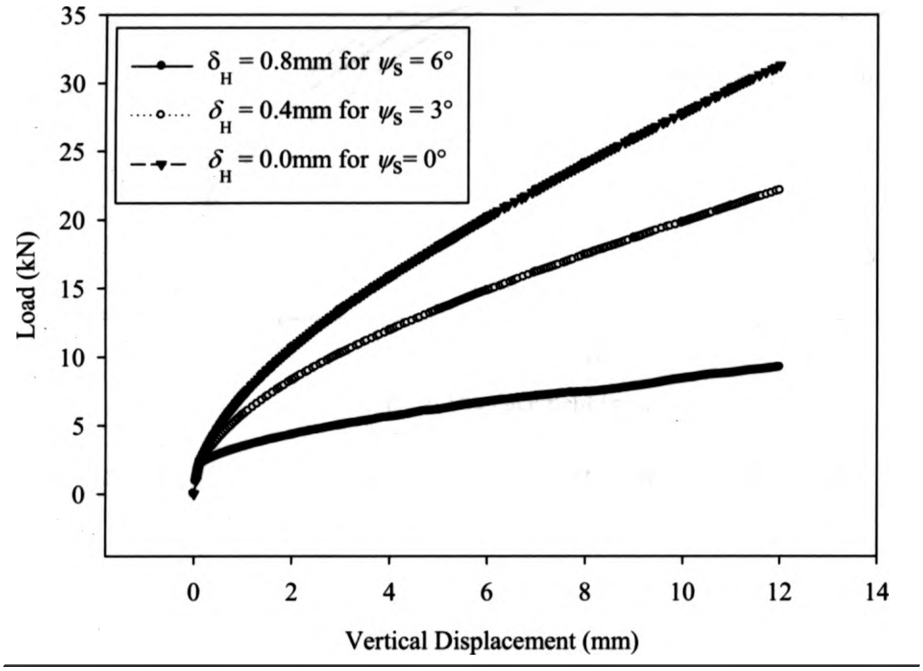

Figure 5.6 *Vertical Load versus Vertical Displacement on the Pile Interface for Horizontal Displacement of 0.8mm, 0.4mm and 0mm*

5.3.2 Axial Load versus Displacement (Measured)

Figure 5.7 shows the measured axial load versus displacement for Micropiles 1-6. The test number is indicated in square brackets next to the corresponding pile load-displacement curve. From ***Figure 5.7***, it can be seen that the ultimate capacity, P_{ult}, of Tests 1-6 varied from 27.5kN to 34kN. In addition, the average load-displacement response is depicted by the solid line in ***Figure 5.7.*** From the average response, the ultimate load is about 30kN. The average response will be used to evaluate the pile response.

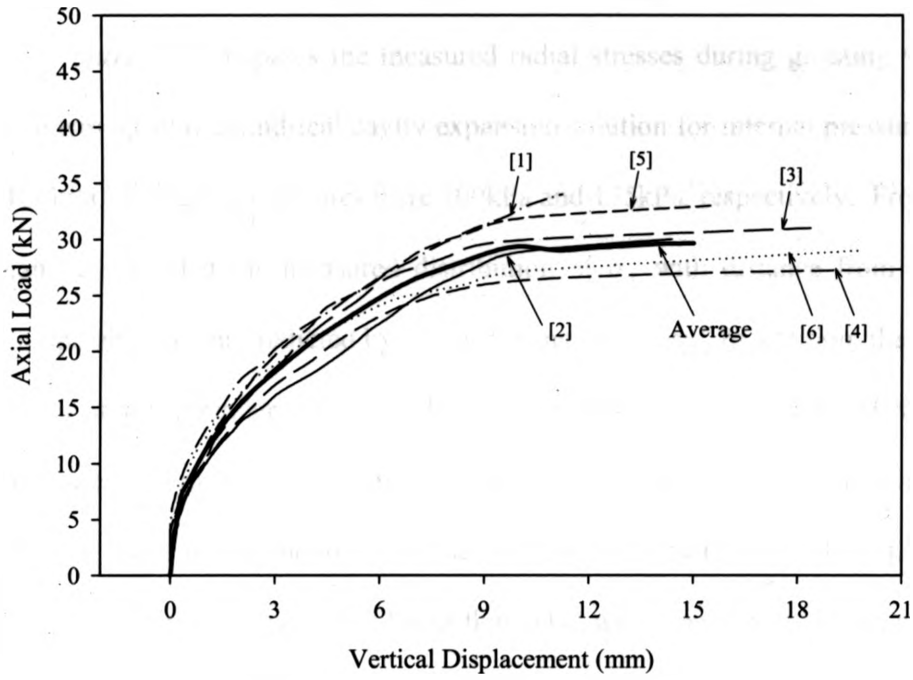

Figure 5.7 *Axial Loads versus Displacement of Monitored Micropiles*

5.3.3 Vertical and Radial Earth Pressures (Measured)

The radial stresses measured at P1 through P5 during construction and loading of micropiles 1-6 are summarized in ***Tables 5.3*** and ***Table 5.4,*** and ***Figure 5.8*** and ***Figure 5.9***. The following is a discussion of the earth pressure measurements.

During Construction

Referring to ***Table 5.3***, it can be seen that the measured radial stress,σ_r, varied between 4.2kPa and 5.9kPa at the depth of 0.6m (P1, P2 and P3) after placing sand in the calibration chamber. The corresponding coefficient of lateral earth pressure at rest is between 0.35 and 0.49, which is consistent with elastic theory (e.g. $K_o' = \nu/(1-\nu)$).

Figure 5.8 compares the measured radial stresses during grouting with the Yu and Houlsby (1990) cylindrical cavity expansion solution for internal pressures of 50kPa and 100kPa. The grout pressures were 100kPa and 175kPa, respectively. From ***Figure 5.8***, it can be seen that the measured distribution of σ_R with distance from the micropile is comparable to that predicted by cavity expansion theory. In addition, the change in radial stress at the boundary of the calibration chamber is negligible. However, the grout pressure used during construction varied from 100 to 175kPa, which is higher than 50 to 100kPa used in conjunction with the Yu and Houlsby (1990) solution. In general, the radial stress measurements are lower than what would be expected for a cylindrical cavity subject to an internal pressure of 100kPa or 175kPa. However, the difference can be attributed to permeation of the grout into the sand during the grouting, which may reduce the effective pressure on the inner wall of the cylindrical cavity.

Table 5.3 *Radial Stresses Measured at P1 through P5 during Micropile Construction*

Micropile Test	Cell Position	Before Grouting		Maximum σ_R During Grouting	After Grouting	
		σ_R	K'_o		σ_R	K'_o
	P1	5.5	0.46	7.0	5.6	0.47
1	P2	5.9	0.49	10.5	6.9	0.58
	P3	5.4	0.45	26.5	20.8	1.75
	P3	4.2	0.35	29.4	19.6	1.65
2	P5	18.6	-	28.8	17.9	-
	P5	16.1	-	23.8	18.1	-
	P2	5.0	0.42	8.7	5.7	0.48
3	P3	5.6	0.47	31.5	18.4	1.55
	P5	9.6	-	10.2	8.6	-
	P2	5.3	0.44	8.3	8.0	0.67
4	P3	4.9	0.41	30.8	17.1	1.44
	P5	17.3	-	20.4	14.0	-
	P3	4.7	0.40	35.1	16.1	1.35
5	P4	6.7	0.41	35.6	16.4	1.00
	P5	27.2	-	37.8	30.4	-
	P3	5.5	0.46	28.5	14.2	1.19
6	P4	7.4	0.45	22.6	17.3	1.06
	P5	24.1	-	33.6	30.9	-

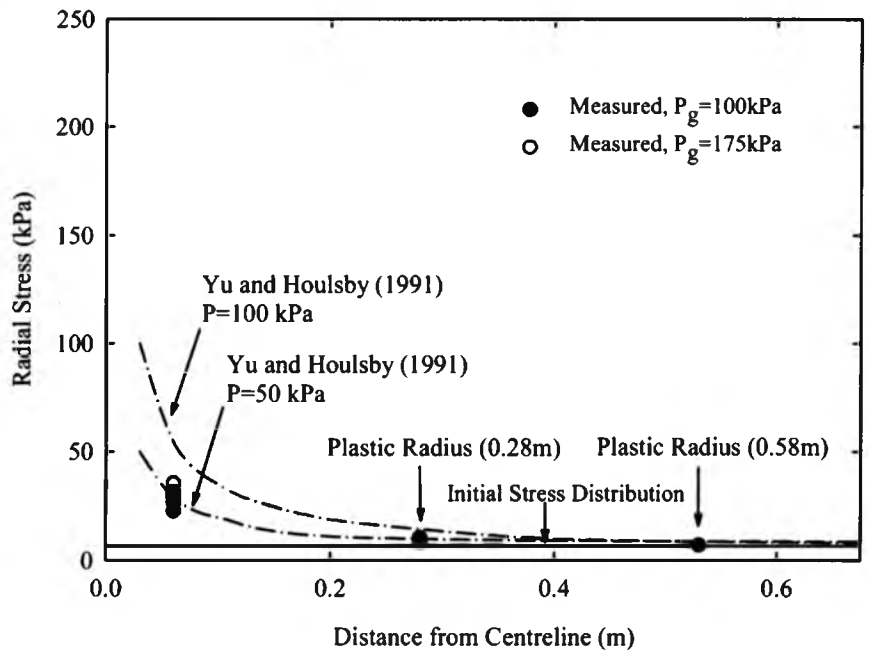

Figure 5.8 *Radial Stresses during Pressure Grouting*

During Loading

The radial stresses, σ_r, measured during micropile loading are summarized in ***Table 5.4*** for loads corresponding to $0.25P_{ult}$, $0.5P_{ult}$, $0.75P_{ult}$, and P_{ult}. In addition, the distribution of σ_r adjacent to the micropiles is presented in ***Figure 5.9***. ***Figure 5.10*** compares the distribution of σ_R at P_{ult} with the cavity expansion solutions (Yu and Houlsby 1990). The following is a discussion of the results.

Table 5.4 *Earth Pressure Cell Readings during Loading*

Micropile Test	Cell Placement	@ Initial	@0.25P_{ult}	@0.50P_{ult}	@0.75P_{ult}	@P_{ult}	p_g (kPa)	P_{ult} (kN)
	P1	5.61	6.66	8.48	10.30	13.26		
1	P2	6.91	8.86	15.77	23.12	32.19	100	34
	P3	20.82	22.40	29.40	38.00	53.61		
	P3	19.58	33.48	41.00	53.52	85.63		
2	P5	17.85	31.24	42.25	60.95	71.00	100	29.5
	P5	18.12	29.23	39.33	59.16	68.00		
	P2	4.66	8.65	17.57	28.68	41.91		
3	P3	18.37	23.44	42.26	68.54	141.44	175	31
	P5	8.55	17.88	34.86	52.23	55.60		
	P2	7.99	10.59	15.56	21.39	23.77		
4	P3	17.09	24.18	44.32	64.69	100.42	175	27
	P5	14.01	29.71	51.58	79.24	89.21		
	P3	16.07	23.81	30.64	41.58	65.94		
5	P4	16.38	24.97	42.78	64.31	98.45	175	33
	P5	30.35	45.96	65.78	81.21	105.22		
	P3	14.17	23.58	44.30	70.36	98.81		
6	P4	17.31	23.91	41.45	65.59	95.19	100	27.5
	P5	30.93	54.44	77.67	85.28	77.14		
	P1	5.40	7.10	9.71	12.10	13.30		
FE	P2	5.30	9.90	14.51	19.45	21.14	-	30
	P3	5.40	24.40	52.20	88.70	95.00		

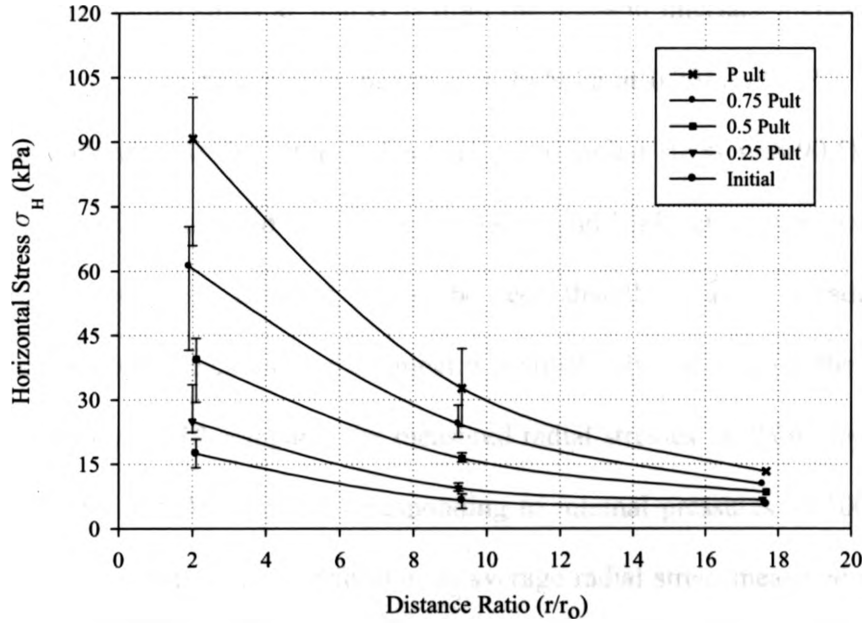

Figure 5.9 *Measured Radial Stresses during Pile Loading.*

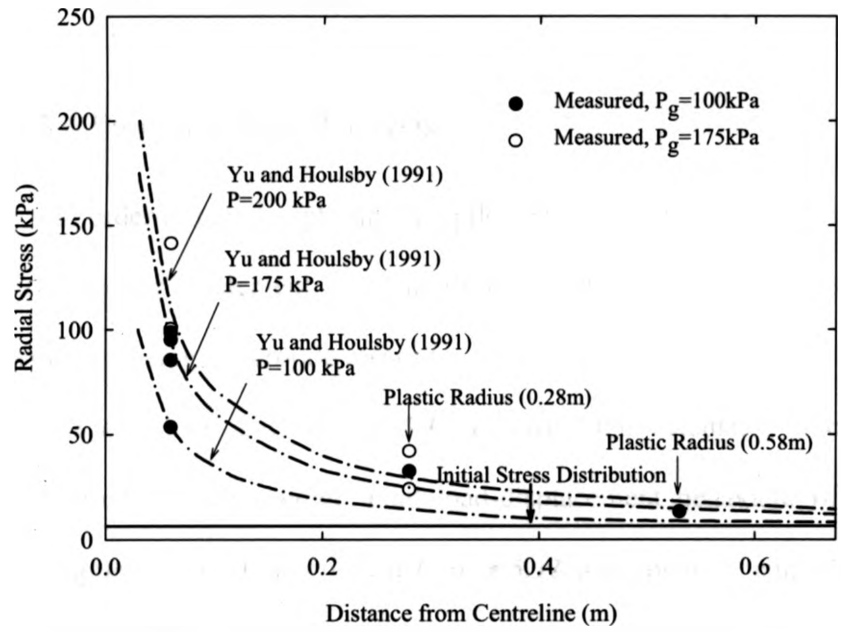

Figure 5.10 *Comparisons of Measured Radial Stresses at the Ultimate Pile Load with the Yu and Houlsby (1990) Solution*

In ***Figure 5.9***, it can be seen that the radial stresses around the micropiles increased with loading and decreased with the distance from the micropile-soil interface. The

average radial stress at 7cm (P3) from the pile-soil interface increased from 18kPa after grouting to 25.5Pa, 40kPa, 62kPa and 90.5kPa at $0.25P_{ult}$, $0.5P_{ult}$, $0.75P_{ult}$, and $1.0P_{ult}$, respectively. At the ultimate load (P_{ult}), the radial stress was 90.5kPa at 7cm from the pile-soil interface and it decreased to 33kPa and 14kPa at 25 and 50cm from the interface, respectively. In addition, it can be seen that the change in radial stresses near the boundary of the calibration chamber were relatively small during the pile load tests.

Figure 5.10 compares the measured radial stresses (at 0.6m depth) with the Yu and Houlsby (1990) solution corresponding to internal pressures of 100, 175 and 200 kPa. From this figure, the distribution of average radial stress measured adjacent to the 6-cm OD micropiles agrees with the Yu and Houlsby (1990) solution corresponding to an internal pressure of 175kPa

5.3.4 Finite Element Analysis

In order to gain insight into the pile response, the 6-cm OD micropiles were modeled using the finite element program *PLAXIS*. This section compares calculated behaviour with the average micropile response.

Figure 5.11 and ***Figure 5.12*** compare the calculated micropile load-deflection response with the average axial load-displacement behaviour of the six instrumented micropiles. The FE solution in ***Figure 5.11*** was obtained using the material parameters listed in ***Table 5.2***; whereas, the solution in ***Figure 5.12*** corresponds to E_s = 40MPa and ϕ_s= 40°. In addition, two finite element analysis were performed for each case: (i) one considering dilation on the pile-soil interface (e.g. ψ_i = 44°) and (ii) the other considering no dilation on the interface (e.g. ψ_i = 0°). Overall, it can be seen that the calculated

behaviour obtained by *FE* analysis corresponding to the dilatant pile-soil interface is comparable to the average load-displacement curve. Both the calculated and measured load-displacement curves reach an ultimate load of about 30kN at a pile head displacement of 12mm. Differences between the calculated and measured load-displacement curve can be attributed to the constant dilation used in the FE analysis whereas the actual behaviour is governed by an initially high dilation angle that decreases until contant volume conditions are achieved at large displacement (see ***Chapter 3***). Similar calculated behaviour can be obtained assuming E_s = 40MPa and ϕ_s= 40°

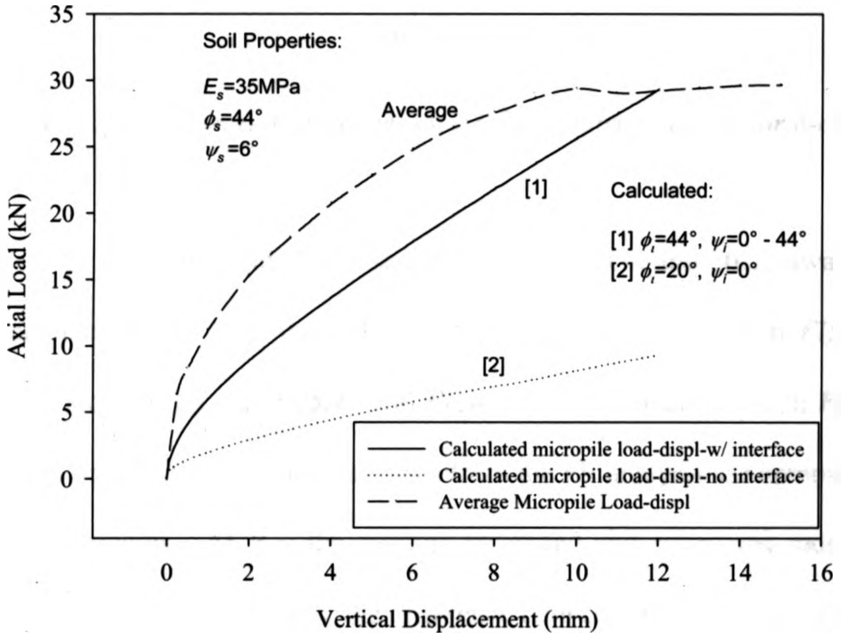

Figure 5.11 *Measured (average) vs. FE Load-Displacement for 6-cm Instrumented Piles*

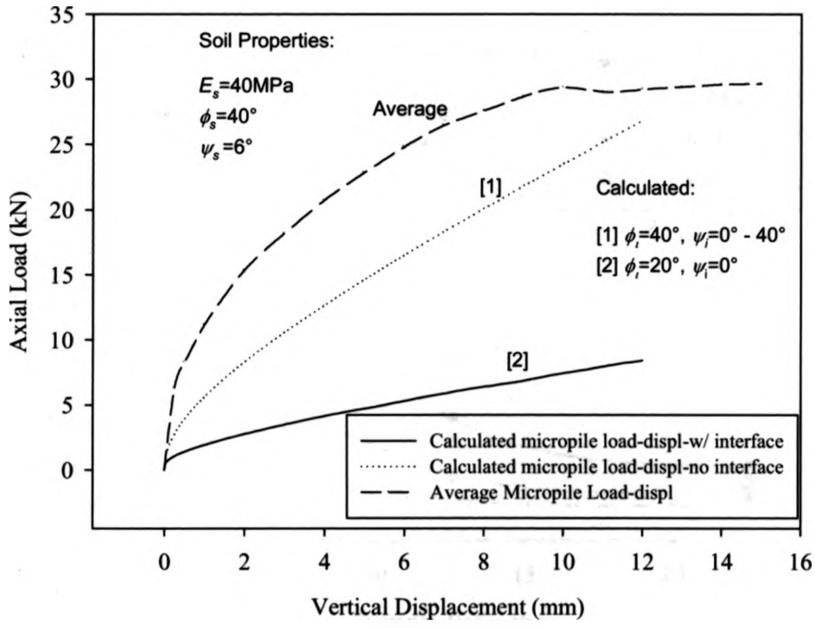

Figure 5.12 *Measured (average) vs. FE Load-Displacement for 6-cm Instrumented Piles*

The calculated radial stresses, σ_R, at 7cm, 25cm and 50cm away from the micropile-soil interface at 0.25, 0.50, 0.75 and 1.0 P_{ult}, are presented in ***Figure 5.13*** and ***Figure 5.14***. Comparing ***Figure 5.13*** and ***Figure 5.14*** (FE analysis) with ***Figure 5.9*** (measured), it can be seen that the radial stresses from the FE analysis are comparable to the measured radial stresses. At P_{ult}, the average measured and calculated radial stresses are within 10%. For 0.75 and 0.5 P_{ult}, the difference between the measured (average) and calculated radial stresses is about 15%. For $0.25P_{ult}$, the difference is 5%. The calculated radial stresses were measured from the output results drawing a section at the set distances away from the micropile, reading the cartesian effective stresses on horizontal direction.

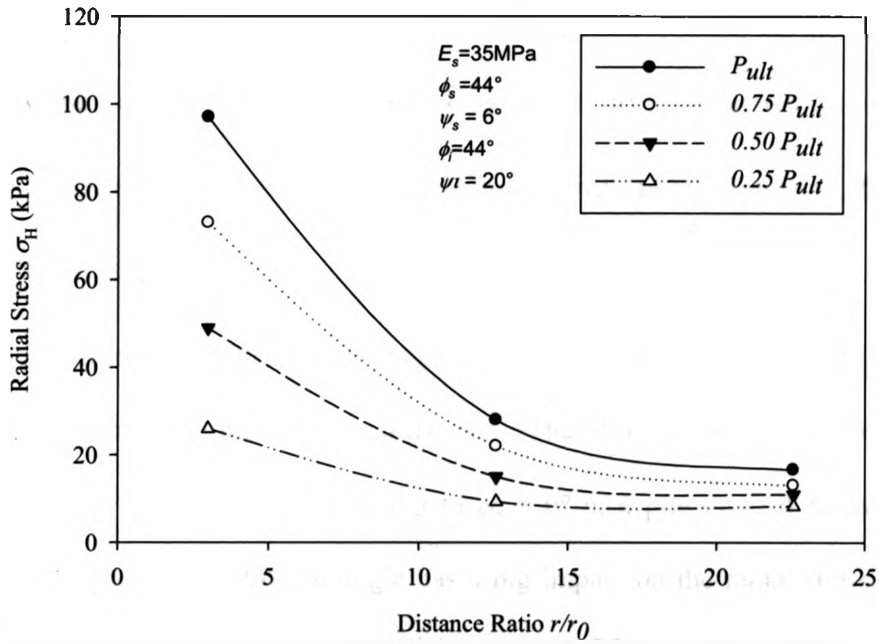

Figure 5.13 *Radial Stresses for Micropile Tests using FE for E_s=35MPa and ϕ_s=44°*

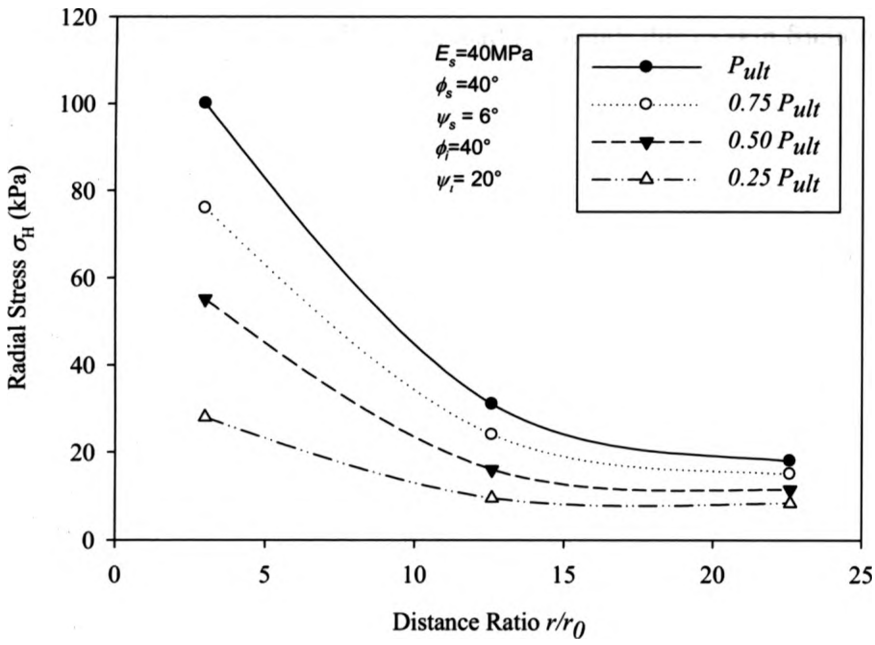

Figure 5.14 *Radial Stresses for Micropile Tests using FE for E_s=40MPa and ϕ_s=40°*

Figures 5.15 and ***5.16*** summarize the results of sensitivity analyses that were performed to investigate the influence of interface dilation on the pile response during loading. ***Figure 5.15*** shows load displacement curves calculated assuming $\psi_s = 0°$, 4°and 8°. ***Figure 5.16*** shows the calculated radial stress distribution at P_{ult} for the different soil dilation angles assumed.

Referring to ***Figure 5.15***, it can be seen that the soil dilation has a strong impact on the ultimate load carried by a micropile. The ultimate load varies from 38kN for ψ_s=8° to as low as 10kN corresponding to ψ_s = 0° at a pile vertical displacement of 12mm. Similarly, the soil dilation angle has a big impact on the radial stresses around the pile. Referring to ***Figure 5.16***, the radial stresses at P3 vary from 155kPa to 24kPa for ψ_s of 8° and 0°, respectively. Thus, it can be concluded that soil dilation around the micropile-soil interface causes the radial stresses in the soil and on the pile-soil interface to increase during loading permitting additional load resistance due to skin friction.

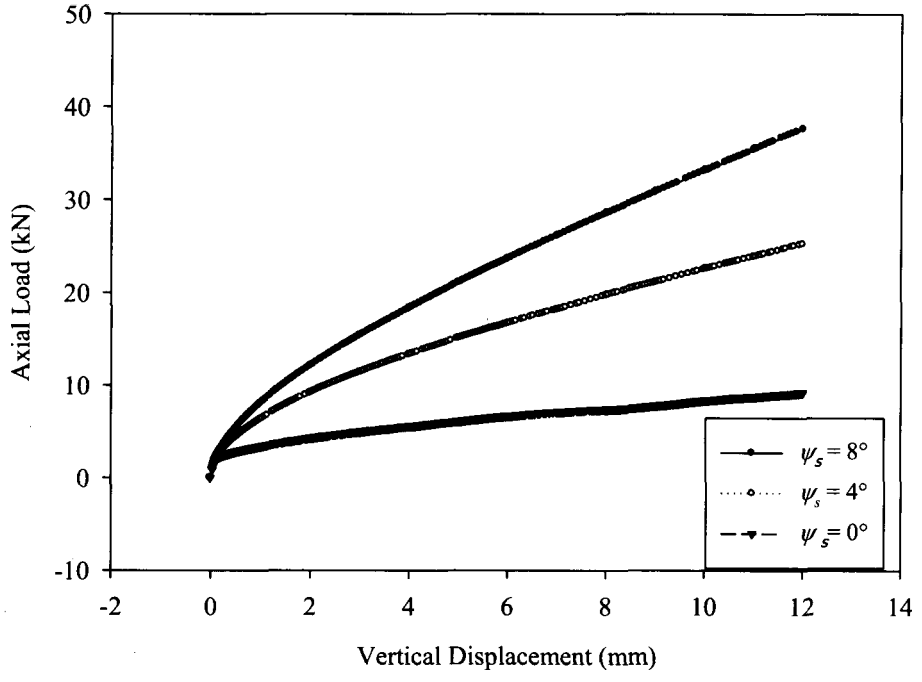

Figure 5.15 *Load-displacement Curves from FE Analysis for Various Soil Dilation Angles Keeping the Interface Dilation Constant*

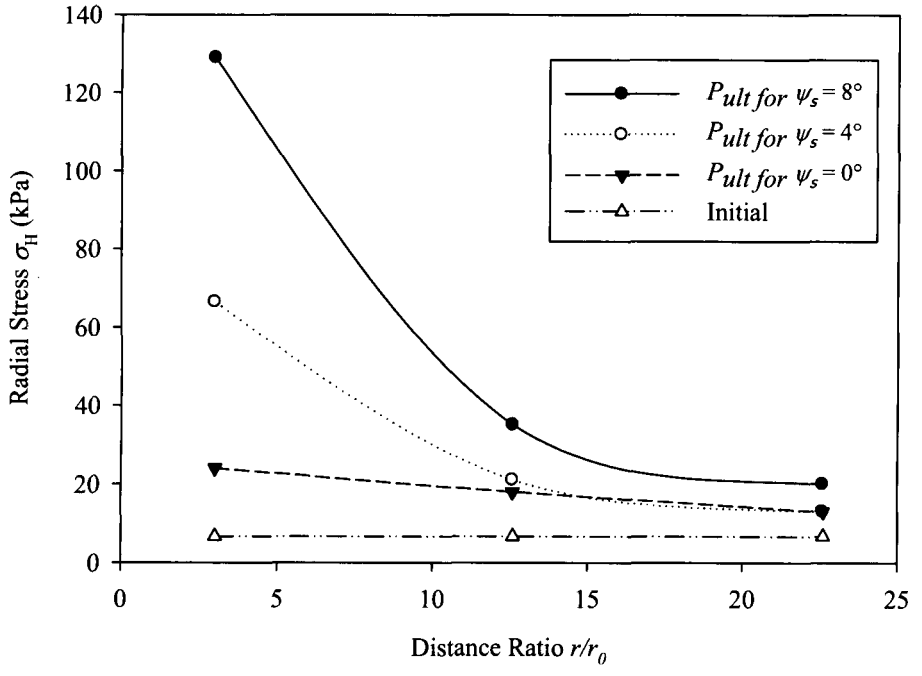

Figure 5.16 *Variation of Radial Stresses with Dilation Angle at P_{ult} from FE Results*

5.3.5 Yielding around Micropiles

Figure 5.17 and ***Figure 5.18*** summarize stages in the development of plastic zones around the 6-cm O.D micropiles for E_s=35MPa and E_s=40MPa corresponding to axial loads of 1.5kN, 20.2kN, 28.9kN and 1.5kN, 8.8kN, 26.8kN, respectively. From the plastic zones in ***Figure 5.17*** and ***Figure 5.18*** it can be seen that the full pile-soil interface yields at an axial load of just 1.5kN and a vertical pile head displacement of 0.08 and 0.075mm respectively. At a load of 8.8kN, as in ***Figure 5.18*** the soil at the micropile tip has fully yielded mobilizing the full tip bearing resistance. In addition, the radius of the plastic zone adjacent to the pile-soil interface expands from 0.03m at P=1.5kN to 0.25m at P=8.8kN. In summary, stresses on the pile-soil interface reach the Mohr Coulomb surface at very low axial loads; whereas, the tip resistance is mobilized at higher loads. With continued loading, however, dilation on the pile-soil interface causes the plastic radius around the pile to expand eventually reaching a radius of 0.35m.

Figure 5.19 and ***Figure 5.20*** shows the relative contribution of the tip and shaft to the load resistance of the micropile. From the above analyses and discussion, dilation around the pile causes a type of cavity expansion, which increases the radial stresses acting on the pile-soil interface and permits additional load capacity to develop. At failure, the normal stress on the pile-soil interface is about 175kPa from cavity expansion theory (see ***Figure 5.10***) and the skin friction accounts for two-thirds of the ultimate pile load.

For comparison purposes, if conventional pile formulae are used in conjunction with a pile-interface stress of 175kPa (deduced from cavity expansion theory and the pressure cells), then the skin friction for a 6cm OD micropile is:

$$Q_s = 175kPa \times \pi \times 0.06m \times 0.9m \times \tan(45°) = 25.5kN \quad [5.25]$$

and the tip resistance is

$$Q_b = 100 \times \pi \times (0.03m)^2 \times 21.6kPa = 6.1\,kN \quad [5.26]$$

Corresponding to a total capacity of 31.6kN. This is very close to the average pile capacity of 30kN (see ***Figure 5.7***). Thus, it appears that the pile capacity can be predicted with reasonable accuracy if the effects of dilation on the pile-soil interface stress can be deduced.

Figure 5.19 and ***Figure 5.20*** show the load-displacement plot for the two finite element cases considered for different elastic moduli and internal friction angles. These plots show the contribution of tip resistance and tip and shaft resistance of a micropile under vertical loading. Points A, B, and C represent the stages during the analysis corresponding to the plastic zones depicted in ***Figure 5.17*** and ***Figure 5.18***.

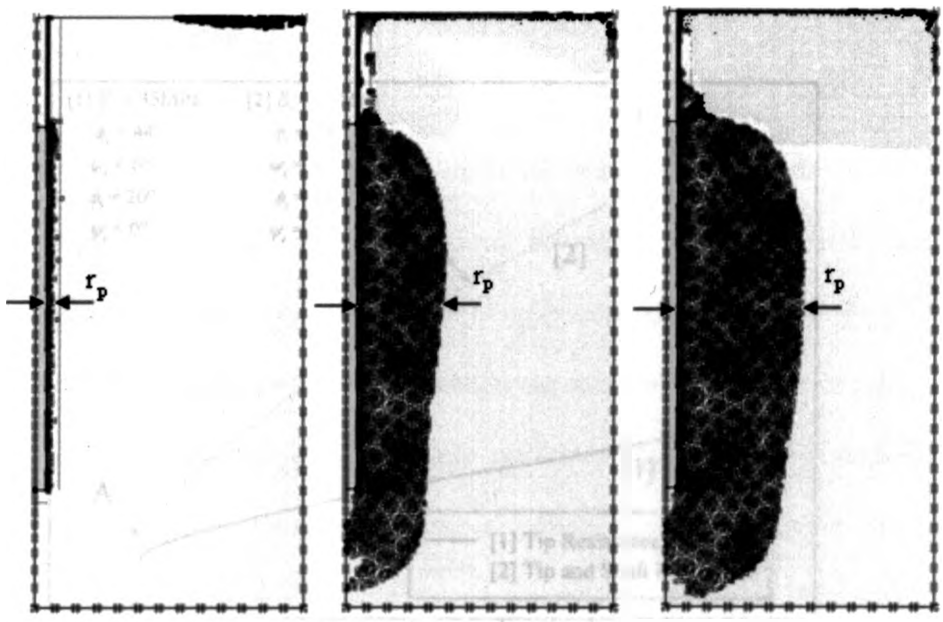

(a) P=1.5kN, δ_v=0.08mm (b) P=20.2kN, δ_v=7.15mm (c) P=28.9kN, δ_v=12mm

Figure 5.17 *Plastic Zones versus Axial Load for FE analysis (E_s=35Mpa, $\emptyset_s$ = 44°, ψ_s = 6°, $\emptyset_i$=44°, ψ_i = 20°)*

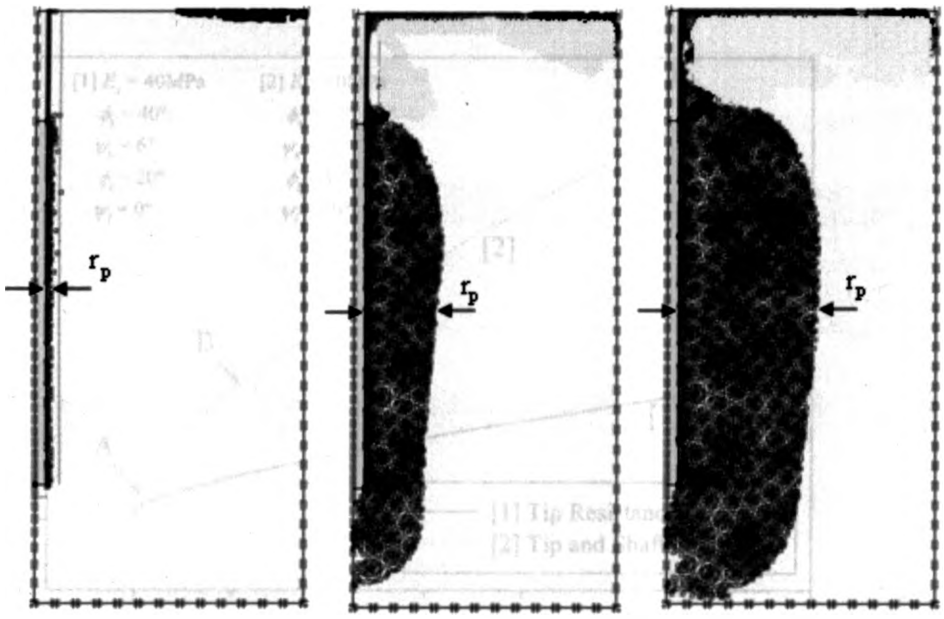

(a) P=1.5kN, δ_v =0.075mm (b) P=8.8kN, δ_v =2.2mm (c) P=26.8kN, δ_v =12mm

Figure 5.18 *Plastic Zones versus Axial Load for FE analysis E_s=40Mpa, $\emptyset_s$= 40°, ψ_s = 6°, $\emptyset_i$=40°, ψ_i = 20°*

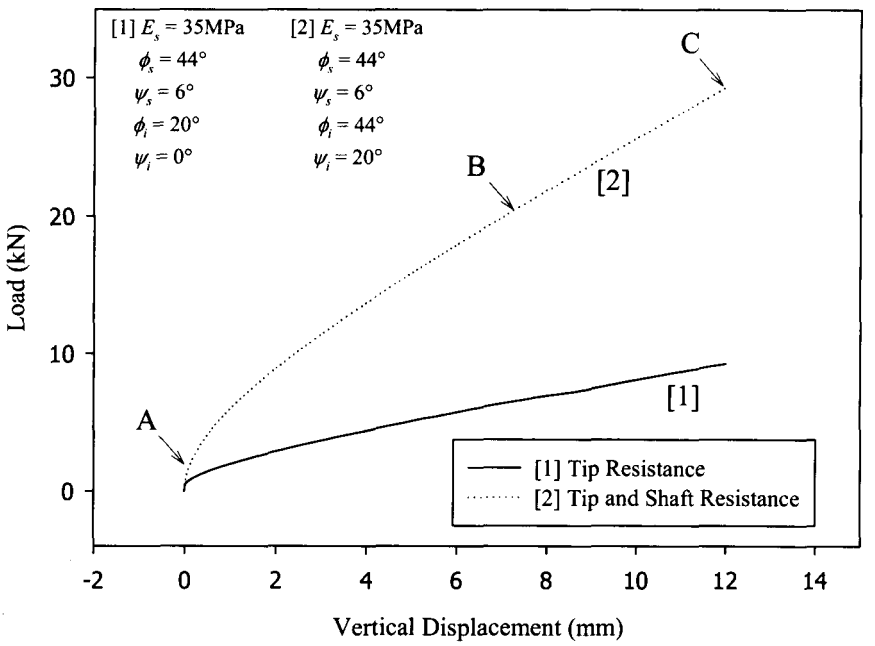

Figure 5.19 *Contribution of tip and shaft resistance during loading for E_s=35MPa and $\emptyset_s$= 44°*

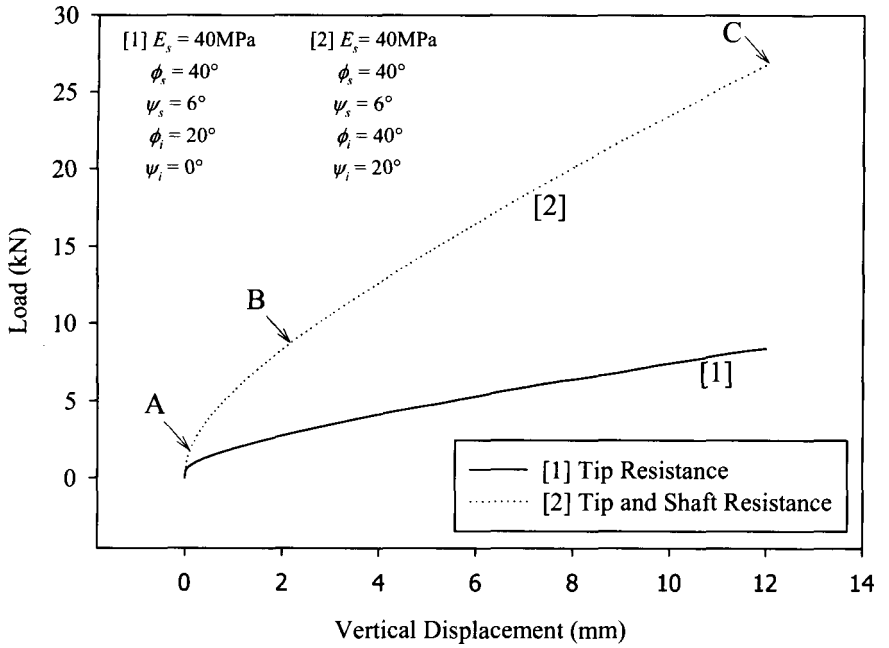

Figure 5.20 *Contribution of tip and shaft resistance during loading for E_s=40MPa and $\emptyset_s$ = 40°*

5.4 Summary and Conclusions

This chapter presented the results of radial stress measurements around micropiles during loading. In addition, the measured behaviour was interpreted using a finite element model to gain insight into the micropile response. Based on the laboratory test results and finite element analyses, the following conclusions may be drawn:

(i) The coefficient of lateral earth pressure at rest, K_o', varied between 0.35 and 0.49 after filling the calibration chamber, which is consistent with elasticity theory $K_0' = \nu/(1-\nu)$.

(ii) During loading, the measured radial stresses at a point 7cm from the pile-soil interface (P3) increased from an initial value of about 14.2-20.8kPa prior to loading to 65-100kPa at the ultimate load. This increase can be attributed to dilation on the pile-soil interface.

(iii) The FE analysis showed that the ultimate capacity of the 6-cm OD micropiles is strongly influenced by the dilation that occurs in the soil adjacent to the pile-soil interface. Based on the FE analysis, the ultimate load increased from 9.5kN corresponding to no dilation on the pile-soil interface to 28.9kN corresponding to soil dilation angle, ψ_s of 6°, elastic modulus of E_s=35kN and internal friction angle of ϕ' =44°.

Chapter 6

Case Study - Tieback Anchors in Sandy Soils

6.1 Introduction

This chapter evaluates the results of pullout tests performed on grouted tieback anchors in the Greater Toronto Area (*GTA*). The primary objective of the work was to assess the influence of soil properties and construction methods on the pullout capacity of tieback anchors in sandy soils. A secondary objective was to see if there is evidence of similar mechanical response of grouted tieback anchors compared to grouted micropiles.

The pullout test data examined in this chapter was provided by Isherwood Associates of Mississauga, Ontario. The company preformed a large number of tieback anchor pullout tests between 1994 and 2007, and load versus elongation curves and failure loads from the tests are presented in this chapter and in ***Appendix C***. In the following sections, the pullout test results are used to study the influence of standard penetration test (SPT) N-values according to American Society for Testing and Materials (ASTM) D1586, and construction methods on the mobilized shear strength at failure along the bonded length of anchors. In addition, a finite element analysis was performed to assist with interpreting the anchor response. This chapter describes the geometry of tieback anchors, construction methods, the load test methodology and results and interpretation of the results.

6.2 Methodology

6.2.1 Tieback Anchor

Tieback anchors are commonly used to provide lateral support for shoring walls. Typically, tiebacks comprise either mechanical anchors (e.g. helical screw anchors) or drilled and grouted anchors, which are the most common anchors for shoring systems. This section provides a brief description of drilled and grouted tieback anchors, which are the focus of this study.

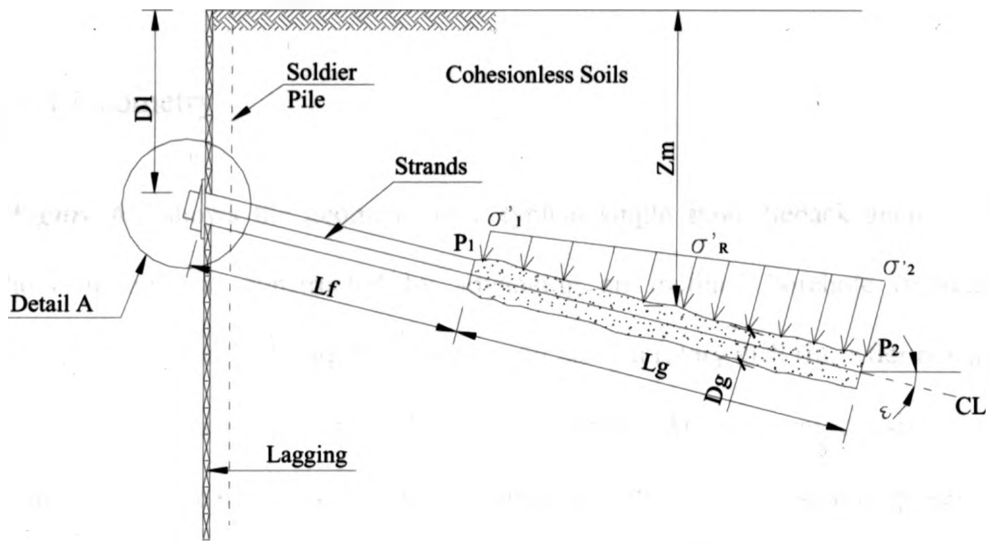

Figure 6.1 *Tieback Geometry and Stresses*

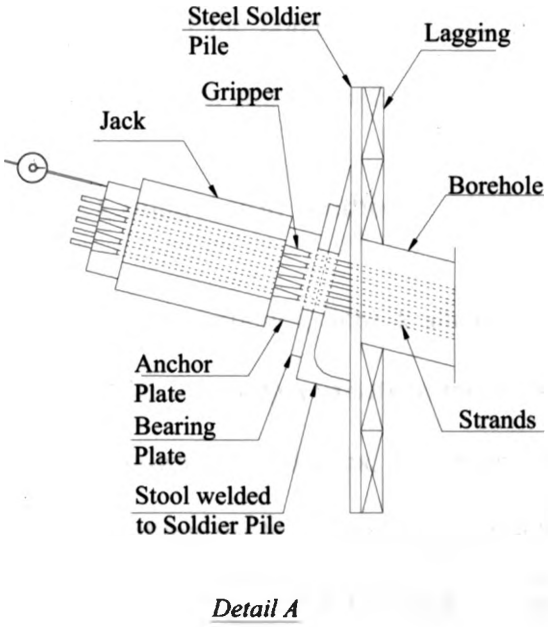

***Figure 6.2** Tieback Testing Setup*

6.2.1.1 Geometry

Figure 6.1 shows the geometry of a typical single stage tieback anchor. Tieback anchors in soil are constructed by advancing an inclined borehole (typically the inclination is between 10° and 45°) through soil using a rotary drill rig. After reaching the required length, strands are inserted into the borehole. Anchors may consist of either a high strength steel bar or several post-tensioning strands. For discussion purposes, strands will be assumed. For single stage anchor systems, the tieback anchor has an unbonded or free length, L_f, as it passes through the active earth pressure zone behind the shoring wall.

In addition, the tieback anchor has a bonded length, L_g, of diameter D_g, which provides the pullout capacity. The anchor strands are encapsulated in a sheath in the unbonded portion of the tieback anchor whereas they are exposed or bare over the bonded length. In most cases, centralizers and spacers are inserted into the borehole to position

the strands, and the borehole is tremie filled with grout. The finished anchor has an anchor head which attaches to the shoring wall (see ***Figure 6.2*** and Macnab 2002).

6.2.1.2 Construction Methods

Similar to micropiles, tieback anchors can be constructed in a variety of geological environments and using a variety of methods. The installation method depends on the soil type, groundwater conditions, site restrictions and equipment availability. The most common drilling methods used by contractors in the *GTA* are either continuous flight augers or rotary duplex drilling using a casing to support the borehole.

Continuous flight hollow stem augers (*CFA*) are the most common auger drilling method for installing tieback anchors in sandy soils. For this construction method, a borehole is drilled with auger to the required length or depth and anchor strands are set in the borehole through the hollow stem of the auger. Next, the borehole is tremie filled with grout while the augers are retracted. After the augers are retracted and the grouting complete, the grout is allowed to cure obtaining the final tieback anchor geometry shown in ***Figure 6.1***. This construction method will be denoted by *CFA* in this study. In some cases, solid stem continuous flight augers can be used in very dense unsaturated sandy soils if the borehole is self-supporting. However, for solid stem augering, the augers are retracted after drilling is complete and the tieback anchor is constructed in the uncased borehole.

In addition to using augers, boreholes are also commonly advanced using rotary drilling with drilling fluid and a casing to support the soil. This construction method, hereafter referred to as rotary duplex drilling (*RDD*), involves the use of a rotary drill rig

to advance a drill bit through overburden. A casing follows closely behind the drill bit to support the borehole. This drilling method creates a borehole by the rotary action of the bit and the jetting action of a drilling fluid, which is pumped through the drill stem[1] under pressure and jetted out of the bit. Soil cuttings are flushed to the surface by the drilling fluid, which is typically water. On completion of the borehole using *RDD*, anchor strands are inserted into the casing and centered using centralizers, and the borehole is tremie filled with grout while the casing is retracted. In some cases, post-grouting is performed when *RDD* is used. The post-grouting is performed by inserting a tube-a-manchette (TAM) into the borehole with the post-tensioning strands. After the initial tremie grout cures, the anchor is post-grouted by injecting grout under high pressure through ports in the TAM. As shown later, this improves the pullout resistance of grouted anchors.

Summarizing, tieback anchors are built using the construction sequences shown in ***Figure 6.3***, and discussed above. Referring to ***Figure 6.3a***, the drilling involves advancing an inclined borehole through cohesionless soils using rotary drilling until it reaches the required length. After reaching the required length (see ***Figure 6.3b***), strands are placed inside the borehole and the drill hole is filled with grout. On completion, the anchor has a free length L_f and an anchor length L_g as in ***Figure 6.3d***.

[1] The drill stem comprises drill rod from the rig to the drill bit.

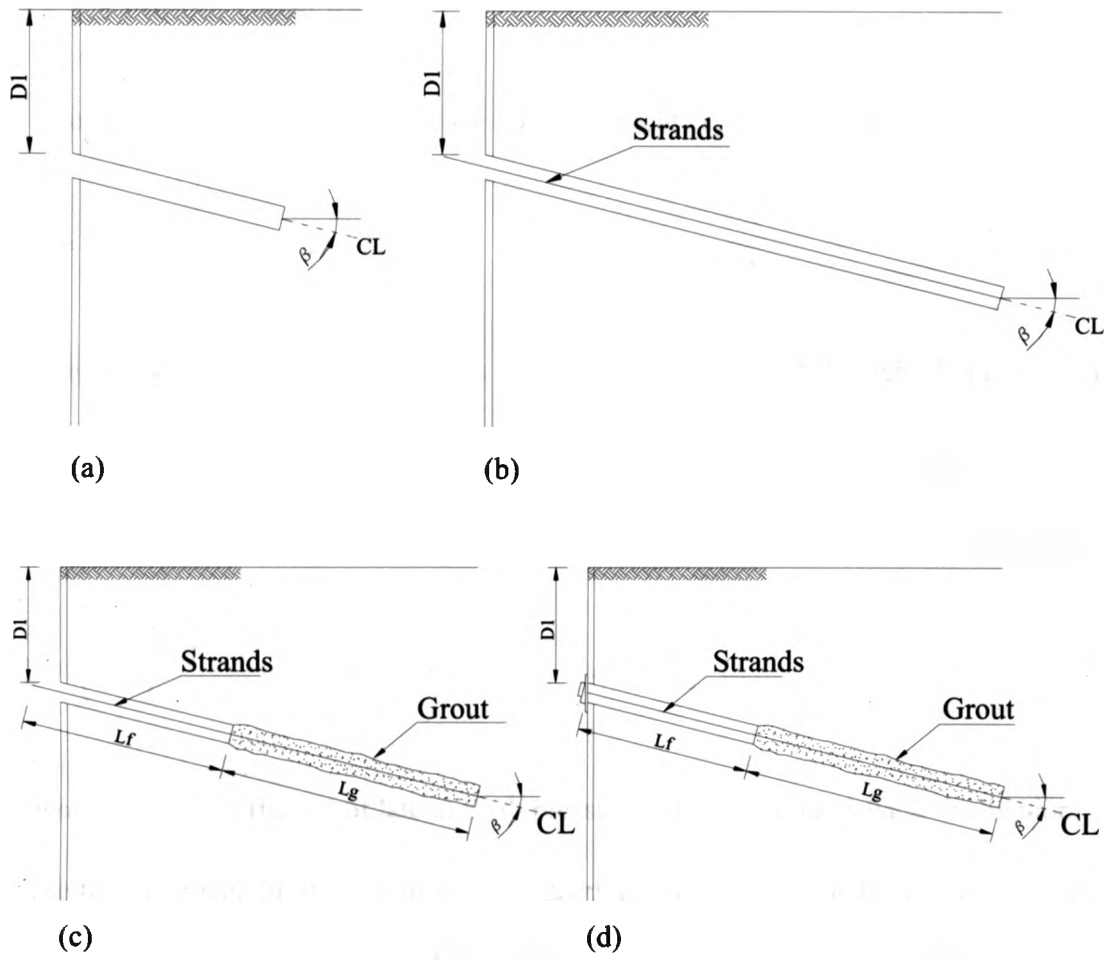

Figure 6.3 *Anchor Construction Sequence*

6.2.1.3 Pullout Capacity

For the anchor presented in ***Figure 6.1***, the pullout capacity in cohesionless soils is

$$P_{ult} = \int_0^{L_g} \sigma_R' \cdot \tan(\delta) \cdot \pi \cdot D_g \cdot dl \qquad [6.1]$$

where σ'_R is the effective radial stress on the bonded section of the tieback anchor, δ is the effective friction angle between the grout and soil, and $\pi D_g L_g$ is the area of the bonded length that is in contact with the soil. If the tieback anchor is gravity grouted, then

$$P_{ult} = \left(\frac{(1+K_0)}{2} - \frac{(1-K_0)}{2} \cdot \cos(2 \cdot \varepsilon) \right) \cdot (\gamma \cdot z_m - u) \cdot \pi \cdot D_g \cdot L_g \qquad [6.2]$$

where K_0 is the coefficient of lateral earth pressure at rest, ε is the tieback inclination, γ is the bulk unit weight of the soil, z_m is the depth to the center of the bonded length and u is the pore water pressure at z_m. If the tieback is post-grouted, then the ultimate pullout capacity is:

$$P_{ult} = (p_g - u) \cdot \tan(\delta) \cdot \pi \cdot D_g \cdot L_g \qquad [6.3]$$

where p_g is the post-grouting pressure. The mobilized shear strength of the tieback, τ_{mob}, can be deduced from the measured pullout capacity of the tieback anchor, P_{ult}, divided by the area of the bonded zone in contact with the soil.

$$\tau_{mob} = \frac{P_{ult}}{\pi \cdot D_g \cdot L_g} \qquad [6.4]$$

6.2.2 Pullout Test Procedures

Test Setup

Figure 6.2 shows a typical setup for tieback pullout tests. A stool or reaction frame is commonly welded to the soldier pile after the anchor grout has cured. Then a bearing plate and hydraulic jack are set on the stool. The strands pass through the stool, bearing plate and the jack. In conjunction with this setup, two sets of mechanical grippers are placed over the post-tensioning strands. One set is situated at the top of the jack to transfer the jack forces to the strands. A second set of grippers is placed over the strands between the jack and the bearing plate and is used to lock in the final anchor loads. Typically, the load applied to the tieback anchor is measured using a pressure gauge attached to the hydraulic jack. Before conducting pullout tests, it is common practice to calibrate the jack and pressure gauge. Displacement or elongation of the strands is measured using a dial gauge supported on a frame that is anchored outside the zone of influence of the test.

Load Sequence

In this study, all tieback anchor pullout tests were performed according to AASHTO-AGC-ARTBA 1990 and FHWA-RD-97-130 standards. Normally, there are two types of load tests performed on tieback anchors: first, all tieback anchors are proof tested to about 1.3 times the design anchor load, P_D. In addition, performance tests are performed on select anchors up to 2 times the design load, P_D. This study examines the response of performance tests only. Performance tests are performed by first applying a seating load of about 0.1 P_D to the anchor and then zeroing the dial gauges. Then, the tieback anchor

is loaded sequentially to loads of 0.25 P_D, 0.5 P_D, 0.75 P_D, 1.0 P_D, 1.25 P_D, 1.5 P_D, 1.75 P_D and finally to 2.0 P_D. At loads of 0.5 P_D, 1.0 P_D, 1.5 P_D and 2.0 P_D, the load is cycled to the seating load and then back to the applied load to measure the inelastic elongation, δ_p, and elastic elongation, δ_e, of the tieback anchor. In addition to cycling the load in the tieback, each load is held for at least 10 minutes during which time the creep deformations are recorded, if any occur. As described below, if the creep exceeds 1mm in 10 minutes then the load is maintained an additional 50 minutes to measure the creep over the time interval 6-60 minutes.

Data Collected

Table 6.1 summarizes the pullout test results evaluated in this study. Full details of the load versus tieback elongation response of each tieback can be found in ***Appendix C***. Each of the tieback tests is identified by the location of the project where the tieback anchor was installed. In addition, the following anchor parameters are provided:

P_D	design anchor load.
P_{max}	maximum load applied during pullout tests.
δ_{cr}	maximum creep deformation.
δ_e	elastic elongation at P_{max}.
δ_p	inelastic elongation at P_{max}.
L_g	anchor bonded length.
L_f	anchor free length.
ε	inclination of the tieback anchor.
D_g	diameter of the tieback anchor.
z_m	depth to the center of the bonded length.
τ_{mob}	mobilized shear strength on the bonded length (calculated according to equation *[6.4]*

***Table 6.1** Tiebacks in Sandy Soils*

Location/Project/ Tieback No.	P_D (kN)	P_{max} (kN)	Pass/ Fail (P/F)	δ_{cr} (mm)	δ_e (mm)	δ_p (mm)	L_g (m)	L_f (m)	ε (dgr)	D_g (mm)	Z_m (m)	Post Grout (Y/N)	Drilling Method	Soil Type in Anchor Zone	GWT (m)	w (%)	SPT N-value	Avg SPT N-value	τ_{mob} (kPa)
73 Lawton Blvd Project 94.37 #7	670	1007	P	0.3/10' 0.4/30'	26	11	6.5	3.2	30	150	8.0	N	CFA	Silty sand, loose	7	22	5	5	328.8
Dundas & St. Patrick Project 95.20 # 32	500	730	P	0.5/10'	19.6	17.6	5.2	8.3	40	460	11.0	N	CFA	Silt and sand layers, hard clayey silt and v dense,	-	15-19	84-82	83	97.1
68 Millwick Dr, Weston Project 96.09 #12	600	1200	F	2/10' 2/30'	68	44	7.0	4.0	25	460	5.0	N	CFA	sand dense to v dense, fine, wet	-	18	36-56	46	118.6
68 Millwick Dr, Weston Project 96.09 #16	150	300	P	1/10' 1/30'	24	13	5.0	3.0	15	460	3.0	N	CFA	sand dense to v dense, fine, wet	-	10-18	73-56	65	41.5
99 Hayden Ave Project 96.32	560	1120	F	6/10' 7/60'	34	30	8.0	5.0	30	460	7.5	N	CFA	Sandy silt till + sand, gravel, v. dense, moist	3	-	22-24	23	96.9
5095 Yonge, NY Project 97.10 #152	1200	1881	P	0/10'	49.7	50.5	12.0	13.2	25	200	15.0	Y	RDD	sand & sand till, dense, fine	12	-	-		249.5
80 Hayden Str Project 2000.07 #18L	700	1388	F	5.4/60'	31.1	10.8	6.3	5.2	35	460	8.0	N	CFA	silty sand with traces of clay		-	26-100	63	152.5
80 Hayden Str Project 2000.07 #72L	810	1645	F	2.4/20'	27.8	39.7	8.5	3.5	30	460	12.5	N	CFA	silty sand with traces of clay		-	26-100	63	133.9
80 Hayden Str Project 2000.07 #75	720	1451	P	0.8/60'	46	13	10.0	5.0	30	460	12.5	N	CFA	silty sand with traces of clay		-	26-100	63	100.4
High tech&Red Maple, Richmond Project 00.39 #15U	290	590	F	0/10' 6.4/60'	29	30.3	4.0	6.0	30	460	7.0	N	CFA	Silty fine sand, v dense, moist to v moist		17-7.3	100	100	102.1
Gates of Bayview Glen - High tech &Red Maple, Richmond Project 00.39 #28U	290	590	F	1.9/10' 5.3/60'	29.5	21.6	4.0	6.0	30	460	7.0	N	CFA	Silty fine sand, v dense, moist		16.9	100	100	102.1
5000 Yonge / 5000 Yonge Str Project 01.32 #10	600	1213	F	0.4 /10' 2.1/60'	29	17	7.0	4.0	25	460	4.5	N	CFA	sandy silt till (compact- v dense)	-	10-12	35-70	53	119.9
5000 Yonge / 5000 Yonge Str Project 01.32 #L53	800	1194	F	2.1/10' 4.8/30'	18	39	8.9	3.9	35	460	8.5	N	CFA	sandy silt till		8-11	35-40	38	92.8
5000Yonge / 5000 Yonge Str Project 01.32 #L54	800	2085	F	0.5/10' 2.5/60'	31	47	11.2	2.3	30	460	10.5	N	CFA	sandy silt till		8-12	35-40	38	128.8

Location/Project/ Tieback No.	P_D (kN)	P_{max} (kN)	Pass/ Fail (P/F)	δ_{cr} (mm)	δ_e (mm)	δ_p (mm)	L_g (m)	L_f (m)	ε (dgr)	D_g (mm)	Z_m (m)	Post Grout (Y/N)	Drilling Method	Soil Type in Anchor Zone	*GWT* (m)	w (%)	*SPT* N-value	Avg *SPT* N-value	τ_{mob} (kPa)
5000 Yonge / 5000 Yonge Str Project 01.32 #55U	900	1402	F	1.3/30'	30	38	8.1	7.5	35	460	9.0	N	CFA	sandy silt till		8-11	35-40	38	119.8
5000 Yonge / 5000 Yonge Str Project 01.32 # 56U	900	1592	F	1.3/10' 2.2/30'	30	138	10.5	4.0	35	460	9.0	N	CFA	sandy silt till		8-12	35-40	38	104.9
The Marquis - 85 Bloor St East Project 01.60 # 25U	550	1251	F	1.7/16'	44.2	29.5	6.6	5.5	30	460	11.5	N	CFA	sandy silt / silty sand	9.5	8-12	50-75	63	131.1
The Marquis - 85 Bloor St East Project 01.60 41U	550	1099	P	0.4/10'	35.1	17.5	5.1	5.5	35	610	9.0	N	CFA	silt till (v dense)	10.5	8-10	50	50	112.4
Gates of Bayview Glen - High tech&Red Maple, Richmond Project 02.82 #80	800	1573	F	1.2/10'	16.9	53.6	10.0	3.0	25	460	6.0	N	CFA	silty sand+gravel,grey-brown,moist,v.dense		-	83	83	108.8
The Regency Yorkville - 1280-1290 Bay Project 03.01 #11M	900	1804	F	1.8/10' 2/30'	33.3	24.2	13.0	4.0	25	460	10.5	N	CFA	sandy silt till,compact-v.dense,clay,wet	-	-	25-66	45	96.0
The Regency Yorkville - 1280-1290 Bay Project 03.01 #30M	850	1706	F	1.5/10' 3.4/30'	46.3	32.8	12.0	4.0	25	460	10.5	N	CFA	sandy silt till,compact-v.dense,clay,wet	-	-	-	40	98.4
The Regency Yorkville - 1280-1290 Bay Project 03.01 #89L	350	696	P	0.8/10' 0.9/30'	23.4	15.6	6.5	1.5	25	460	9.5	N	CFA	silt -sandy silt+sand,moist,compact-.dense	-		23-52	38	74.1
Glenlake Park - 2505 Dundas St W Project 03.03 #18U	170	334	F	13/ 30'	15.7	55.8	3.7	1.5	15	140	3.0	Y	RDD	sand			12-25	17	205.2
Glenlake Park - 2505 Dundas St W Project 03.03 #33U	400	800	P	0.9/30'	42.5	32.8	10.0	3.0	25	140	6.0	Y	RDD	silty fine sand			-		181.9
Circa RR7 Town Centre Blvd Project 03.10 #92	350	847	P	0/10`	23.1	4.7	4.0	3.0	25	460	5.0	N	CFA	sand, v. dense, brown, fine to medium, grained silty sand + gravel, damp to moist			80-90	85	146.5

Location/Project/ Tieback No.	P_D (kN)	P_{max} (kN)	Pass/ Fail (P/F)	δ_{cr} (mm)	δ_e (mm)	δ_p (mm)	L_g (m)	L_f (m)	ε (dgr)	D_g (mm)	Z_m (m)	Post Grout (Y/N)	Drilling Method	Soil Type in Anchor Zone	GWT (m)	w (%)	SPT N-value	Avg SPT N-value	τ_{mob} (kPa)
Novex Pharma - 380 Elgin St, Richmond Hill Project 03.13 #46	623	1208	P	-	22	25	9.2	4.5	25	460	4.0	N	CFA	sandy silt			44-48	46	90.9
Cosmo - 5255 Yonge (Yonge & Sheppard) Project 03.45 #38	450	758	F	1.8/10'	18.6	14.1	10.0	5.5	25	460	9.0	N	CFA	sandy silt	-		50	50	52.5
22 Wellesley E Condos Project 03.66 #23U	600	1198	P	0/10' 0/30'	30.8	12	6.0	5.0	30	150	6.5	Y	RDD	silty sand + sandy silt, dense to v. dense			31-57	44	423.7
23 Wellesley E Condos Project 03.66 #56U	850	1771	F	1.3/10' 2.3/30'	50.1	27.5	8.5	5.0	25	150	8.0	Y	RDD	silty sand trace of clay and gravel , gray, moist			33-86	60	442.1
Villages of Guildwood - 3622 Kingston Road Project 03.78 #7U	300	600	P	0.4/10' 1.3/30'	9.8	10.2	3.0	3.5	25	460	4.5	N	CFA	Sandv, dense, fine-medium, damp-wet	1.5	5-10	150	150	138.4
Villages of Guildwood - 3622 Kingston Road Project 03.78 #74U	300	788	F	1.5/10' 3.3/30	9.4	13.5	4.1	3.5	25	460	6.0	N	CFA	sandy silt till,compact-v.dense,+gravel,ligthly cemented,damp-moist	5.5	5-10	100	100	133.0
Europa - 507 College Street Project 04.34 #24	600	1198	P	0/10'	30.5	32.1	7.0	3.0	30	460	6.5	N	CFA	sandy silt till, grey, moist, v.dense with trace of clay	9.5	-	102-136	119	118.4
Europa - 507 College Street Project 04.34 #56	550	1115	P	0.4/10'	38.6	27.5	7.5	4.0	30	460	5.5	N	CFA	sandy silt till, grey, moist, v.dense with trace of clay	-	-			102.9
912-940 Mt Pleasant Project 04.41 #8	350	694	F	1.1/10' 1.9/30'	26.5	39.2	5.0	4.0	25	460	4.0	N	CFA	fine to medium sand,v.dense, silty fine sand, moist-saturated, +fine gravel,	4	-	120-140	130	96.3
912-940 Mt Pleasant Project 04.41 #16	350	696	P	0.4/10' 0.6/30'	26.7	46.3	5.0	4.0	25	460	5.5	N	CFA	fine sand,v.dense, +silty,moist-saturated,	5	-	120-140	130	96.3
912-940 Mt Pleasant Project 04.41#115	600	1200	P	0.3/10' 0.4/30'	31.7	10	9.0	4.0	25	460	4.0	N	CFA	silty sand,moist-wet,dense-v.dense	2	-	39-100	70	92.3
912-940 Mt Pleasant Project 04.41 #139	400	800	P	0/10' 0/30'	35	9.1	6.0	4.0	25	460	4.0	N	CFA	silty sand,moist-wet,compact-v.dense	2	-	44-59	52	92.3

Location/Project/ Tieback No.	P_D (kN)	P_{max} (kN)	Pass/ Fail (P/F)	δ_{cr} (mm)	δ_e (mm)	δ_p (mm)	L_g (m)	L_f (m)	ε (dgr)	D_g (mm)	Z_m (m)	Post Grout (Y/N)	Drilling Method	Soil Type in Anchor Zone	*GWT* (m)	w (%)	*SPT* N-value	Avg *SPT* N-value	τ_{mob} (kPa)
RC Harris Water Filtration Plant - Queen St E & Victoria Par Project 04.50 #A88L	750	1506	P	0.1/10' 0.2/30'	30.5	10.2	12.0	5.0	30	460	12.0	N	CFA	silt			20-34	27	86.8
RC Harris Water Filtration Plant - Queen St E & Victoria Park Project 04.50 #A89U	500	1010	P	0.2/10'	31.4	2.2	8.0	6.5	15	150		Y	RDD	sand, sandy silt			20-34	27	267.9
RC Harris Water Filtration Plant - Queen St E & Victoria Park Project 04.50 #A90U	500	1010	P	0.8/10'	56.3	15.8	8.0	14.5	20	150		Y	RDD	sand, sandy silt			20-34	27	267.9
RC Harris Water Filtration Plant - Queen St E & Victoria Park Project 04.50 #B15U	500	952	F	4.7/10' 8.3/12	51.9	51.8	8.0	9.4		150		Y	RDD	silt			20-34	27	252.5
The Legends at Tam O'Shanter - 190 Bonis Ave, Scarb Project 04.88 #15	750	1125	F	0.8/10' 1.5/30'	22.1	36.9	7.5	4.0	35	460	8.5	N	CFA	sandy silt till, comp-dense, moist,+gravel	10	8-15	-	70	104.4
The Legends at Tam O'Shanter - 190 Bonis Ave, Scarb Project 04.88 #38	700	1238	F	4/10' 4.1/30'	21.5	51.3	7.0	3.5	30	460	6.0	N	CFA	sandy silt till, comp-dense, moist,+gravel	12	7-12	50	50	122.4
The Legends at Tam O'Shanter - 190 Bonis Ave, Scarb Project 04.88 #58	700	1400	P	0.7/10'	26	59.7	7.0	3.5	30	460	6.5	N	CFA	sandy silt till, comp-dense, moist,+gravel	15	8-10	80	80	138.4
Murano Condo - 825 Bay Str Project 05.05 #15M	750	1197	F	1.5/10' 2.7/30'	20.5	24.8	8.0	6.2	25	200	8.5	Y	RDD	silty sand, moist to wet,v dense	9.5	-	>100	100	238.1
Murano Condo - 825 Bay Str Project 05.05 #23U	750	1504	P	0.8/10'	34.8	19.8	7.5	8.4	25	200	9.0	Y	RDD	silty sand, moist to wet,v dense	9	-	>100	100	319.2
Murano Condo - 825 Bay Str Project 05.05 #35U	750	1504	P	0.8/10'	36.4	20.6	7.5	8.4	20	200	8.0	Y	RDD	sand , moist, dense to v dense	9	-	>100	100	319.2

Location/Project/ Tieback No.	P_D (kN)	P_{max} (kN)	Pass/ Fail (P/F)	δ_{cr} (mm)	δ_e (mm)	δ_p (mm)	L_g (m)	L_f (m)	ε (dgr)	D_g (mm)	Z_m (m)	Post Grout (Y/N)	Drilling Method	Soil Type in Anchor Zone	*GWT* (m)	*w* (%)	*SPT* N-value	Avg *SPT* N-value	τ_{mob} (kPa)
Murano Condo - 825 Bay Str Project 05.05 #39M	750	1356	P	0.9/10'	74.5	23.1	7.5	7.2	20	200	12.5	Y	RDD	sand , wet, dense to v dense	9	-	40-55	48	254.6
Murano Condo - 825 Bay Str Project 05.05 #39L	1050	1310	F	1.5/10'	40	20	8.0	6.2	20-25	200	12.0	Y	RDD	silty sand	20		>100	100	260.6
Murano Condo - 825 Bay Str Project 05.05 #69U	1050	1578	F	1/10' 3.1/30'	36.8	15.1	11.0	8.4	25	200	5.5	Y	RDD	silty sand, moist to wet,v dense	7	-	>100	100	228.4
Murano Condo - 825 Bay Str Project 05.05 #80U	750	1125	F	0.7/10' 1.8/30'	21.1	25.3	7.5	8.4	25	200	8.0	Y	RDD	sandy silt till, moist to wet, v dense	10	-	-		238.8
ARC Bayview Village - 603 Sheppard E Project 05.53 #43U	600	1200	P	0/10'	36.2	7.9	7.0	5.0	30	115	7.5	Y	RDD	brown sand +gravel, moist , v. dense			60-100	80	474.5
ARC Bayview Village - 603 Sheppard E Project 05.53 #89U	450	900	P	0.1/10'	38.5	8.6	5.0	5.0	45	115	8.0	Y	RDD	brown sand +gravel, moist , v. dense	7		100	100	498.2
CN Plains Rd Project 05.56 #10U	712	1070	P	0.7/60'	35.5	7.1	9.0	4.0	25	175	7.5	Y	RDD	clayey silt with sand and gravel			150	150	216.2
88 Broadway Project 05.68 #59	600	1136	F	1.7/10' 3.6/30	42.7	83.3	7.0	5.0	30	510	7.5	N	CFA	silty clay+sand, gravel, moist , hard / silty fine sand, greyish brown, moist, v.dense		3-23	45-75	60	101.3
The Renaissance - 10097 Yonge Project 05.94 #N20	400	800	P	0.4/10' 0.7/30'	25.9	21.8	8.0	3.5	30	460	5.0	N	CFA	sandy silt, +gravel			100-150	125	69.2
The Renaissance - 10097 Yonge Project 05.94 #E20	275	555	P	1.3/10' 1.8/60'	18.9	32.8	6.2	3.0	30	460	5.0	N	CFA	sandy silt, +gravel			100	100	61.9
Solstice- Webb Drive & Duke of York Project 06.04 #C18	125	251	P	0.6/10'	4.1	3.7	3.5	1.0	25	75	2.0	N	CFA	silty clay till (hard to stiff)			50-100	75	304.4
Solstice- Webb Drive & Duke of York Project 06.04 #C49	125	251	P	0.4/10'	3.6	2.7	3.5	1.0	25	75	2.0	Y	RDD	silty clay till (hard to stiff?)			50-100	75	304.4
Royal Gate-3625 Dufferin Street Project 06.04 #E2	650	1198	P	1.4/10' 1.7/30'	28.8	34.6	8.3	3.5	25	460	6.0	N	CFA	silty sand / sandy silt, +gravel, brown, moist to wet, dense	2		40-100	70	99.9

Location/Project/ Tieback No.	P_D (kN)	P_{max} (kN)	Pass/ Fail (P/F)	δ_{cr} (mm)	δ_e (mm)	δ_p (mm)	L_g (m)	L_f (m)	ε (dgr)	D_g (mm)	Z_m (m)	Post Grout (Y/N)	Drilling Method	Soil Type in Anchor Zone	GWT (m)	w (%)	SPT N-value	Avg SPT N-value	τ_{mob} (kPa)
Royal Gate-3625 Dufferin Street Project 06.04 #N39	700	1198	P	0.8/10' 0.8/20'	38.1	15.4	6.5	5.0	25	150	6.0	Y	RDD	sandy silt till + gravel, grey, moist, v. dense / silty sand +gravel, brown, moist to wet, dense	4		33-68	50	391.1
Royal Gate-3625 Dufferin Street Project 06.04 #W2	550	1095	P	0/10'	31	12.8	6.0	3.5	35	150	8.5	Y	RDD	sandy silt till + gravel, grey, moist, v. dense / silty sand +gravel, brown, moist to wet, dense	5		>100	100	387.3
EQ Town Centre Court, Scarborough Project 06.73 #16	1200	2388	P	0.3/10'	43.1	19.4	12.0	5.5	45	178	5.0	Y	RDD	sandy silt and silty sand, vdense			100-300	200	355.9
EQ Town Centre Court, Scarborough Project 06.73 #40	1200	2388	P	0/10'	54.8	14.7	12.0	5.5	25	178	8.0	Y	RDD	sandy silt,	9		16-52	34	355.9
EQ Town Centre Court, Scarborough Project 06.73 #97	600	1204	P	0.3/10'	38.6	15.1	6.0	3.0	25	178	2.0	Y	RDD	sandy silt,	7.5		20-55	37	358.8
EQ Town Centre Court, Scarborough Project 06.73 #98	600	1204	P	0.2/10'	41.4	15.4	7.0	3.0	25	178	2.0	Y	RDD	sandy silt,	7.5		20-55	37	307.6
EQ Town Centre Court, Scarborough Project 06.73 #138	1000	2009	P	0.2/10'	45.5	21.7	10.0	4.0	25	178	9.0	Y	RDD	sandy silt,	-		16-52	34	359.3
Bauer Building 187 King St, Waterloo Project 06.89 #50	250	374	F	17/10' 23/40'	18.2	44.7	4.5	3.0	25	150	6.0	Y	RDD	sand and gravel, brown, dense to v dense, saturated,	7.5		36-78	56	176.4
Bauer Building 187 King St, Waterloo Project 06.89 #51	250	504	F	8.7/10' 22/20'	13	50.5	4.5	3.0	25	150	6.0	Y	RDD	sand and gravel, brown, dense to v dense, saturated,	7.5		36-78	56	237.7
Bauer Building 187 King St, Waterloo Project 06.89 #83U	250	504	F	2.5/10' 8.1/30'	4.1	34.3	4.5	3.0	25	150	5.5	Y	RDD	sandy silt and sand			12-25	18	237.7
Bauer Building 187 King St, Waterloo Project 06.89 #105	250	374	F	4/10' 29/40'	18.2	44.7	4.5	3.0	25	150	5.5	Y	RDD	silty sand dense, brown, / sand, moist, saturated			20-30	25	176.2
Bauer Building 187 King St, Waterloo Project 06.89 #106	250	439	F	13/10'	4.8	45.8	4.5	3.0	25	150	5.5	Y	RDD	silty sand dense, brown, / sand, moist, saturated			20-30	25	207.0
Guelph Civic Centre Project 06.92 #50U	270	521	P	1/10' 1.3/30'	16.6	6.9	9.0	2.0	15	100	6.0	Y	RDD	silt			27-35	31	184.3

Location/Project/ Tieback No.	P_D (kN)	P_{max} (kN)	Pass/ Fail (P/F)	δ_{cr} (mm/ min)	δ_e (mm)	δ_p (mm)	L_g (m)	L_f (m)	ε (dgr)	D_g (mm)	Z_m (m)	Post Grout (Y/N)	Drilling Method	Soil Type in Anchor Zone	*GWT* (m)	*w* (%)	*SPT* N-value	Avg *SPT* N-value	τ_{mob} (kPa)
McVean Pumping Station, Brampton Project 06.116 #N8U	450	923	P	0/10' 1/60'	43.3	11.7	7.5	4.5	30	150	7.0	Y	RDD	silty sand			150	150	261.2
McVean Pumping Station, Brampton Project 06.116 #S2	450	923	P	0.1/10' 1.1/60'	51.3	10.7	7.5	4.5	30	150	8.0	Y	RDD	silty sand			300	300	261.2
The Rosewood - 133 Wynford Drive Project 06.128 #105	700	1402	F	1.8/10' 3.7/30'	18.9	71.2	8.9	4.0	30	460	8.0	N	CFA	sandy silt till			20-23	22	109.0
The Rosewood - 133 Wynford Drive Project 06.128 #107	400	1004	F	2.6/10' 3.8/20'	26.8	35.7	4.0	4.0	30	460	8.0	N	CFA	sandy silt till			20-23	22	173.7
The Rosewood - 133 Wynford Drive Project 06.128 #108	400	1308	P	0.5/10' 1.5/30'	34.8	40.5	4.0	4.0	30	460	8.0	N	CFA	sandy silt till			20-23	22	226.3

where z_m distance from the tieback midpoint to the ground surface, ε is the inclination angle of the tieback anchor, L_g is the bonded length of the anchor, L_f is the free or unbonded length, D_g is the diameter of the tieback anchor, P_D – design load, P_{max} is the maximum load applied during performance tests, τ_{mob} – mobilized average shear stress in the bonded zone, δ_{cr} – creep movement at 10min or other time interval at the performance test load, P_{max}, δ_e – elastic movement at P_{max}, δ_p – plastic or inelastic displacement at P_{max}, *GWT* - ground water table, *CFA* – continuous flight auger, *RDD/PG* – Rotary Duplex Drilling with post grouting

6.2.3 Interpretation of Pullout Test Results

Figure 6.4 and ***Figure 6.5*** illustrate the two most common failure modes of tieback anchors during pullout tests. ***Figure 6.4*** depicts the response of a tieback anchor that failed due to excessive creep. Creep deformations are normally recorded while holding the tieback load constant for 10 minutes. During this 10-minute period, if the creep deformation exceeds 1mm, then the load is held for an additional 50 minutes. The tieback anchor is considered to have failed if the creep movement exceeds 2mm over the time-period 6-60 minutes. The tieback anchor depicted in ***Figure 6.4*** failed due to excessive creep at a load of $1.75P_D$.

Figure 6.5 illustrates the second type of failure commonly encountered during tieback anchor tests. For the load-elongation results presented in ***Figure 6.5***, the tieback anchor pulled out when the load was increased from $1.0P_D$ to $1.125P_D$. Thus, the anchor failed prior to reaching twice the design load. In most cases, this type of failure is associated with very high rates of deformation in the tieback anchor and consequently high rates of relaxation in the load jack. Under most circumstances, it is not possible to maintain constant load in the jack as the anchor pulls out.

As noted above, ***Table 6.1*** summarizes the performance of seventy-eight tieback anchor tests in sandy soils in the *GTA*. In many cases, the tieback anchors remained stable during the tests and did not fail. These tests are labeled "P" for "Pass" in the fourth column. However, several tests failed due to pullout or creep and these tests are labeled "F" in the fourth column.

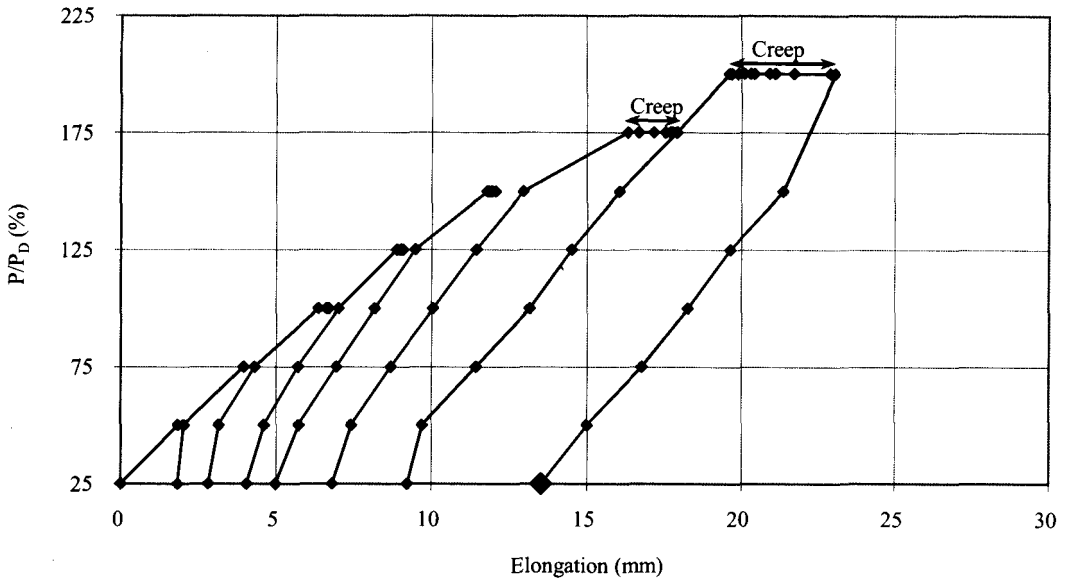

Figure 6.4 *Anchor Failures Due to Excessive Creep*

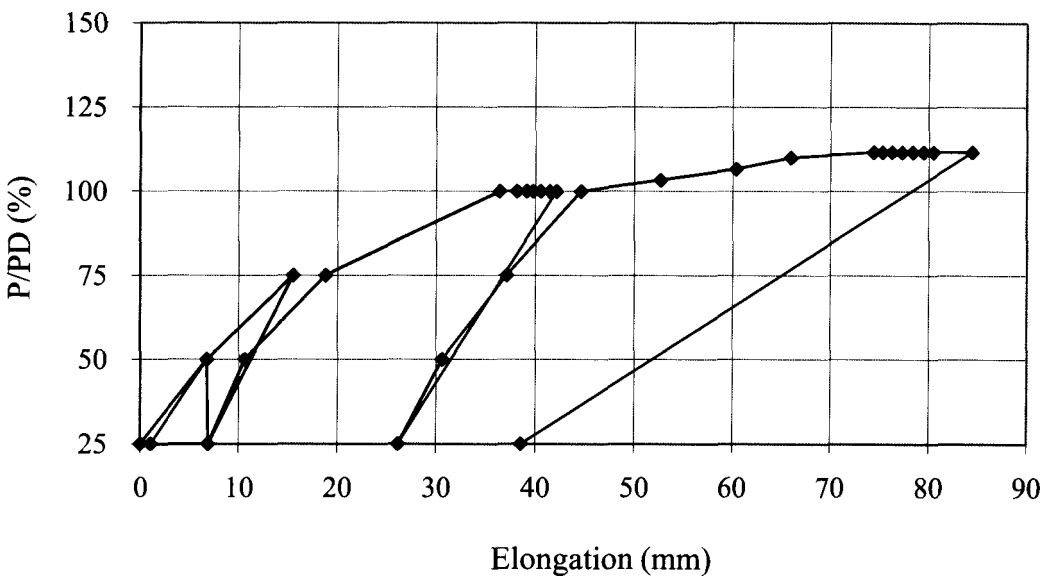

Figure 6.5 *Anchor Failures Due to Pullout*

6.2.4 Finite Element Calculation

A finite element (*FE*) analysis was performed using PLAXIS (version 8) to study the behaviour of a typical tieback anchor. The geometry and soil parameters considered are presented in ***Figure 6.6.*** The anchor was idealized for analysis by assuming axisymmetric conditions and considering a vertical anchor. The anchor and soil was discretized using 691 15-noded cubic strain triangles and 37 interface elements, respectively. The geometric layout includes has a rough rigid boundary at the base and a smooth rigid boundary at a radial distance of 7m from the anchor centerline. The *FE* calculations were performed by prescribing displacements at the anchor head and allowing PLAXIS to interactively solve for the reaction at the anchor head. The anchor was modeled as a linear elastic material. In the 9-m long bonded zone, the *EA* of the anchor was 4985 MN, whereas *EA* was 330MN in the 4-m long unbonded zone corresponding to the axial stiffness of the grout and strands, respectively. The soil was modeled as an elastic-plastic material with Young's modulus (E=50MPa), Poisson's ratio (ν=0.4), and failure governed by the Mohr-Coulomb failure envelope. The plastic material parameters comprised the effective cohesion intercept, (c'=0.5kPa), effective friction angle ($\emptyset'$=40°) and various dilation angles (ψ_0=0°, 10° and 20°). A complete set of parameters may be found in ***Table 6.2.*** Non-associated plastic flow was assumed using a flow rule similar to that of Davis (1982).

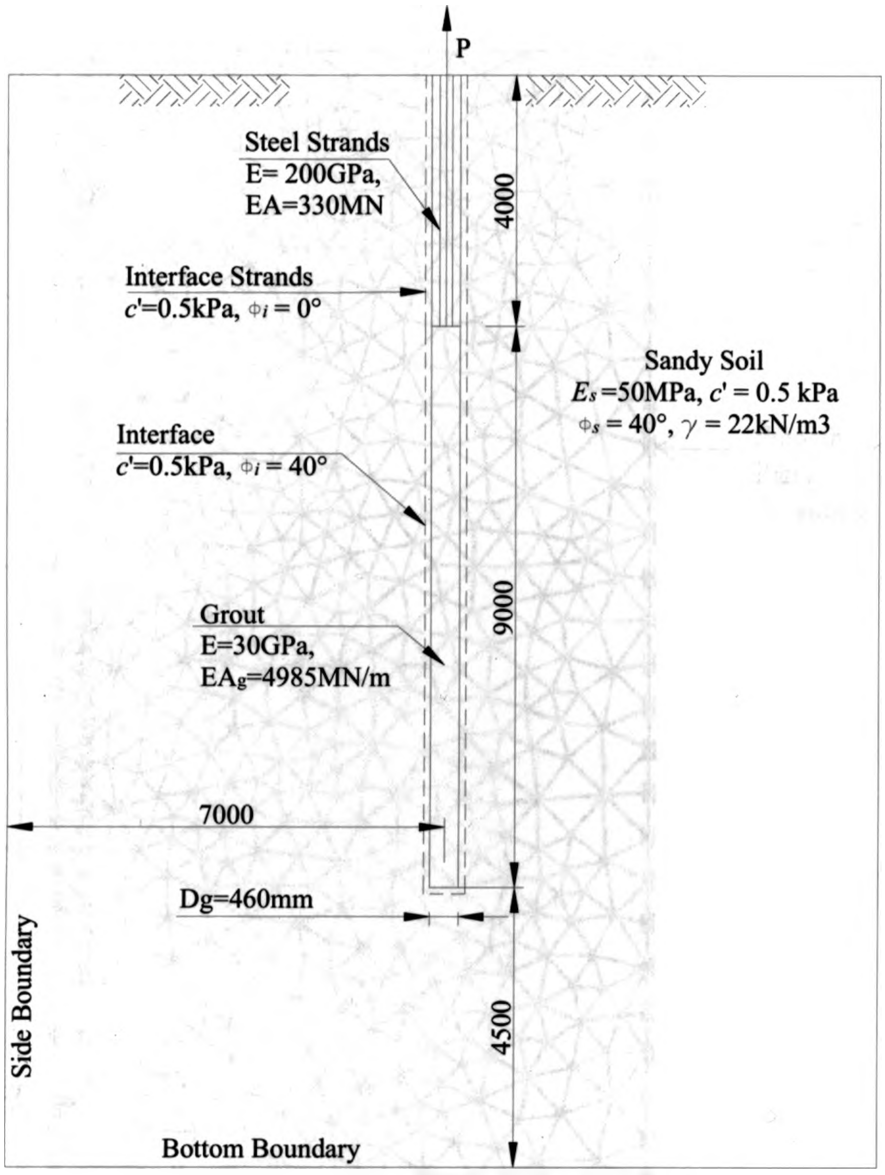
P
Steel Strands
E= 200GPa,
EA=330MN
4000
Interface Strands
c'=0.5kPa, ϕi = 0°
Sandy Soil
Es =50MPa, c' = 0.5 kPa
ϕs = 40°, γ = 22kN/m3
Interface
c'=0.5kPa, ϕi = 40°
Grout
E=30GPa,
EAg=4985MN/m
9000
7000
Dg=460mm
Side Boundary
4500
Bottom Boundary

(a) Geometry

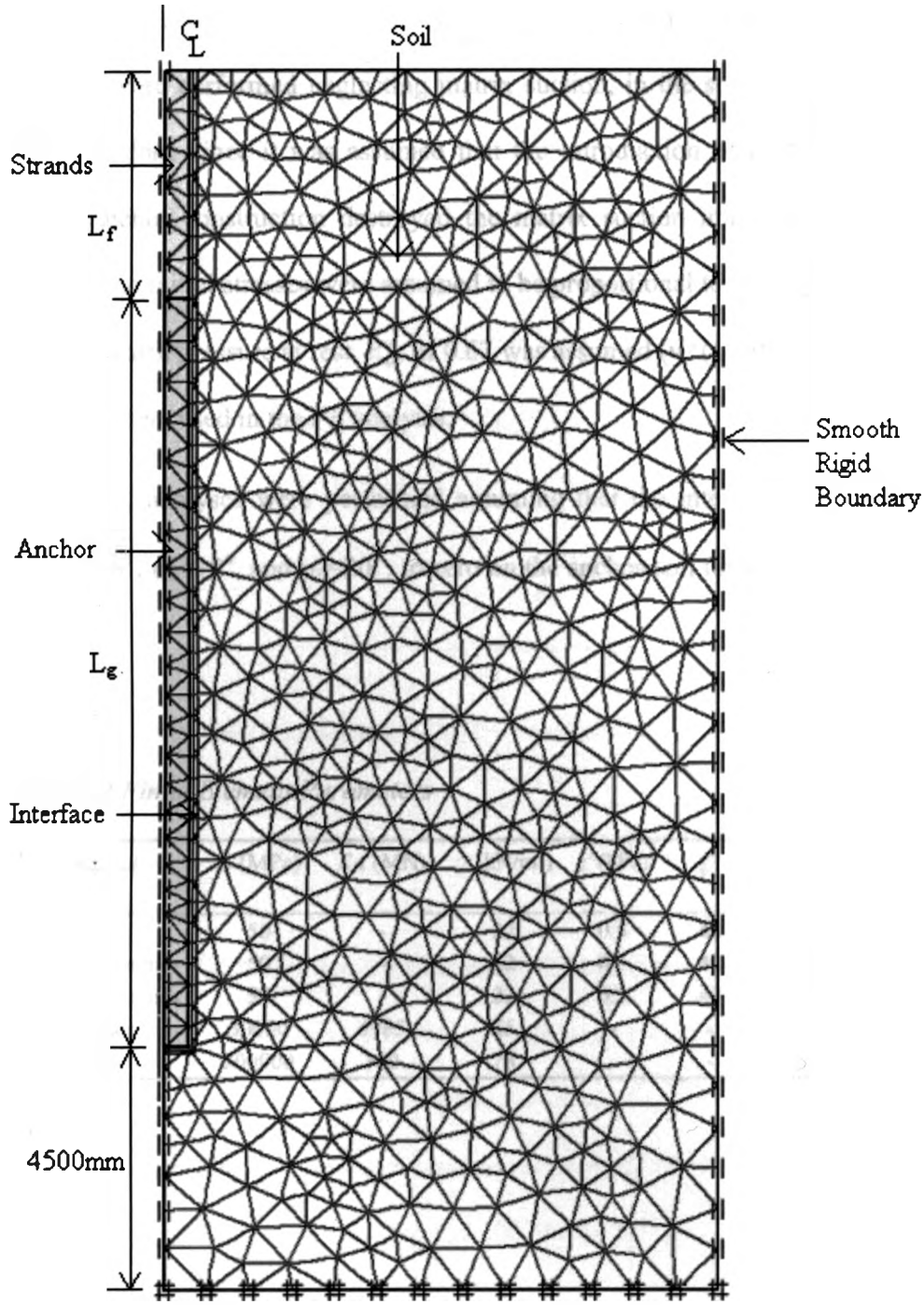

(b) Mesh

Figure 6.6 *Geometry and Finite Element Mesh for Tieback*

Although most of the anchors summarized herein were installed in unsaturated soils, analyses were performed neglecting matrix suction, in the soil surrounding the anchor. This was done since it was assumed that the introduction of drilling fluids and grout during anchor construction destroyed the matrix suction immediately adjacent to the anchor. The initial stresses were assumed to be proportional to the depth and a coefficient of lateral earth pressure at rest, K_0', of 0.67 was assumed ($\nu/(1-\nu)$). ***Table 6.2*** summarizes the parameters used in the *FE* analysis.

Finally, analyses were performed assuming that the interface dilation angle varied from $\psi_0=0^\circ$, $\psi_0=10^\circ$, and $\psi_0=20^\circ$, to zero on the anchor-soil interface as shown in ***Figure 6.7***.

Table 6.2 *Finite Element Parameters*

Material	E (MPa)	EA (MN)	γ (kN/m^3)	c' (kPa)	$\emptyset'$	ψ_0	ν	R_0
Sand	50	-	22	0.5	40	0,10,20	0.4	1
Interface Anchor	50	-	22	0.5	40	0,10,20	0.4	1
Interface Strands	50	-	22	0.5	40	0,10,20	0.4	0.01
Anchor	30000	4985	25	-	-	-	0.2	1
Stands	200000	330	78	-	-	-	0.2	1

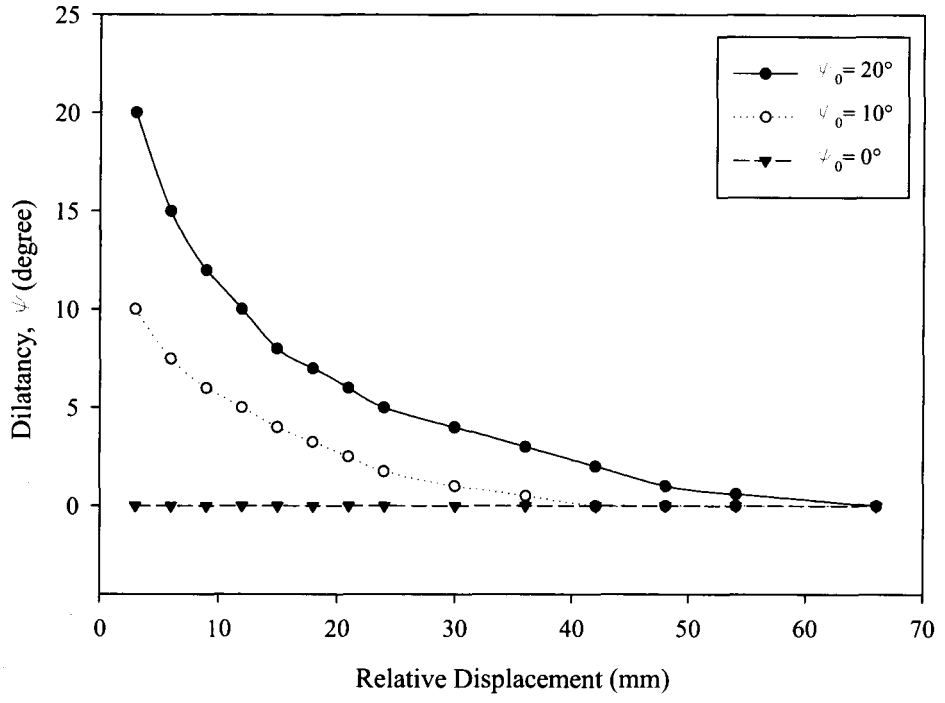

***Figure 6.7** Distribution of Dilation Angle Considered in FE Analysis*

6.3 Evaluation

As noted in the introduction of this chapter, the purpose of this study was to evaluate the response of tieback anchors during pullout load tests to see if there are trends in the mechanical behaviour at failure. ***Table 6.1*** presents the geometric parameters, soil conditions, ultimate load and mobilized shear strength of 78 tieback tests performed by Isherwood Associates between 1994 and 2007 in the *GTA*.

First, considering the anchors listed in ***Table 6.1*** that failed during performance testing; ***Figure 6.8*** shows the variation of mobilized shear strength versus average *SPT N-values*. It can be seen from this figure that the mobilized shear strength of tieback

anchors during pullout is not influenced by average *SPT N-values*. Thus, it appears that the density of the soil in which the anchors are constructed is not an important parameter.

Figure 6.8 also distinguishes between anchors that were constructed using continuous flight augers (*CFA*) and those that were constructed using rotary duplex drilling in conjunction with post grouting (*RDD-PG*). From the data and labels in ***Figure 6.8***, it can be seen that *RDD-PG* has a significant impact on anchor capacity compared with cases where *CFA* was used without post grouting. The mobilized shear strength for tiebacks that failed during performance tests varied from 92.8kPa to 173.7kPa for the *CFA* tiebacks. When the tiebacks were built using *RDD-PG*, the mobilized shear strength varied from 173.6kPa to 254.6kPa. Thus, it is concluded that construction method has a pronounced impact on the pullout capacity of tieback anchors. Unfortunately, there are no grouting records for the *RDD-PG* anchors and consequently it was not possible to examine the effect of grout pressure on these results.

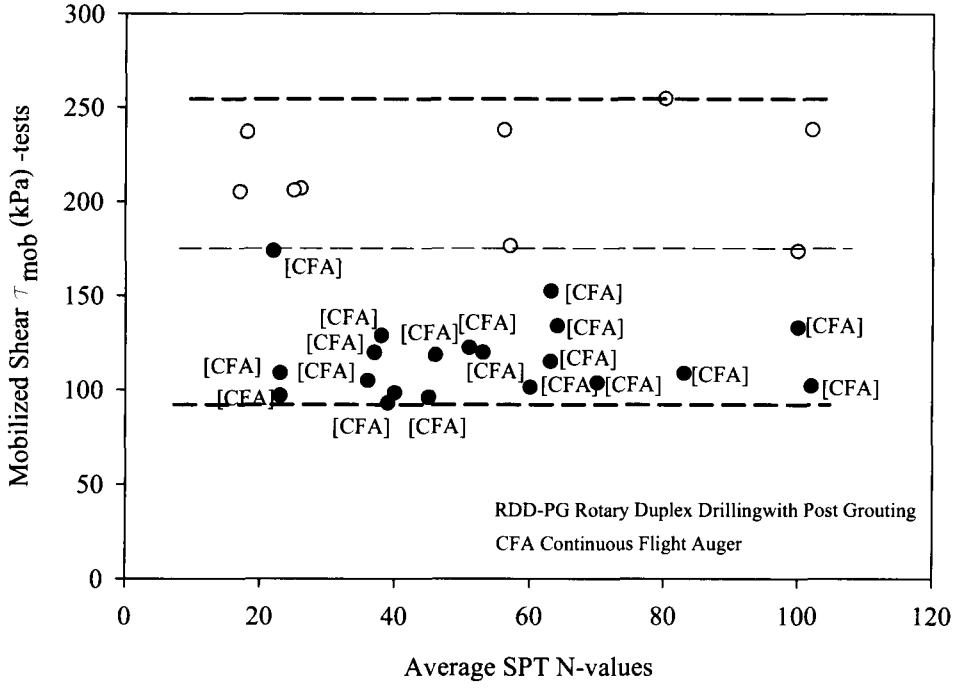

Figure 6.8 *Mobilized Shear Strength versus Average Blow Counts for Failed Tiebacks*

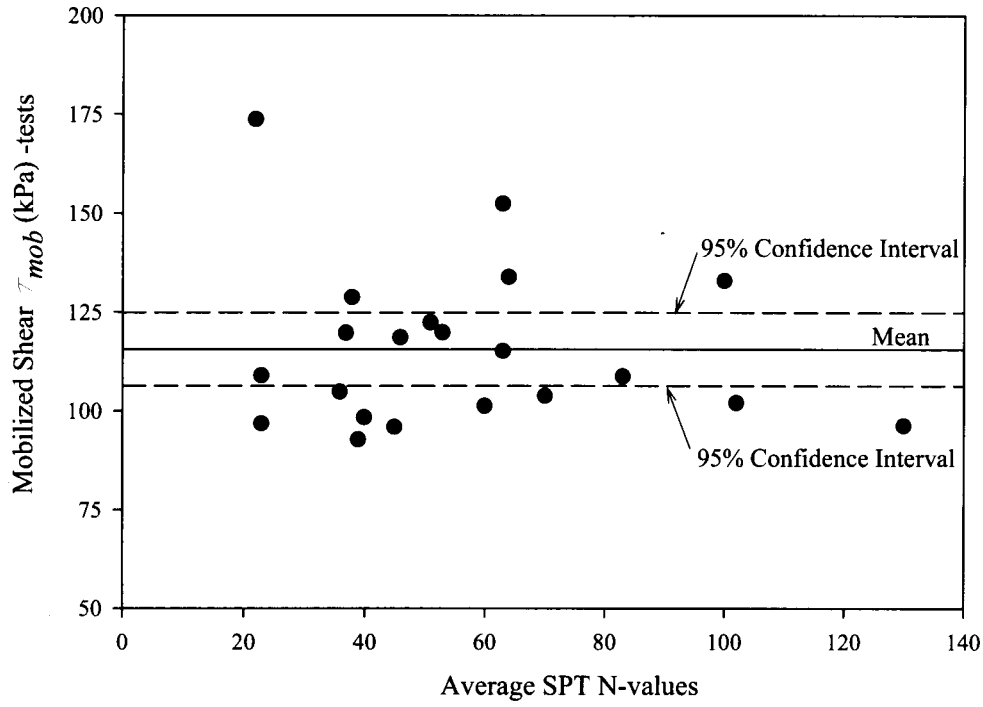

***Figure 6.9** 95% Confidence Intervals for Continuous Flight Auger Drilling Method*

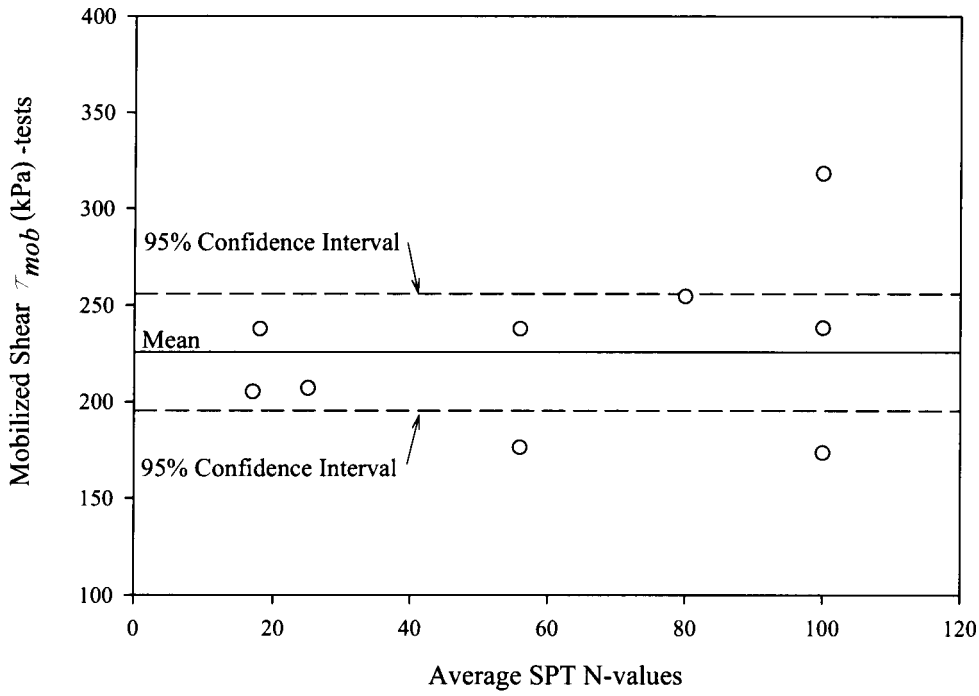

***Figure 6.10** 95% Confidence Intervals for Tiebacks made using RDD-PG Method*

Figures 6.9 and ***Figure 6.10*** show ninety-five percent (95%) confidence intervals for τ_{mob} deduced from the *CFA* and *RDD-PG* anchor tests, respectively. From ***Figure 6.9*** and ***Figure 6.10*** the mobilized average shear stress on L_g at failure is 115.6kPa ± 9.3kPa for *CFA* anchors and 225.6kPa ± 30.3kPa for *RDD-PG* anchors.

Figure 6.11 shows a plot of the mobilized shear strength versus inelastic movement for anchors that failed during performance tests. Given the materials used to construct the anchors, it is reasonable to assume that the majority of inelastic movement during pullout load tests is due to plasticity in the soil mass rather than in the grout or anchor strands. On inspection of ***Figure 6.11***, it is evident that the inelastic movement of the anchors and the mobilized shear stress at failure are not related parameters.

Figure 6.12 shows mobilized shear stress versus depth to the midpoint of the bonded zone, L_g, below the original ground surface. Again, it can be seen that there isn't an obvious trend of increasing mobilized shear stress versus anchor depth. Thus, the anchor capacity appears to be influenced primarily by the construction method whereas the state of the soil (deduced from average *SPT N-values*) and the depth of the anchors play a relatively minor role in the anchor capacity.

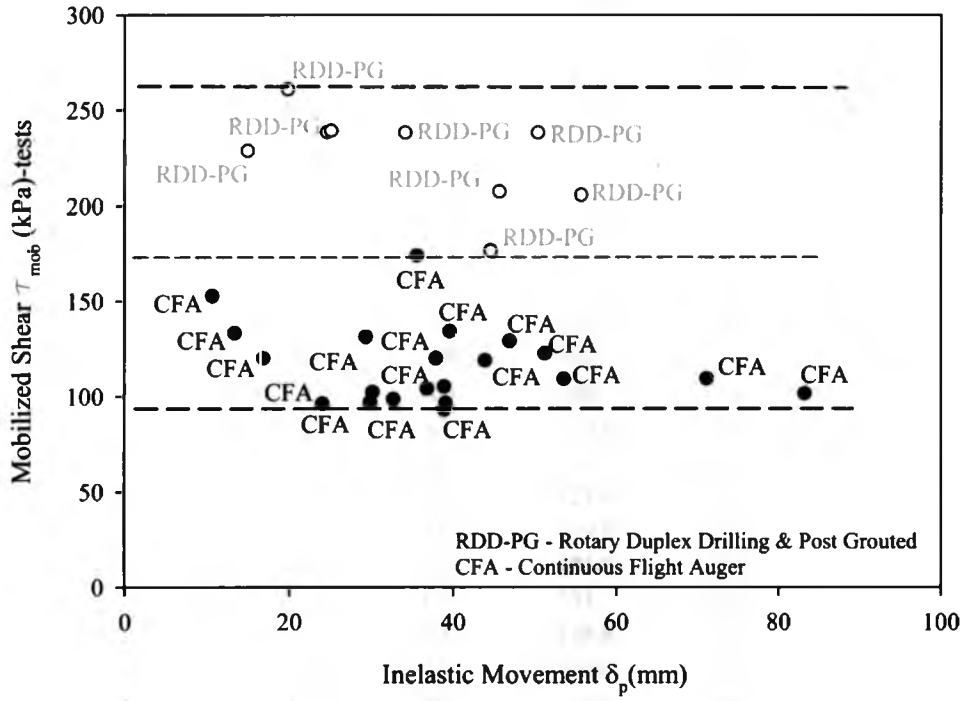

Figure 6.11 *Mobilized Shear Strength versus Inelastic Movement at Maximum Load*

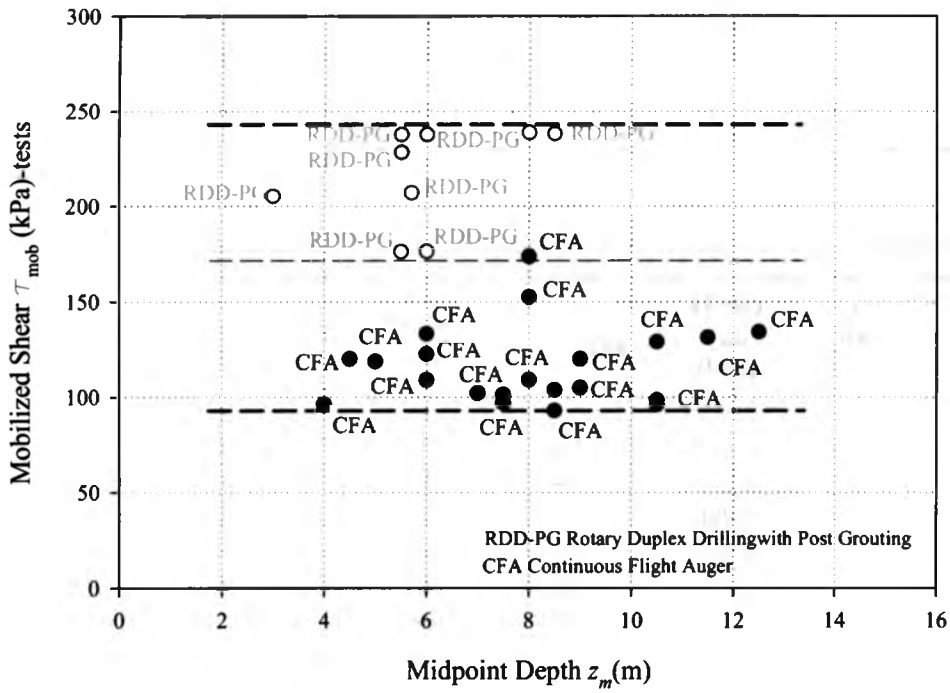

Figure 6.12 *Mobilized Shear Strength versus Distance from Ground Surface to Midpoint of Anchor Bonded Length*

Table 6.3 *Tested versus Theoretical Mobilized Shear for (CFA) Tiebacks*

L_g (m)	β (dgr)	D_g (mm)	z_m (m)	Average SPT	Test τ_{mob} (kPa)	Theory τ_{mob} (kPa)	Ratio	Anchor-soil displ $\delta_e + \delta_p$ (mm)
7	25	460	5	46	118.6	76.3	1.6	90.1
8	30	460	7.5	23	96.9	118.1	0.8	38.4
6.3	35	460	8	63	152.5	130.4	1.2	22.59
8.5	30	460	12.5	63	133.9	196.9	0.7	50.13
4	30	460	7	100	102.1	110.3	0.9	35
4	30	460	7	100	102.1	110.3	0.9	26.8
7	25	460	4.5	53	119.9	68.6	1.7	31.89
8.9	35	460	8.5	38	92.8	138.6	0.7	40.75
11.2	30	460	10.5	38	128.8	165.4	0.8	66.05
8.1	35	460	9	38	119.8	146.7	0.8	44.31
10.5	35	460	9	38	104.9	146.7	0.7	148.6
6.6	30	460	11.5	63	131.1	181.1	0.7	43.44
10	25	460	6	83	108.8	91.5	1.2	57.7
13	25	460	10.5	45	96.0	160.1	0.6	35.5
12	25	460	10.5	40	98.4	160.1	0.6	58.3
4.1	25	460	6	100	133	91.5	1.5	14.33
5	25	460	4	130	96.3	61.0	1.6	49.07
7.5	35	460	8.5	70	104.4	138.6	0.8	44.32
7	30	460	6	50	122.4	94.5	1.3	36.63
7	30	510	7.5	60	101.3	118.1	0.9	103.36
8.9	30	460	8	22	109.0	126.0	0.9	76.9
4	30	460	8	22	173.7	126.0	1.4	32.1

Table 6.4 *Tested versus Theoretical Mobilized Shear for (RDD-PG) Tiebacks*

L_g (m)	β (dgr)	D_g (mm)	z_m (m)	Average SPT	Test τ_{mob} (kPa)	Theory τ_{mob} (kPa)	Ratio	Anchor-soil displ $\delta_e + \delta_p$ (mm)
3.7	15	140	3	17	205.2	43.4	4.7	57.54
8.5	25	150	8	60	442.1	122.0	3.6	54.19
8	25	200	8.5	100	238.1	129.6	1.8	16.72
8	20	200	12	100	260.6	177.8	1.5	36.79
11	25	200	5.5	100	228.4	83.9	2.7	18.76
7.5	25	200	8	80	238.8	122.0	2.0	10.64
4.5	25	150	6	56	176.4	91.5	1.9	31.39
4.5	25	150	6	56	237.7	91.5	2.6	51.48
4.5	25	150	5.5	18	237.7	83.9	2.8	31.87
4.5	25	150	5.5	25	176.2	83.9	2.1	54.28
4.5	25	150	5.5	25	207.0	83.9	2.5	50.34

For evaluation purposes, ***Table 6.3*** and ***Table 6.4*** compare the mobilized shear stress at failure[2] with the theoretical shear stress at failure estimated using Equation *[6.2]* in ***Section 6.2.1.3***, in conjunction with Poisson's ratio $v = 0.3$ for dense sands in the *GTA* and a coefficient of lateral earth pressure at rest of $K_0' = 0.50$. Theoretical mobilized shear strength is presented in the seventh column of ***Table 6.3*** and ***Table 6.4***. On examination of ***Table 6.3***, the ratio of measured to theoretical shear stress at failure (see the eighth column) varies from 0.6 to 1.7. For the CFA anchors, however, the typical value is around 1.0 ± 0.3. As observed in ***Figure 6.12***, however the shear stress mobilized at failure does not clearly increase with the depth of the anchor. Consequently, the agreement between measured and calculated P_{ult} is considered to be coincidental and that other factors overshadow the influence of anchor depth on the shear stress mobilized over the bonded length of the tieback anchors.

From ***Table 6.4***, it can be seen that for the *RDD-PG* anchors, there is poor agreement between the shear stress mobilized at failure during pullout and the theoretical shear stress estimated using Equation *[6.2]*. Equation *[6.2]* leads to underestimation of the pullout capacity and available shear strength on the bonded length of *RDD-PG* anchors by a factor of about 1/3. The ratio of measured to theoretical shear strength varies from 1.5 to 4.7 and most of the results are around 2.35 ± 0.4. This shows that the post grouting has a significant impact on the mobilized shear strength of a tieback.

Again, the field data does not exhibit a clear trend of increasing mobilized shear stress versus depth to the midpoint of anchor-bonded length. This suggests that the

---

[2] Note: $\tau_{mob} = P_{ult} / \pi D_g L_g$

anchor capacity is governed by mechanisms other than those accounted for in Equation *[6.2]* using classical soil mechanics.

From ***Table 6.1, Table 6.3*** and ***Table 6.4*** (from the last column), it can be seen that the plastic displacement of the soil at the end of the performance tests has almost the same value as the summation of soil elastic displacement with plastic displacement minus the elastic deformation of strands under pullout loads. This shows that the soil elastic deformation has low value and ranges up to 20% of the inelastic displacement of the anchor. In ***Figure 6.13***, the mobilized shear stress is plotted versus elastic and plastic soil displacement of anchors along the bonded length ($\delta_e+\delta_p$). The figure shows that the anchor capacity of *RDD-PG* anchors is higher than the anchor capacity of *CFA* anchors.

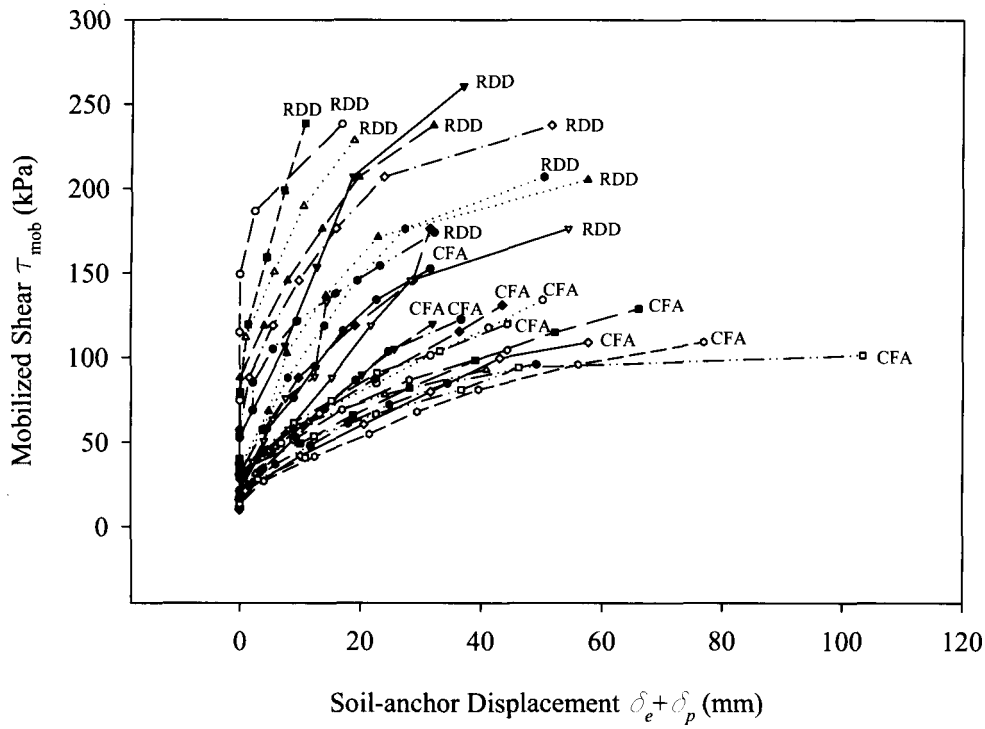

Figure 6.13 *Mobilized Shear versus Soil-anchor Displacement for Failed Anchors*

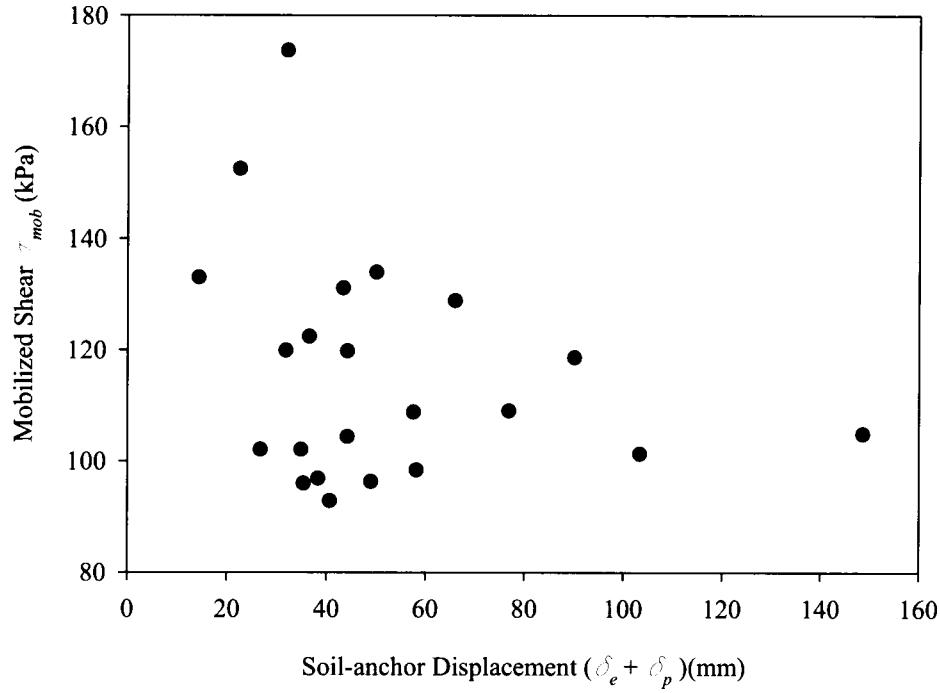

Figure 6.14 *Mobilized Shear vs. Soil-anchor Displacement for CFA Failed Anchors*

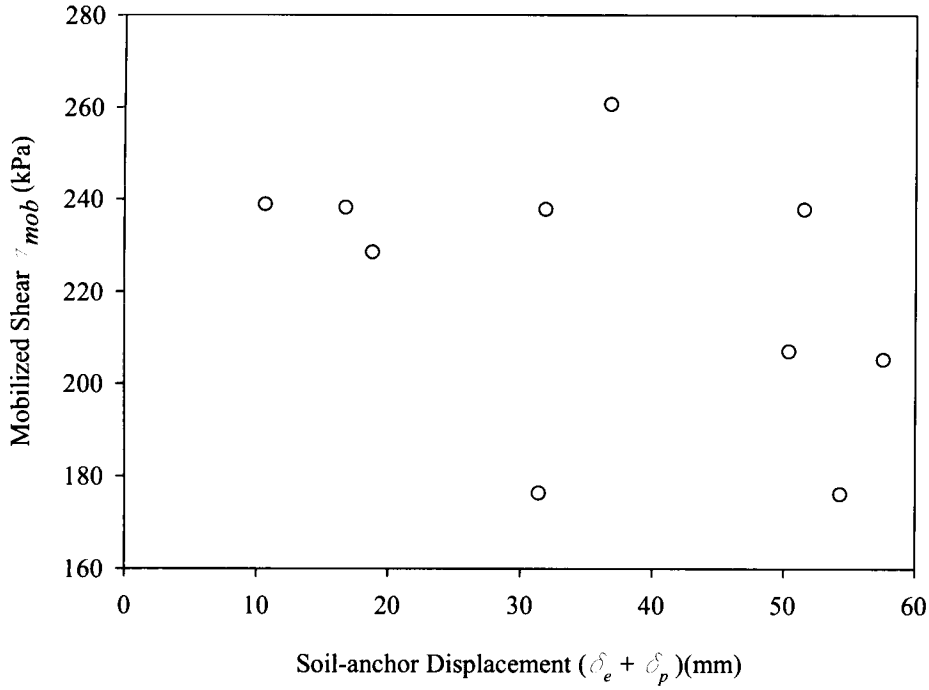

Figure 6.15 *Mobilized Shear vs. Soil-anchor Displacement for RDD-PG Failed Anchors*

Figure 6.14 and ***Figure 6.15*** show the plot of mobilized shear stress versus plastic and elastic soil-anchor displacement. As it can be seen, there is no influence of plastic and elastic soil-anchor displacement on the anchor mobilized shear and consequently on the capacity of anchor. The results are comparable with the ones presented in ***Figure 6.11***.

6.4 Finite Element Analysis

Figure 6.16 summarizes load-displacement curves calculated using PLAXIS assuming $\psi_0 = 0°$, $\psi_0 = 10°$, $\psi_0 = 20°$, and using the material parameters in ***Table 6.2***. It is noted that the dilation angle, ψ, varies from ψ_0 to 0° according to ***Figure 6.7***. From ***Figure 6.16*** it can be seen that the dilation, ψ, along the anchor-to-soil interface has a major impact on the anchor capacity and the load-displacement response. ***Figure 6.13*** shows the load-displacement curves for *CFA* and *RDD-PG* anchors. Comparing ***Figure 6.13*** and ***Figure 6.16***, the response of *RDD-PG* anchors is similar to the *FE* results for high dilation along the anchor-soil interface whereas the *CFA* anchor is similar to *FE* results for low dilation. From this analogy, it can be seen that the behaviour of anchors is strongly influenced by the dilation angle. As the initial dilation angle, ψ_0, is higher than zero, the curve has a post-yield stiffness. Thus, it is hypothesized that *RDD-PG* appears to preserve the dilatant characteristics of the anchor-to-soil interface whereas *CFA* destroys or degrades the dilatant behaviour. This is due probably to the drilling process and could make the subject of future research.

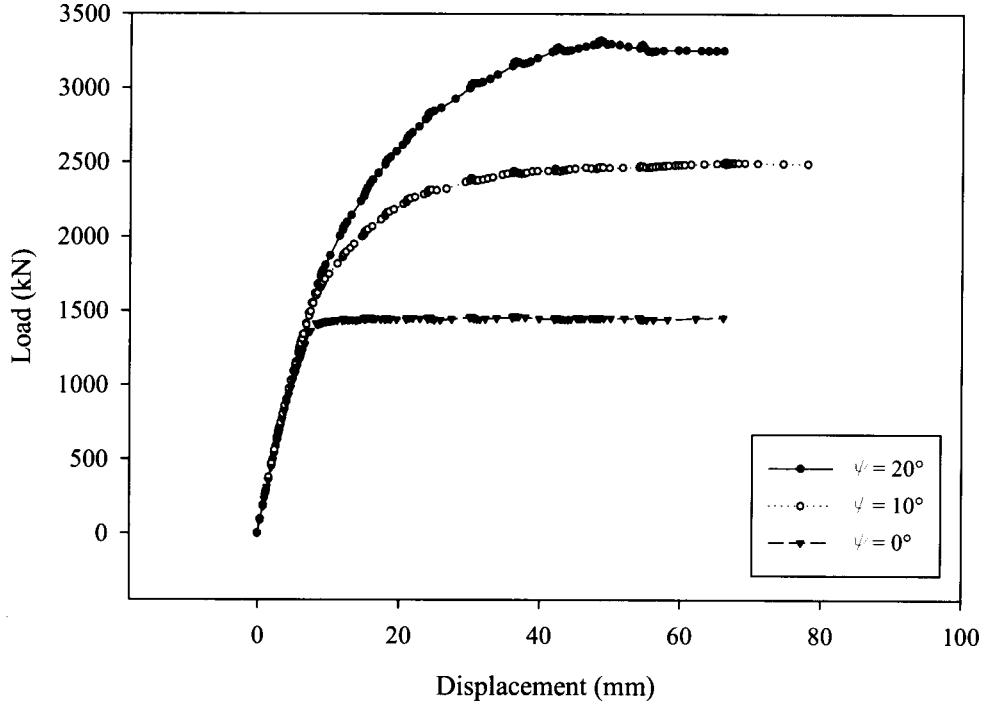

Figure 6.16 *FE Results for Various Dilation Angles (0°, 10° and 20°)*

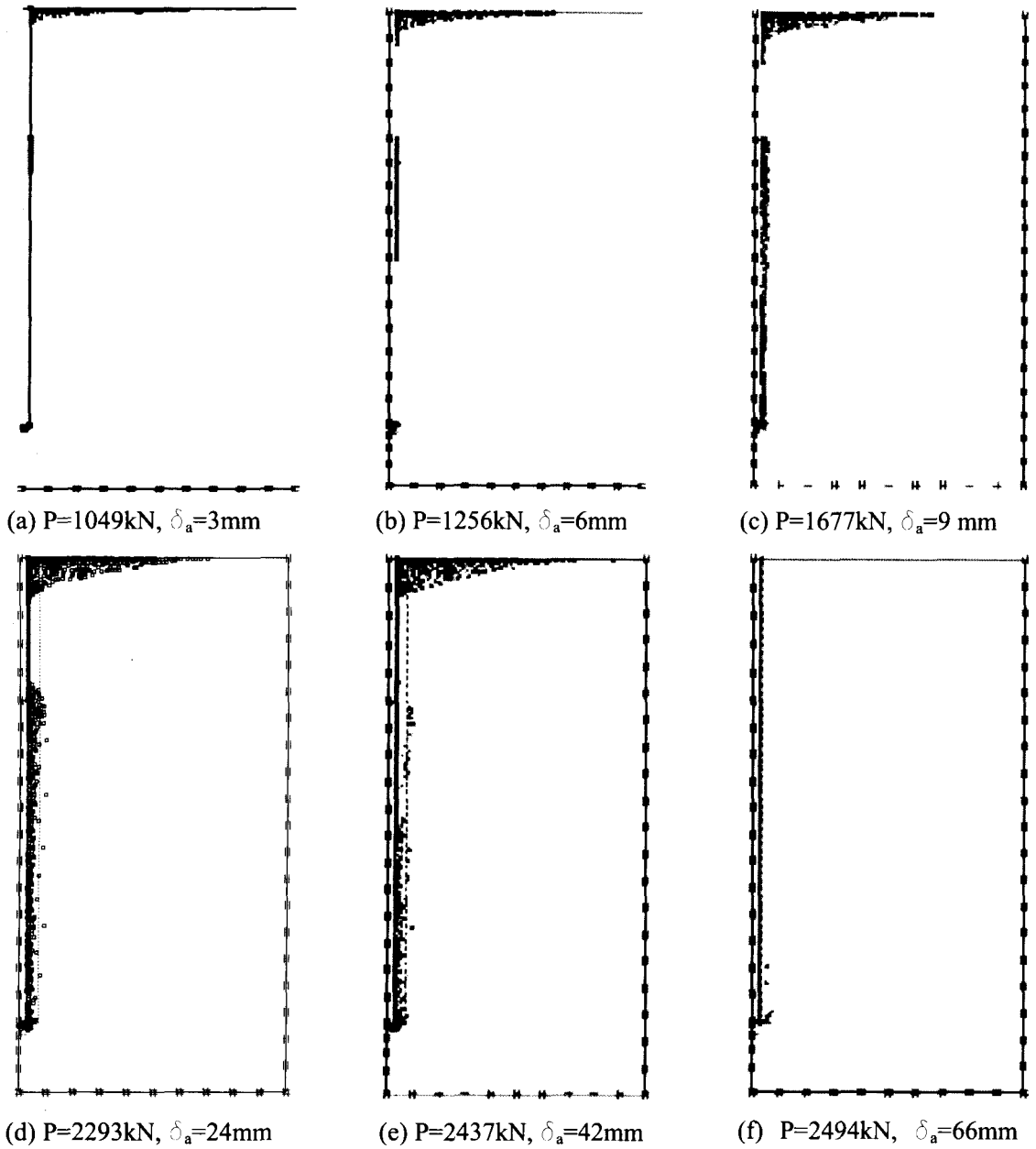

(a) P=1049kN, δ_a=3mm (b) P=1256kN, δ_a=6mm (c) P=1677kN, δ_a=9 mm

(d) P=2293kN, δ_a=24mm (e) P=2437kN, δ_a=42mm (f) P=2494kN, δ_a=66mm

Figure 6.17 *Plastic Point Formations along the Bonded Length*

Figure 6.17 shows the plastic point formation along the bonded length of the anchor considered in the *FE* analysis according to the situation considered in ***Figure 6.18***. ***Figure 6.18*** shows the load-displacement curve with the position of cases considered in *FE* analysis to show the plastic point formation as follows: around 3 mm displacement,

some plastic points start to form along the bonded length of the anchor. In case (c), at about 9mm anchor displacement, the plastic points are present along the bonded length and in case (d) the plastic point reaches its maximum plastic radius, r_p. As the test continues, the dilation angle decreases and also the plastic radius decreases. Case (f) corresponds to the critical state of soil where there is soil failure and no plastic radius.

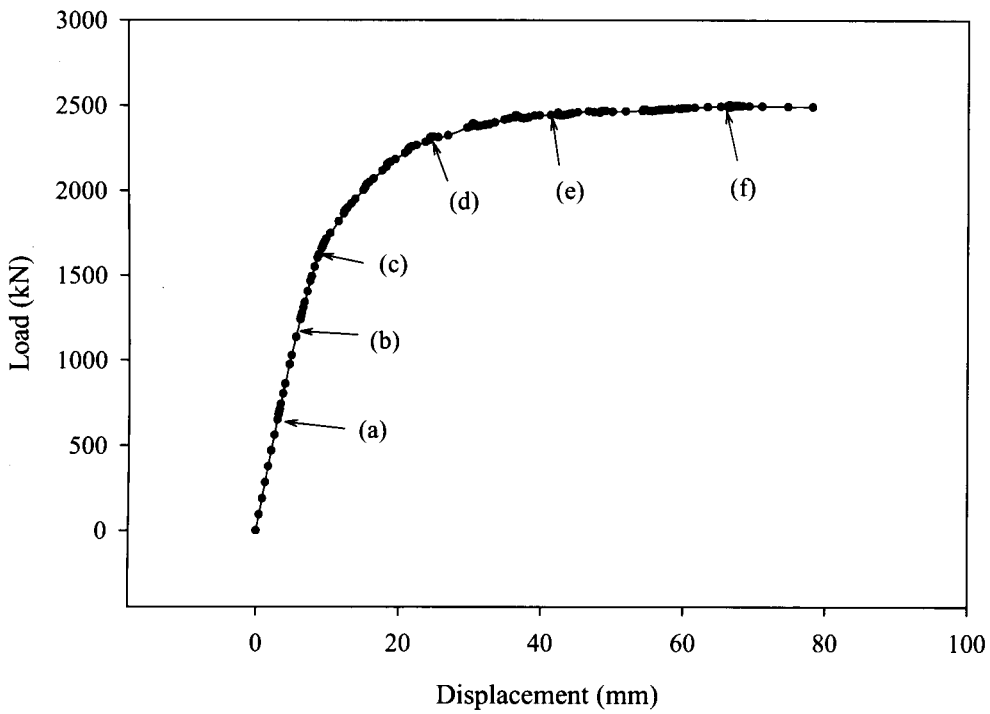

Figure 6.18 *Load-displacement FE Analysis with Formation of Plastic Points*

6.5 Summary and Conclusions

This chapter examined the pullout response of seventy-eight tieback anchors installed in cohesionless soils in the *GTA*. The effect of drilling method, grouting pressure, inelastic movement at failure, and average *SPT N-values* on the mobilized shear resistance along the anchor bonded length have been investigated.

From the discussion and evaluation presented above, some conclusions can be drawn:

(i) The pullout capacity of grouted tieback anchors is strongly influenced by the method used to install the anchors. The pullout loads at failure for anchors installed using Rotary Duplex Drilling in conjunction with post-grouting were 2 times higher than anchors installed using continuous flight augers and no post-grouting.

(ii) The mobilized shear stress at failure on the bonded length of the anchors is not related to the *SPT N-values* or blow count number. This suggests that the ultimate pullout capacity is independent of the soil density prior to drilling.

(iii) The mobilized shear strength for tiebacks in cohesionless soils in the *GTA* varied from 92.8kPa to 173.7kPa for *CFA* and from 173.6kPa to 252kPa for *RDD-PG* anchors.

(iv) The mobilized shear strength of the tieback anchor is independent of the overburden stress for the limited range of depths considered.

(v) The load-displacement response of *RDD-PG* anchors is comparable to *FE* calculations performed assuming strong dilation on the anchor-soil interface. Similarly, the response of *CFA* anchors was comparable to *FE* calculations performed assuming low dilation on the anchor-soil interface. As a result, it is hypothesized that *RDD-PG* preserves the dilatant behaviour of the soil-anchor interface whereas *CFA* appears to destroy the dilatant behaviour leading to lower anchor capacity.

Chapter 7

Summary, Conclusions and Recommendations for Further Research

7.1 Summary and Conclusions

Micropiles and tiebacks are structural elements that have been used for many years, but recently they are being used more for consolidation or soil reinforcement and as a tool for retaining the vertical walls, respectively.

This thesis examines the mechanical behaviour of micropiles constructed in the lab in addition to numerical analysis with the following objectives:

i) To evaluate current methods for estimating the ultimate compressive axial capacity of micropiles in cohesionless soils and compare the ultimate capacity estimated using design equations with the measured ultimate capacity.

ii) To assess the influence of grout pressure and micropile roughness upon its capacity.

iii) To investigate the distribution of radial stresses during grouting and micropile loading.

iv) To find out whether dilation on micropile interface has an impact on the ultimate capacity of micropiles in axial compression.

This study also examines tieback performance tests when they are subjected to pullout loads and uses a finite element (FE) analysis with the following objectives:

i) To investigate the influence of standard penetration test (SPT) N-values, overburden pressure and construction methods on the mobilized shear strength of tiebacks in Greater Toronto Area (GTA) in cohesionless soils.

ii) To compare the finite element analysis results of tiebacks with the measured ones.

iii) To assess the influence of dilatancy angle on the anchor capacity.

In ***Chapter 4***, an experimental setup was developed and the design and testing procedures were described. The experimental results were used to study the behaviour of grouted micropiles when subjected to vertical loads. It was found that the design equations presented in the Federal Highway Administration *(FHWA 1997)* Manual do not agree well with the measured capacity of the micropiles constructed in this study. There is up to 75% variation between calculated and measured ultimate loads for P_{ult} calculated using equations presented in ***Chapter 4.*** Occasionally, the calculated P_{ult} was 50% lower than the measured $P_{ult,}$ which is also undesirable.

The diffrence is significant for the controlled conditions of the research micropiles reported in this study, suggesting that the *FHWA* design equations do not account for all aspects of the mechanical response of micropiles.

Micropiles were built using grout pressures of 100kPa and 175kPa. Factors such as grout pressure and micropile roughness were studied to assess if the micropile capacity was influenced by these parameters. It was found that the grout pressure has a minor influence on micropile capacity. In addition, micropile roughness has a negligible influence on the ultimate capacity of the tested micropiles and it is not affected by grout pressure.

Due to the discrepancy between calculated and measured axial capacity observed in ***Chapter 4, Chapter 5*** describes the results of six instrumented micropile load tests on 6-cm OD micropiles constructed in sand with earth pressure cells embedded in the sand around each micropile to measure the radial stress field during grouting and loading of micropiles. It is noticed that during loading, the radial stresses increase around micropiles constructed in sand and vary with distance related to micropile, values being very large close to micropile and decreasing with distance. This behaviour follows cavity expansion theory. Using cavity expansion theory, accurate predictions of micropile capacity could be obtained if the dilation on the micropile-soil interface could be estimated in addition to the resultant radial stress field around the micropile. In addition, the micropiles were modeled using the finite element (*FE*) program PLAXIS to interpret the load-test results.

The experimental results from the 6 piles with pressure cells embedded around them show that the coefficient of lateral earth pressure at rest, K_o', varies between 0.35 and 0.49 after filling the calibration chamber, which is consistent with elasticity theory $K_o' = \nu/(1-\nu)$. During loading, the measured radial stresses at a point 7cm from the pile-soil interface (P3) increased from an initial value of about 14.2-20.8kPa prior to loading to 65-100kPa at the ultimate load. This increase can be attributed to dilation on the pile-soil interface.

Finally, the FE analysis in ***Chapter 5*** showed that the ultimate capacity of the 6-cm OD micropiles is strongly influenced by the dilation that occurs in the soil adjacent to the pile-soil interface. Based on the FE analysis, the ultimate load increased from 9.5kN corresponding to no dilation on the pile-soil interface to 28.9kN corresponding to soil dilation angle, ψ_s of 6°, elastic modulus of E=35kN and internal friction angle of ϕ=44°.

In the next stage of this research, in ***Chapter 6***, seventy-eight performance tests performed on grouted tieback anchors in the Greater Toronto Area (*GTA*) were used to predict the influence of soil properties and construction methods on the pullout capacity of tieback anchors in sandy soils and to see if there is evidence of similar mechanical response of grouted tieback anchors compared to grouted micropiles. In addition to this, a finite element (*FE*) analysis was performed using PLAXIS (version 8) to study the anchor behaviour. The anchor analysis was idealized by assuming axisymmetric conditions and considering a vertical anchor only.

The study revealed that the pullout loads at failure for anchors installed using Rotary Duplex Drilling in conjunction with post-grouting were 2 times higher than anchors installed without post-grouting and using continuous flight augers. The mobilized shear strength on the bonded length of the anchors is not related to the *SPT N-values* or blow count number. This suggests that the ultimate pullout capacity is independent of the soil density prior to drilling. The drilling process that could cause disturbance of soil influences the pullout capacity and, as a result, the dilation is destroyed and pullout capacity lowered. Also, the mobilized shear strength of the tieback anchor is independent of the overburden stress.

Prescribing displacements at the anchor head and allowing PLAXIS to interactively solve for the reaction, the load-displacement response of *RDD-PG* anchors is comparable to *FE* calculations performed assuming strong dilation on the anchor-soil interface. It is also concluded that dilation has an important impact on pullout capacity of tieback anchors.

From ***Chapter 5*** and ***Chapter 6*** it is concluded that there is similar mechanical response of grouted micropiles compared to grouted tieback anchors where dilation plays a major role in micropiles and tieback anchors capacities.

7.2 Recommendations for Further Research

With the understanding obtained from this research, the following recommendations for further research may be made:

i) The drilling has different impacts on micropile capacities. In most of the cases, the drilling loosens the soil around the borehole causing a decrease in dilation angle at the micropile-soil interface. There is considerable empiricism in the design of micropiles, with considerable variation in design parameters leading to high uncertainty. Reduction factors for every drilling technique can be studied to narrow the range of β coefficient.

ii) Dilation has a major impact on micropile and tieback capacities and finding a way to express this in pile and tieback capacity equations would improve the accuracy in calculations.

References

A Pile Buck – *Earth Support Systems and Retaining Structures.*

Abdul-Meguid, M., Rowe, R.K. and Lo, K.Y., (2002), – *3D Effect of Surface Construction over Existing Subway Tunnels*, The International Journal of Geomechanics, vol.2, No.4, pp. 447-469.

Atkinson J., (1993) - *An Introduction to the Mechanics of Soils and Foundations through Critical State Soil Mechanics*, McGraw-Hill.

Bhushan, Kul, (November 1982) - *New Design Correlations for Piles in Sands*, (Proc. Paper 16379), Journal of the Geotechnical Engineering Division, ASCE, Vol. 108, No. GT 11, Proc. Paper 17435, pp. 1508-1510.

Bolton, M.D, (1986) - *The Strength and Dilatancy of Sand*, Geotechnique 36, No.1,pp. 65-78.

Bowles, J. E., (1982) - *Foundation Analysis and Design*, McGraw-Hill Book Company, New York, NY.

Bowles, Joseph, (1988) – *Foundation Analysis and Design*, 4th Ed.

Brachman,R.W.I, Moose I.D, Lo,K.Y., (1998) – *Analysis and Performance of a Shoring System with Tie-Back Anchors*, Proc 51st Canadian Geotechnical Conference, Edmonton, Alberta, Oct. 4-7, vol. I, pp 439-446.

Bruce, D.A, DiMillio, A F. and Juran, I., (1995) – *Introduction to Micropiles: An International Perspective*, New York.

Canadian Geotechnical Society, (2006)- *Canadian Foundation Engineering Manual*, 4th Edition.

Craig, R.F., (1997) – *Soil Mechanics*, Sixth Edition.

Das, Braja M., (2004) - *Principles of Foundation Engineering*, 5th Edition.

DD EN 1997-1 Eurocode 7, (1995) - *Geotechnical Design.* Part 1: general rules.

Description of and applications for grouts used in the civil engineering field, (Dec.1996), J.G.T.

Donald Coduto, (2001) - *Foundation Design: Principles and Practices*, 2nd Ed.

Coduto, Donald, (1999) – *Geotechnical Engineering: Principles and Practices*, 2nd Ed.

Evett, J.B., Liu C., (2003)_ – *Soil Properties: Testing, Measurement and Evaluation*, 5th Ed.

Excavation and Support for the Urban Infrastructure, (1992), Geotechnical Special Publication No.33.

FHWA, (Sept. 1982) - *Permanent Ground Anchors*, Soletanche Design Criteria – U.S. Department of Transportation, FHWA.

FHWA, (1997 & 2000) – *Drilled and Grouted Micropiles*: State-of-Practice Review,Vol.1-4.

Franke, E. ,(1993) - *Design of bored piles, including negative skin friction and horizontal loading*, Proc., 2nd Int. Geotech. Seminar on Deep Foundations on Bored and Auger Piles, Van Impe, ed., Balkema, Rotterdam, The Netherlands, 43–57.

Geospec - *Model Specification for Prestressed Ground Anchors*, Geotechnical Control Office- Civil Engineering Department, Hong Kong.

Guidelines of Engineering Practice For Braced and Tied - Back Excavations, (1997) – Geotechnical Special Publication No. 74, ASCE.

Hanna, T. H., (1982) – *Foundations in tensions: Ground Anchors*, 1st Ed., New York: McGraw-Hill.

Hausmann, Manfred R., (1990) – *Engineering principles of Ground Modification*, McGraw-Hill.

Holtz, R., Kovacs, W., (1981) – *An Introduction to Geotechnical Engineering.*

Hsu, S.T. and Liao, H.J.,(1998) – *Uplift behaviour of anchors in sand*, Canadian Geotechnical Journal 34: pp. 70-80.

Karol, Reuben H., (2003) - *Chemical Grouting and Soil Stabilization*, Third Edition.

Lambe, T. William, Whitman, Robert V., (1969) – *Soil Mechanics*, MIT.

Lee, J. H. and Salgado, R., (Aug. 1999) – *Determination of pile base resistance in sands*, Journal of Geotechnical and Geoenvironmental Engineering.

Lehane, Barry M. and White, David, (Aug 2005) – *Lateral stress changes and shaft friction for model displacement piles in sand*, Canadian Geotechnical Journal, Vol 42, No. 4.

Li, X. S. and Dafalias, Y. F., (2000) - *Dilatancy for cohesionless soils*, *Geotechnique*, 50(4),pp. 449-460.

Littlejohn, G.S., (1997) - *Ground Anchorages and Anchored Structures.*

Lo, K.Y., Ogawa, T., Lukajic B. and Dupak D., (Dec. 1991) – *Measurement of Strength Parameters of Concrete-Rock Contact at the Dam-Foundation Interface*, Geotechnical Testing Journal, GTJODJ, Vol. 14, No. 4, pp 383-394.

Macnab, A., (2002) - *Earth Retention Systems Handbook*, New York, London, McGraw-Hill .

Mana and Clough, (1981) - *Behavior of Stiff Excavation Support System in Soft to Medium Clay.*

Newson, T., Hinchberger, S and Liang, Y., (2007) – *The Mechanics of Inflatable Anchors in Cohesionless Soil.*

Nonveiller, E., (1989) – *Grouting Theory and Practice*, Developments in Geotechnical Engineering, 57, Elsevier.

O'Neill, M. W. and Reese, L. C., (1999) - *Drilled Shafts: Construction Procedures and Design Methods*, ADSC: The International Association of Foundation Drilling, Publication No. ADSC-TL4, Vol. I.

O'Rourke T.D., Turner J.E, Stewart, H.E., (2005) – *Soil-Structure Interaction Under Extreme Loading Conditions*, The 13th Spencer J. Buchanan Lecture.

Ou, Chang-Yu, (2006) – *Deep Excavation: Theory and Practice*, Taipei.

Paunescu, M., Pop V., Silion T., (1982) - *Geotehnica si Fundatii.*

PLAXIS, Version 8, *Reference Manual.*

Poulos, H.G., Davis E.H., (1980) - *Pile Foundation Analysis and Design*, New York.

Prakash, S., Sharma, H., (1990) – *Pile Foundations in Engineering Practice*, Wiley .

Puller, Malcolm, (2003) - *Deep Excavations: a Practical Manual*, 2nd Edition.

Reese, L., O'Neill. M., (1988) - *Drilled Shafts*, Publication FHWA-HI-88-042 FHWA, U.S, Department of Transportation.

Rowe, R.K., Davis, E.H., 1982 – *The Behaviour of Anchor Plates in Sand*, Geotechnique, vol. 32, pp 25-41.

Salgado, R., Mitchell, J.K and Jamiolkowski, M., (Apr. 1997) – *Cavity Expansion and Penetration Resistance in Sand*, Journal of Geotechnical and Environmental Engineering, Vol. 123, No. 4.

Schnabel, Harry, (1982) – *Tieback in Foundation Engineering and Construction.*

Soletanche – *Ground Anchors - Design Manual.*

Soletanche Design Criteria, Sept. (1982) – *Permanent Ground Anchors*, U.S. Department of Transportation, FHWA.

Strom, Ralph & Ebeling, Robert M., (Dec 2002) - *Methods Used in Tieback Wall Design and Construction to Prevent Local Anchor Failure*, Progressive Anchorage Failure, and Ground Mass Stability Failure Research Program U.S. Army Corps of Engineers.

Systat, (2007) - *Sigma Plot*, Version 10.0.1, User's Manual.

Tatiya, Ratan, (2005) - *Surface and underground excavations.*

Tenter, N.A. , (2001) - *Earthworks: a guide.*

Tomlinson M.J. , (1977) - *Pile Design and Construction Practice.*

Tomlinson, M.J. , (2001) - *Foundation Design and Construction*, Seventh Edition.

Xanthakos, Petros, (1991) - *Ground Anchors and Anchored Structures*, New York.

Xanthakos, Petros, Abramson, Lee and Bruce, Donald - *Ground Control and Improvement.*

Yu, H. S. & G.T. Houlsby, (1991) - *Finite Cavity Expansion in Dilatant Soils*, Geotechnique, pp. 173-183.

Wernick, E. (1977) - *Stresses and strains on the surface of anchors.* Proc. 9th Int. Conf. Soil Mechanics and Foundation Engineering, Tokyo, Special Session 4, Ground Anchors, pp. 113–119.

Whitaker, Thomas, (1976) - *The Design of Piled Foundations*, 2nd Edition, Pergamon.

Appendix A

Roughness Study

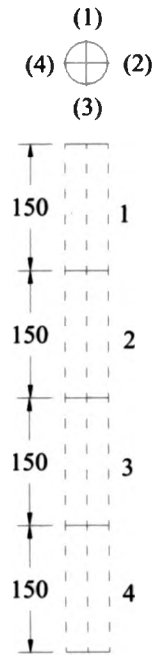

Pile No.	28	
Grout Pressure (P_g)	100	kPa
Pile Length (L_g)	92	cm
Pile Diameter (D_c)	6	cm
Ultimate Capacity (P_{ult})	50	kN

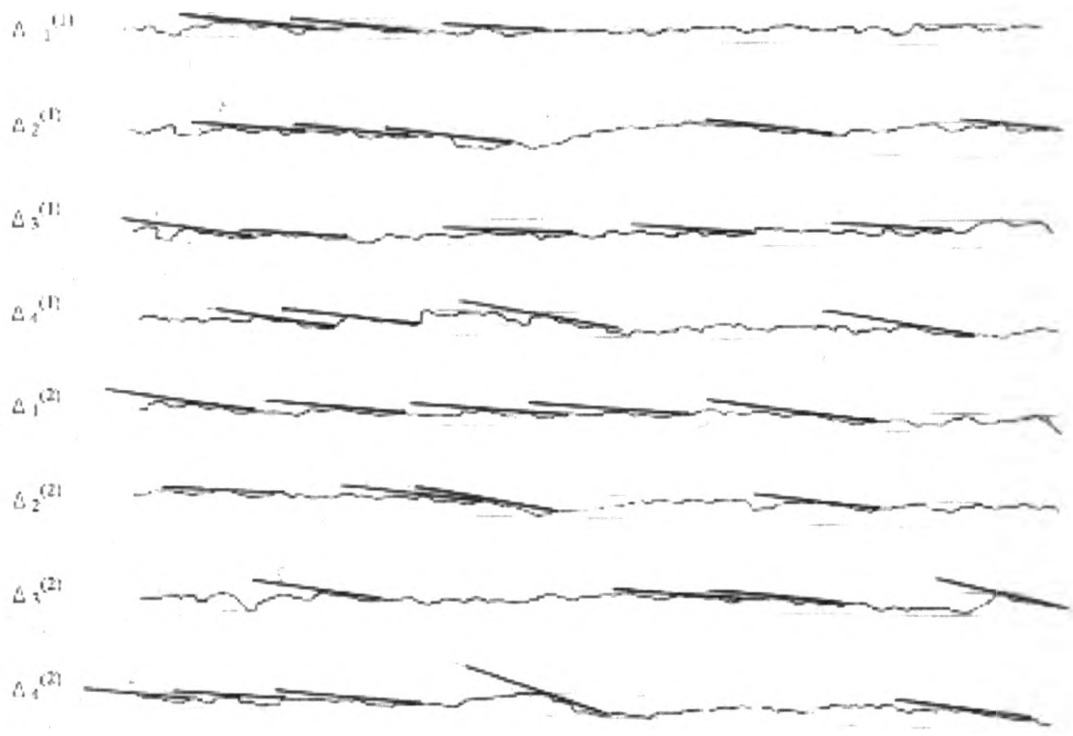

Figure A. 1 *Roughness Micropile # 28, Side 1 and 2*

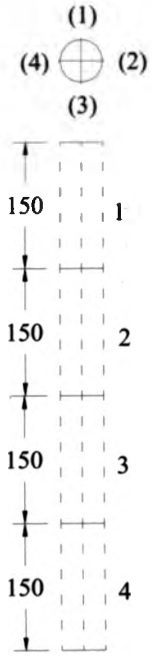

Pile No.	28	
Grout Pressure (P_g)	100	kPa
Pile Length (L_g)	92	cm
Pile Diameter (D_c)	6	cm
Ultimate Capacity (P_{ult})	50	kN

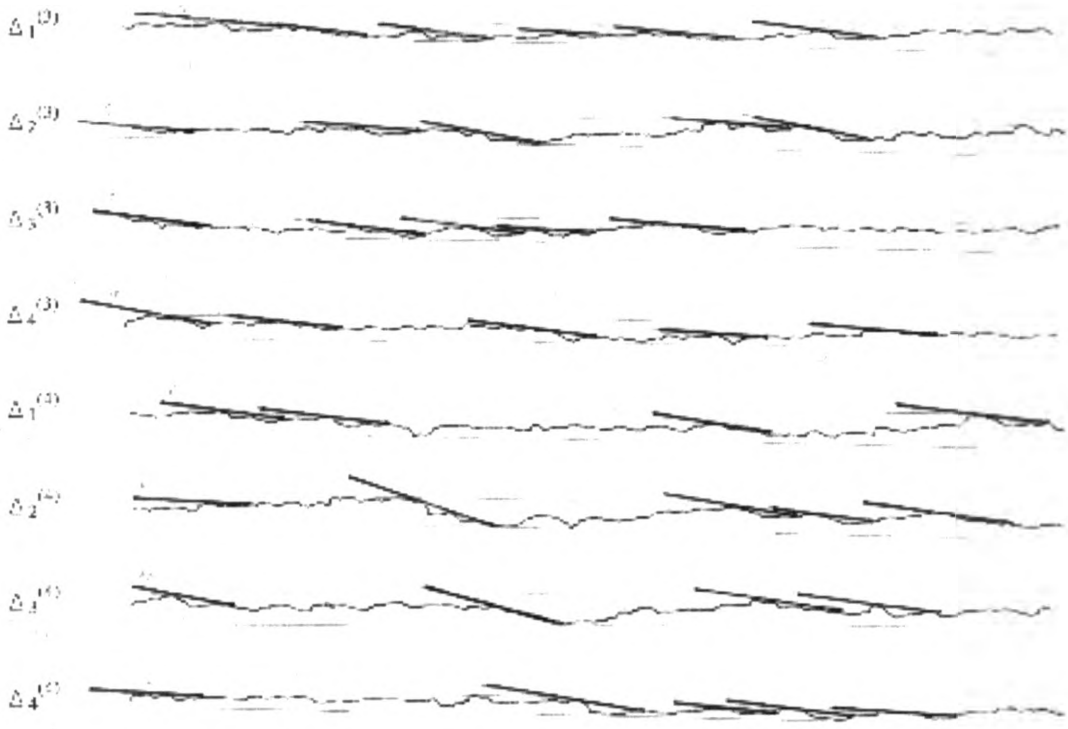

Figure A.2 *Roughness Micropile # 28, Side 3 and 4*

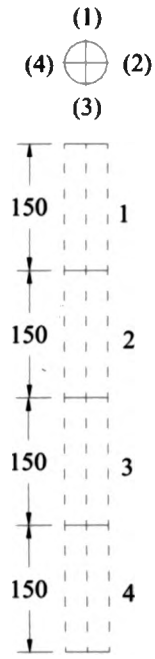

Pile No.	29	
Grout Pressure (P_g)	175	kPa
Pile Length (L_g)	92	cm
Pile Diameter (D_c)	6	cm
Ultimate Capacity (P_{ult})	54.5	kN

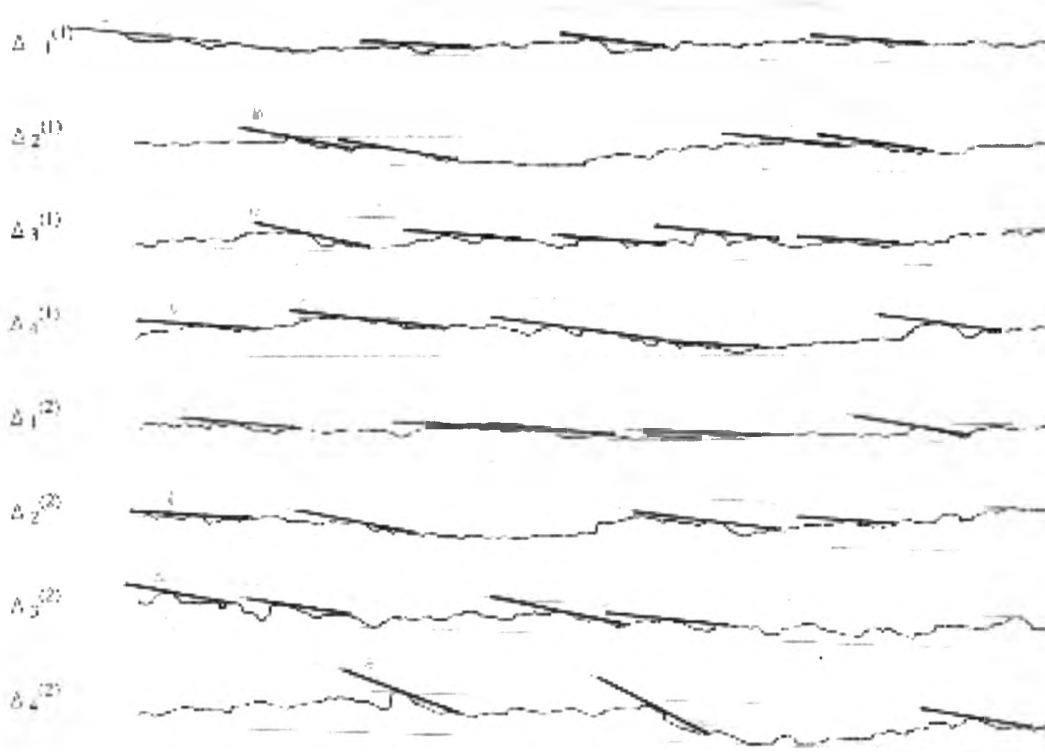

Figure A.3 *Roughness Micropile # 29, Side 1 and 2*

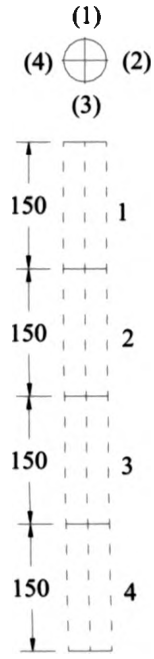

Pile No.	29	
Grout Pressure (P_g)	175	kPa
Pile Length (L_g)	92	cm
Pile Diameter (D_c)	6	cm
Ultimate Capacity (P_{ult})	54.5	kN

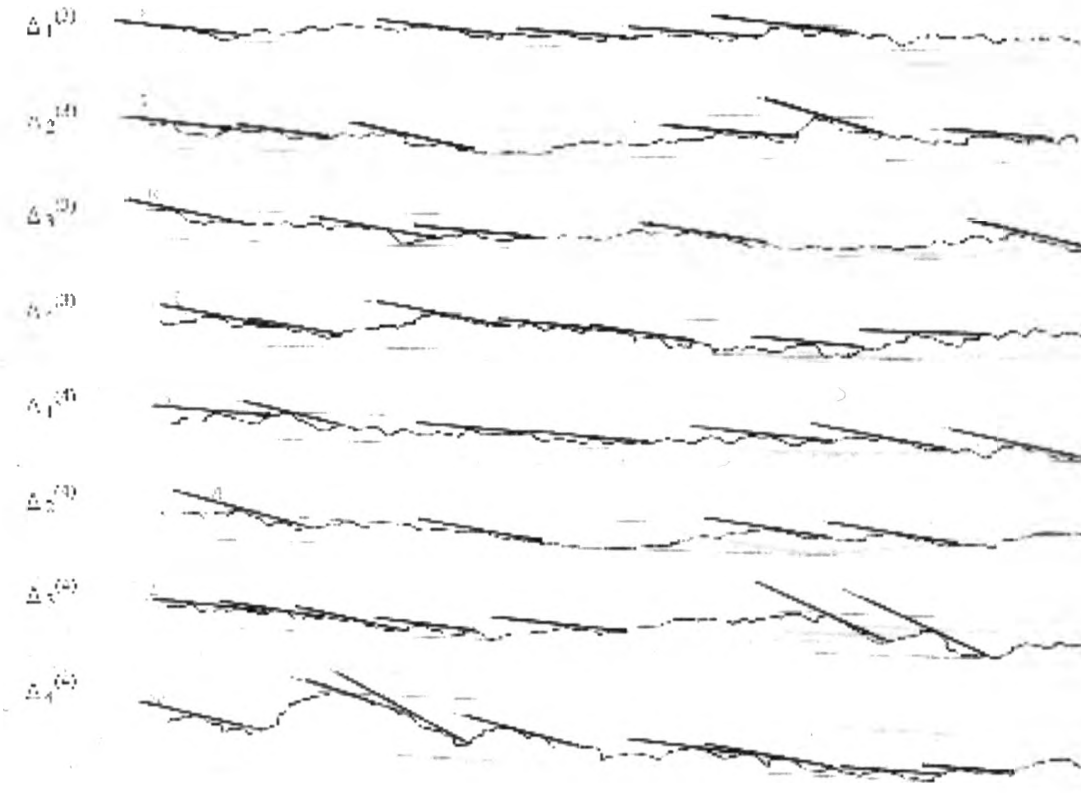

Figure A.4 *Roughness Micropile # 29, Side 3 and 4*

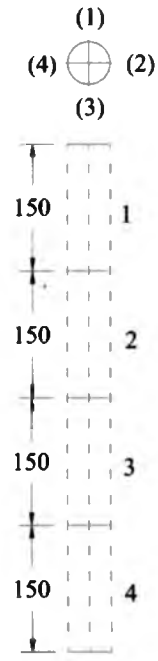

Pile No.	30	
Grout Pressure (P_g)	175	kPa
Pile Length (L_g)	90	cm
Pile Diameter (D_c)	6	cm
Ultimate Capacity (P_{ult})	57	kN

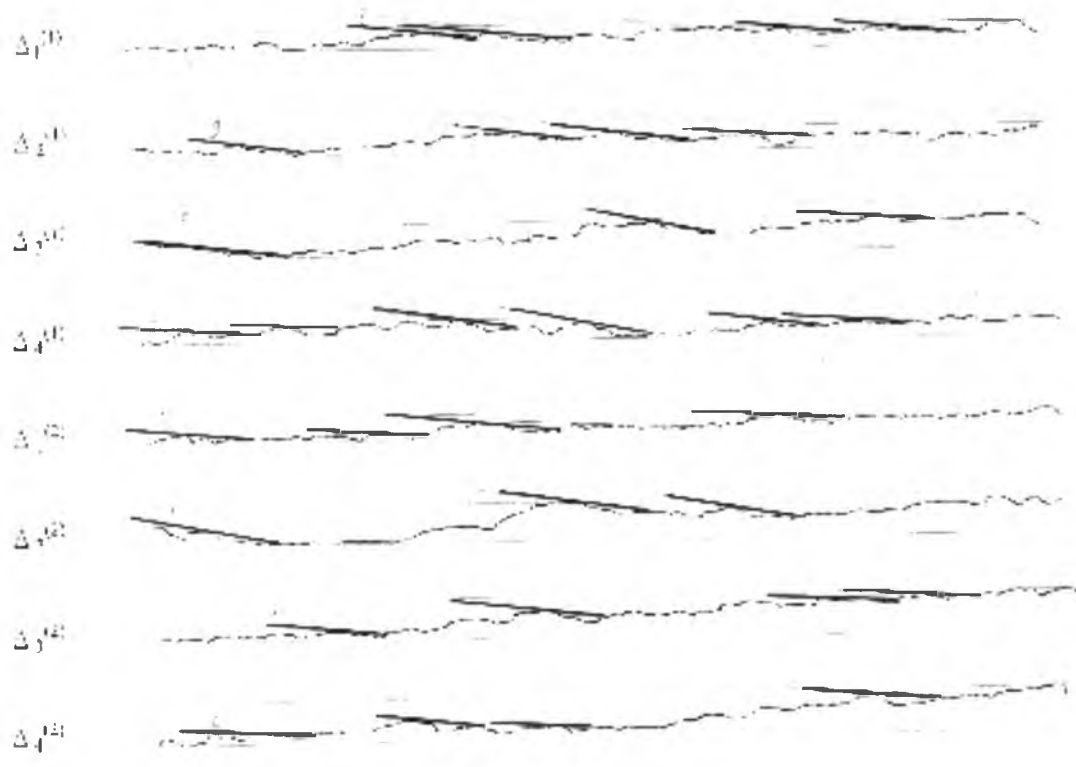

Figure A.5 *Roughness Micropile # 30, Side 1 and 2*

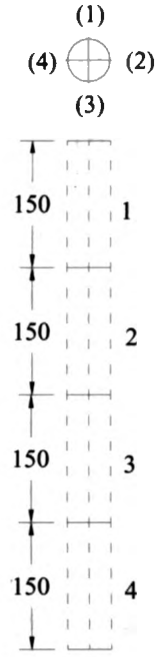

Pile No.	30	
Grout Pressure (P_g)	175	kPa
Pile Length (L_g)	90	cm
Pile Diameter (D_c)	6	cm
Ultimate Capacity (P_{ult})	57	kN

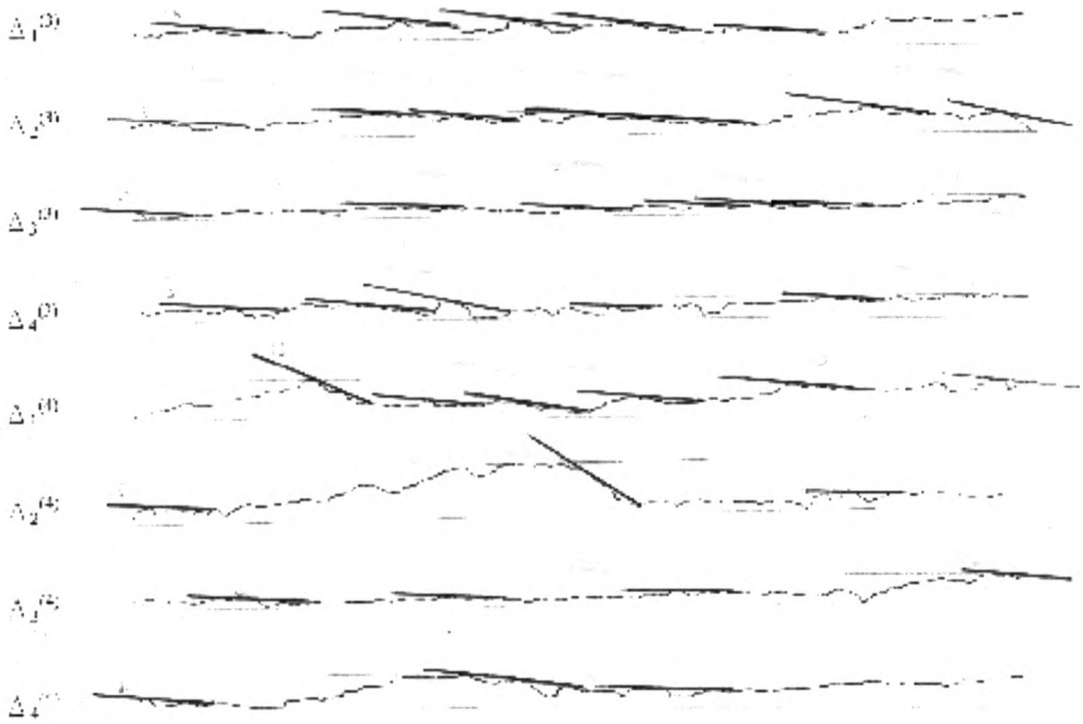

Figure A.6 *Roughness Micropile # 30, Side 3 and 4*

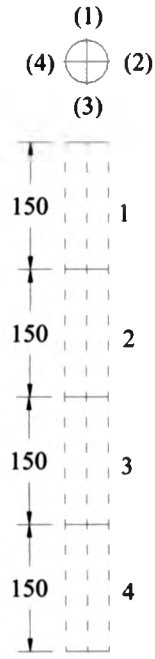

Pile No.	19	
Grout Pressure (P_g)	100	kPa
Pile Length (L_g)	91	cm
Pile Diameter (D_c)	6	cm
Ultimate Capacity (P_{ult})	27	kN

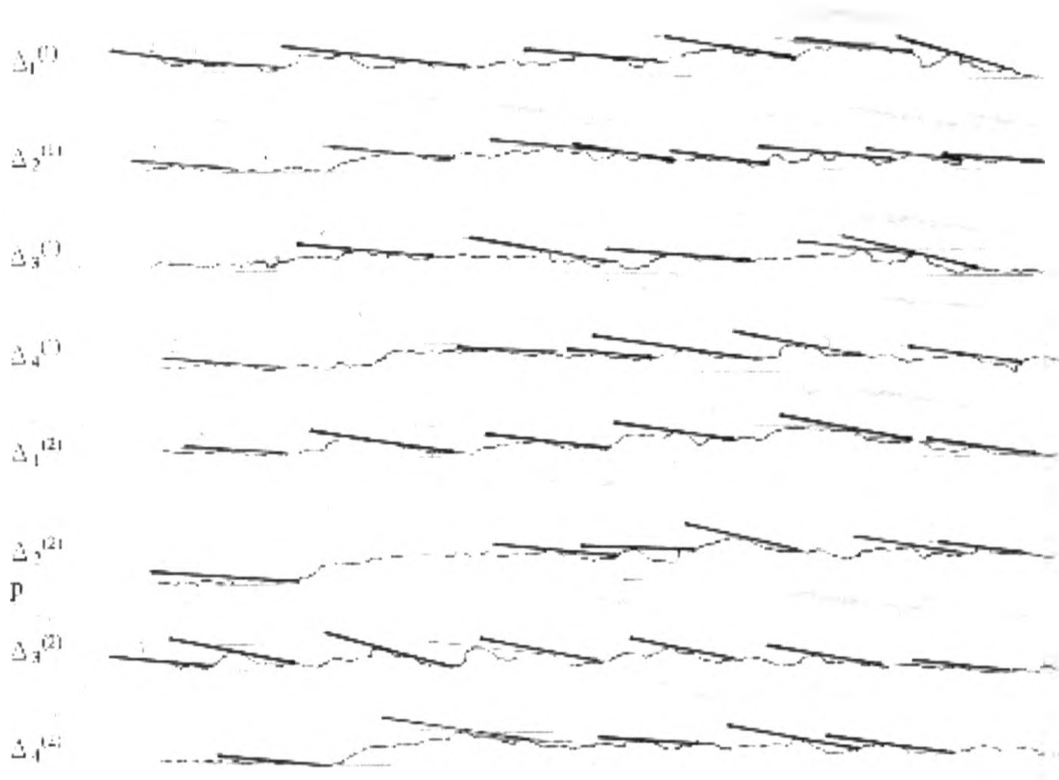

***Figure A.7** Roughness Micropile # 19, Side 1 and 2*

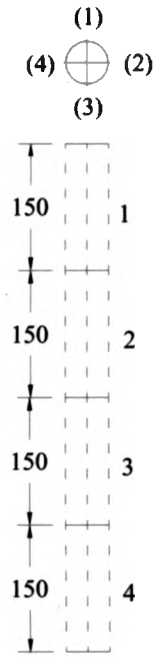

Pile No.	19	
Grout Pressure (P_g)	100	kPa
Pile Length (L_g)	91	cm
Pile Diameter (D_c)	6	cm
Ultimate Capacity (P_{ult})	27	kN

***Figure A. 8** Roughness Micropile # 19, Side 3 and 4*

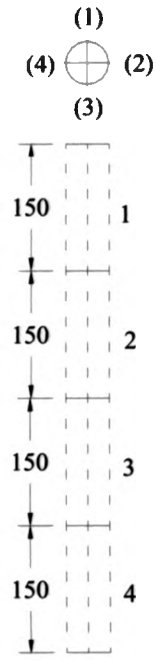

Pile No.	20	
Grout Pressure (P_g)	100	kPa
Pile Length (L_g)	86	cm
Pile Diameter (D_c)	6	cm
Ultimate Capacity (P_{ult})	28	kN

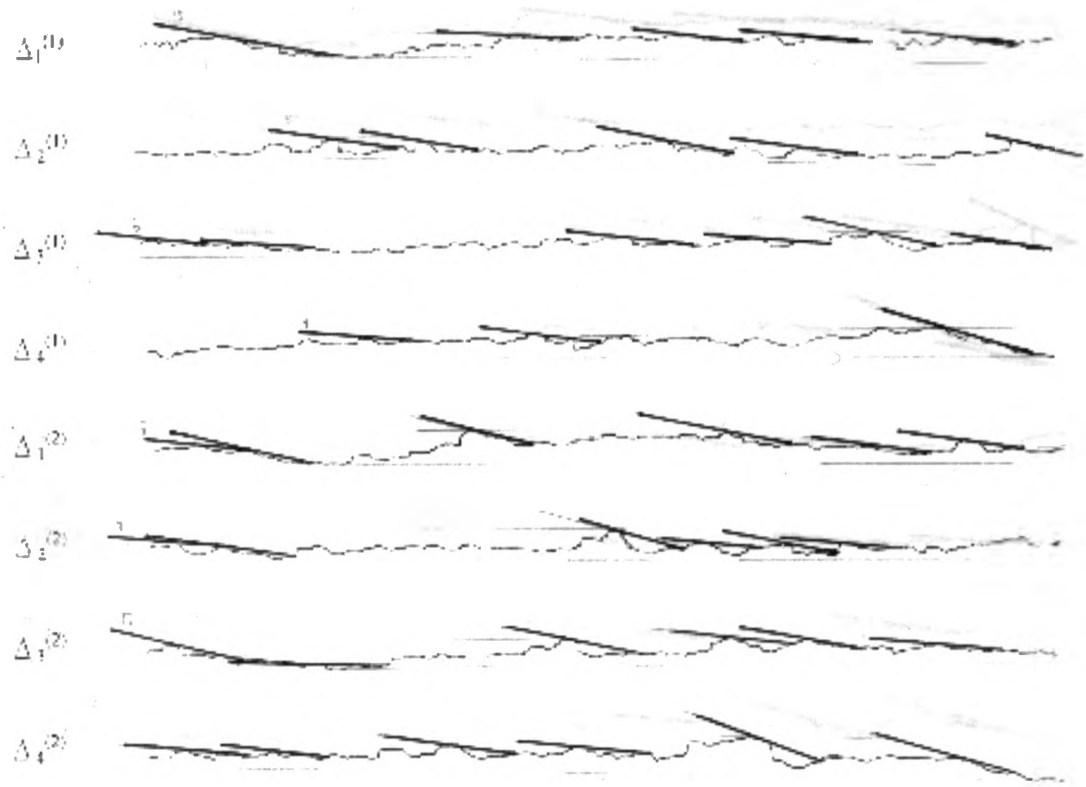

Figure A. 9 *Roughness Micropile # 20, Side 1 and 2*

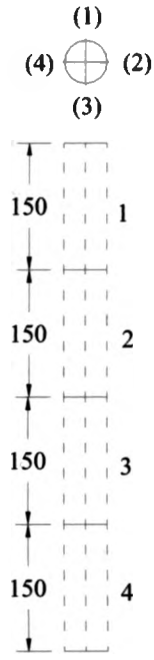

Pile No.	20	
Grout Pressure (P_g)	100	kPa
Pile Length (L_g)	86	cm
Pile Diameter (D_c)	6	cm
Ultimate Capacity (P_{ult})	28	kN

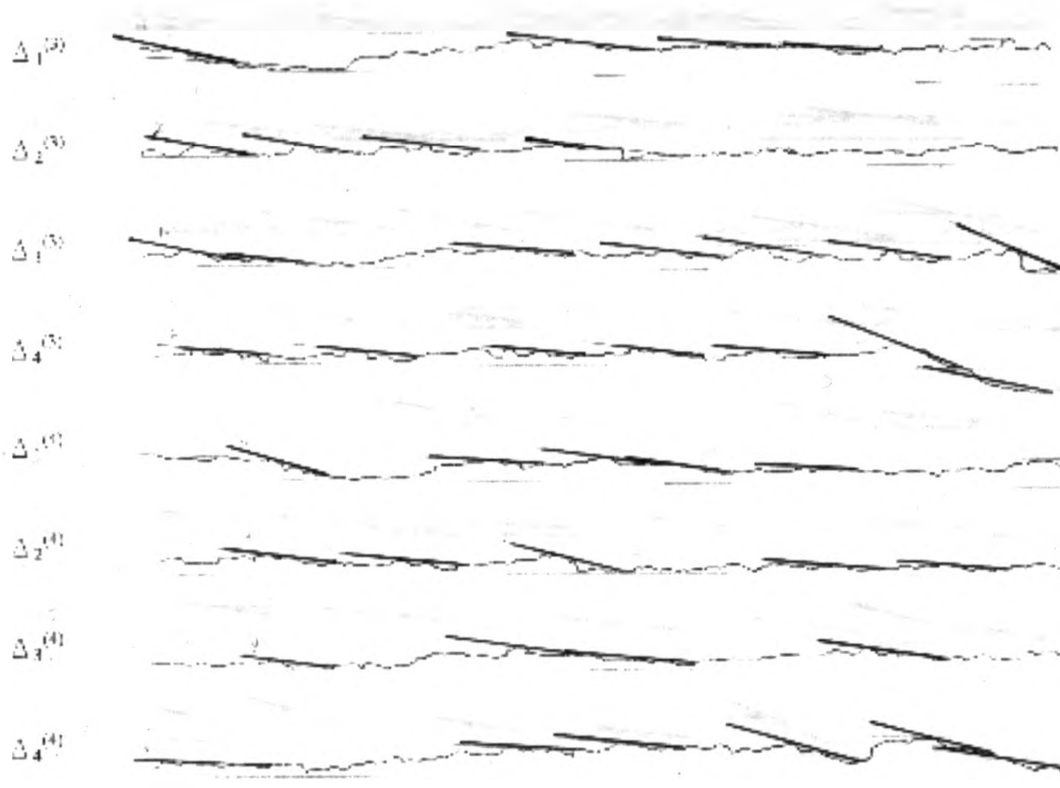

Figure A.10 *Roughness Micropile # 20, Side 3 and 4*

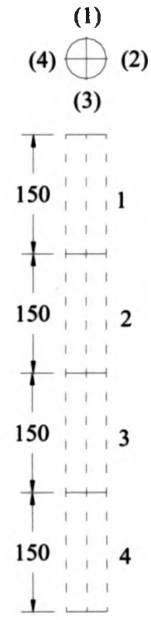

Pile No.	21	
Grout Pressure (P_g)	100	kPa
Pile Length (L_g)	91	cm
Pile Diameter (D_c)	6	cm
Ultimate Capacity (P_{ult})	34	kN

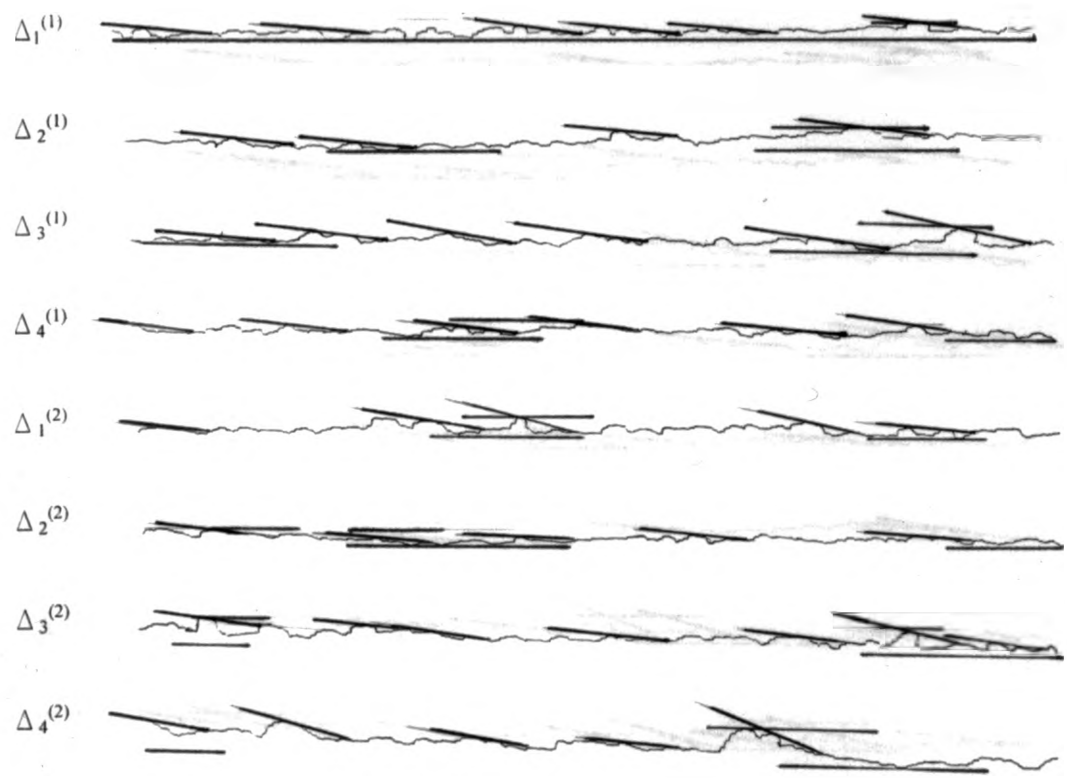

Figure A.11 *Roughness Micropile # 21, Side 1 and 2*

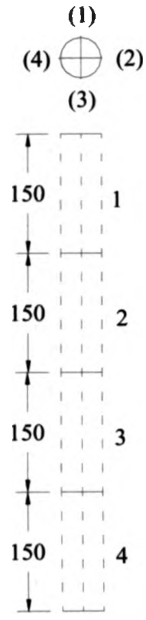

Pile No.	21	
Grout Pressure (P_g)	100	kPa
Pile Length (L_g)	91	cm
Pile Diameter (D_c)	6	cm
Ultimate Capacity (P_{ult})	34	kN

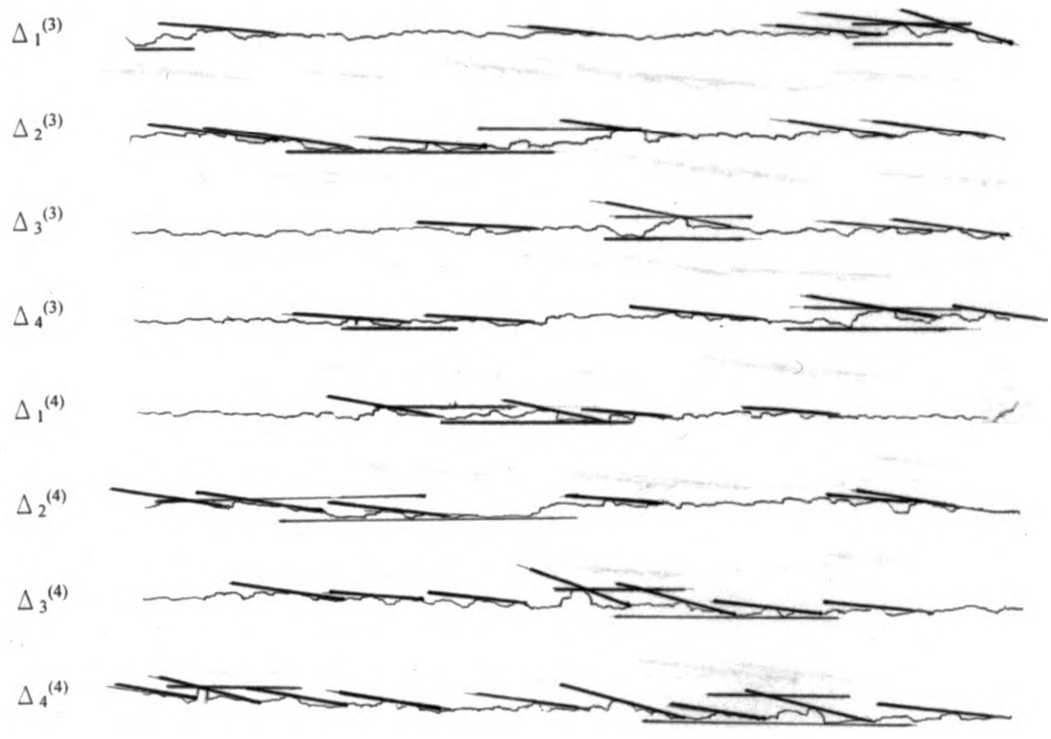

Figure A.12 *Roughness Micropile # 21, Side 3 and 4*

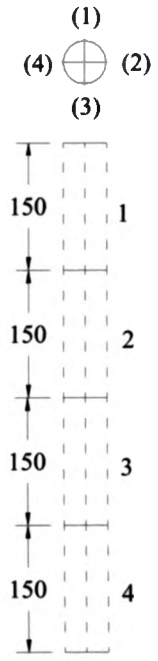

Pile No.	22	
Grout Pressure (P_g)	100	kPa
Pile Length (L_g)	92	cm
Pile Diameter (D_c)	6	cm
Ultimate Capacity (P_{ult})	42.5	kN

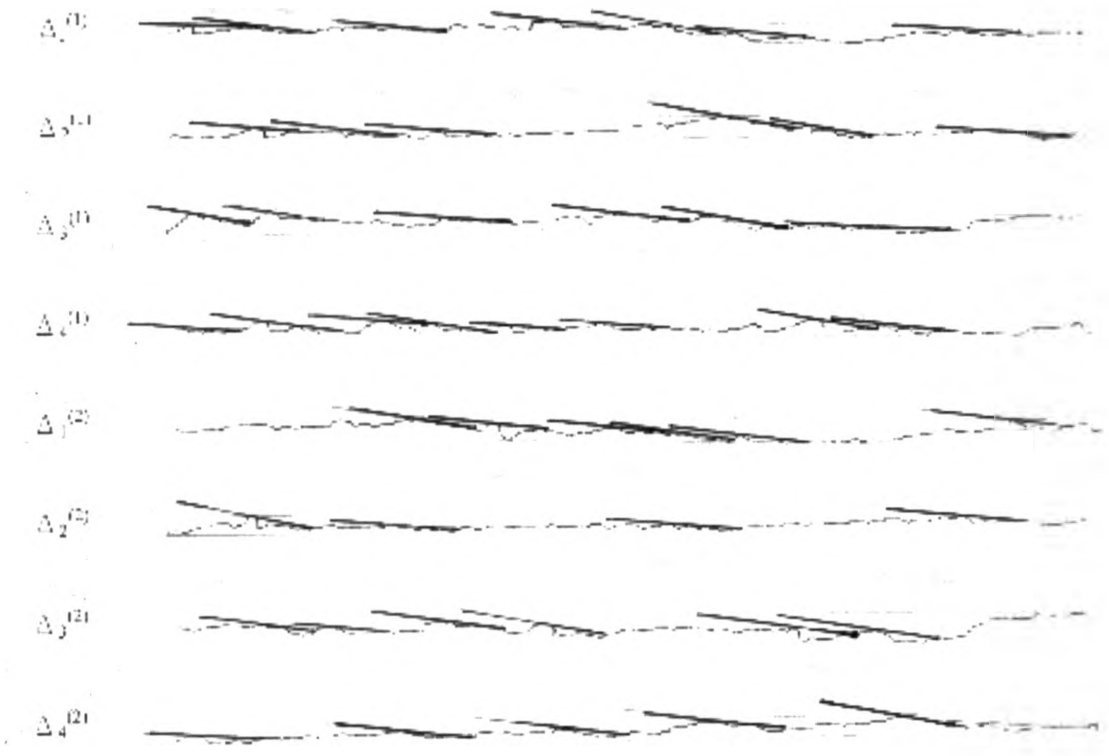

Figure A. 13 *Roughness Micropile # 22, Side 1 and 2*

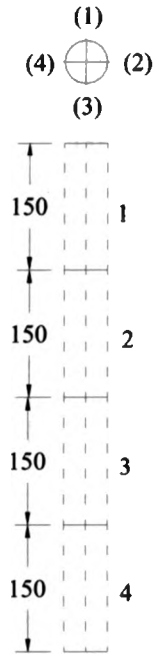

Pile No.	22	
Grout Pressure (P_g)	100	kPa
Pile Length (L_g)	92	cm
Pile Diameter (D_c)	6	cm
Ultimate Capacity (P_{ult})	42.5	kN

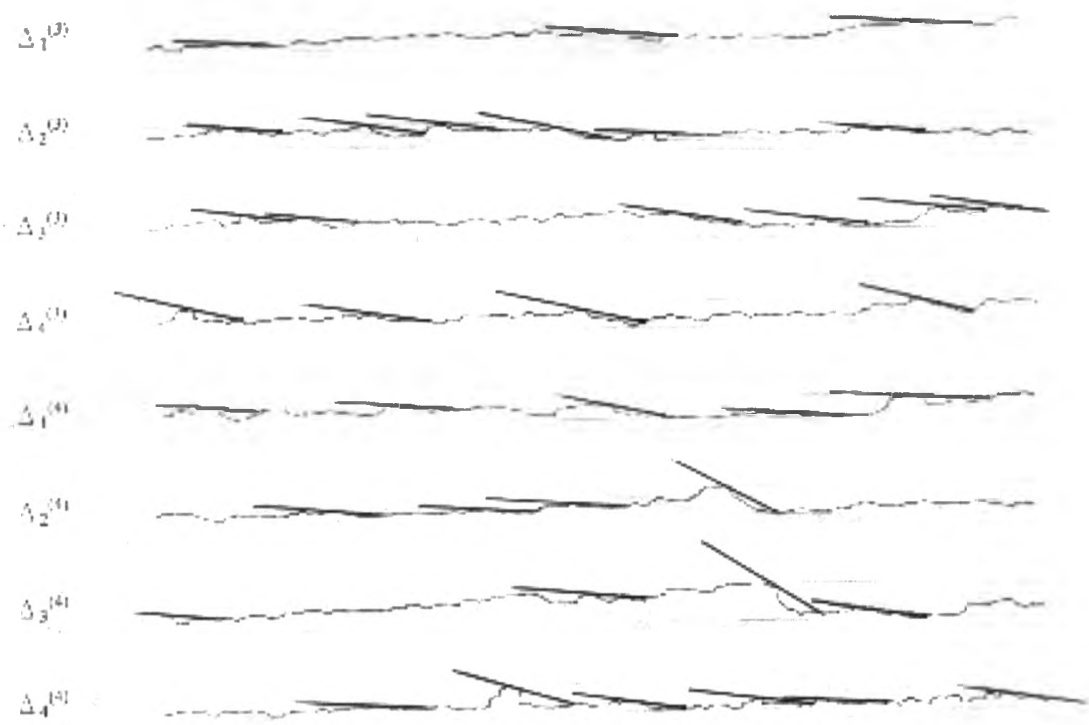

Figure A.14 *Roughness Micropile # 22, Side 3 and 4*

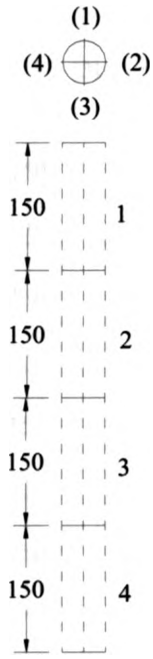

Pile No.	23	
Grout Pressure (P_g)	100	kPa
Pile Length (L_g)	89	cm
Pile Diameter (D_c)	6	cm
Ultimate Capacity (P_{ult})	29.5	kN

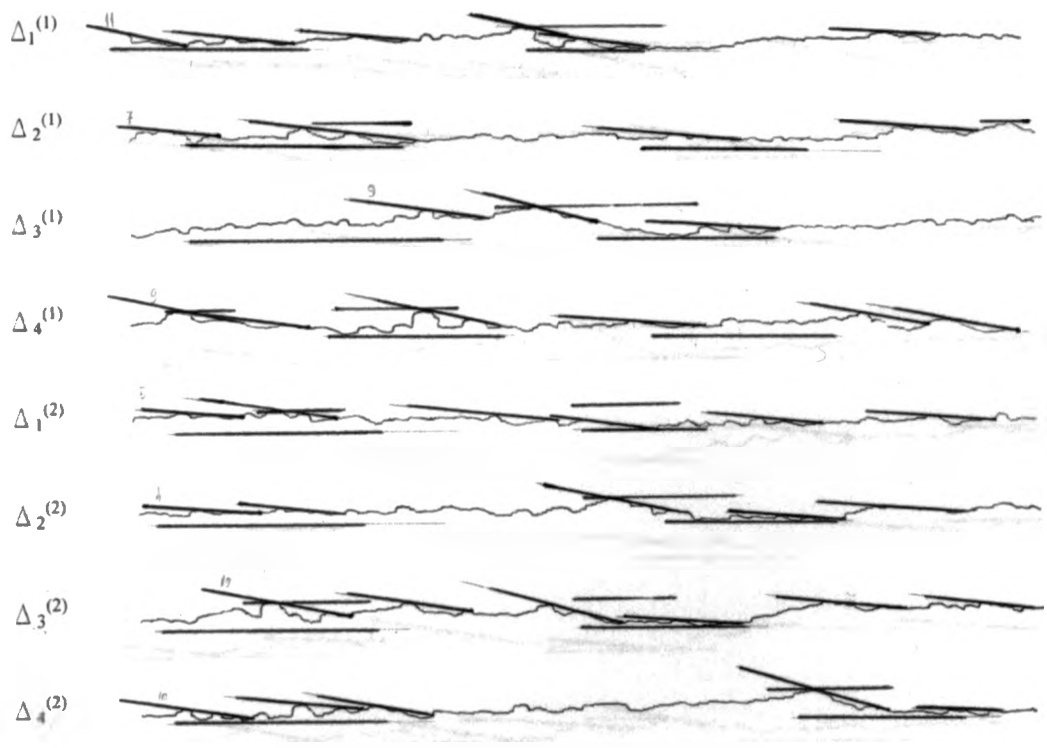

Figure A.15 *Roughness Micropile # 23, Side 1 and 2*

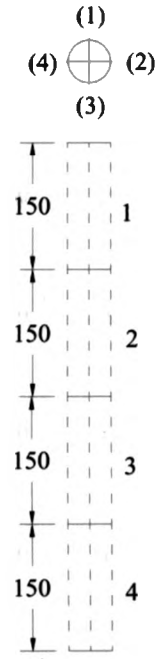

Pile No.	23	
Grout Pressure (P_g)	100	kPa
Pile Length (L_g)	89	cm
Pile Diameter (D_c)	6	cm
Ultimate Capacity (P_{ult})	29.5	kN

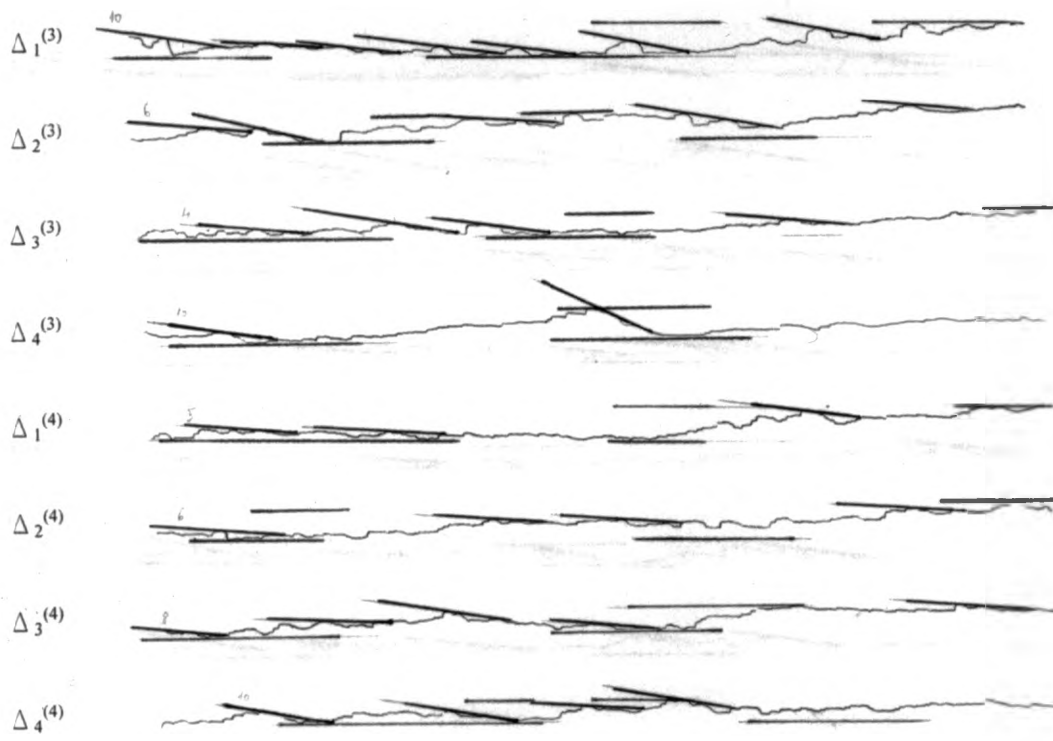

Figure A.16 *Roughness Micropile # 23, Side 3 and 4*

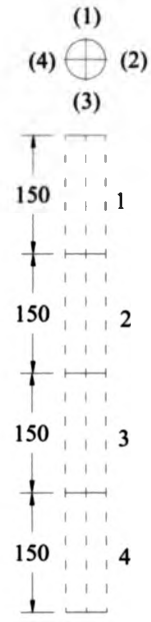

Pile No.	24	
Grout Pressure (P_g)	175	kPa
Pile Length (L_g)	93	cm
Pile Diameter (D_c)	6	cm
Ultimate Capacity (P_{ult})	31	kN

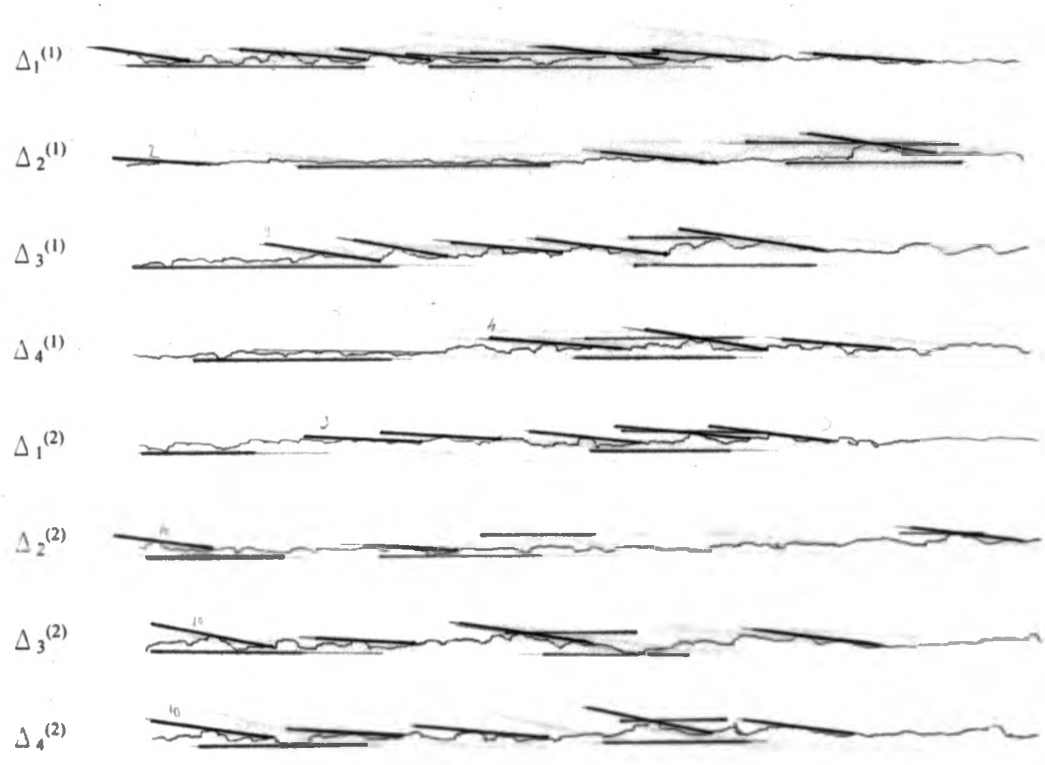

Figure A.17 *Roughness Micropile # 24, Side 1 and 2*

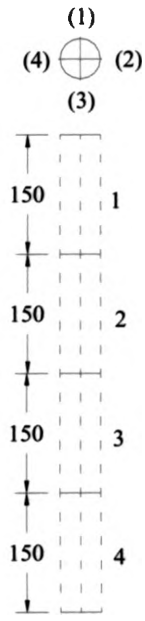

Pile No.	24	
Grout Pressure (P_g)	175	kPa
Pile Length (L_g)	93	cm
Pile Diameter (D_c)	6	cm
Ultimate Capacity (P_{ult})	31	kN

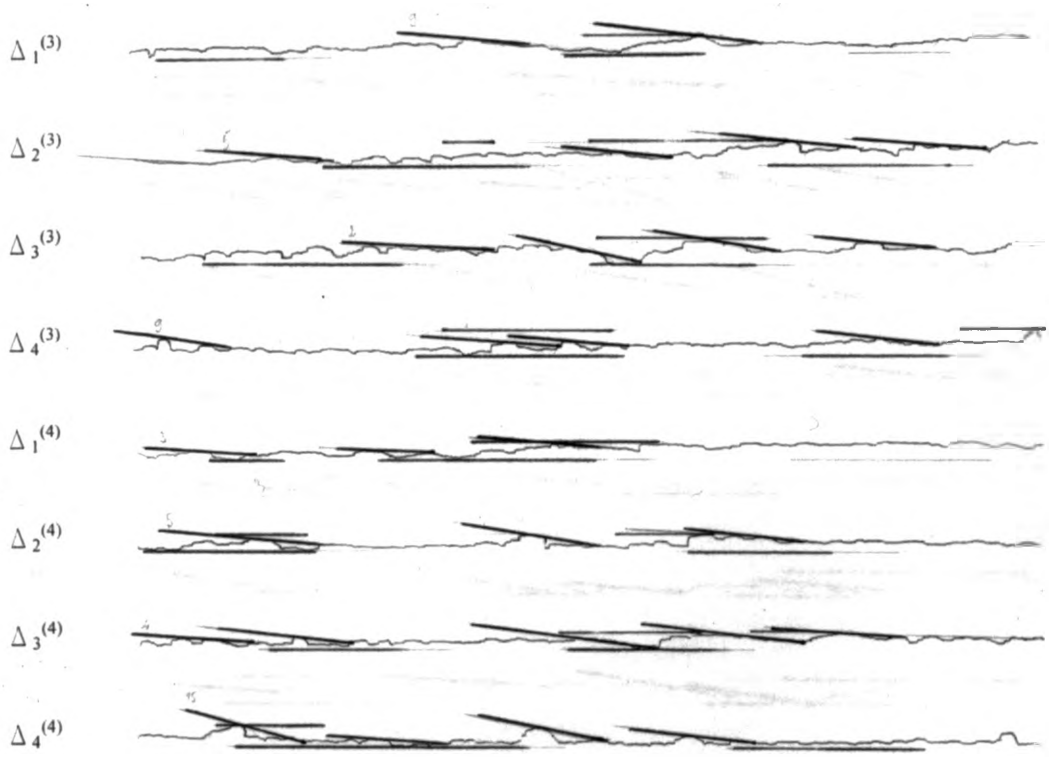

Figure A.18 *Roughness Micropile # 24, Side 3 and 4*

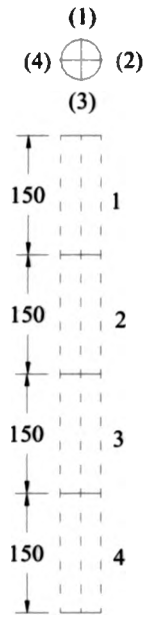

Pile No.	25	
Grout Pressure (P_g)	175	kPa
Pile Length (L_g)	94	cm
Pile Diameter (D_c)	6	cm
Ultimate Capacity (P_{ult})	28	kN

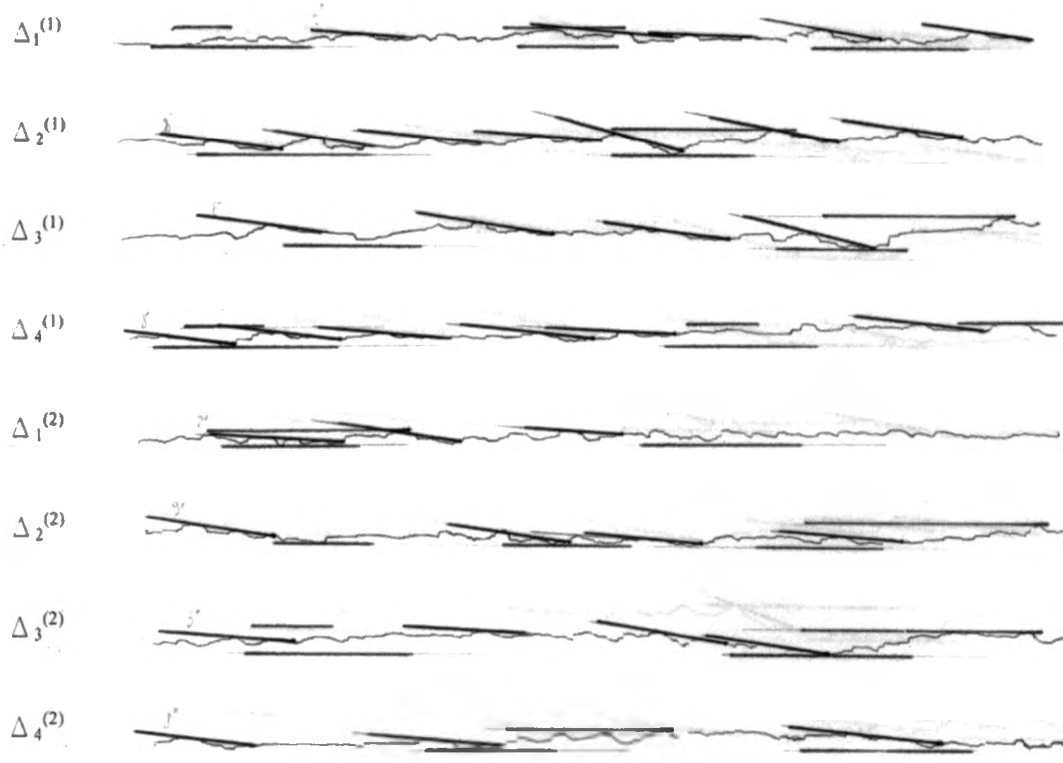

Figure A. 19 *Roughness Micropile # 25, Side 1 and 2*

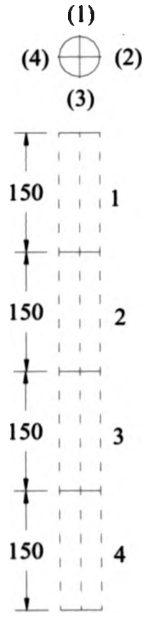

Pile No.	25	
Grout Pressure (P_g)	175	kPa
Pile Length (L_g)	94	cm
Pile Diameter (D_c)	6	cm
Ultimate Capacity (P_{ult})	28	kN

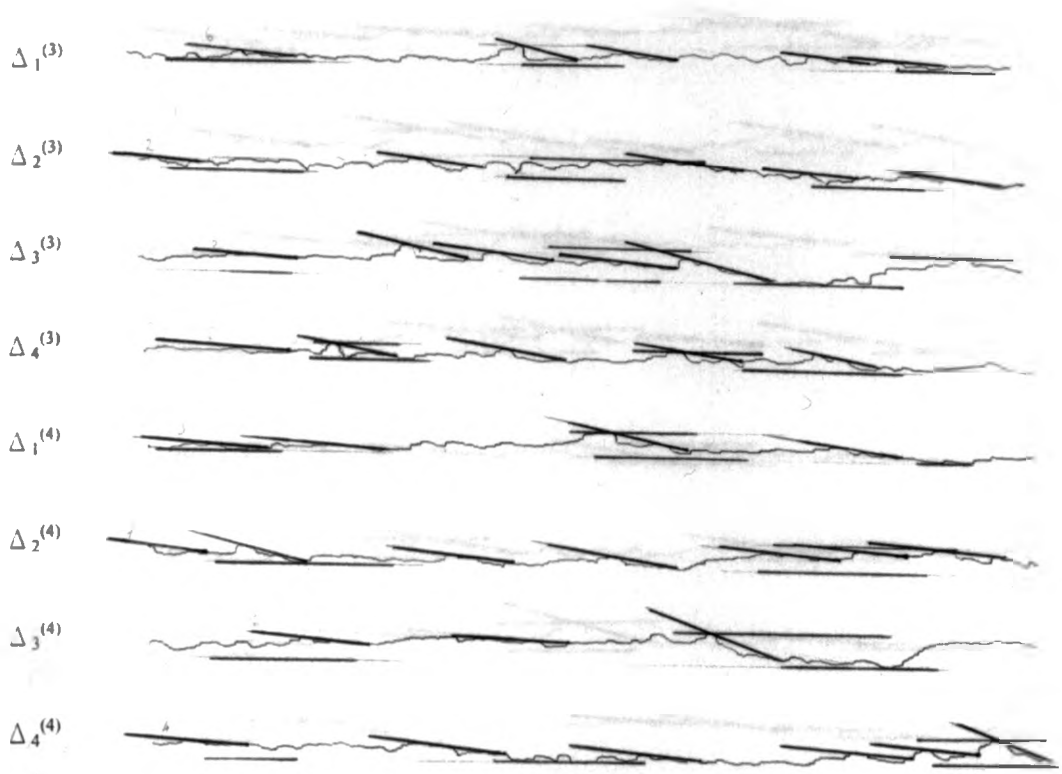

Figure A.20 *Roughness Micropile # 25, Side 3 and 4*

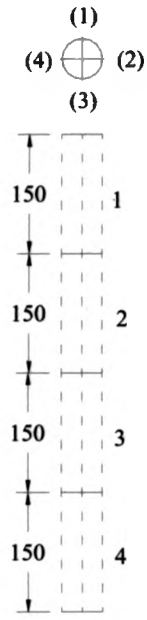

Pile No.	26	
Grout Pressure (P_g)	175	kPa
Pile Length (L_g)	94	cm
Pile Diameter (D_c)	6	cm
Ultimate Capacity (P_{ult})	33	kN

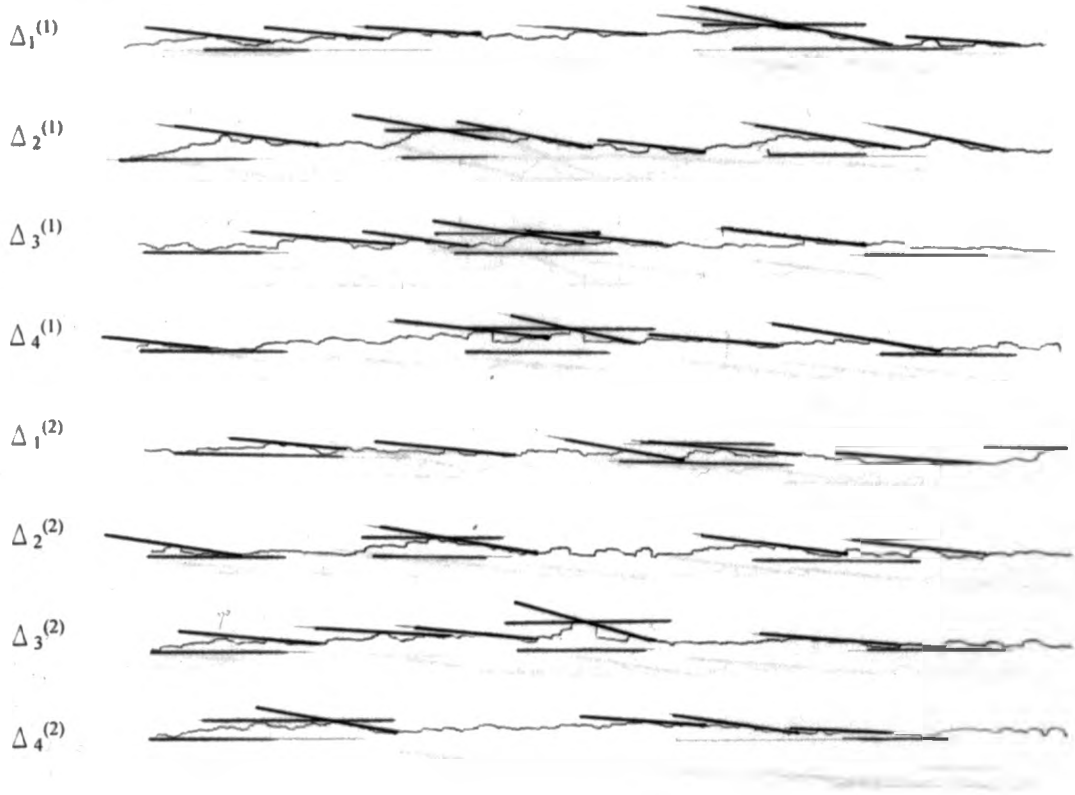

Figure A.21 *Roughness Micropile # 26, Side 1 and 2*

Pile No.	26	
Grout Pressure (P_g)	175	kPa
Pile Length (L_g)	94	cm
Pile Diameter (D_c)	6	cm
Ultimate Capacity (P_{ult})	33	kN

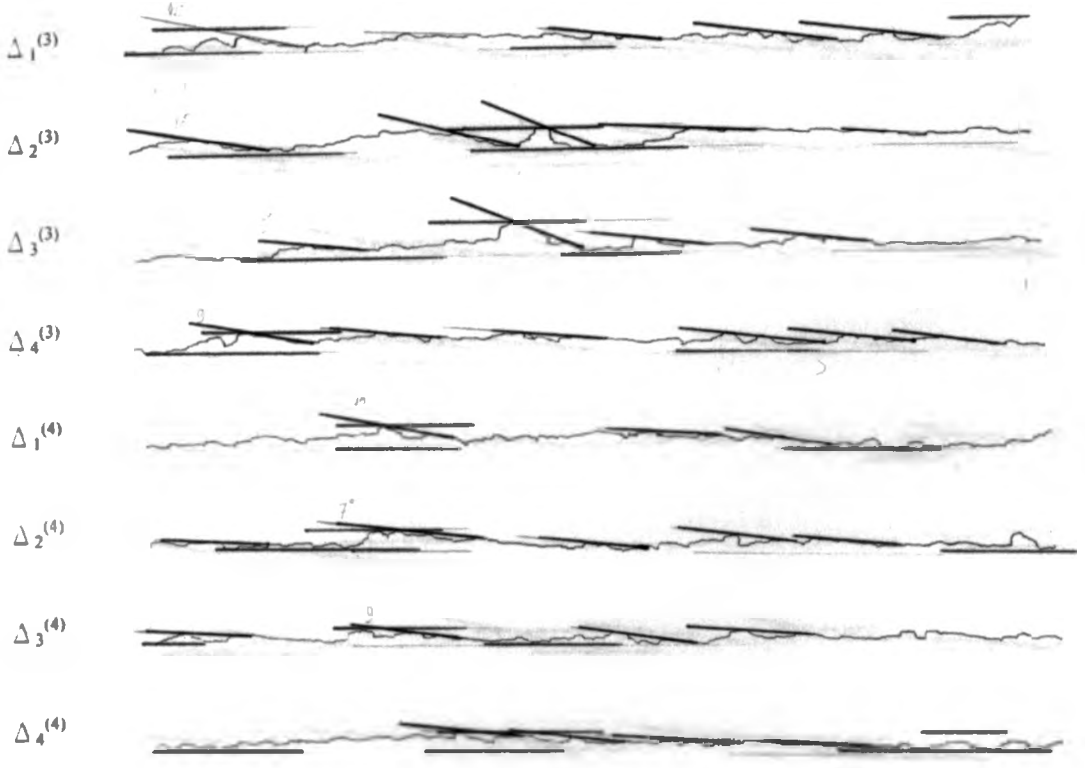

***Figure A.22** Roughness Micropile # 26, Side 3 and 4*

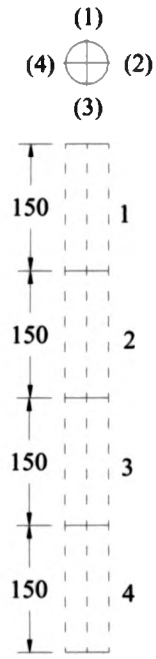

Pile No.	27	
Grout Pressure (P_g)	100	kPa
Pile Length (L_g)	96	cm
Pile Diameter (D_c)	6	cm
Ultimate Capacity (P_{ult})	27.5	kN

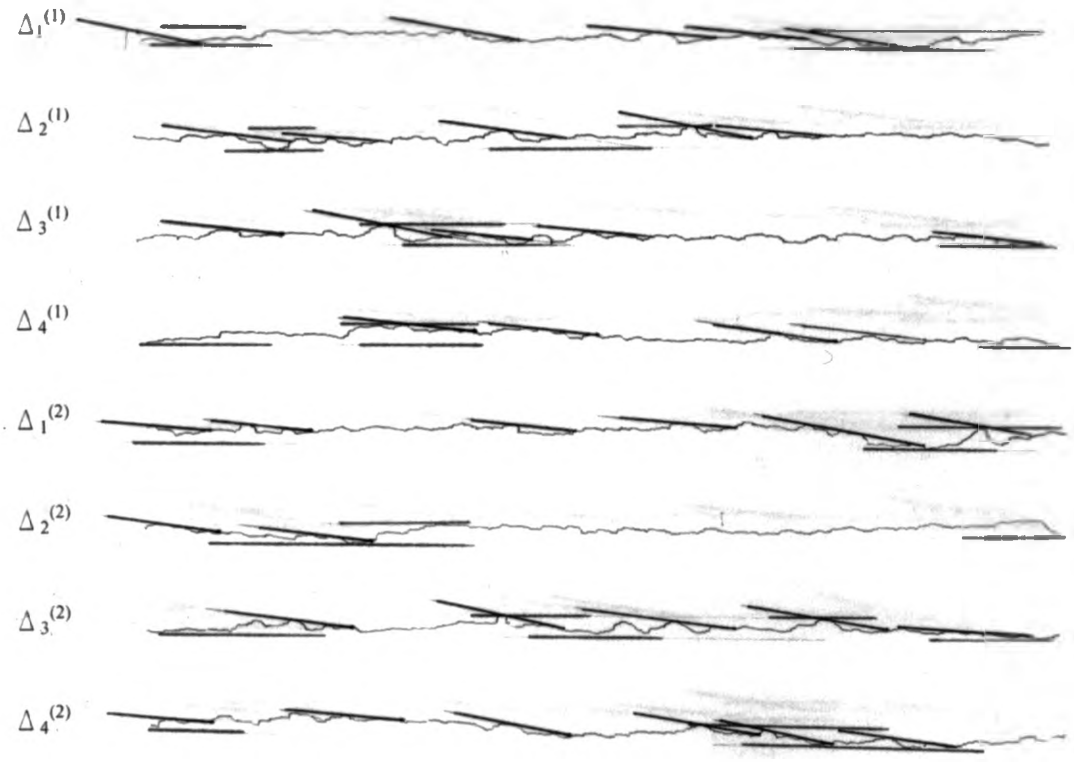

Figure A.23 *Roughness Micropile # 27, Side 1 and 2*

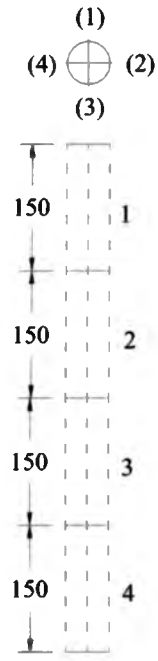

Pile No.	27	
Grout Pressure (P_g)	100	kPa
Pile Length (L_g)	96	cm
Pile Diameter (D_c)	6	cm
Ultimate Capacity (P_{ult})	27.5	kN

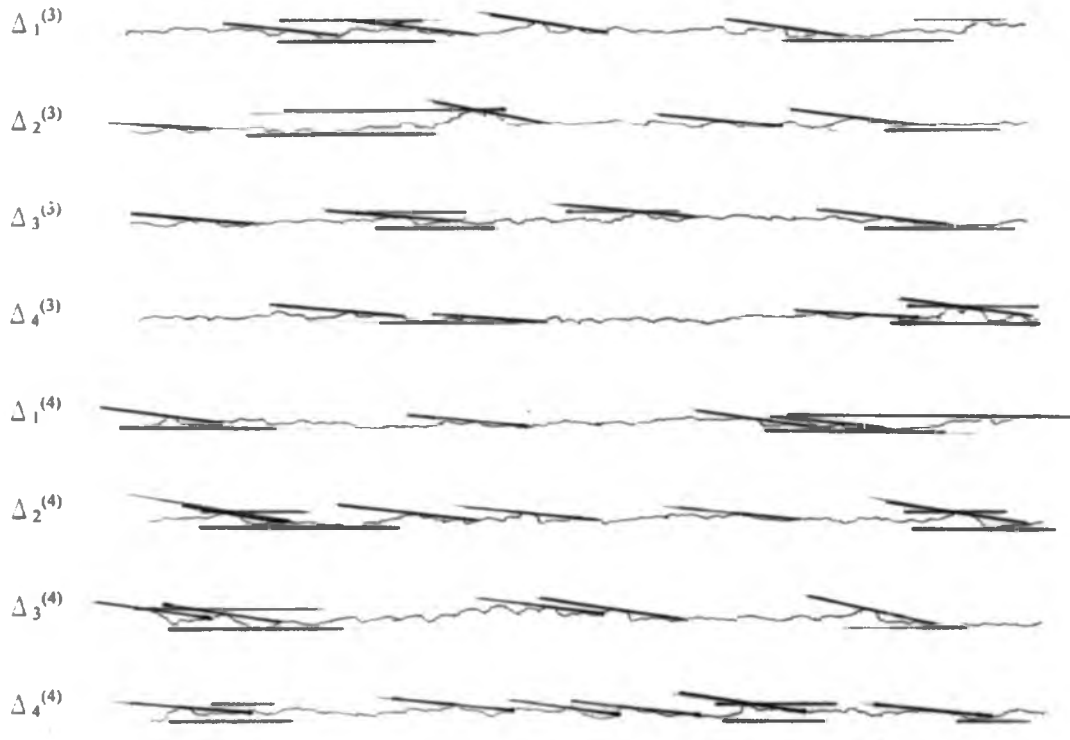

Figure A.24 *Roughness Micropile # 27, Side 3 and 4*

Appendix B

Earth Pressure Cells

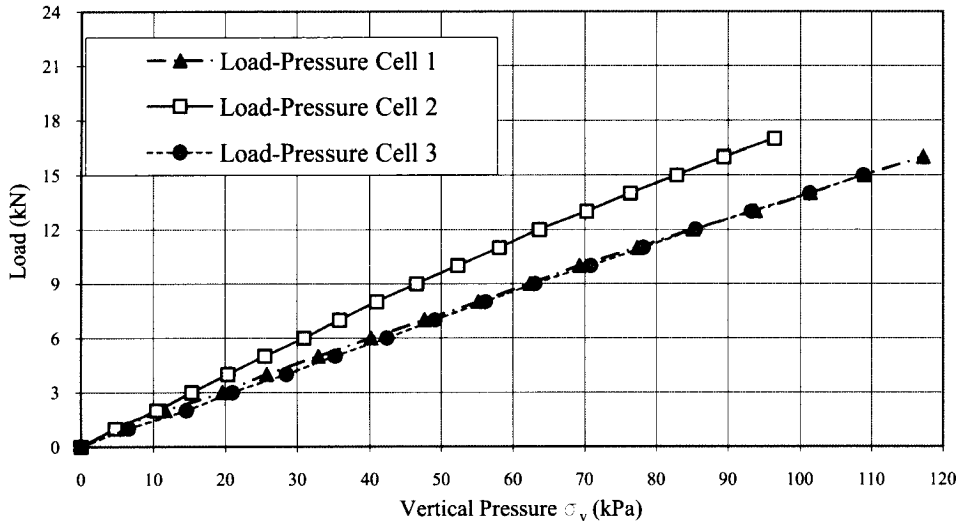

Figure B.1 *Test #1 –Load vs. Vertical Pressure for Earth Pressure Cell 1, 2, 3.*

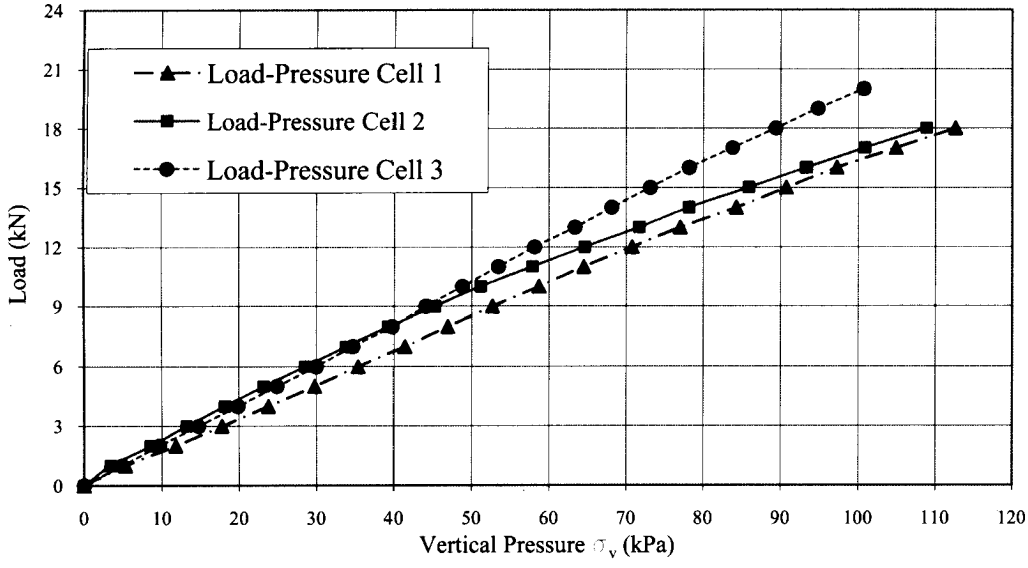

Figure B.2 *Test #2 –Load vs.Vertical Pressure for Earth Pressure Cell 1, 2, 3.*

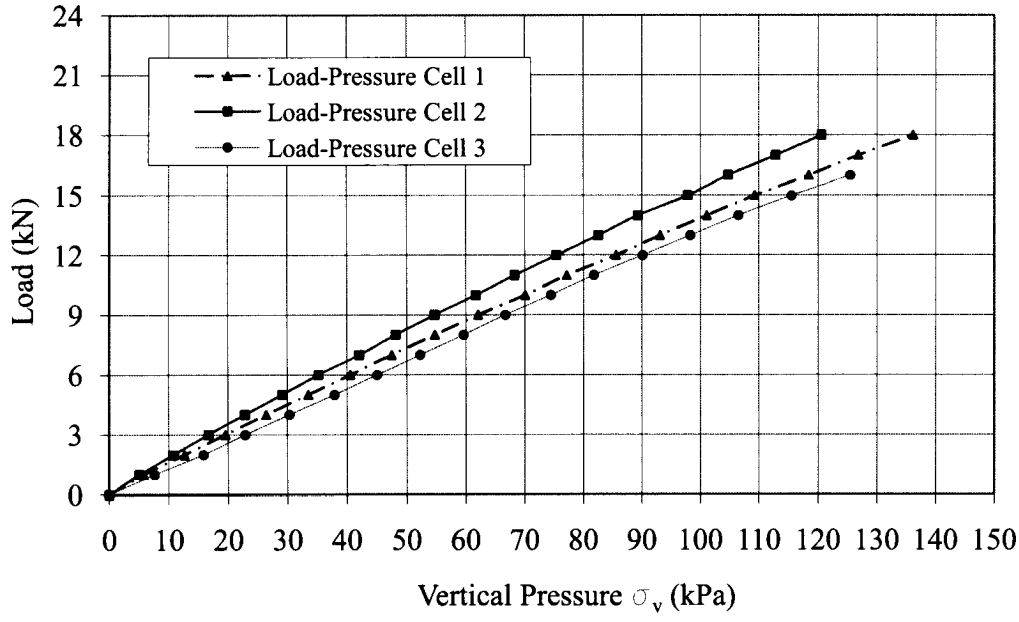

Figure B.3 *Tests #3 –Load vs. Vertical Pressure for Earth Pressure Cell 1, 2, 3*

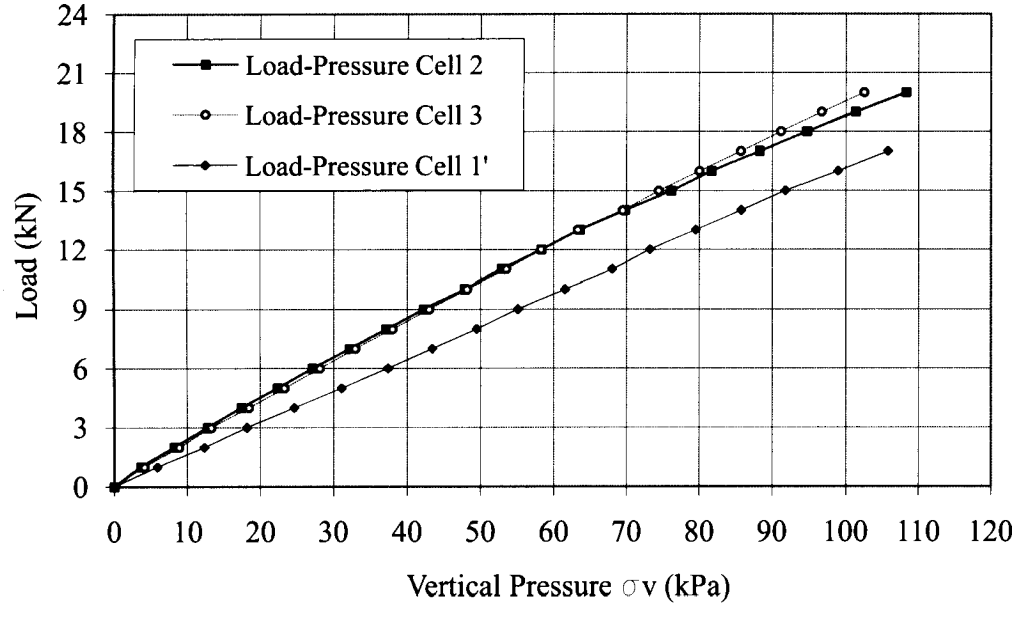

Figure B.4 *Tests #4 –Load vs. Vertical Pressure for Earth Pressure Cell 1, 2, 3.*

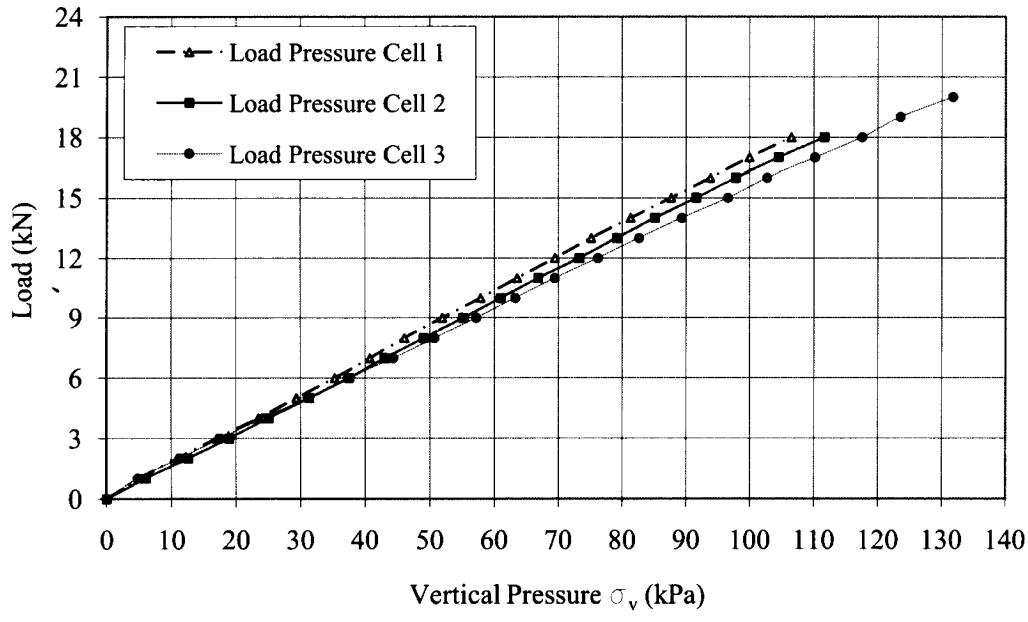

Figure B.5 *Test #5–Load vs. Vertical Pressure for Earth Pressure Cell 1, 2, 3*

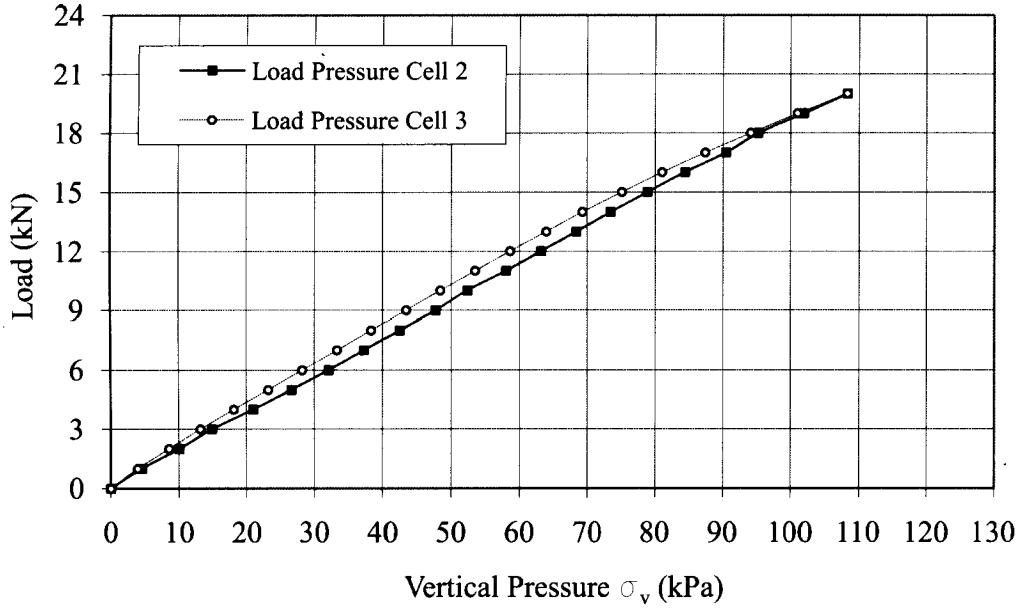

Figure B.6 *Test #6 –Load vs. Vertical Pressure for Earth Pressure Cell 2, 3*

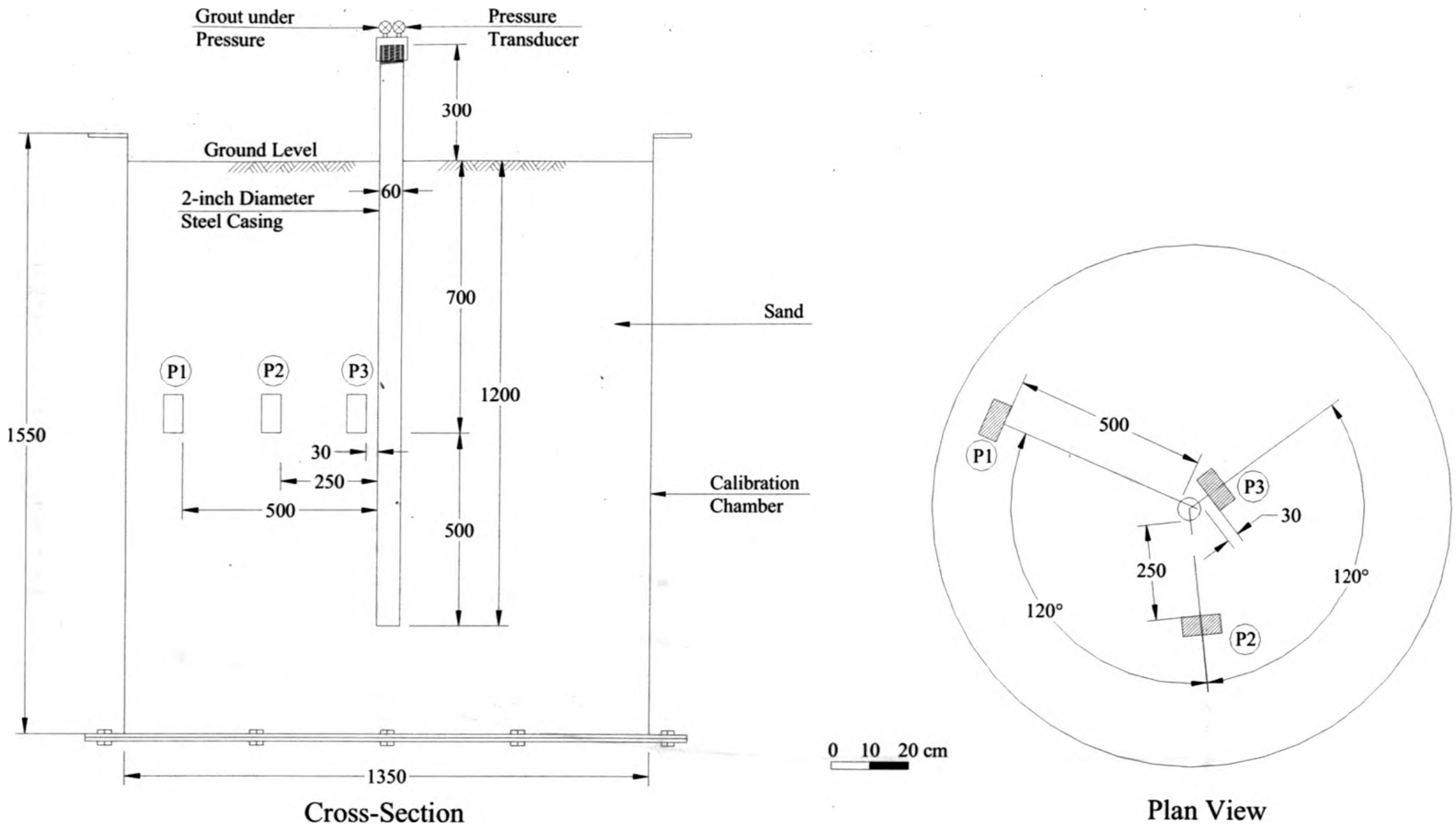

***Figure B.7** Position of Earth Pressure Cells for Micropile Test #1*

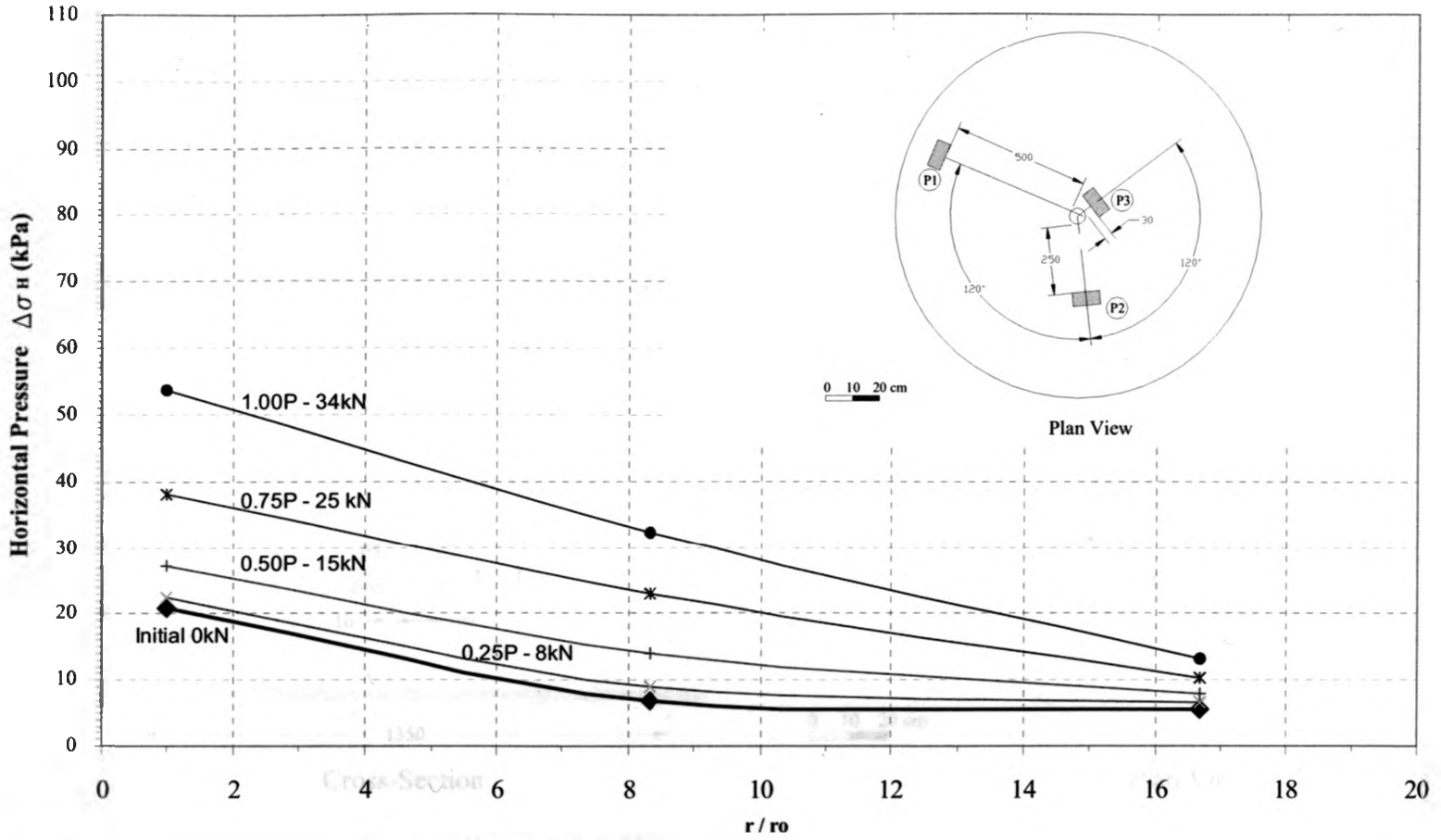

Figure B.8 *Horizontal Stress vs. Distance Ratio for P3 at Initial, 25%, 50%, 75% and 100% of Ultimate Load for Micropile Test #1*

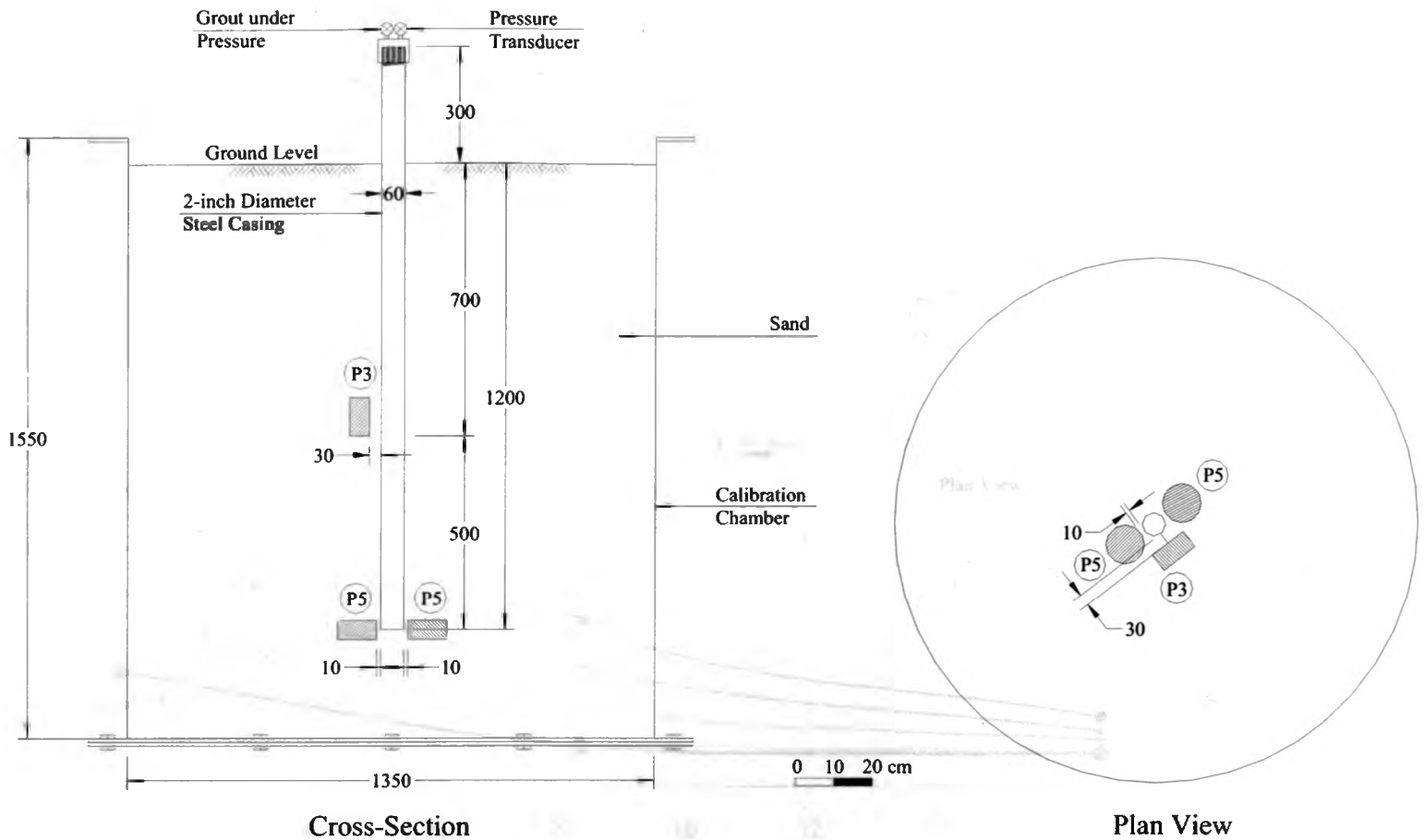

Figure B.9 *Position of Earth Pressure Cells for Micropile Test #2*

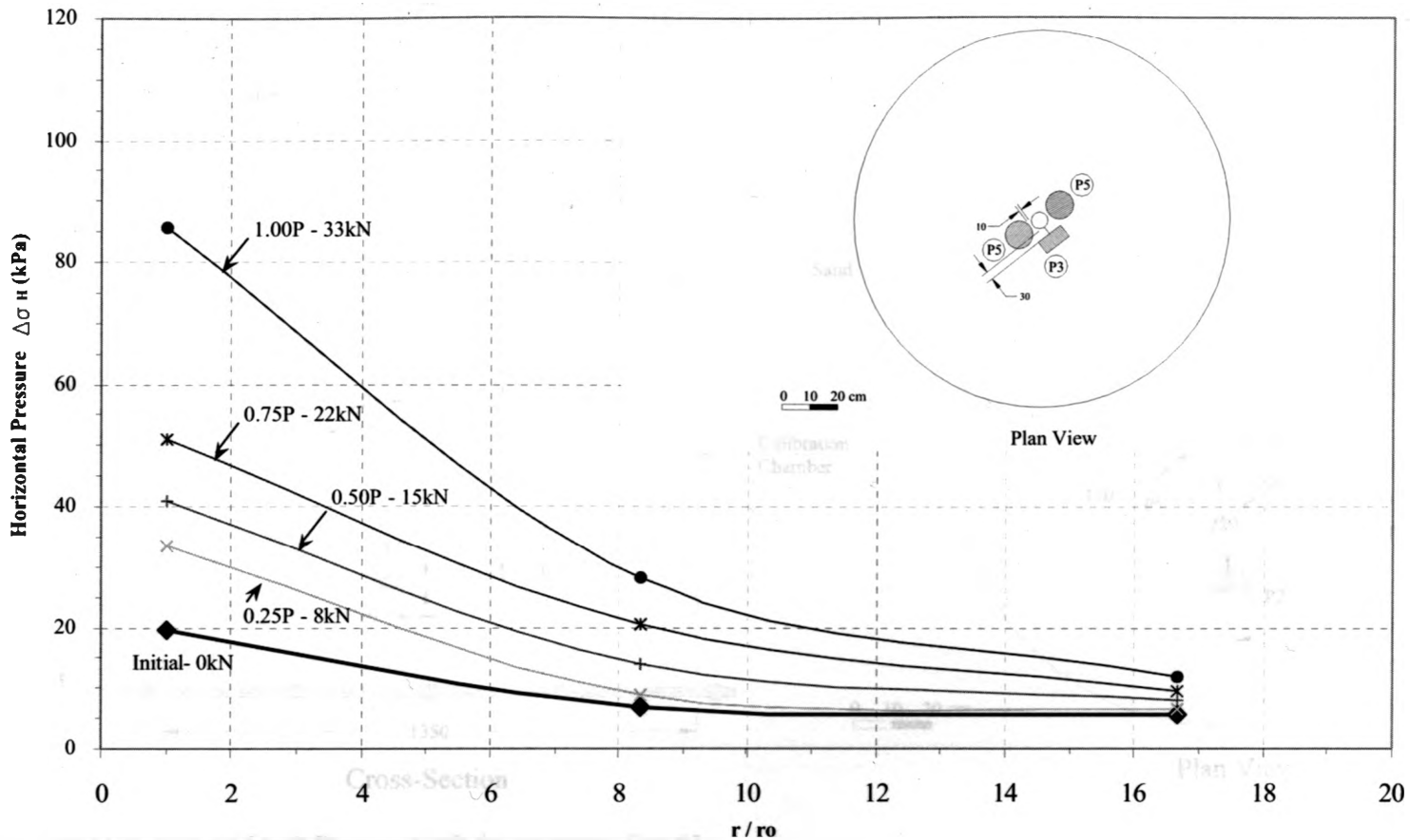

Figure B.10 *Horizontal Stress vs. Distance Ratio for P3 at Initial, 25%, 50%, 75% and 100% of Ultimate Load for Micropile Test #2*

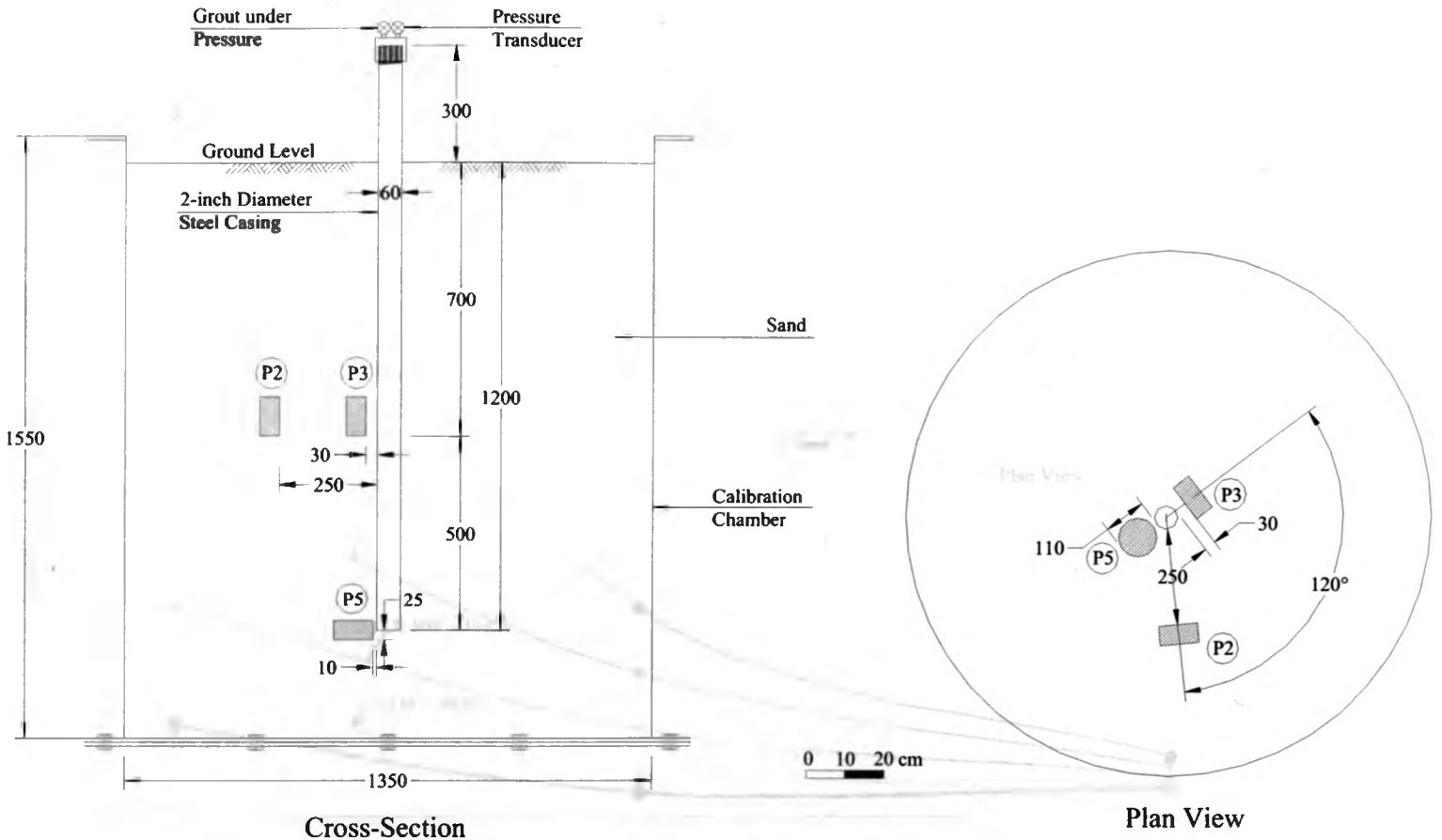

Figure B.11 *Position of Earth Pressure Cells for Micropile Test #3*

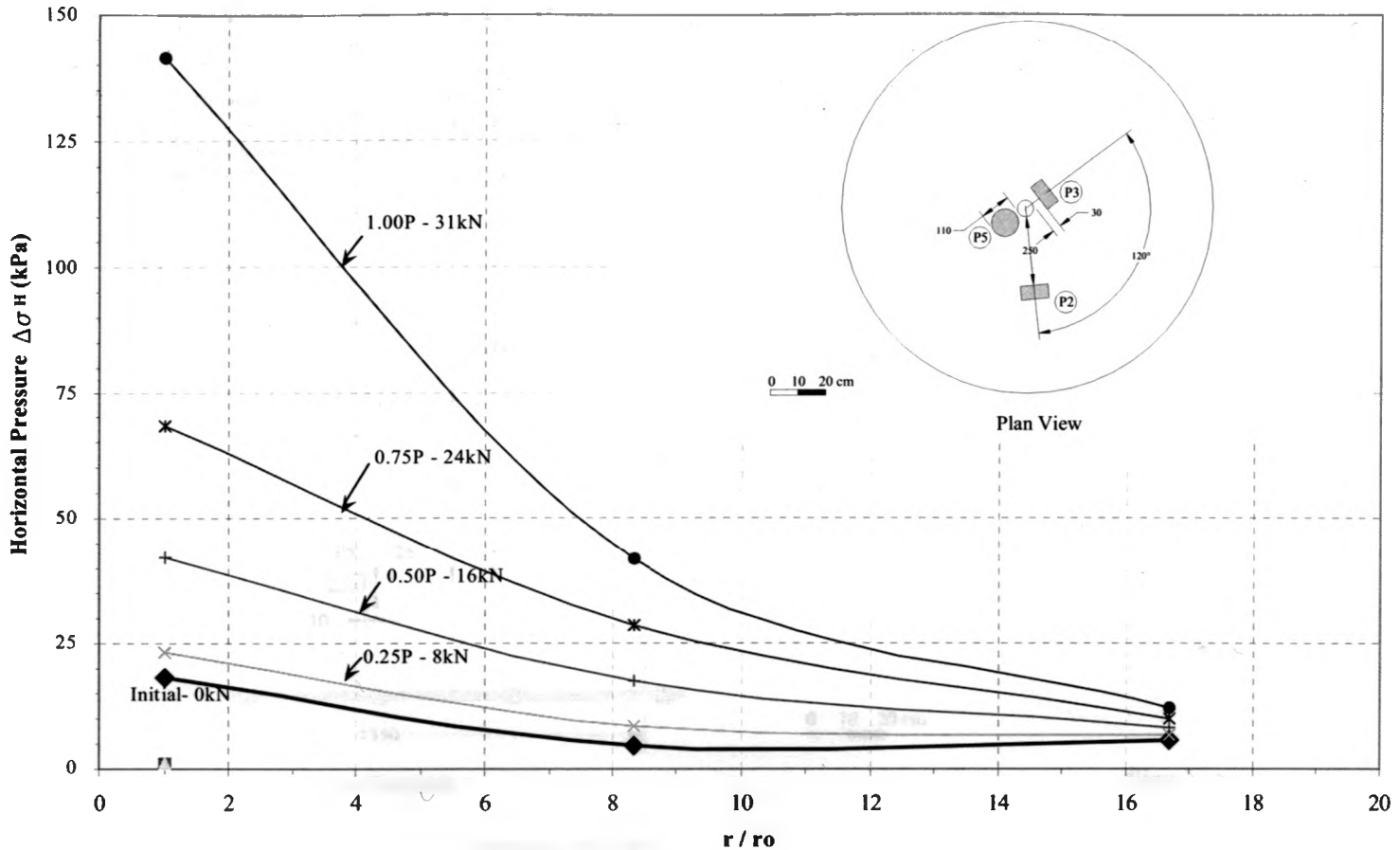

Figure B.12 *Horizontal Stress vs. Distance Ratio for P3 at Initial, 25%, 50%, 75% and 100% of Ultimate Load for Micropile Test #3*

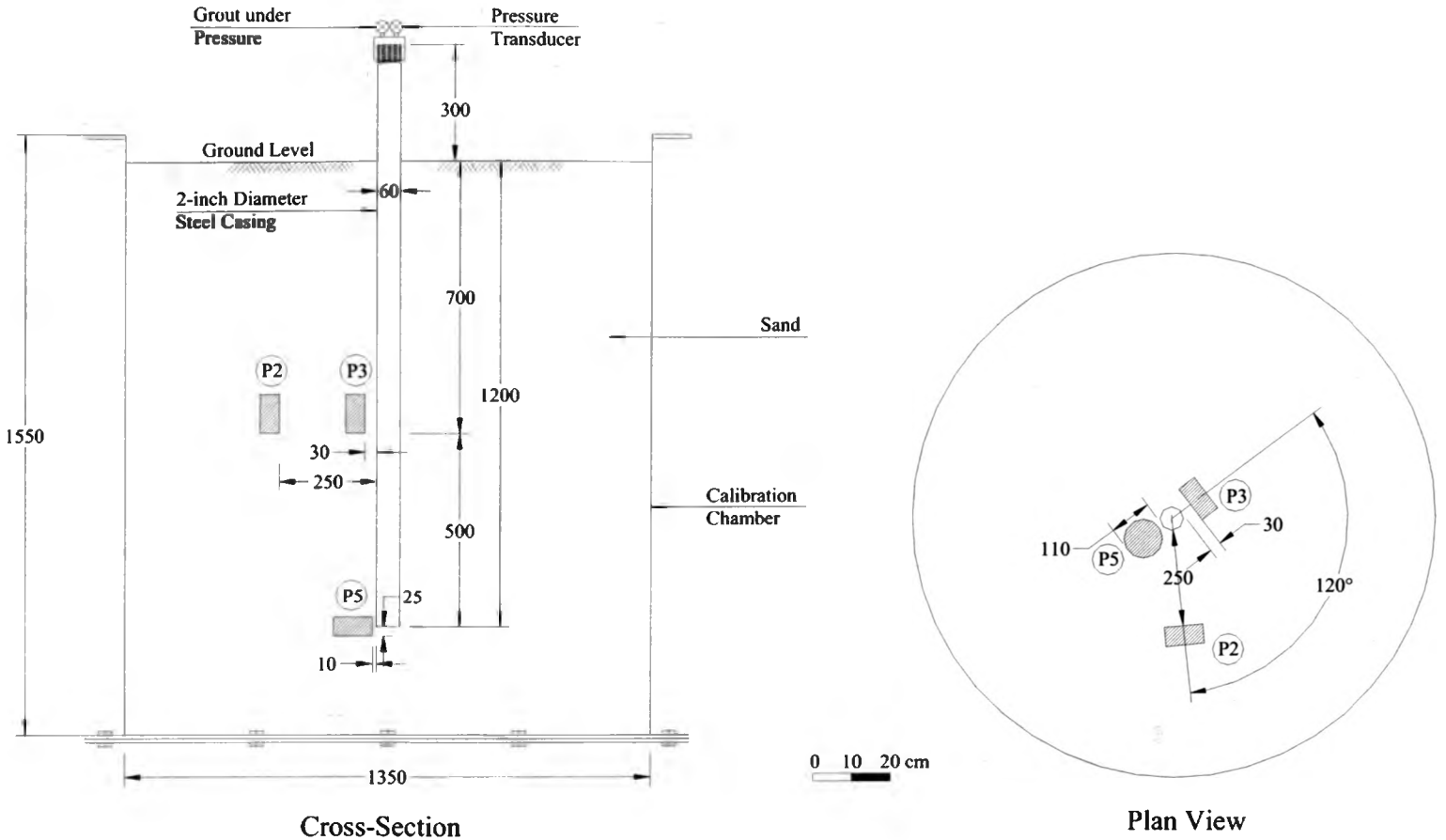

Figure B.13 *Position of Earth Pressure Cells for Micropile Test #4*

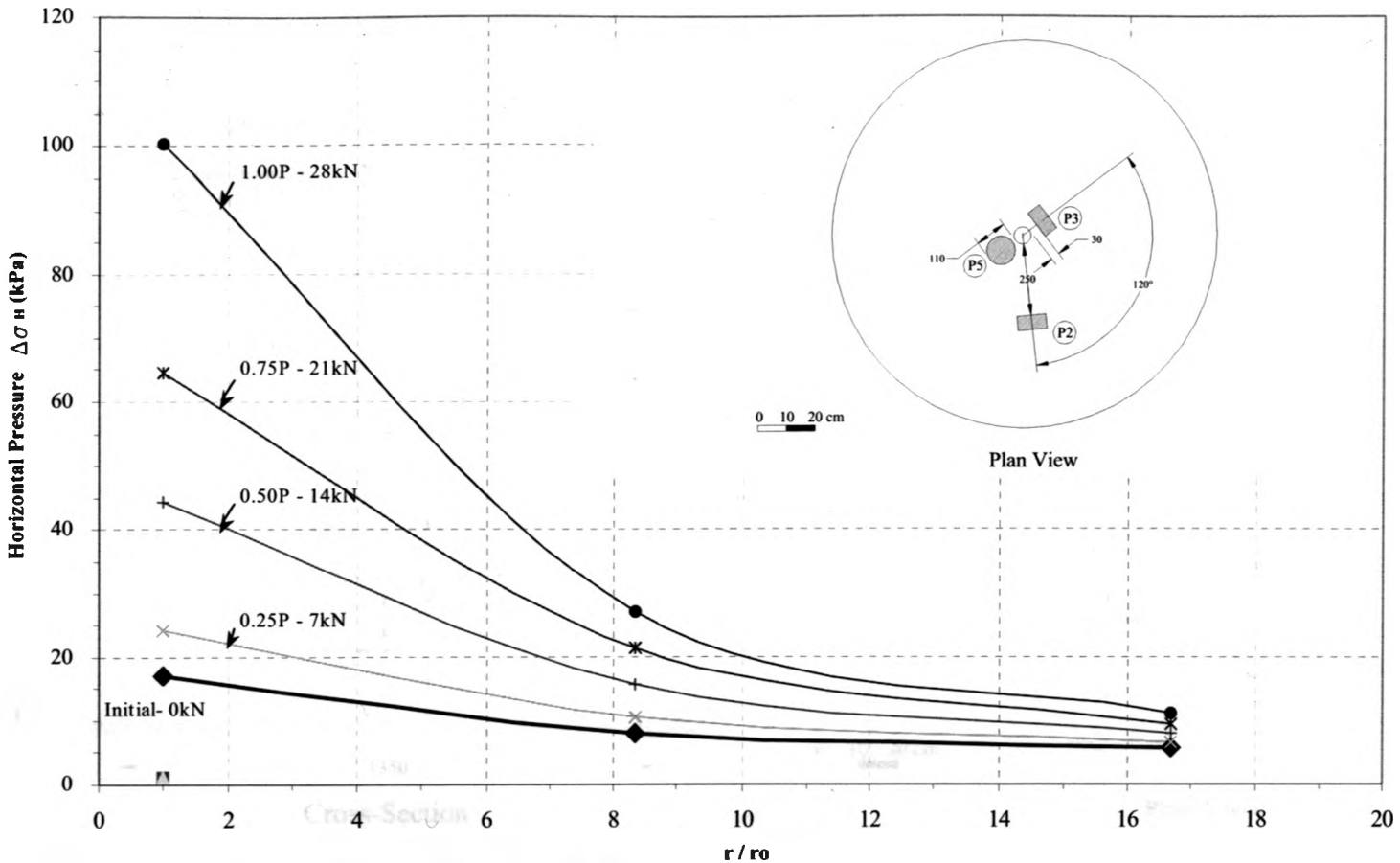

Figure B.14 *Horizontal Stress vs. Distance Ratio for P3 at Initial, 25%, 50%, 75% and 100% of Ultimate Load for Micropile Test #4*

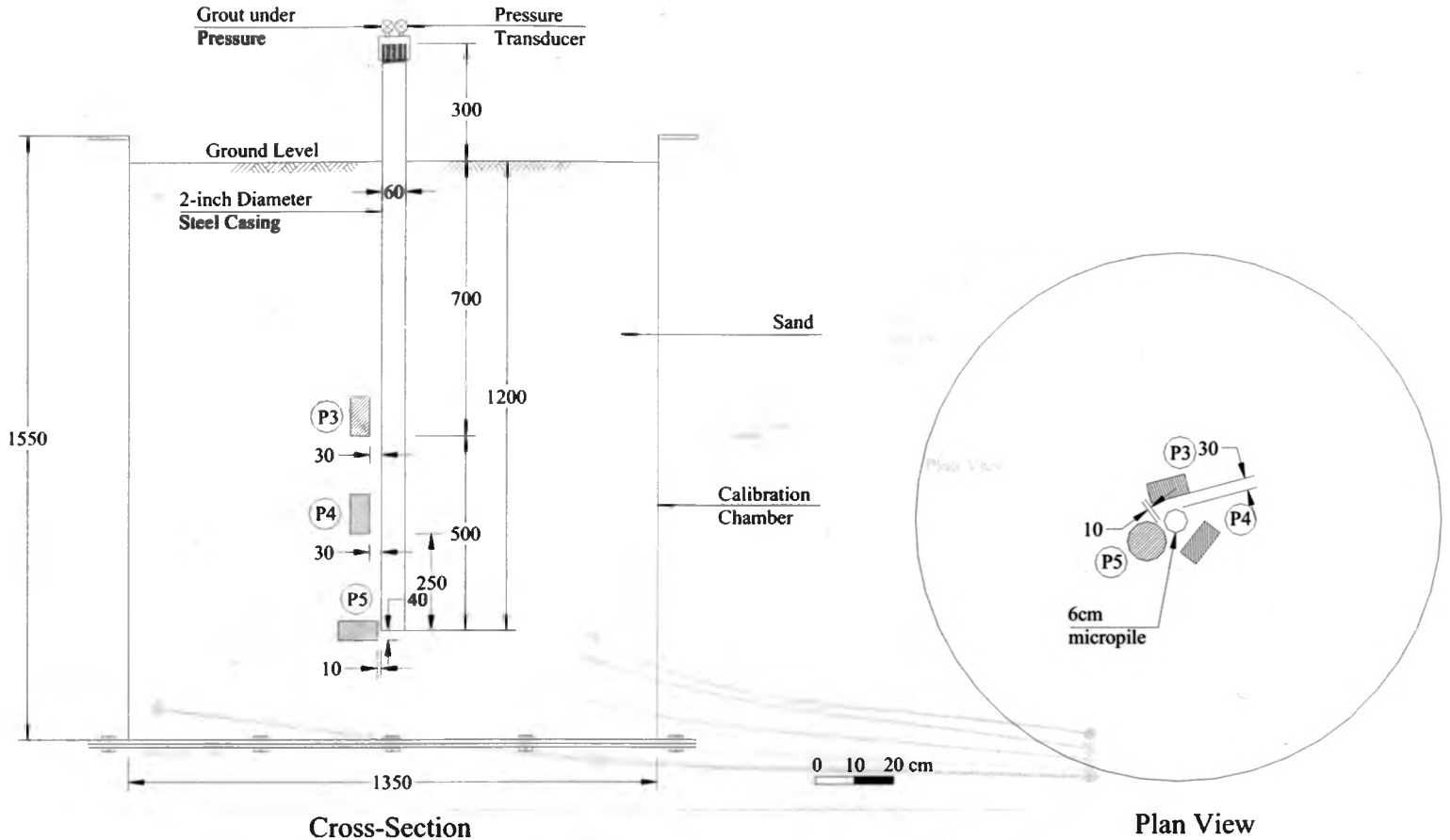

Figure B.15 *Position of Earth Pressure Cells for Micropile Test #5*

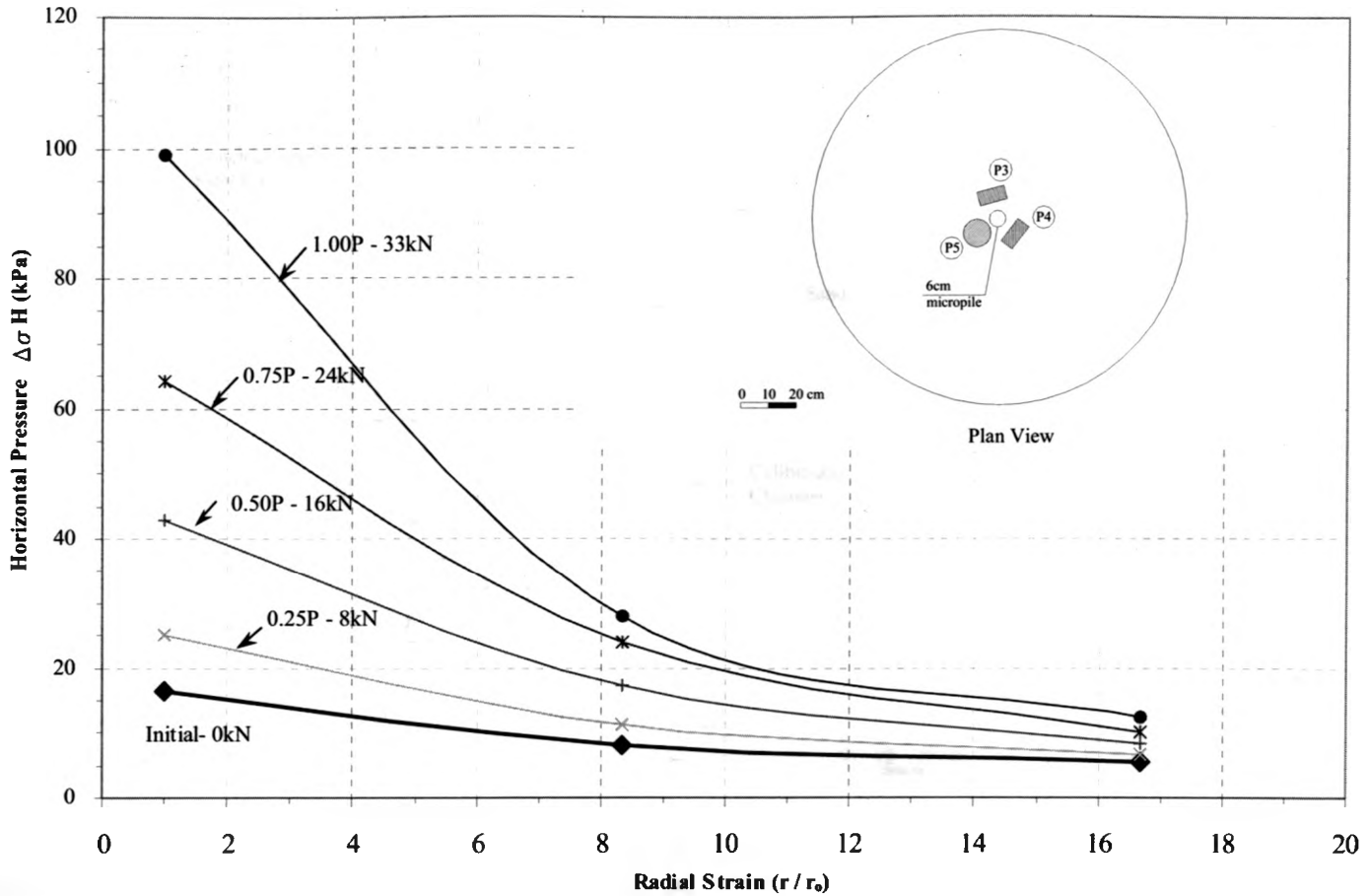

Figure B.16 *Horizontal Stress vs. Distance Ratio for P4 at Initial, 25%, 50%, 75% and 100% of Ultimate Load for Micropile Test #5*

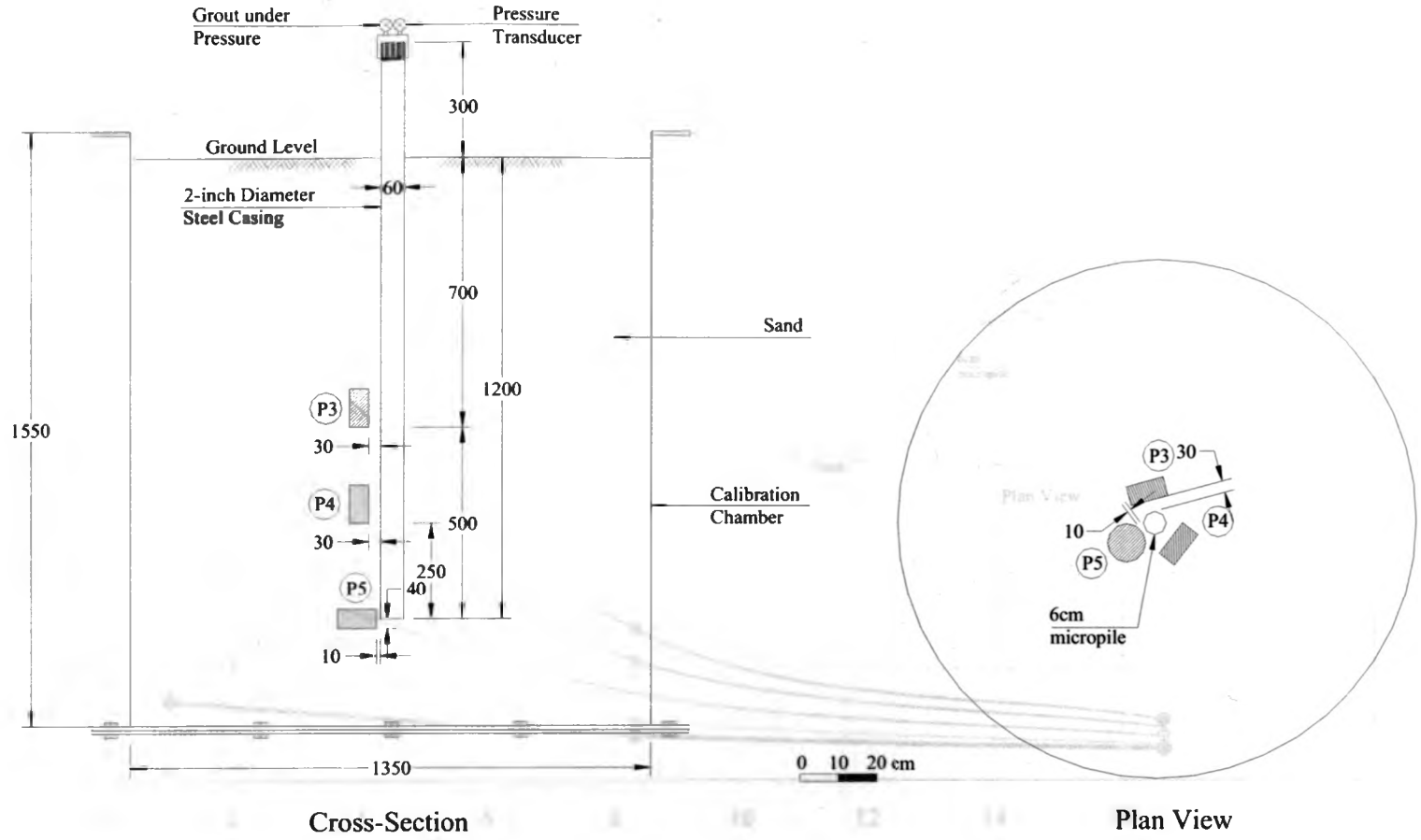

***Figure B.17** Position of Earth Pressure Cells for Micropile Test #6*

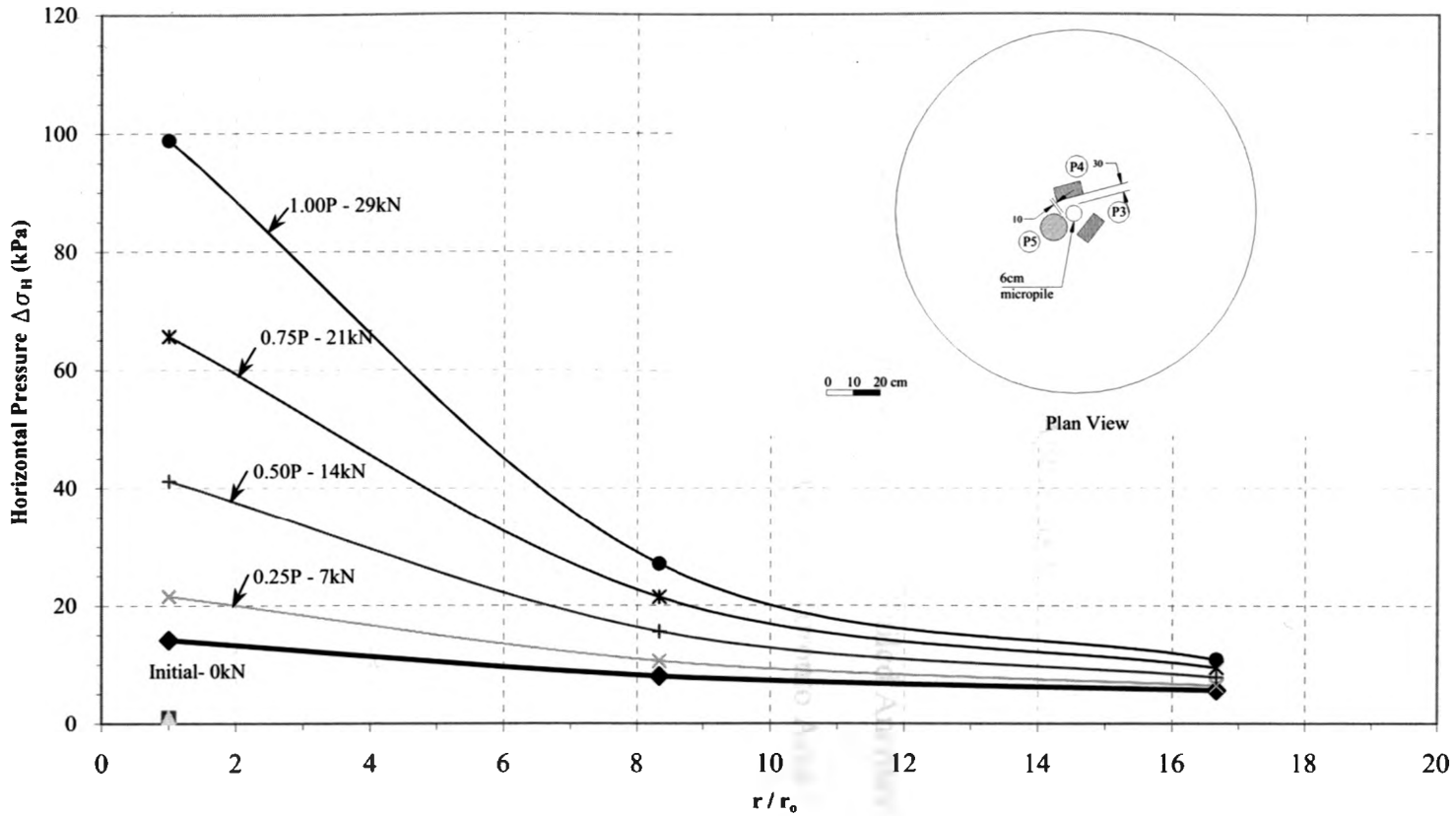

Figure B.18 *Horizontal Stress vs. Distance Ratio for P3 at Initial, 25%, 50%, 75% and 100% of Ultimate Load for Micropile Test #6*

Appendix C

Load Displacement Curves for Failed Anchors in Sandy Soils in the Greater Toronto Area

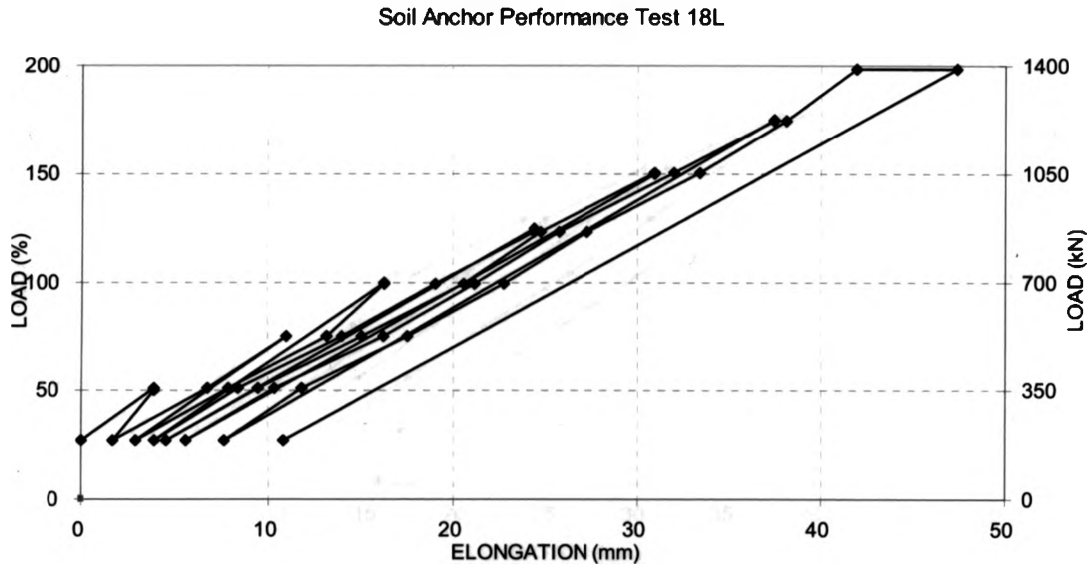

Figure C.1 *Tieback Test # 18L, Project 2000.07(CFA)*

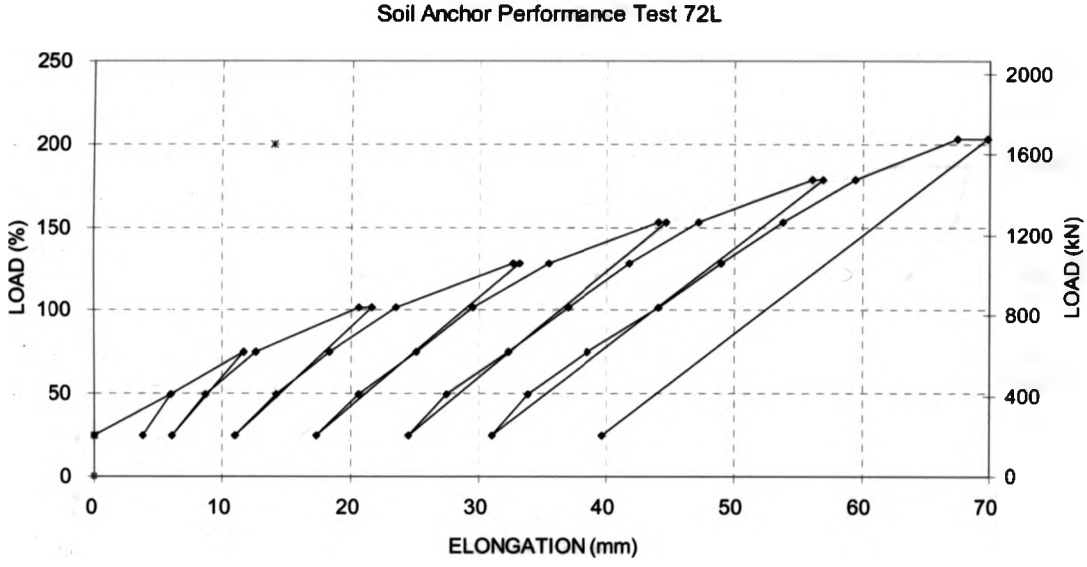

Figure C.2 *Tieback Test # 72L, Project 2000.07(CFA)*

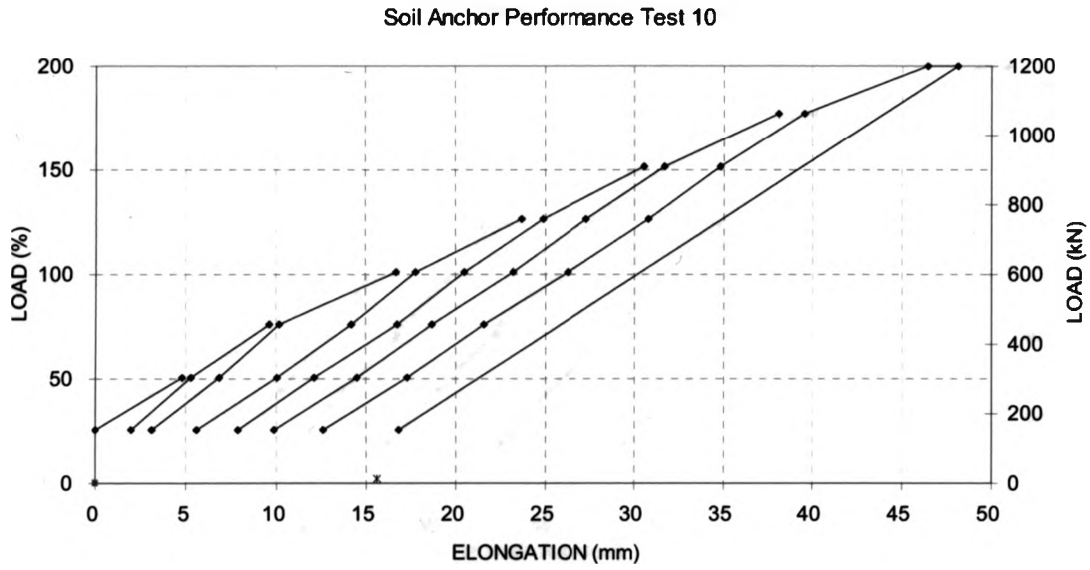

Figure C.3 *Tieback Test # 10L, Project 2001.32(CFA)*

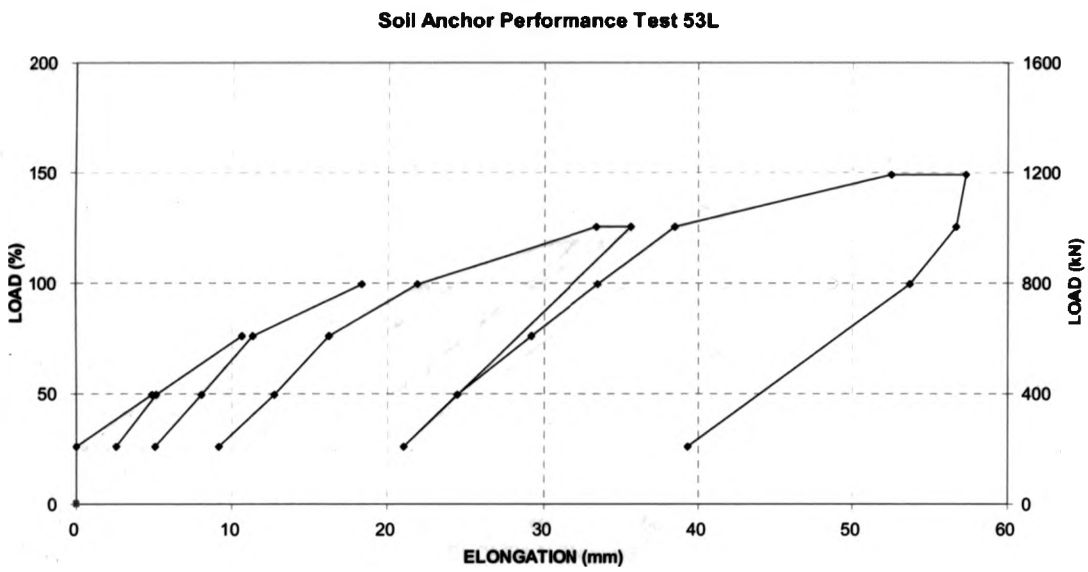

Figure C.4 *Tieback Test # L53, Project 2001.32(CFA)*

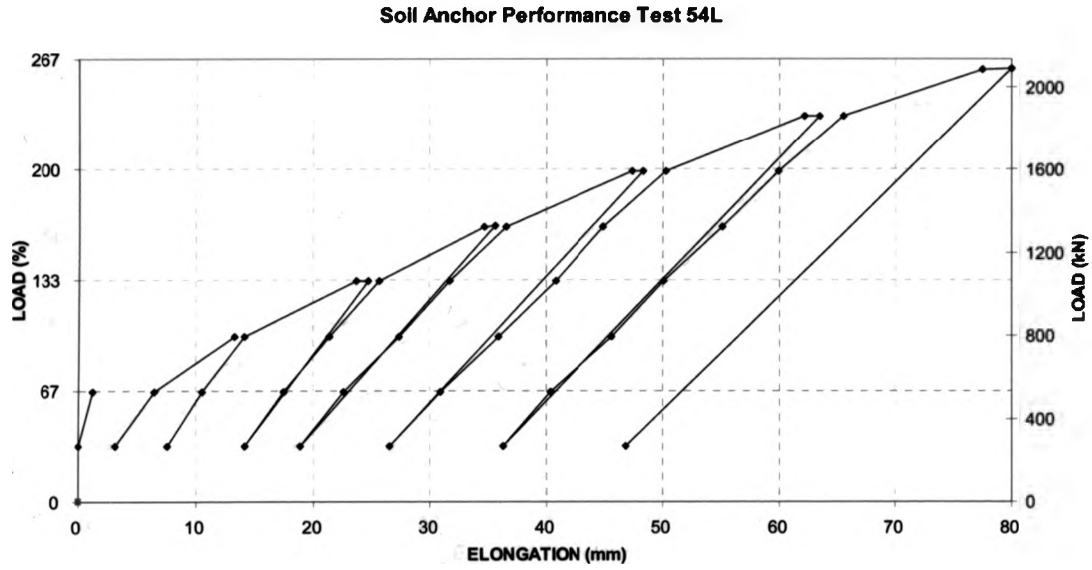

Figure C.5 *Tieback Test # L54, Project 2001.32(CFA)*

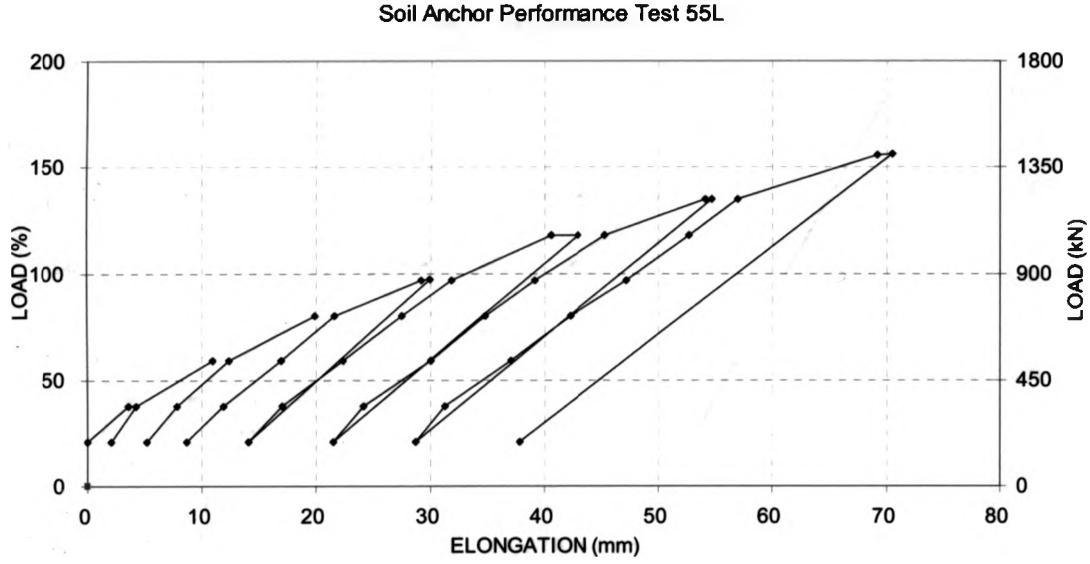

Figure C.6 *Tieback Test # L55, Project 2001.32(CFA)*

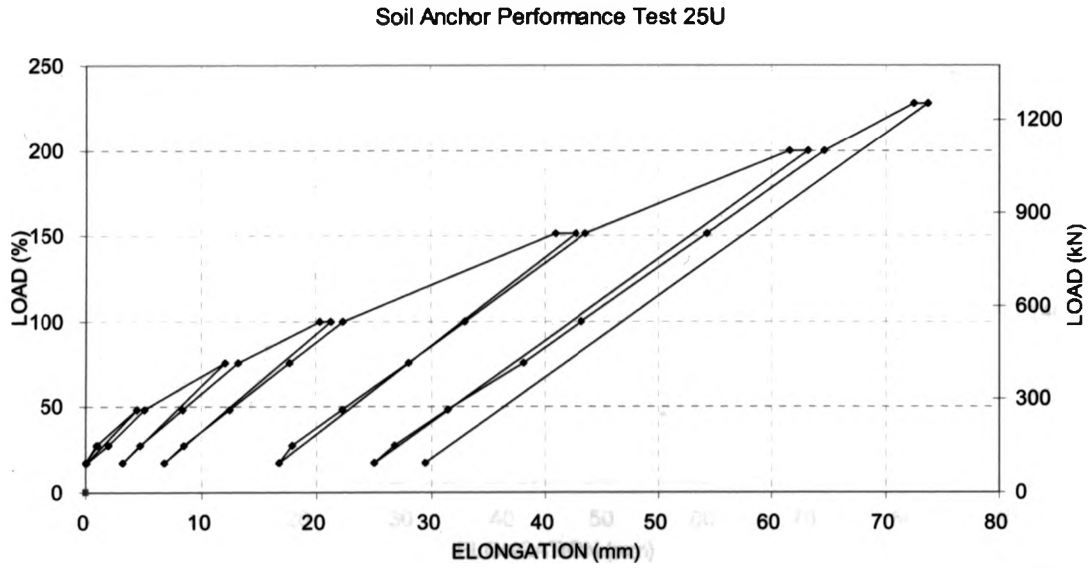

***Figure C.7** Tieback Test # 25U, Project 2001.60(CFA)*

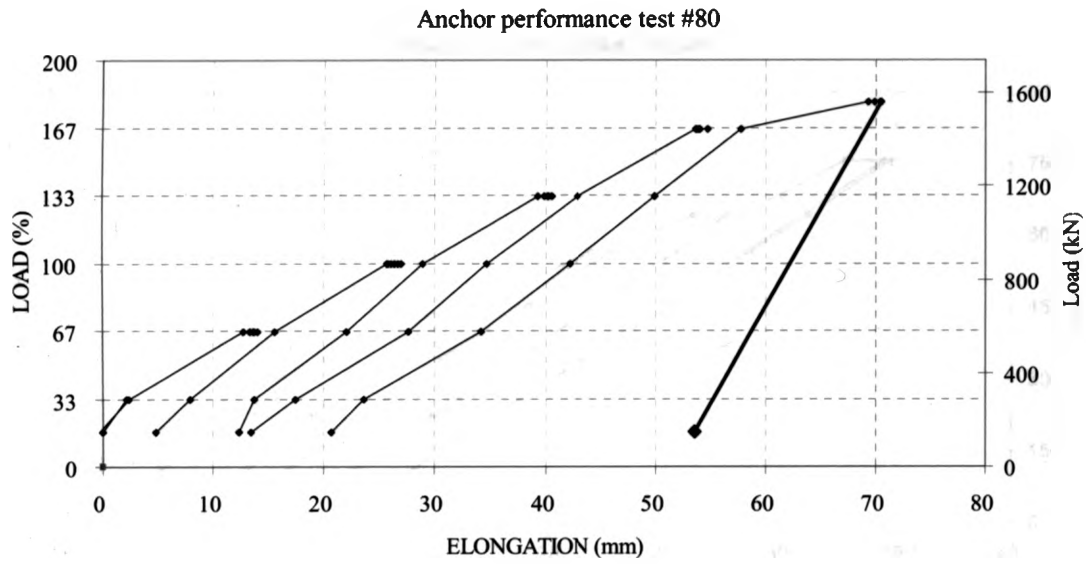

***Figure C.8** Tieback Test # 80, Project 2002.82(CFA)*

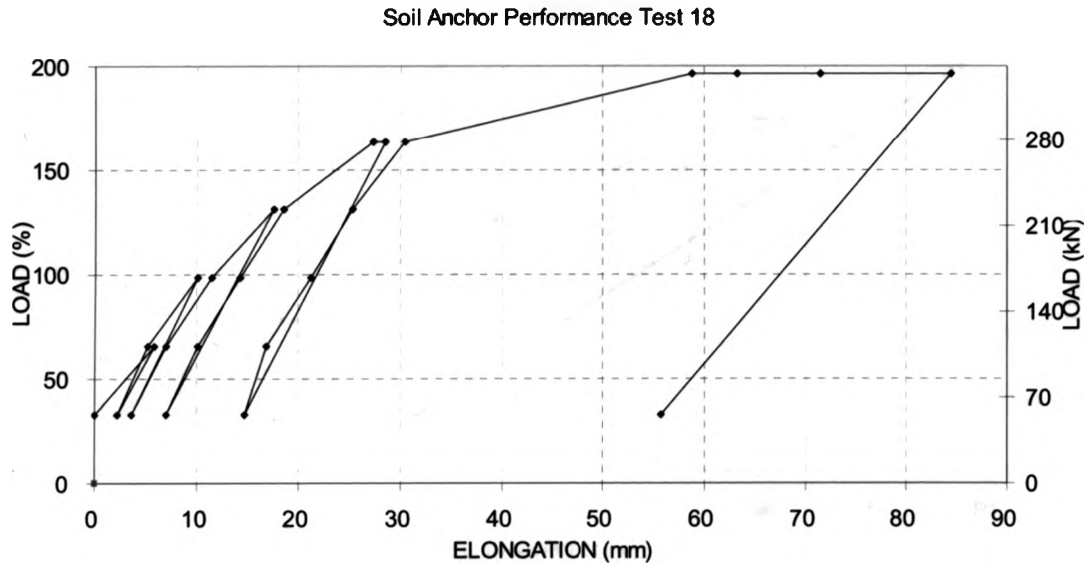

Figure C.9 *Tieback Test # 18U, Project 2003.03(RDD)*

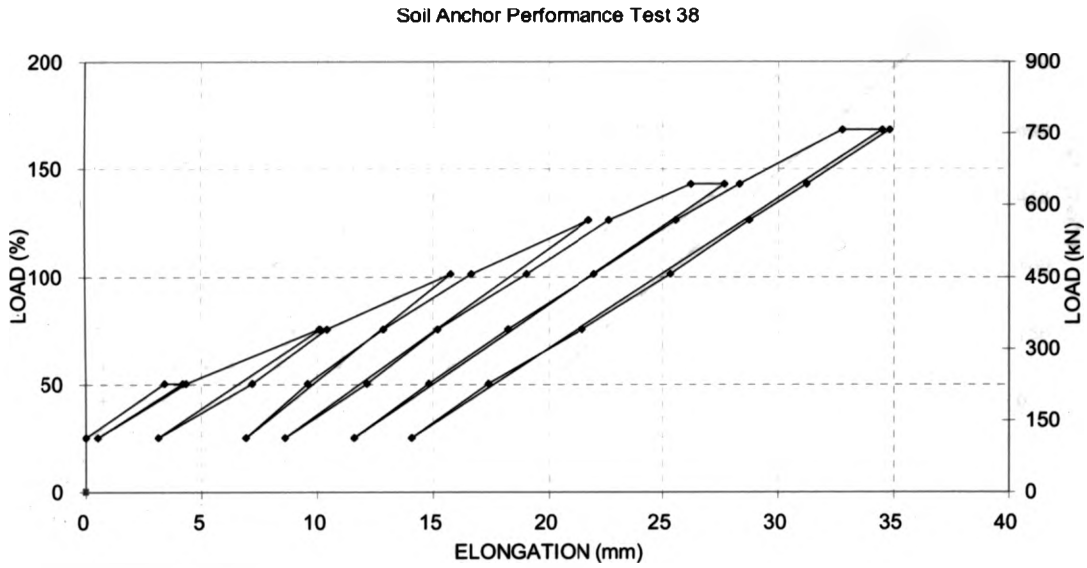

Figure C.10 *Tieback Test # 38, Project 2003.45(CFA)*

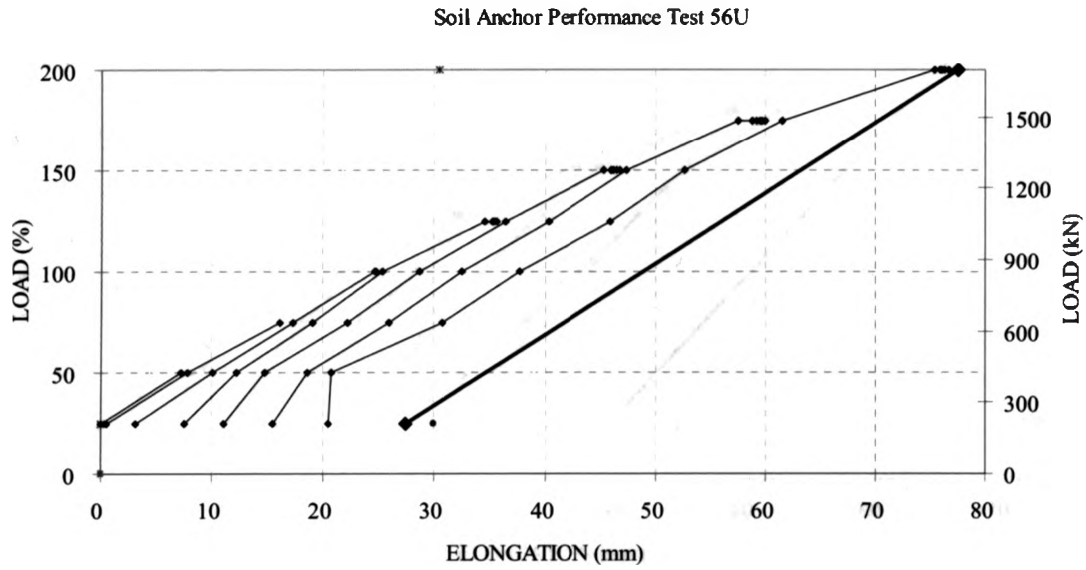

Figure C. 11 *Tieback Test # 56U, Project 2003.66(RDD)*

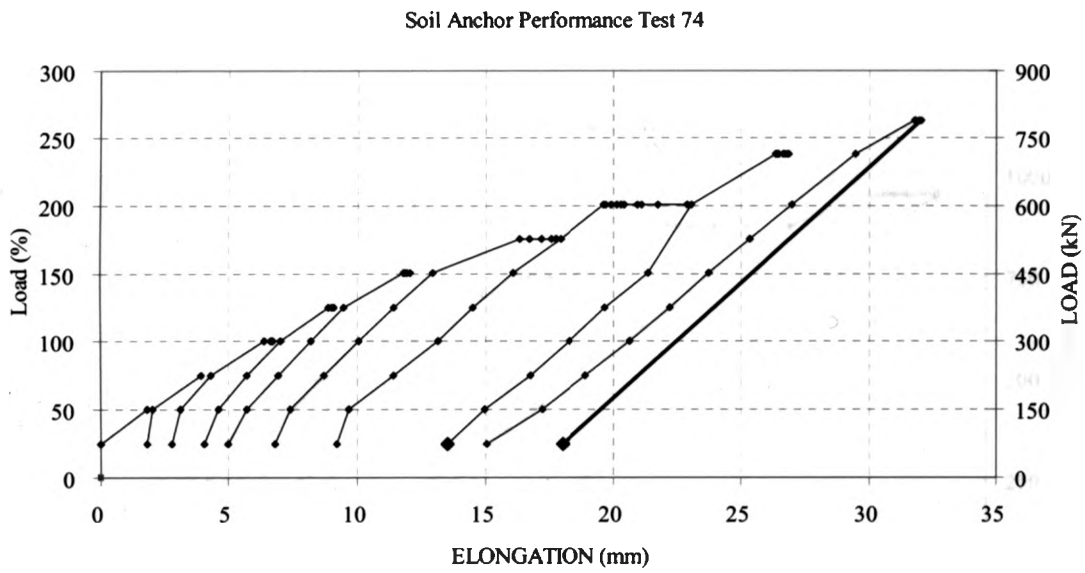

Figure C. 12 *Tieback Test # 74U, Project 2003.78(CFA)*

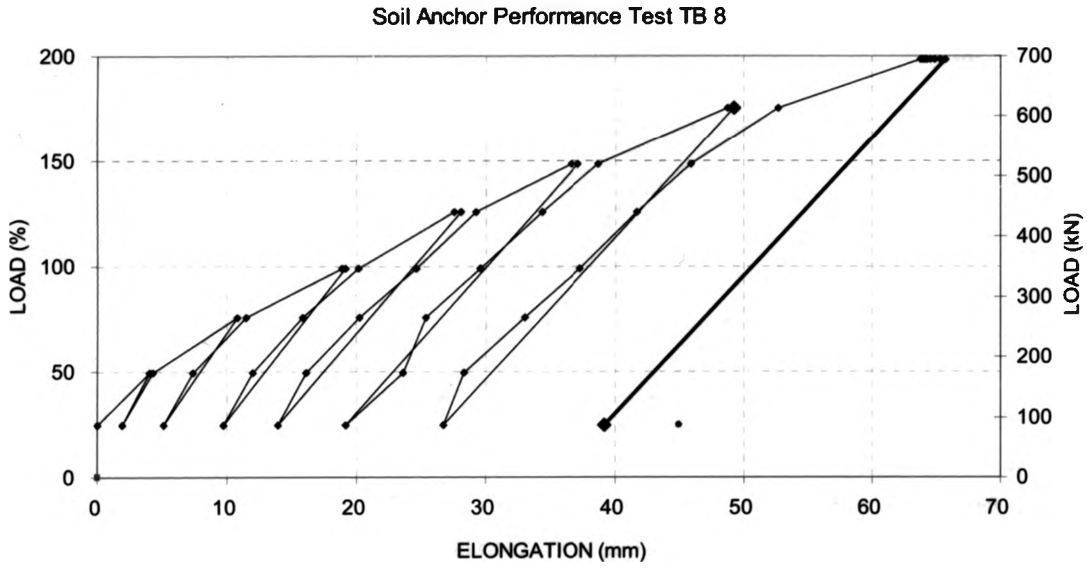

***Figure C. 13** Tieback Test # 8, Project 2004.41(CFA)*

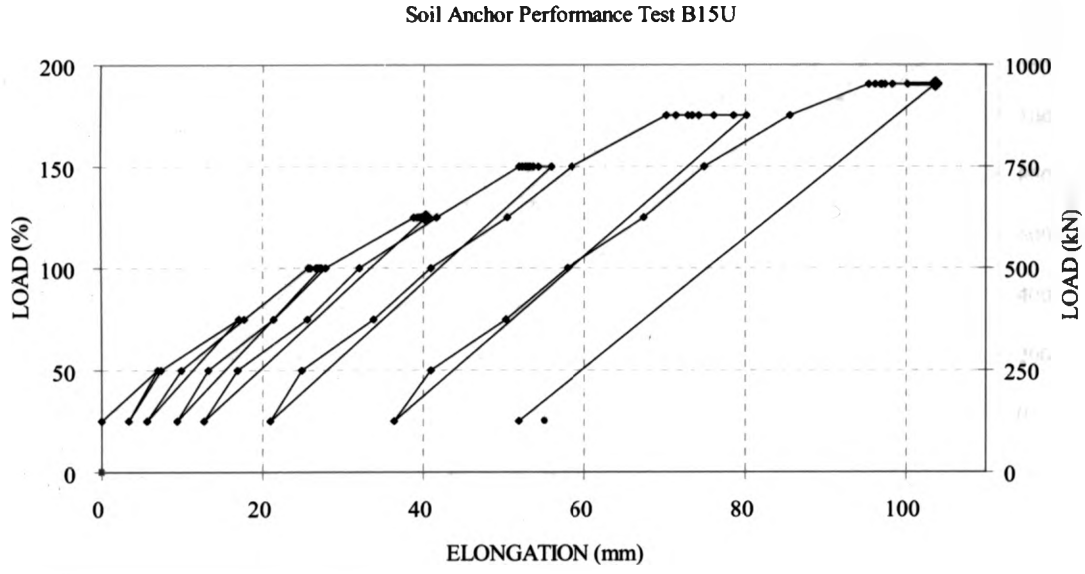

***Figure C.14** Tieback Test # B15U, Project 2004.50(RDD)*

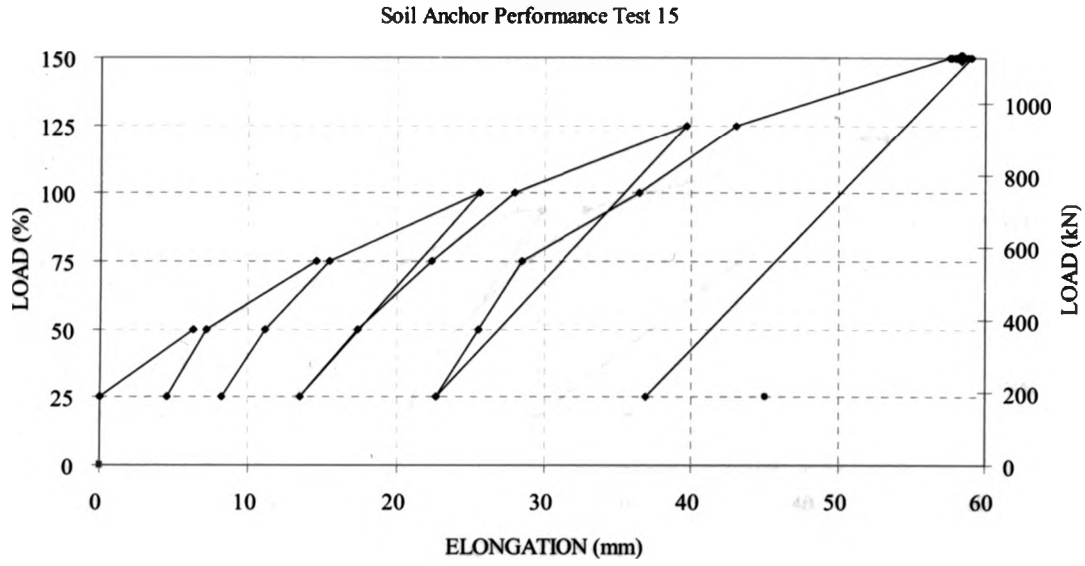

Figure C.15 *Tieback Test # 15, Project 2004.88(CFA)*

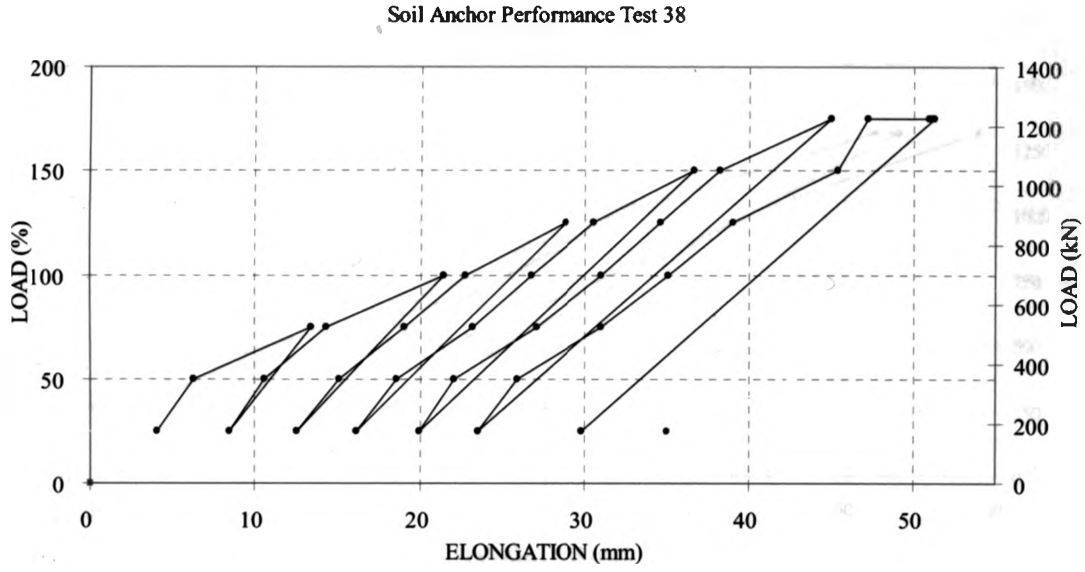

Figure C. 16 *Tieback Test # 38, Project 2004.88(CFA)*

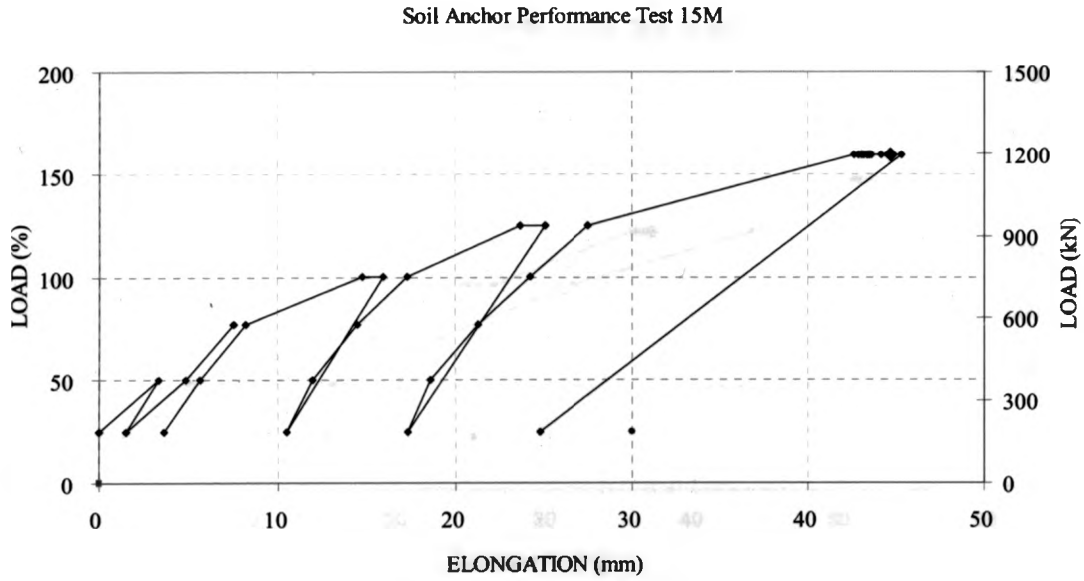

***Figure C.17** Tieback Test # 15M, Project 2005.05(RDD)*

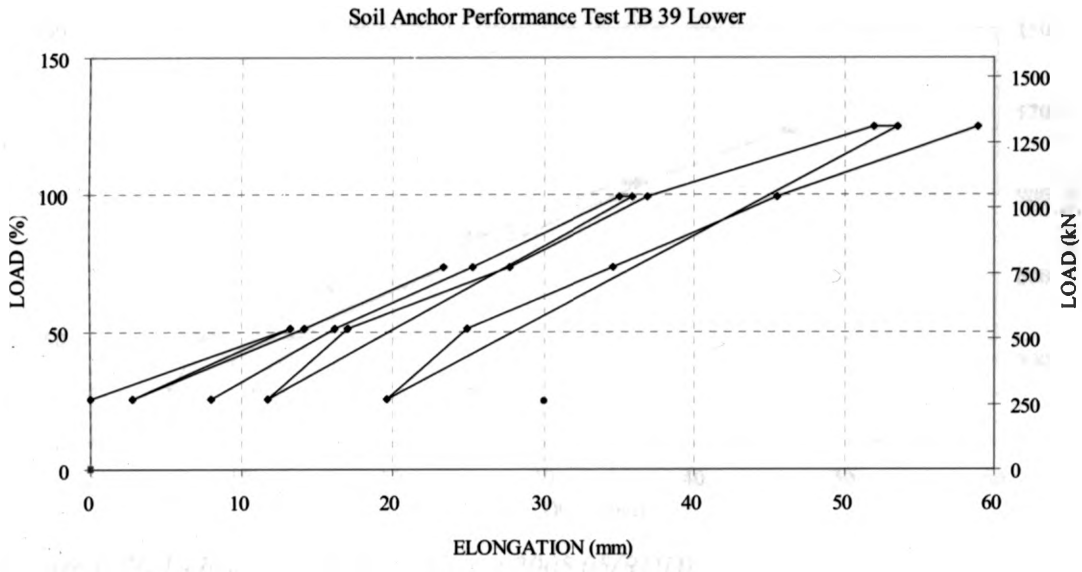

***Figure C.18** Tieback Test # 39L, Project 2005.05(RDD)*

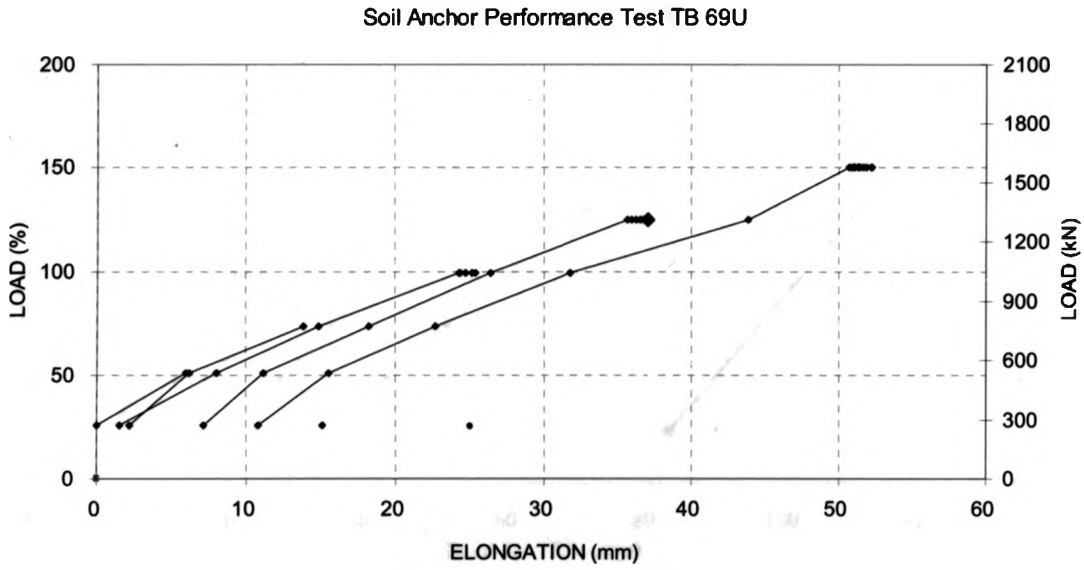

Figure C.19 *Tieback Test # 69U, Project 2005.05(RDD)*

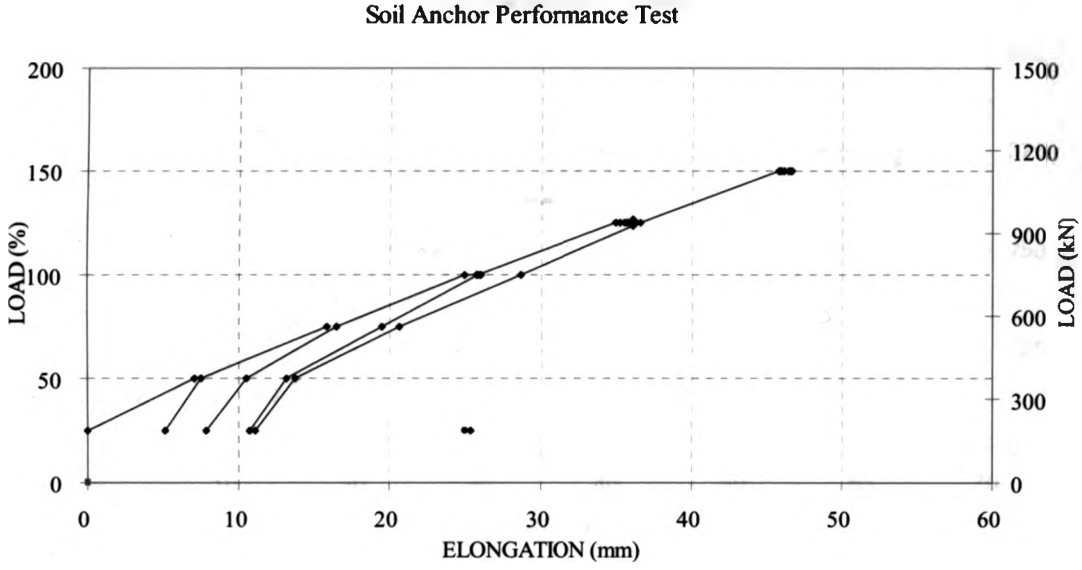

Figure C.20 *Tieback Test # 80U, Project 2005.05(RDD)*

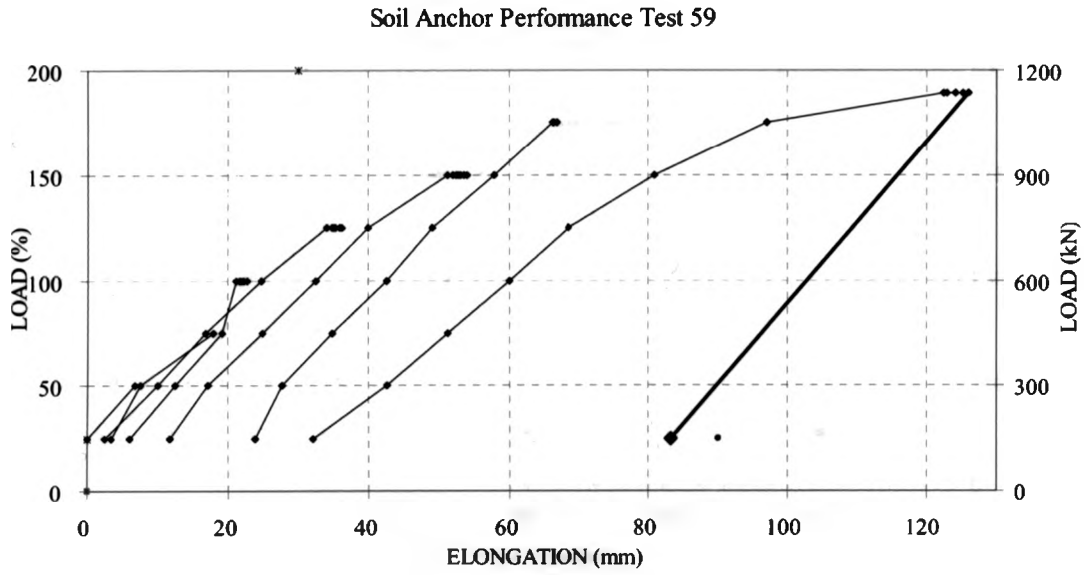

Figure C.21 *Tieback Test # 59, Project 2005.68(CFA)*

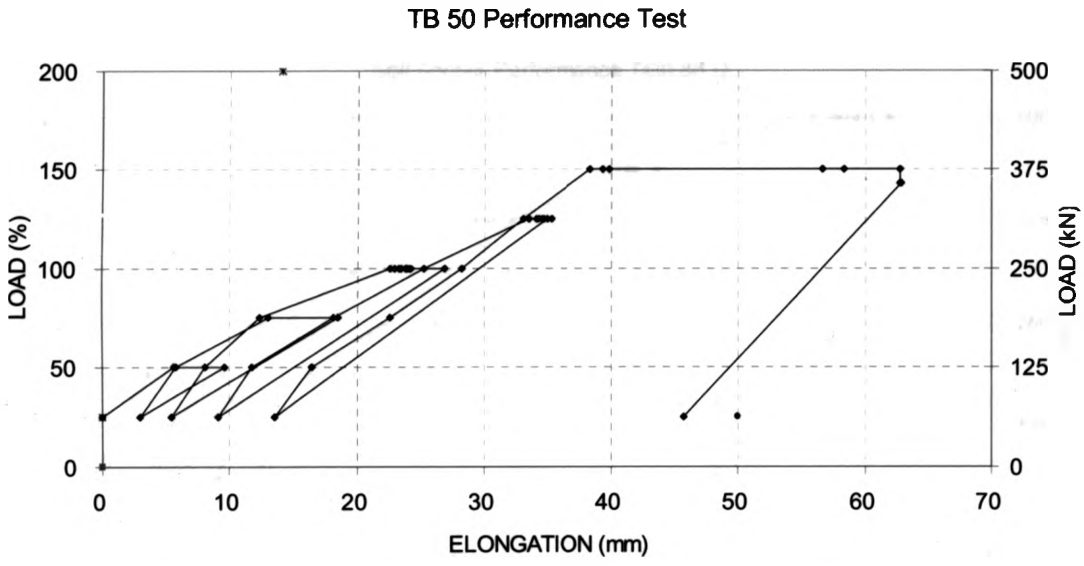

Figure C.22 *Tieback Test # 50, Project 2006.89(RDD)*

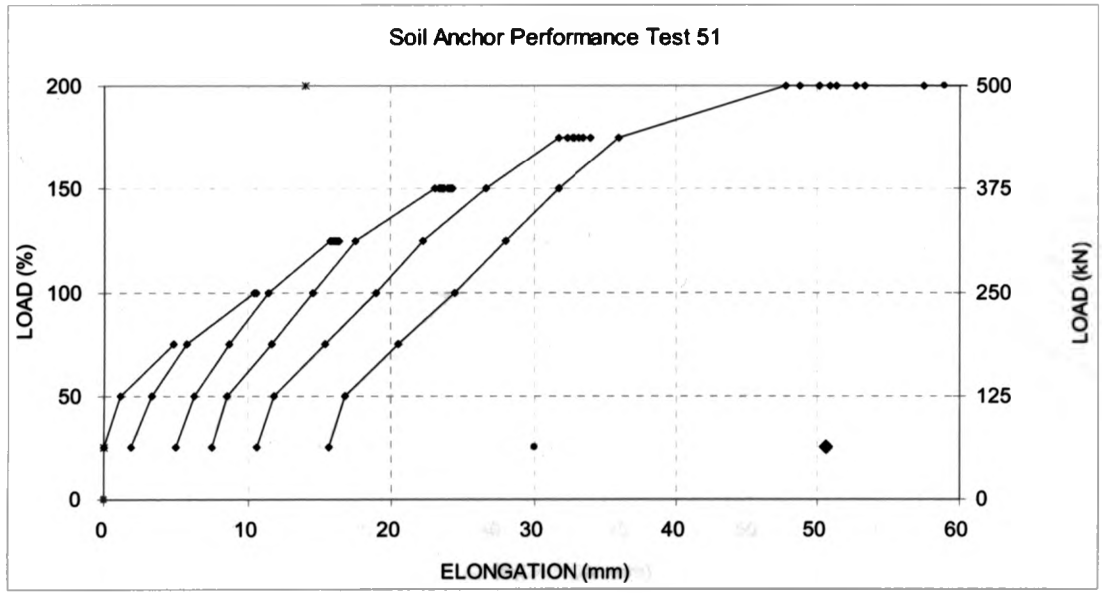

Figure C.23 *Tieback Test # 51, Project 2006.89(RDD)*

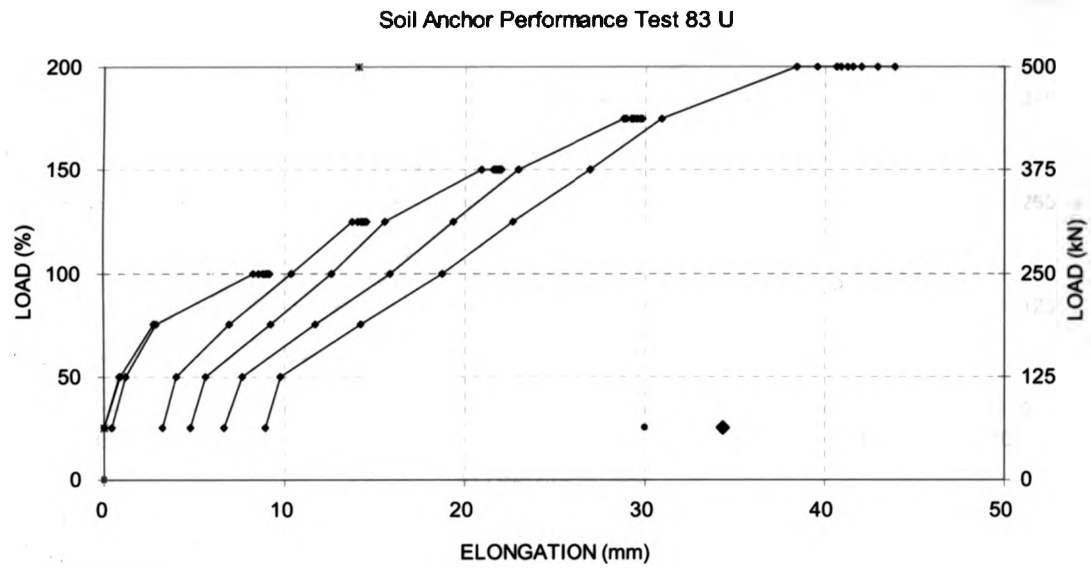

Figure C.24 *Tieback Test # 83U, Project 2006.89(RDD)*

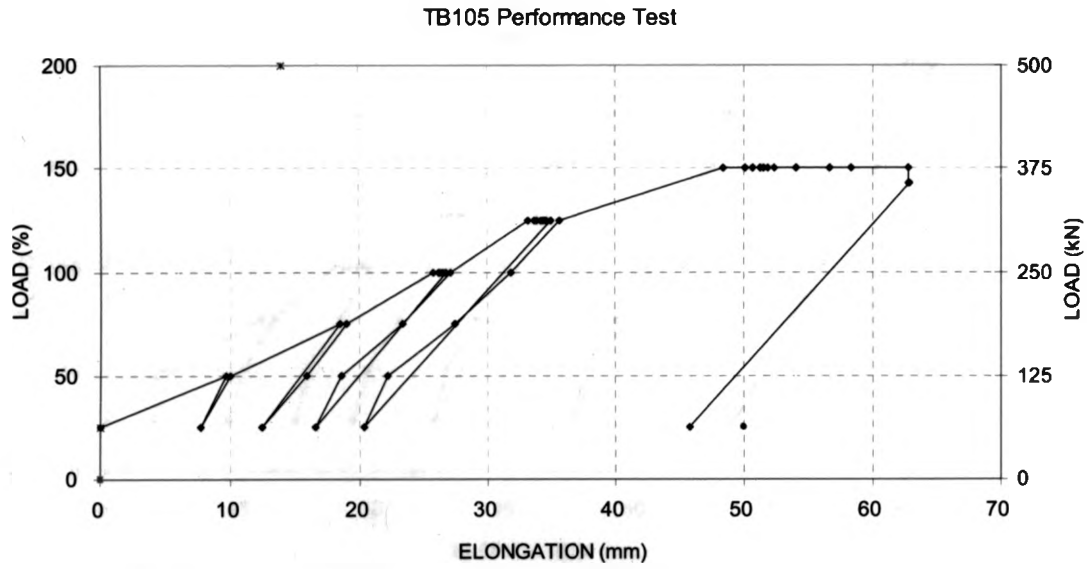

Figure C.25 *Tieback Test # 105, Project 2006.89(RDD)*

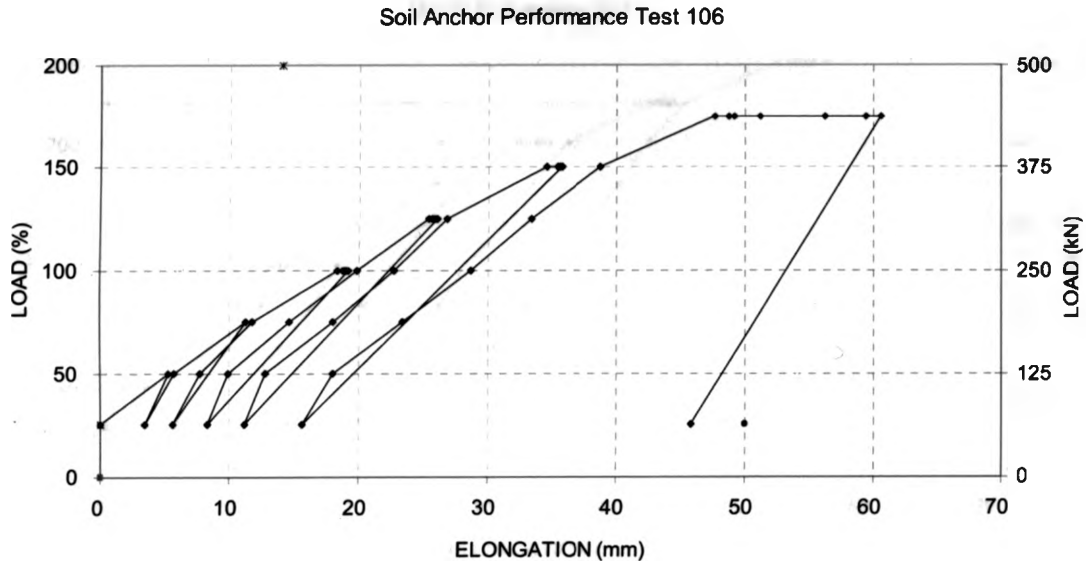

Figure C.26 *Tieback Test # 106, Project 2006.89(RDD)*

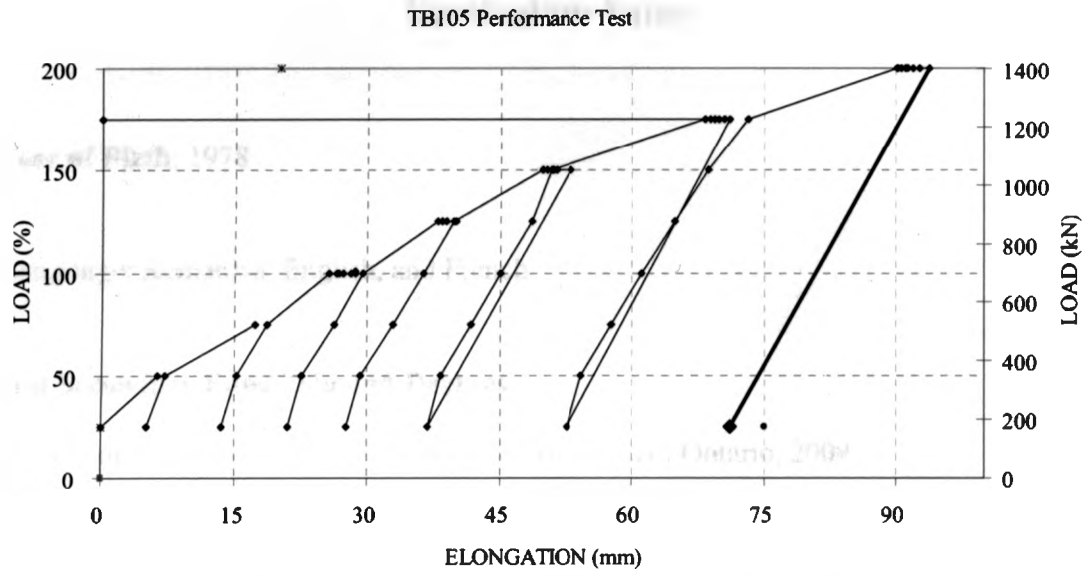

***Figure C.27** Tieback Test # 105, Project 2006.128(CFA)*

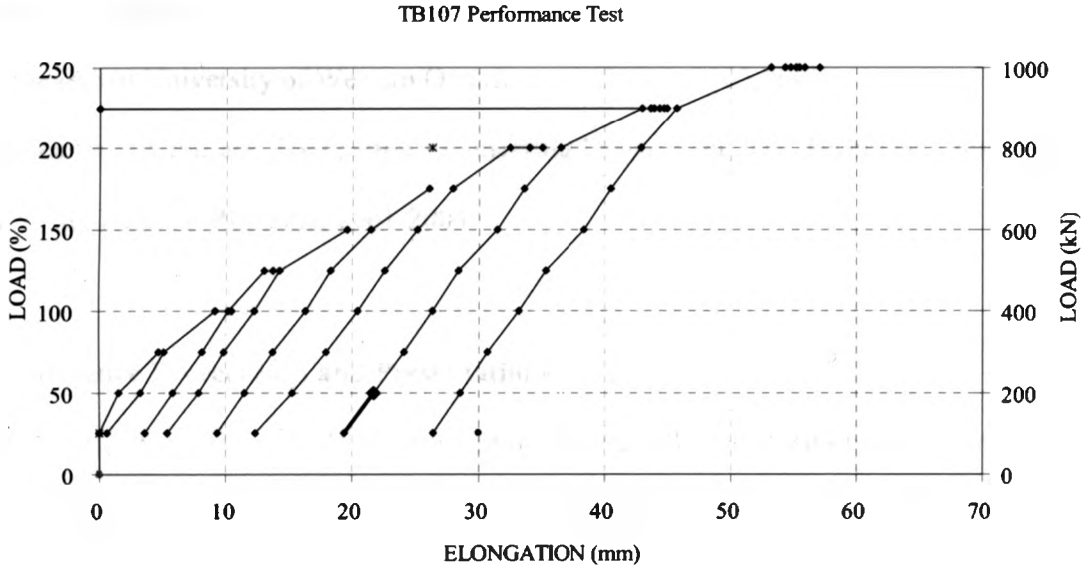

***Figure C. 28** Tieback Test # 107, Project 2006.128(CFA)*